ROCK TEXTURES AND MICROSTRUCTURES RELATED
TO CATACLASTIC PROCESSES

by

Helen Elizabeth Moore, MSc, FGS.

March, 1980.

A thesis submitted for the degree of Doctor of Philosophy
of the University of London

Geology Department,
Imperial College,
LONDON, SW7.

ABSTRACT

This thesis is concerned with faulting in quartzo-feldspathic crust, in particular that which is controlled by elastic and frictional processes which lead to the formation of the cataclastic series of fault rocks. Theoretical aspects of fault initiation, reshear and geometry are considered along with the modes of fault slip, fault displacement and earthquake source instabilities that are involved in the faulting process in the upper 10 to 15 km of the crust. The energy balance in faulting, state of stress in the crust, fault rocks and conceptual fault zone models are discussed and related to results from friction sliding experiments.

Sections along the Walls Boundary Fault zone, Shetland Islands, and a series of low angle reverse faults in the Moine Thrust zone at Loch Eribol, Sutherland, have been studied in detail to gain an understanding of the intermediate depth processes accompanying fault slip from their record in the structures and textures of the fault rocks.

Textural descriptions of the cataclastic rocks are given. Rocks from both areas show the importance in natural fault zones of inter- and post-slip fault strengthening and healing brought about by pressure solution, hydrothermal alteration and metamorphic grain growth and recrystallisation. These are not considered in experimental frictional sliding.

A series of experiments have been performed to assess the importance of frictional heating during faulting. Theoretical analysis and these experiments show that fractures may result from both steep, transient thermal expansion in polycrystalline aggregates, but they are restricted to a few centimetres from the fault's surface. This, when added to the mechanical effects of fault slip, provides another mechanism for the development of gouge which does not require the presence and interaction of asperities, central to many current hypotheses.

TABLE OF CONTENTS

LIST OF FIGURES

LIST OF TABLES

LIST OF PLATES

ACKNOWLEDGEMENTS

CHAPTER 1

INTRODUCTION

This thesis is concerned with faults and faulting in the upper 10 to 15 km of quartzo-feldspathic crust. Central to the thesis is the belief that by studying the structures and deformation textures of rocks in ancient, deeply eroded fault zones, information can be gained on the processes involved in faulting over a range of depths. This information will supplement that gained from surface observations in currently active fault zones.

The project falls into three parts based on theory, fieldwork and experiment. Chapters 2 to 5 are concerned with theoretical aspects of faulting. Current theories of faulting are based upon the premise that, in the upper 10 to 15 km of the crust at least, faulting is friction controlled. This is strongly supported by the widespread application of Anderson's theory of faulting (Chapter 2) which is consistent with a linear friction law (Byerlee, 1978), derived from experiments on sliding friction in rocks (Chapter 3). As a result of these experiments, intermittent seismic slip on faults has been equated to experimental stick-slip and aseismic fault creep to stable sliding (Brace and Byerlee, 1966). For this experimental work to be relevant to faulting, the laws of friction must be scale-independent and the geometrical problems inherent in all experimental configurations, unimportant.

The energy budget of faulting is considered in Chapter 4. For strike-slip faults the bulk of the elastic energy released during a seismic slip increment is divided between the energy converted to heat, the radiated seismic energy and the fracture surface energy. The partitioning of energy between these sinks depends upon the physical conditions under which slip takes place. The frictional heat capability of a fault is strongly dependent on the tectonic stress levels under which faulting occurs. There is controversy over whether these are low ($<$ 10 MPa) or high (about 100 MPa (Hanks, 1977)). Although it is possible for frictional heating during seismic slip, to raise the temperature of a fault's surface to melting point (McKenzie and Brune, 1972; Sibson, 1975), surface temperature rises of a few hundred degrees centigrade are likely to be more common (Cardwell et al., 1978). Melting will only occur when slip is confined to a narrow, planar zone, in the absence of pore fluids and at fast slip rates with comparatively high

levels of shear resistance on the fault (Sibson, 1973).

The temperature distribution and associated thermal stresses adjacent
to a fault plane which may potentially arise from frictional heating
are considered in Chapter 5. The zone in which thermal damage is expected
is narrow. The maximum width of this zone (0.1 m) is achieved when the
fault's surface is at melting point, the maximum attainable temperature.
The microfracturing in this thermally affected zone will, in natural
faults, facilitate the plucking and rotation of mineral fragments from
the sidewall of the fault, into the gouge zone that results from mechanical
wear.

Friction controlled deformation, which is dominant at low ambient
temperatures (below between $250°$ and $300°C$) in quartzo-feldspathic crust
(Chapter 6), consists primarily of fracture and frictional sliding.
At higher ambient temperatures, at depths which correspond to lower
greenschist metamorphic conditions under normal geothermal gradients,
dislocation controlled intracrystalline plastic deformation becomes
increasingly important. The fault rocks which result from different
modes of fault slip under varying crustal conditions are also discussed
in Chapter 6.

Two major problems arise when natural fault zones are compared with
theoretical or experimental models. The first is the geometrical hetero-
geneity of natural fault zones, which generally consist of several sub-
zones across which movement occurs. Secondly, the textures seen today
in ancient fault zones are the product of the entire movement history of
the fault. This probably comprises a great number of slip increments,
each presumably accompanied by a build-up and release of stress. With
progressive displacement over a long period of time, successive slip
increments may have occurred under differring environmental conditions;
this problem is especially severe on major faults with a large component
of dip-slip. In this type of study, there is a problem over whether
the observed microstructural features are the cumulative product of all
episodes of deformation or whether they result from textural overprinting
by the last deformation phase or phases.

A field-based textural study of two contrasting fault zones is
discussed in Chapters 7 and 8. The first of these is the Walls Boundary
Fault Zone, where it affects granitoid rocks in the Shetland Islands.
This major, dextral transcurrent fault is considered by Flinn (1961, 1969)
to be the northern continuation of the Great Glen Fault. Textures from

this region are compared with those developed adjacent to a series of thrusts cutting Cambrian quartzite in the Moine Thrust Zone at Loch Eribol, Sutherland.

The rock textures of these fault zones are essentially cataclastic in nature. In comparison with rocks of the mylonite series which have been extensively discussed in the geological literature (e.g. Christie, 1960, 1964; Bell and Etheridge, 1973), rocks of the cataclasite series, although widespread, have been neglected, possibly because of their intrinsically "unstructured" appearance. This neglect is surprising in view of their importance in being derived from the seismically active regions of a fault zone.

From the microstructural study it is apparent that the cataclastic textures do not result solely from fault slip but are extensively modified by processes occurring between and after slip episodes. The importance of pressure solution, hydrothermal alteration and metamorphic reactions are all very important. These factors are not considered in short term rock deformation experiments. The passage of fluids through these zones is strongly indicated and, by hydrothermal and metamorphic processes, provides a mechanism for healing and strengthening the fault zone. This effect is potentially more powerful than any time-dependent effect yet investigated in the laboratory.

In Chapter 9, a series of experiments are described in which the degree of thermal damage resulting from dissipation of frictional heat, without the effects of shearing, is assessed. Frictional heating on a fault is simulated by the electrical dissipation of energy across a modelled fault. The experimental results support theoretical predictions (Chapter 5) that thermal damage is restricted to microfracturing of a narrow zone adjacent to the fault's surface.

CHAPTER 2

FAULTS AND FAULTING

Throughout this thesis the three mutually perpendicular principal stresses are denoted by $\sigma_1 > \sigma_2 > \sigma_3$. Positive values for these stresses signify compression.

2.1. Fault Geometry

Anderson (1951), put forward a simple theory to explain many commonly observed features of faults in the upper crust, especially their attitude in relation to their slip sense. He suggested that because the earth's surface is a free boundary, parallel to which there can be no shear tractions, one principal stress must be nearly vertical and the other two nearly horizontal in country with other than Alpine topography. Combining this boundary condition with the Mohr-Coulomb criterion for brittle shear failure (Section 2.1.2.), whereby faults form at about $30°$ to σ_1, three types of fault occur in homogeneous material depending which of the principal stresses is vertical (Fig. 2.1.).

1. If σ_1 is vertical, normal faults result, dipping at about $60°$ with dip-slip displacement.

2. If σ_2 is vertical, transcurrent or wrench faults result. The fault planes are nearly vertical and the displacement is predominantly strike-slip.

3. If σ_3 is vertical, thrust faults result. The fault planes dip shallowly at less than $45°$ and displacement is predominantly dip-slip.

Stress measurements, in deep mines in South Africa (McGarr and Gay, 1978), have shown that there are significant departures from the assumption that one of the principal stresses is always vertical. However, geometrically, Anderson's theory describes the orientations and movement sense of faults seen in many areas (King, 1978; Price, 1966).

2.1.2. Importance of Anderson's Theory

Anderson's theory depends upon the boundary condition imposed by the earth's surface making one principal stress vertical and the adoption of the Mohr-Coulomb failure criterion for fault initiation:

σ_1

σ_2

σ_3

σ_2

σ_3

σ_3 σ_1

σ_3

σ_1

σ_2

σ_1

σ_2

σ_3

σ_1 σ_1

σ_2

σ_2

σ_3

σ_1

Normal   **Transcurrent**   **Thrust**
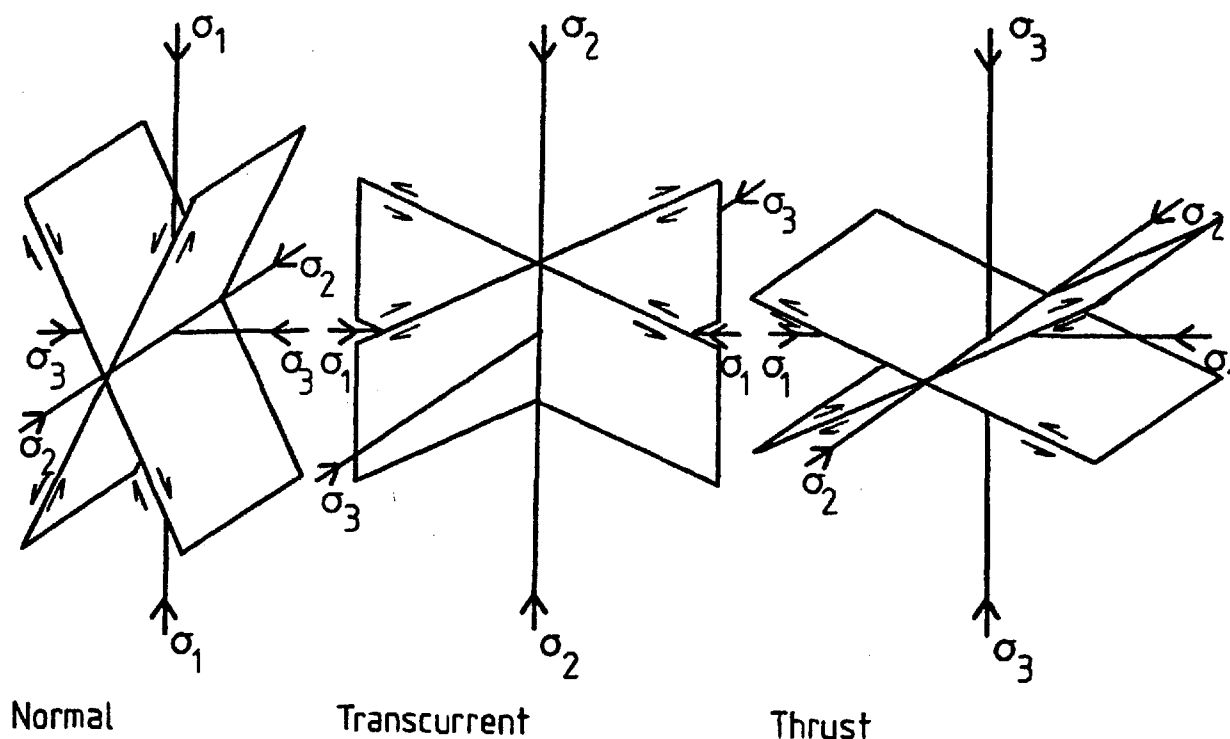
Fig. 2.1. The three fault types as outlined by Anderson,(1951)

$$\tau = S_0 + \mu_i(\sigma_n - p) \tag{2.1}$$

where τ = shear stress acting on failure surface

S_0 = cohesive shear strength

μ_i = coefficient of internal friction

σ_n = normal stress

p = pore fluid pressure

The inclusion of the pore fluid pressure term in equation (2.1) assumes that the law of effective stress holds (Hubbert and Rubey, 1959).

In fact the adoption of any linear frictional criterion, with or without a term for the cohesive shear strength, leads to the same relationship between fault orientation and slip sense (Hubbert, 1951). It is because Anderson's theory is successful in explaining the orientations of many faults, that it is reasonable to infer that some form of frictional criterion controls shear failure in at least the upper crust. This is strongly supported by experimental rock deformation tests (Chapter 3).

2.2. Reshear and the Development of Minor Structures.

When continued slip on faults is considered, the stress theories which predict the initial orientation of the fault no longer apply. Reshear on an established fault can occur under a different stress field than that required for its initiation (McKenzie, 1969).

Many minor fractures associated with a major fault are thought to be kinematically controlled by motion being constrained to the weakened fault zone. This induces local stress fields in which the small fractures develop. The first of these fractures recognised were Riedel shears but more detailed experimental work (Logan et al., 1979) has suggested that a complex fracture array may develop in a fault zone (Fig. 2.2.). The relative abundance of the fractures, in models, in decreasing order is generally: R_1, R_2, X, P and T.
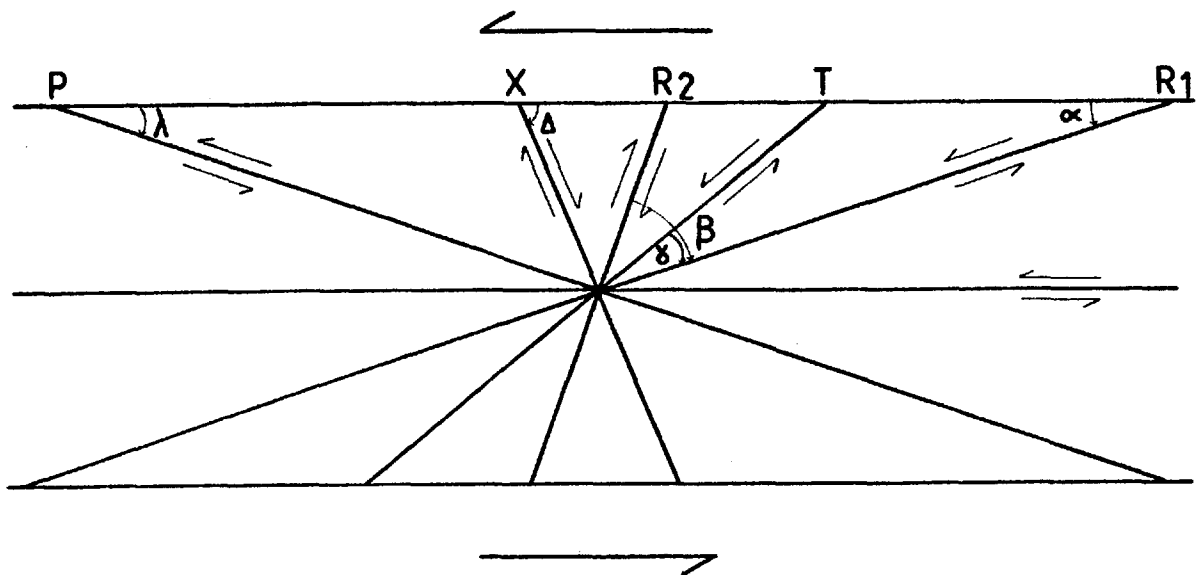
	Average
∝	15°
β	53°
ծ	23°
∆	72°
λ	16°

Fig. 2.2. Kinematically controlled minor fractures in experimental fault zones (after Logan et al., 1979).

2.3. Complexity of Faults

Depending upon the scale of deformation, the size of faults varies through many orders of magnitude, from an edge dislocation in a single crystal, to Benioff zones or transform faults at plate boundaries. In general, the surficial expression of a major fault

at any geological scale is a linear array of smaller faults. The
pattern of these relatively small faults together form a fault zone.
It is from differential movement across these faults that the bulk
displacement occurs. One remarkable feature of fault zones is their
striking geometrical similarity regardless of ... scale (Tchalenko,
1970). Ancient fault zones exhumed by erosion have a similar com-
plexity, commonly consisting of an anastomosing or braided network
of intensely deformed rock which is often crossed by discrete fault
planes (Chapter 6).

Many factors probably contribute to the complexity of crustal
fault zones, but some comparison may be drawn with laboratory experi-
ments where, as a result of increasing confining pressure there is a
transition from slip on a single or conjugate pair of discrete faults,
through slip on several sub-parallel conjugate faults, to ductile
barrelling accomodated by pervasive cataclastic flow accompanied by
slip on many tiny shears (Fig. 2.3.) (Griggs and Handin, 1960).

Thus the complexity of fault zones results not only from the
heterogeneity of natural rocks but also from both kinematically con-
trolled minor fractures and the conditions under which the fault
initiated and developed.

It is of fundamental importance when interpreting a faulted
region, to consider not just a single fault but the entire zone of
which the fault is a part. Tectonic interpretation of large-scale
faulting requires the study of very large areas. If the overall
deformation is known, investigation of small scale structures in
regionally significant areas may give information on the mechanical
processes involved in faulting.

2.4. Modes of Fault Slip

Observations show that movement on faults may occur with or
without the radiation of elastic energy as seismic waves, and the
different slip modes may be classified by their rise-time (the time
for , slip to be completed at a point on the fault). In the
case of seismic faulting, where the rise-time is typically of the order
of 1 to 10 secs. [Table 2.1.,(Geller, 1976)], displacement is achieved
by sudden rupture which propagates over part or all of the fault's
surface. Rupture is accompanied by release of shear stress on the
fault and the radiation of seismic energy. In aseismic faulting
with, effectively, an infinite rise-time, steady movement occurs on the

	1	2	3	4	5
Typical strain before failure or faulting (%)	<1	1-5	2-8	5-10	>10
Compression $\sigma_1 > \sigma_2 = \sigma_3$					
Extension $\sigma_3 < \sigma_1 = \sigma_2$					
Typical stress-strain curves					
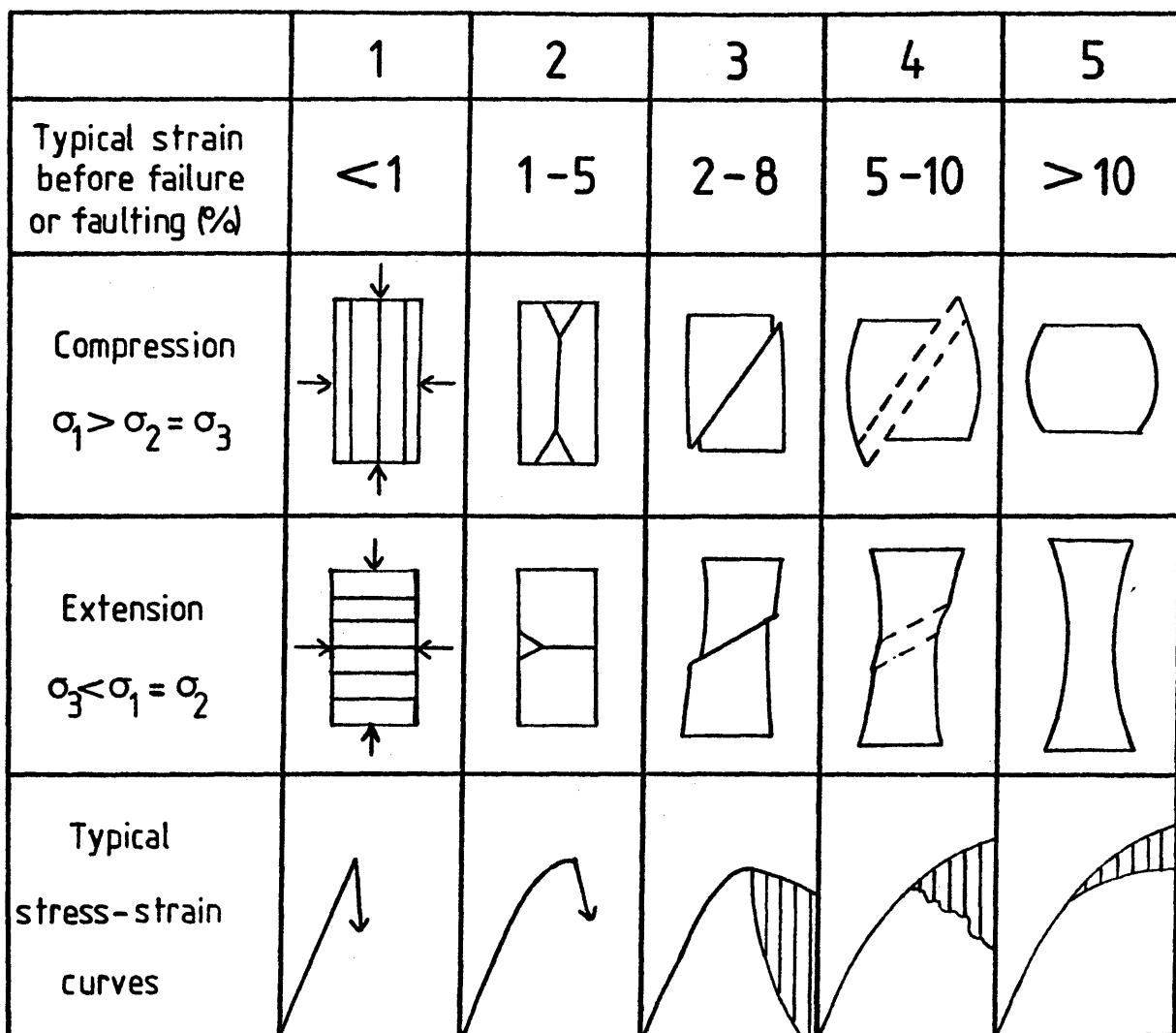
Fig. 2.3. Schematic representation of the spectrum from brittle
fracture to ductile flow, with typical strains before
fracture and stress-strain curves for uniaxial compression
and extension (after Griggs and Handin, 1960).

Shaded portion of stress-strain curves represents possible
variation.

fault in response to the shear stress, without seismic radiation
(Sacks et al., 1978; Kanamori and Stewart, 1979). It is coming to
be realised that slip modes may also exist with intermediate rise-
times, one example being episodic creep (Scholz et al., 1969). After-
slip on faults may accomodate significant displacement. Afterslip is

a period of aseismic creep that occurs in the weeks or months follow-
ing seismic slip. It may produce displacements of up to 50% of those
achieved during the seismic slip increment (Bucknam et al., 1978).

Table 2.1

Earthquake Source Data (after Geller, 1976)

Location	Date	Ms(Mw)	Mo $(x10^{20}N.m)$	L(km)	W(km)	$\bar{u}(m)$	T(s)	$\bar{u}/T(ms^{-1})$
Kanto	1.9.23	7.9*	7.6	130	70	2.1	7	0.3
Tango	27.3.27	7.75	0.46	35	13	3.0	6	0.5
Sanriku	2.3.33	8.4*	43	185	100	3.3	7	0.47
Long Beach	11.3.33	6.25	0.028	30	15	0.2	2	0.10
Tottori	10.9.43	7.4	0.36	33	13	2.5	3	0.83
Fukui	28.6.48	7.3	0.33	30	13	2.0	2	1.0
Kern County	21.7.52	7.7	2	60	18	4.6	1	4.6
Kitamino	19.8.61	7.0	0.09	12	10	2.5	2	1.25
Wakasa Bay	27.3.63	6.9	-0.033	20	8	0.6	2	0.3
Parkfield	28.6.66	6.4	0.032	26	7	0.6	0.7	0.86
Saitama	1.7.68	5.8	0.019	10	6	0.92	1	0.92

* denotes Mw from Kanamori (1977).

Ms = magnitude derived from 20 s period surface waves

Mw = moment derived magnitude

L = length of area on fault undergoing slip

$\bar{u}$ = average fault slip

T = rise-time

W = width of area on fault undergoing slip

2.5. Earthquake Source Instabilities.

Physically, an earthquake must be the result of a sudden
mechanical instability. A mechanical instability arises when the
resistance to deformation of the deforming material begins to decrease
with further deformation (Jaeger and Cook, 1971). In the case of a
sudden instability, the stress required to deform the material drops
very rapidly and elastic energy is radiated.

Several different source instabilities have been suggested;
brittle shear fracture of intact rock in compression (Reid, 1911),
frictional stick-slip (Brace and Byerlee, 1966), shear melting (Orowan,
1960; Griggs and Baker, 1969), creep instability (Orowan, 1960) and
phase changes (Bridgeman, 1945; Benioff, 1964; Griggs and Handin, 1960).
Of these, frictional stick-slip and brittle fracture are thought to

be important at shallow crustal levels, although the remaining instabilities may be important for deep focus earthquakes where fracture or frictional sliding are unlikely.

To this point it has been assumed that earthquakes result from slip on faults. Evidence for this assumption comes from geodetic surveys, direct observation of surface fault breaks and the analysis of seismic radiation, which shows the earthquake source to be a single or double-couple type initial disturbance (Stacey, 1977).

2.6. Earthquake Fault Displacements

Geodetic surveys show that aseismic creep rates vary from a few millimetres to several centimetres per year. Displacements occurring during seismic slip have only been directly measured on faults which cut either the earth's surface or mine workings, but can be estimated indirectly from instrumental determinations of seismic moment, Mo.

$$M_o = G.A.\bar{u} \qquad (2.4)$$

where G = modulus of rigidity

$\bar{u}$ = average fault slip

A = rupture area

For seismic slip there is a broad relationship between earthquake magnitude, M_s or M_w (a measure of the radiated energy, Richter, 1958; Kanamori, 1977) and slip (Table 2.2.). This relationship is only an approximation but shows that a finite fault displacement of, say 10 km, results from a very great number of slip increments.

Table 2.2

General Relationship between Slip and Earthquake Magnitude

$M_s^-(M_w^-)$	$\bar{u}(m)$
9	> 7
8	3-7
7	0.5-3
6	0.05-0.5
5	< 0.05

Gutenberg and Richter (1954) proposed an empirical magnitude-frequency relation:

$$\log N = a - bM_s^- \qquad (2.5)$$

where   N = number of shocks greater than magnitude Ms.

        a and b = constants.

This relationship has been found to hold for both earthquakes and
microfractures (Scholz, 1968; Wyss, 1973). Although it predicts
that small earthquakes are much more common, it is thought that larger
earthquakes account for most of the displacement across a fault
(Stacey, 1977). Davies and Brune (1971) have suggested that 70% of
the total displacement at most plate boundaries is accommodated by
earthquakes of magnitude, (M_s), 7 and greater.

CHAPTER 3

FRICTION

3.1. Introduction

It is now generally accepted that most shallow crustal earth-
quakes are caused by sudden slip on pre-existing faults, which arises
from a frictional instability (Dieterich, 1974). The laboratory
study of rock friction, as well as fracture, is therefore an important
contribution to the physical understanding of the earthquake source
mechanism. Knowledge of the parameters controlling frictional sliding
between two rock surfaces, should shed light on those parameters which
influence and control the faulting process. The work of Bowden on the
friction of metals is fundamental to rock friction and is briefly
reviewed.

3.2. Metallic Friction

Friction is a measure of the resistance to sliding that exists
between two surfaces. There are two empirical laws of friction:

1. Friction is independent of the area of contact between the two
   solids.

2. Friction is proportional to the load W, normal to the surface
   between the two solids.

Together these laws form Amontons' Law of Friction:

For any two bodies with an approximately planar surface of contact,
pressed together, the ratio of friction, F (or the force required to
start sliding) to normal load, W is a constant called the coefficient
of friction, μ (Fig. 3.1).

$$F = \mu W \tag{3.1}$$

Dividing this relationship on each side by the interface area yields:

$$\tau = \mu \sigma_n \tag{3.2}$$

where τ = shear stress and σ_n = normal stress acting between the
surfaces during sliding. Coulomb distinguished between the coefficient
of static friction (μ_s) and dynamic friction (μ_k) and defined what is
occasionally called the third law of friction: Kinetic friction is
nearly independent of the speed of sliding. Two possible explanations
for the existence of friction were proposed by Coulomb. The first,
that friction is due to adhesion of the two surfaces, he rejected as

W

F
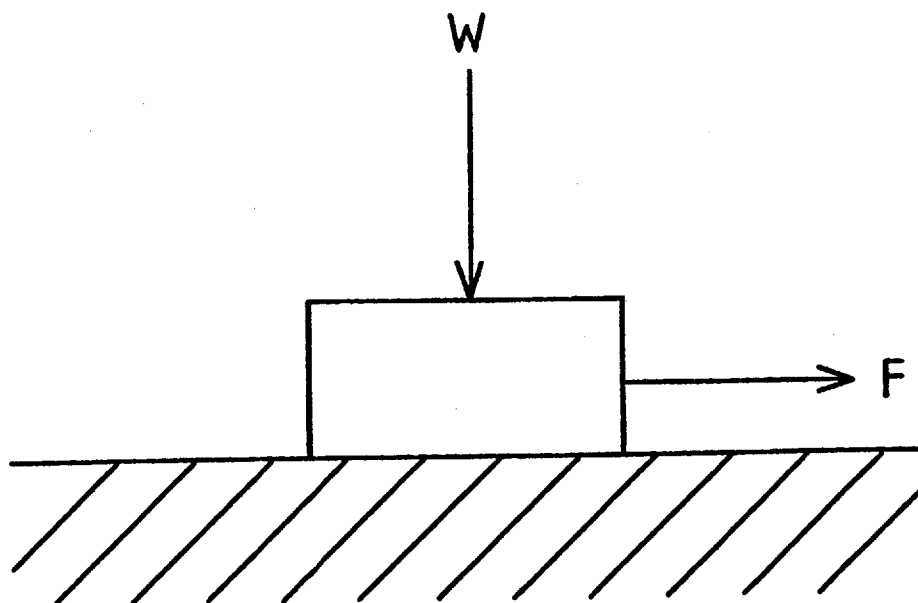
Fig. 3.1. Simple method to measure friction.

the frictional force to start sliding is independent of the surface
area. The second explanation was based on the fact that all surfaces,
however smooth, are in fact rough on a fine scale and are made up of
many protuberances or asperities. Coulomb thought that these asperities
interlocked and the frictional force represented the work done in
lifting the load on the surface over their summits.

The work of Bowden and Tabor (1967) showed that for metallic
friction, Coulomb's first explanation was correct. Their experiments
show that when two surfaces are held in intimate contact, under a
normal load, there is cold welding at the tips of the asperities and
the frictional force is the force required to shear these junctions.
This suggests that friction should be related to the number and size
of welded junctions rather than the normal load (Amontons' Law). Two
surfaces will touch only at the tips of their asperities and the area
of real contact may be less than one thousandth of the apparent area
of contact. The area of real contact depends upon the normal load
across the surface which determines the amount of plastic deformation
the asperities undergo (Fig. 3.3), and it is because of this factor
that Amontons' Law holds.
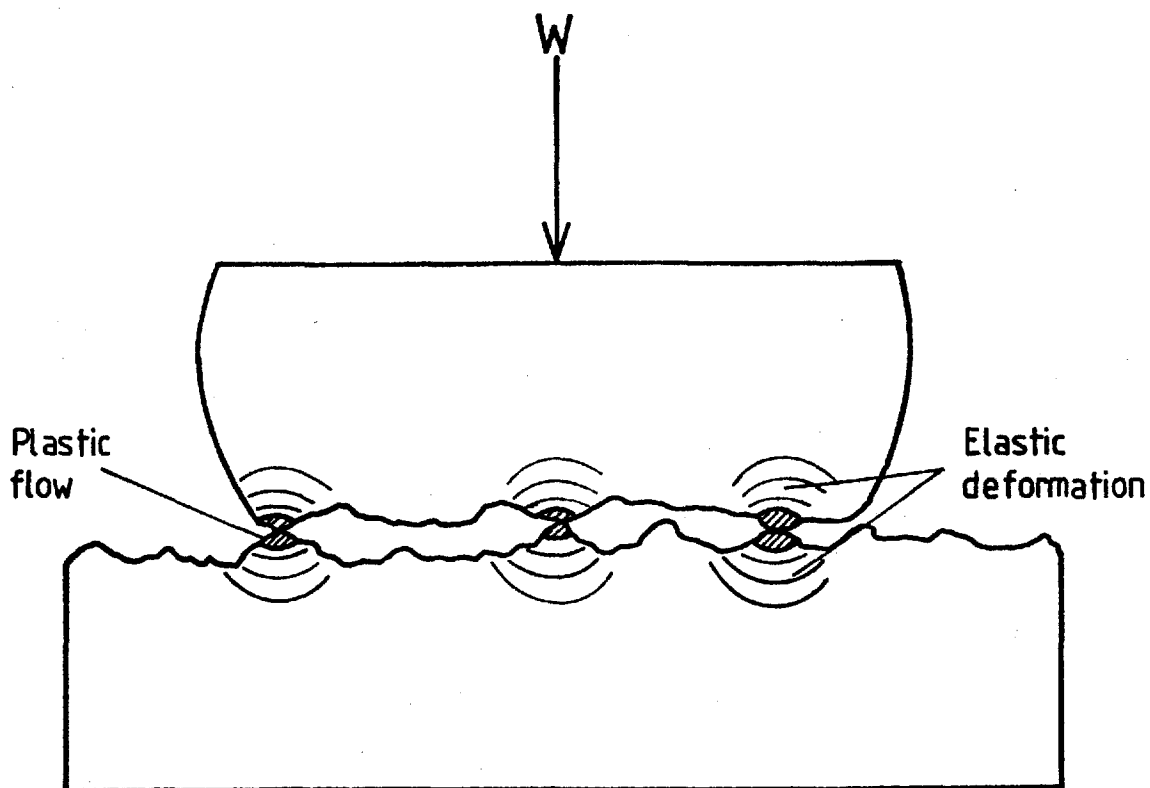
Fig. 3.2. Sketch showing plastic and elastic deformation at the points of real contact (after Bowden and Tabor, 1967).

In metals, surface wear results from the shearing of the welded junctions. Lubrication of metallic surfaces greatly reduces both μ and the amount of surface damage. In fact, if two metallic surfaces are cleaned under vacuum, thereby removing the chemically bound oxide film (generally some tens of angstroms thick) sliding between the surfaces is impossible. Under these conditions, the area of real contact grows until it equals the geometric area. If the moving surfaces are completely separated by a continuous film of lubricant, the resistance to motion arises solely from the viscosity of the lubricant itself. Surface wear in this case is greatly reduced since no welded junctions occur. Thus, for metals, the frictional behaviour is greatly modified by surface contaminants and fluids.

3.3. Rock Friction

The theory of Bowden and Tabor requires that the material being considered can flow plastically, will weld on contact and that the material near the asperity tips fails in shear. It is known that

under shallow crustal conditions where much earthquake faulting takes place and where temperatures are generally below about 300°C, most silicate rocks behave in a brittle manner, on the grain to grain scale, when deformed under fast strain rates (Sibson, 1977b).

Rock friction experiments are performed to simulate movement on pre-existing faults under crustal conditions. While much current work is based upon that of Bowden and Tabor, many different approaches have been used to investigate the frictional behaviour peculiar to rock.

3.3.1. Rock Friction Experiments

When two surfaces of rock slide over one another in laboratory experiments, two main types of motion are observed: smooth continuous displacement (stable sliding), and a jerky motion where the surfaces lock together for a period, then suddenly slip (stick-slip). In this latter process, some or all of the driving shear stress is released and elastic energy is radiated. Typically, the amplitude of the stress drop in one cycle of stick-slip, amounts to a fraction of the shearing stress required to cause the sliding. Stick-slip is common in geological materials under a wide range of laboratory conditions. Brace and Byerlee (1966) have suggested that it may be the fundamental process giving rise to intermittent seismic slip on faults. This is an attractive idea, as it could explain why the stress drop calculated for even the largest earthquake is small relative to the frictional strength of most crustal rocks (Hanks, 1977). It also provides a mechanism for spasmodic energy release in material containing many existing fractures. Similarly, stable sliding has been equated with aseismic creep on faults (Byerlee and Brace, 1968; Scholz et al., 1969), although experimentally, low level seismic activity has been recorded accompanying stable sliding in granite (Stesky, 1975). Work by Simkins (1967) has also suggested that displacement in stable sliding is discontinuous on a microscopic scale. It may be that discrimination between stable sliding, episodic sliding (most of the sliding occurring in short spurts with little or no sliding in between, Scholz et al., 1972) and stick-slip is merely a function of the sensitivity of displacement measurements.

Not all the displacement during frictional sliding is manifest in stick-slip events. Stick-slip is commonly preceded and followed

by variable amounts of stable sliding; accelerating premonitory creep
and afterslip. Little is known of the mechanism of premonitory slip.
It was observed on faults only after its recognition in the laboratory.

It is clearly of interest to geologists to discover whether different
physical mechanisms control these different modes of fault movement and
if so, whether distinct deformation features can be recognised in fault
zones and associated with the separate stages of fault slip.

Many types of experiment have been performed to investigate
different features of faulting, ranging from the effect of a single
asperity, to the sliding of large rock surfaces. Experimental tests
performed include slider experiments (Engelder and Scholz, 1976),
direct shear (Jaeger, 1971; Drennon and Handy, 1972), double shear
(Hoskins et al., 1968; Dieterich, 1972; Ohnaka, 1973, 1975), rotary
shear, (Jaeger, 1971), biaxial shear (Scholz et al., 1972) and
triaxial shear (Byerlee, 1967a;Stesky et al., 1974). All these testing
modes suffer from disadvantages which include the major problem of scale.
The experiments involve a single slip increment of at most a few milli-
metres, on faults of a few square centimetres in area. In contrast,
natural faulting involves repeated slip increments, each in the order
of centimetres to metres, occurring over much larger areas (Section
2.5.). In all these methods, displacements occur as rigid body trans-
lations with stress concentrations arising from the geometrical changes
resulting from slip. In view of these problems, it is surprising
how results derived from different experimental configurations, combine
to obey a linear friction law (Section 3.3.3).

3.3.2. The Rider Model

A schematic representation of the experimental stick-slip process
is given in terms of a spring-rider model (Jaeger and Cook, 1971), Fig.
3.3. A rider of mass m, may slide on a rigid surface. The tangential
force required to move the rider is applied through a spring AB. If the
point B is moved at a constant, low velocity v, the force in the spring
increases until it is sufficient to overcome the frictional force
between the rider and the surface. If the rider moves forward at a
velocity greater than v, the force in the spring will decrease and the
rider eventually stop. The rider will remain stationary until the
force in the spring is again large enough to overcome the frictional
force.

The classical explanation for this jerky motion is that static
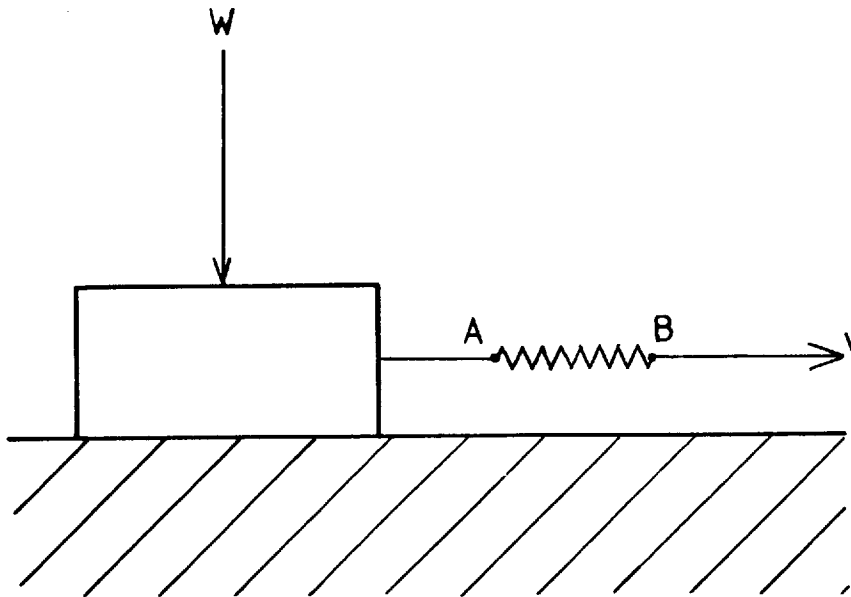
Fig. 3.3. The Rider Model

friction, μ_s, is greater than kinetic friction, μ_k and it is assumed
that once motion begins between the rider and flat, friction falls
instantaneously to the lower value. Nur (1978) describes three physical
models, based on the rider model (Fig. 3.4) which he calls the slip,
stress and stiffness models. In the slip model the displacement,
velocity and time functions are prescribed, whereas in the stress and
stiffness models they are calculated from static and dynamic friction,
and variable friction respectively. The slip model is used in
Chapters 5 and 6 in an analysis of frictional heating.

If the force in the spring is plotted as a function of the dis-
placement of the point B, then the curve that is typically obtained
is shown in Fig. 3.5.. Force increases elastically to point C (stretch-
ing of the spring) where the curve departs from a straight line.
This indicates relative displacement between the rider and flat or
non-elastic deformation of the rider or flat. At point D a maximum
is reached, the rider slides forward and the force in the spring drops
to E. Force in the spring increases again to F where the rider slides
again. If, instead of this stick-slip response to the applied force,
stable sliding were to occur, continuous smooth displacement between
the rider and flat occurs and the force displacement curve follows

	Slip Model	Stress Model	Stiffness Model
displacement			
velocity			
acceleration			
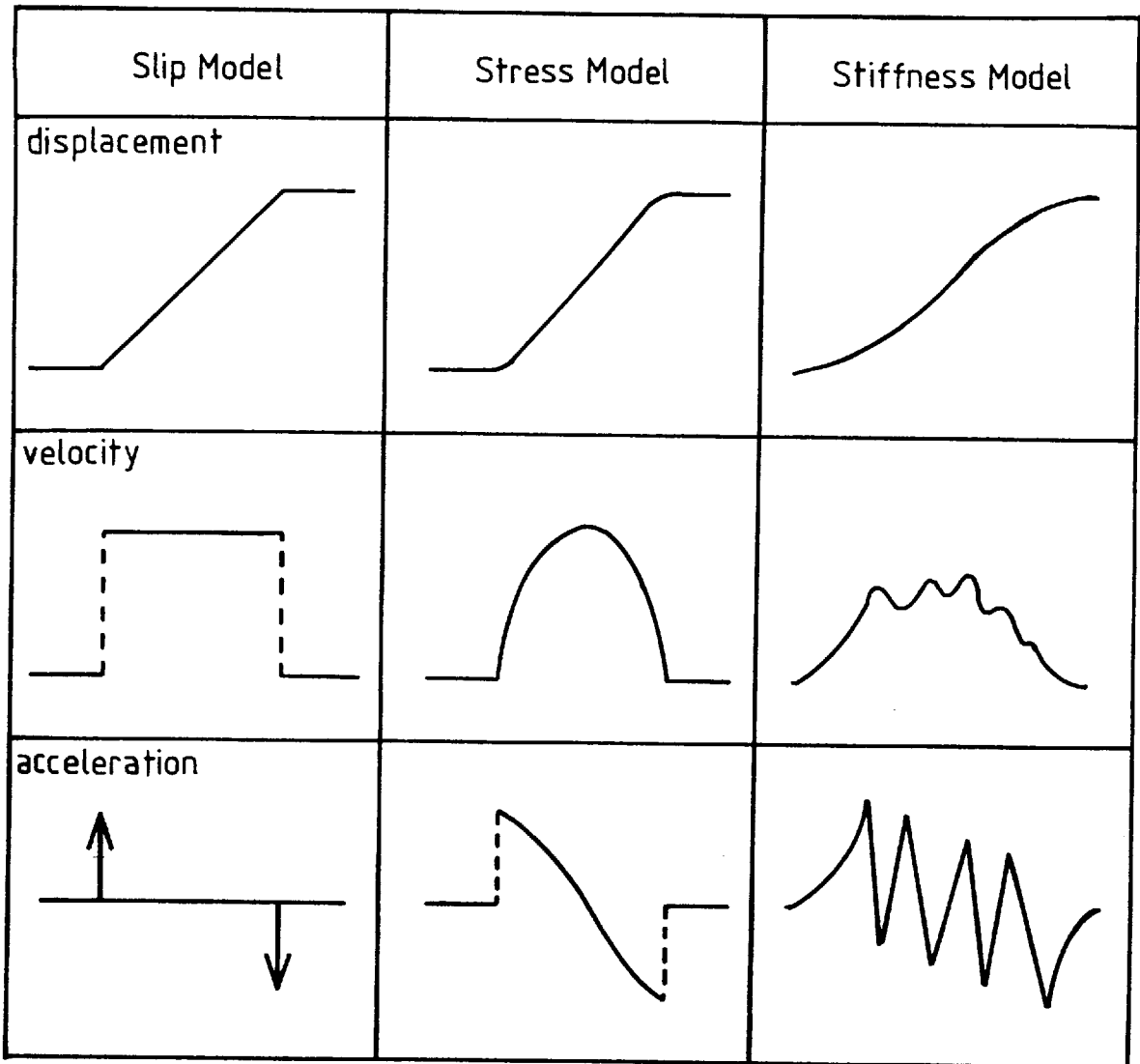
Fig. 3.4. Physical models of fault slip (after Nur, 1978)
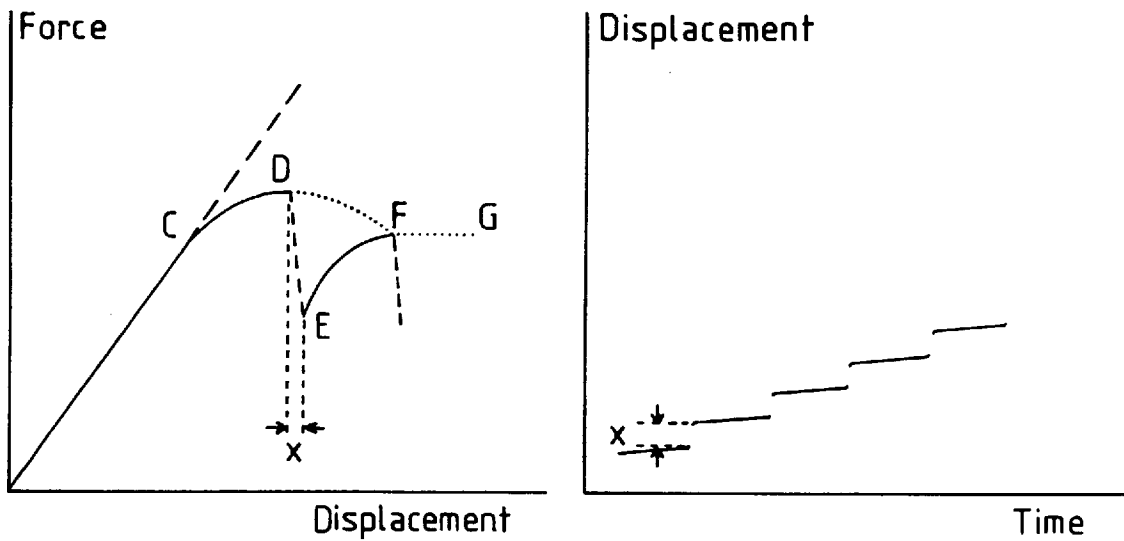
Fig. 3.5. Force-displacement and displacement-time graphs for the Rider Model.

the dotted line. The force at the points C, D and G are known as the initial, maximum and residual friction.

3.3.3. Empirical Laws of Friction

From laboratory observations, friction in rocks appears to follow, to a first approximation, Amontons' Law;

$$\tau = \mu \sigma_n \tag{3.2}$$

where μ, the coefficient of friction is assumed to be constant. Most experiments indicate that for rocks, μ is generally insensitive to hardness and composition and has values between 0.5 and 1.0. More detailed observations indicate that μ is not constant and that Amontons' Law does not precisely describe the relationship between the shear stress and normal stress acting on the surface at the time of slip. Several more exact empirical relationships have been proposed. Archard (1958) gave theoretical justification for a power law of the form:

$$\tau = \mu \sigma_n^n \tag{3.4}$$

where μ is constant and $\frac{2}{3} < n < 1$. Although this was specified for a highly elastic material with surface contact at relatively few points, Murrell (1965) interprets his triaxial tests on sandstone as obeying such a power law.

Jaeger (1959) used a linear law derived from the Coulomb criterion:

$$\tau = S_0 + \mu \sigma_n \tag{3.5}$$

where S_0 = cohesive shear strength
S_0 and μ = constant

He found good agreement with experimental results, particularly at low stresses. In this case the absolute value of S_0 will depend upon the units in which τ and σ_n are expressed.

In a comprehensive review, Byerlee (1978) combines data from a variety of rock types and experimental methods, distinguishing between measurements of maximum and initial friction and fits a linear friction relationship which is independent of the rock type tested (Fig. 3.6). His relationship:

$$\left.\begin{array}{l} \tau = 0.85\,\sigma_n \quad , \quad \sigma_n < 200 \text{ MPa} \\ \tau = 50 + 0.6\,\sigma_n, \quad \sigma_n > 200 \text{ MPa} \end{array}\right\} \tag{3.6}$$

is valid for finely ground surfaces, totally interlocked surfaces or irregular faults produced in initially intact rocks, regardless of the experimental method used.
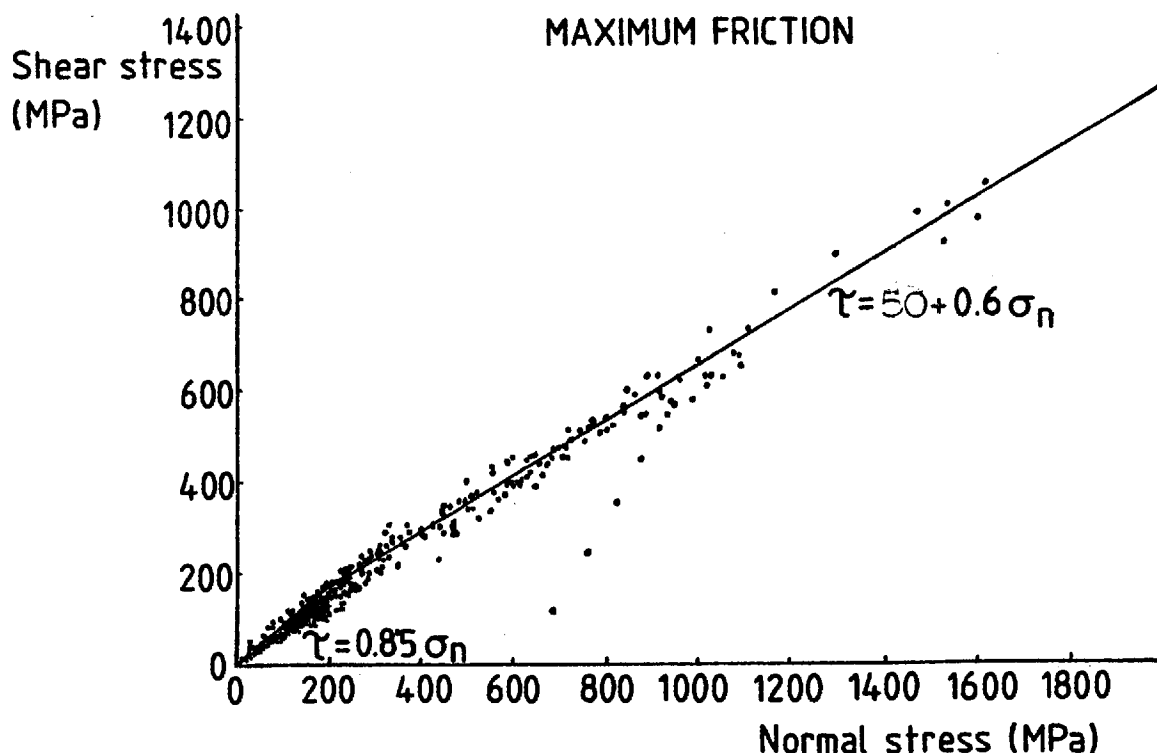
Fig. 3.6. Compilation of experimental friction data (after Byerlee, 1978)

From a similar survey, Stesky (1978) also proposed a linear law:

$$\tau = A + B\sigma_n \tag{3.7}$$

where A = 30 ± 10
       B = 0.6 ± 0.1

When a term for the pore pressure is introduced this law becomes:

$$\tau = A + B(\sigma_n - p) \tag{3.8}$$

Scatter in these data is caused by other parameters which have a slight effect on friction (Section 3.4.) and which may be important in determining the deformation mechanisms occurring during slip.

More exact relationships are seldom universally applicable and for most geophysical problems the linear law is adequate in the top 10 to 15 km of the crust. Temperature effects have not been found to be important below 400°C, although the nature of the sliding process may alter. Stesky (1978) suggests that at pressures above

10 kb or temperatures above $400^{\circ}C$, the linear law breaks down and the frictional strength becomes less dependent on normal stress.

The coefficient of friction, μ, for the linear law is generally accepted as being:

$$\mu = B + \frac{A}{\sigma_n}$$ (3.9)
(Byerlee, 1978)

Some investigators define it as simply B (Stesky, 1978). At very high normal stresses negligible errors are introduced by neglecting the second term but it is significant at low normal stress.

3.4. Theories of Rock Friction

As with metallic friction, the role of asperities is thought to be fundamental to the frictional sliding of rocks. It is from studies of surface damage produced during experimental slip, that theories explaining the physical processes involved in sliding have been proposed.

Byerlee (1967b) suggested that when two surfaces of a brittle material are placed together, the asperities on the surfaces in contact become locked together. If the normal load is high enough to prevent the surfaces from lifting over the irregulatities, sliding occurs when the locked regions fail in a brittle manner. The frictional force is therefore, the force required to break the interlocking asperities. Slider experiments on rock and mineral surfaces (Jaeger, 1959; Bowden, et al., 1964; Steijn, 1964; Byerlee, 1967b) also suggest that brittle failure of asperities occurs.

Interlocking of two surfaces may occur by both brittle and ductile penetration, caused by ploughing or adhesion of asperities (Ohnaka, 1975; Engelder, 1976; Scholz and Engelder, 1976). Ploughing has been identified by the existence of carrot-shaped wear grooves in polished surfaces that have undergone slip. The sharp ends of these grooves point in the direction of motion of the surface in which the grooves lie. Their lengths are limited to the distance slipped in an individual stick-slip event. After slip, the groove producing asperity lies deeply buried at the blunt end of the groove and must then fracture at the onset of the next stick-slip event.

A second proposed mechanism for stick slip, arises from creep of the sliding surfaces (Scholz et al., 1972). The observed increase in μ_s with duration of stationary contact (Dieterich, 1972, 1978; Stesky et al.,

1974) is equated with an increase in the real areal contact (Teufel and Logan, 1978) as a result of asperity creep (Fig. 3.7).

Apparent contact area

Asperity contact area
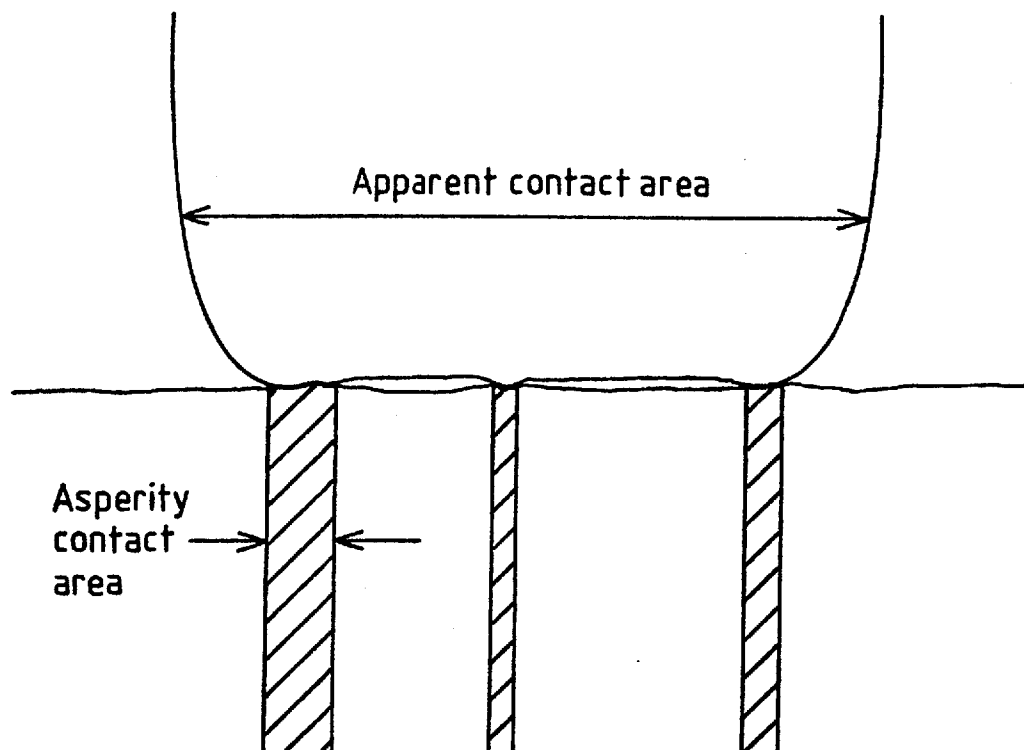
Fig. 3.7. Sketch showing the relationship between real and apparent contact area.

Real contact area = sum of asperity contact areas

Other theories which have been proposed to explain the stick-slip mechanism and the reason for a higher static than kinematic coefficient of friction have been reviewed by Byerlee (1969).

3.5. Parameters Affecting Rock Friction

Laboratory studies indicate that the most important parameters affecting the nature of frictional sliding are: temperature, effective confining pressure, stiffness of the loading machine, surface roughness, mineralogy, gouge, porosity and the presence of water. Parameters of lesser importance are: strain rate, time of stationary contact and cumulative displacement. For natural faults, the structure of the fault zone will also be important. It is the combined effect of all these factors which controls the microscopic deformation mechanisms of sliding and thus the microstructural features recorded in fault rocks.

3.5.1. Temperature

Elevated temperatures have a complex effect on experimental frictional strengths. Both increases and decreases in the frictional strength with elevated ambient temperature have been recorded, depending upon the rock type (Handin and Hager, 1958; Griggs et al., 1960; Raleigh and Paterson, 1965; Drennon and Handy, 1972; Stesky et al., 1974).

Stable sliding tends to occur at high temperatures, but the actual temperature of the transition from stick-slip to stable sliding depends on the rock type (Brace and Byerlee, 1970; Friedman et al., 1974).

The relevance of friction experiments performed above 250 or $300^{o}C$ to natural faulting is questionable. Above these temperatures it is known that intracrystalline dislocation controlled deformation occurs at low strain rates especially in quartz (White, 1976).

3.5.2. Effective Confining Pressure

Frictional strength increases with increasing effective normal stress, which in experiments is directly proportional to the effective confining pressure. Scholz et al. (1972) described a pattern of transition with stable sliding, episodic sliding and stick-slip occurring at successively higher values of effective normal stress. Typical experimental results are shown in the schematic force-displacement graph (Fig. 3.8).
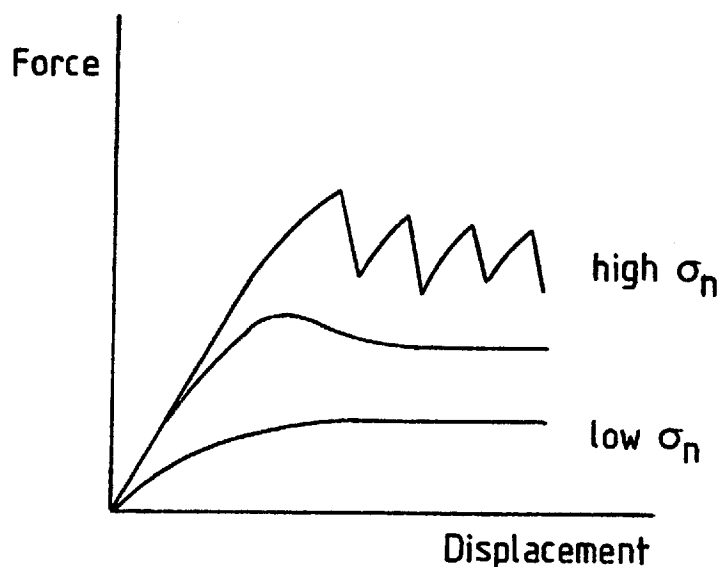
Fig. 3.8. Experimental force-displacement curves showing variation in the frictional force and slip mode with increasing normal stress.

The combined effects of temperature and effective pressure on the mode of frictional sliding are shown in Fig. 3.9.

Confining pressure (MPa)
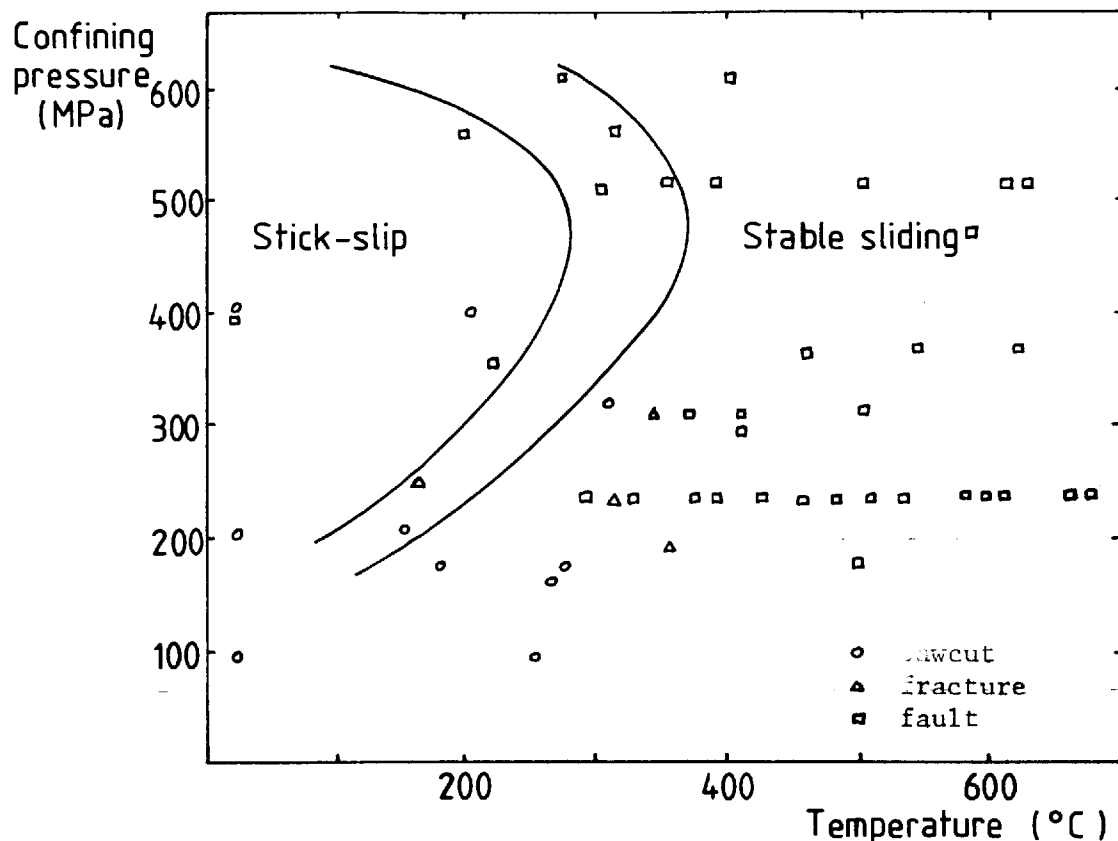
Fig. 3.9. Effect of confining pressure, temperature and surface on frictional sliding (after Stesky, 1978).

The stress drop in each stick-slip event increases at first sharply with increasing effective pressure and at a lesser rate at higher effective stresses (Scholz et al., 1972).

3.5.3. Surface Roughness

In geological terminology, the roughness of a fault is taken to include any deviation from a flat, planar surface. Scholz et al. (1969) measure asperities on the San Andreas fault with wavelengths in the order of kilometers. Experimentalists apply the term 'roughness' only to relatively close spaced surface irregularities such as those produced by sawing, grinding and lapping. Roughness has its greatest effect on friction at the initiation of sliding at low normal stresses. Smoother surfaces have a lower initial frictional strength. The roughness/friction relationship is highly dependent on rock type (Ohnaka, 1975). Very smooth surfaces enhance stick-slip while rougher surfaces in some cases, promote stable sliding.

3.5.4. Stiffness of the Loading System

Stiffness is defined as the rate of change with displacement, of either the applied force or stress. In some experiments no stiffness effect has been found (Byerlee and Brace, 1968), but elsewhere it has been concluded that low machine stiffness enhances the tendency for stick-slip to occur (Dieterich, 1972; Ohnaka, 1973), Fig. 3.10.
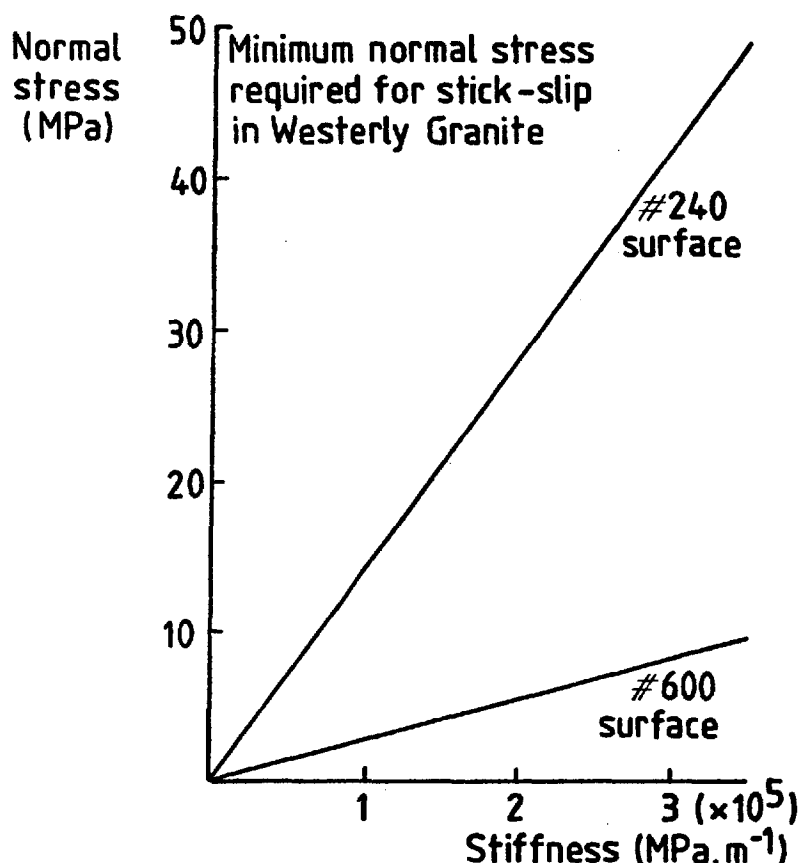
Fig. 3.10. Effect of stiffness on experimental sliding.

The relevance of these findings to natural faulting remains unclear as there is controversy over whether a natural fault has low (Walsh, 1971) or high stiffness (Ohnaka, 1973a).

3.5.5. Mineralogy

In general, rocks containing weak minerals undergo stable sliding rather than stick-slip. Weak minerals include calcite, dolomite, talc and serpentine (Byerlee and Brace, 1968; Ohnaka, 1975). Byerlee and Brace (1968) noted that only 3 per cent of serpentine distributed on the grain boundaries of dunite is sufficient to influence the sliding behaviour. Conversely, they note that large amounts of other platy silicates such as chlorite and micas, have relatively little effect.

3.5.6. Gouge

A time-dependent increase in friction has been noted in many experiments and attributed to the development of adhesive and/or abrasive wear particles on sliding surfaces with increasing displacement (Drennon and Handy, 1972; Dieterich, 1972; Ohnaka, 1975). Experiments using a simulated gouge (Engelder et al., 1975) have shown that its primary effect is to dampen the magnitude of stick-slip events and to increase the normal stress at which the stable sliding/stick-slip transition occurs. The behaviour of gouges depends very much upon their mineralogy, thickness, grain size and the absence or presence of water (Section 4.2.5). Quartz and feldspar gouges show violent stick-slip above confining pressures of 1.5 kb. Gouges of illite, talc, kaolinite and chlorite have lower frictional strengths but still show stick-slip above 1.5 kb. Montmorillonite and vermiculite have very low frictional strengths and undergo stable sliding to at least 6 kb confining pressure.

3.5.7. Porosity and Pore Fluids

Experiments on different rock types show that as a general rule, high porosity promotes stable sliding (Byerlee and Brace, 1969). Fluids have at least two functions. One is the purely mechanical effect whereby non-reactive fluids, including water, reduce the effective confining stress. Anomalous pore pressure changes may increase the frictional strength of low permeability rocks when they are deformed with high loading rates (Brace and Martin, 1968). The chemical interaction between fluids and the minerals in a rock, has not yet been adequately investigated. Early results (Rutter and Mainprice, 1978) suggest that there is a weakening effect.

3.5.8. Strain Rate

The strain rate is determined by the nominal shortening rate imposed by the testing machine on the rock specimen. When stick-slip occurs, particle velocities adjacent to the sliding surface may be several orders of magnitude greater than the shortening rate of the apparatus.

There is dispute over the effect of strain rate, which may decrease frictional strength (Ohnaka, 1975) and enhance stable sliding (Teufel and Logan, 1978) when it is fast (Fig. 3.11). The amplitude of the stress drops are high at fast strain rates (Teufel and Logan, 1978).
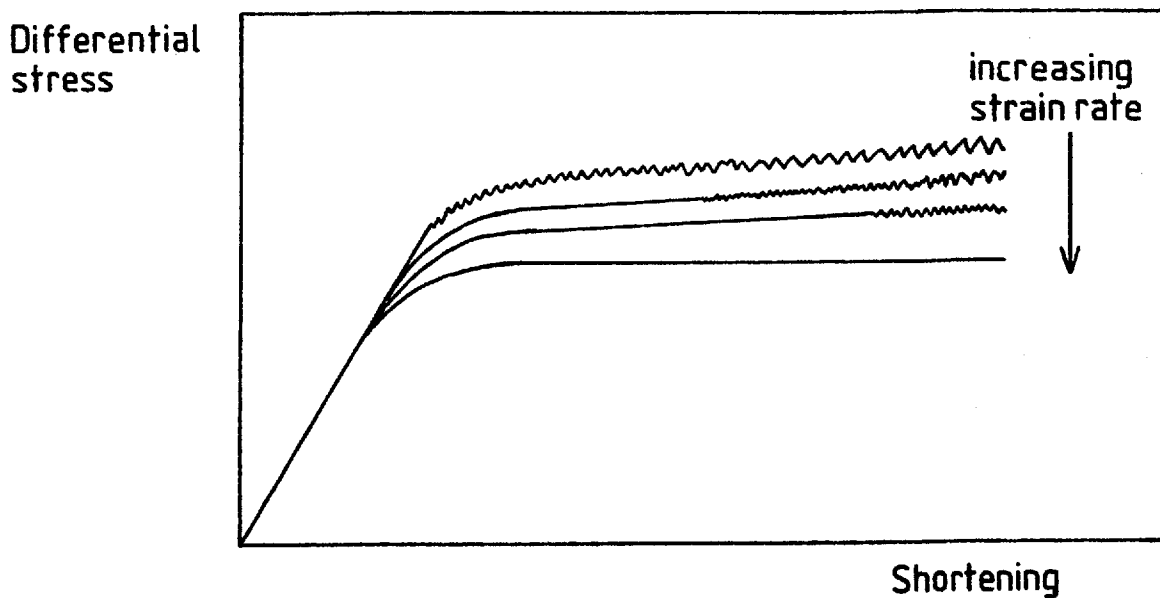
Fig. 3.11. Effect of strain rate on frictional sliding

3.6. Summary and Application to the Natural Faulting Environment

Experimental work suggests that frictional sliding on a fault is a complex process depending upon many parameters. In general, stick-slip is enhanced by high normal stresses, low temperatures, the presence of strong, brittle minerals such as quartz and feldspar, by the absence of gouge and by very smooth surfaces.

The application of experimental results to natural faults poses problems as values for many of these parameters are not known. The variation with depth of pore pressure, gouge thickness and composition, and temperature are not known. The definition of roughness when applied to faults is vague. Mineralogy may vary across and along the fault as well as with depth; likewise differential stress, effective normal stress and temperature. The laboratory model is usually a simple planar feature, whereas most fault zones, both ancient and active, map out as complex, locally branching zones made up of several faults. From observed patterns of ground breakage accompanying major earthquake rupturing (Tchalenko and Ambraseys, 1970) movement, at any time, may occur across one, several or all of the subsidiary faults. Thus a fault and its geometry is much more complex than any system studied in

the laboratory. The effect of this complexity may potentially, be enormous.

3.7. Numerical Modelling of Rock Friction

Of the numerical models that have been applied to rock friction, one of the most interesting for the geologist is that of Nur (1978). He suggests that assuming tectonic loading is uniform, a spatial variation in frictional strength along a fault explains the main features of seismic faulting: the mechanical instability, the frequency-magnitude relationship, seismic and aseismic slip, the incoherence of seismic radiation and rupture stoppage. The significance of non-uniform friction, is that it forms a link between laboratory studies and those on natural faults. His model relates the experimental results to slip on a small segment of the fault where friction may be considered uniform. Thus a fault may be visualised as an infinite number of small elements controlled by different parameters, but whose behaviour is linked.

CHAPTER 4

STRESS LEVELS AND ENERGY BALANCE IN FAULTING

Faulting, whether it occurs seismically or aseismically, leads
to energy dissipation within the fault zone. The amount of energy
dissipated depends upon the level of the average shear stress, $\bar{\tau}$,
on the fault.

4.1. State of Stress in the Crust

The state of deviatoric stress in the crust is a matter of con-
troversy. There are two main schools of thought (Hanks, 1977): one
maintains that the deviatoric stress is low ($\lesssim$ 10 MPa), the same order
of magnitude as stress drops recorded for the majority of earthquakes;
the other suggests stresses are high (about 100 MPa), similar to the
frictional stresses measured in rocks during experiments simulating
crustal deformation under hydrostatic pore fluid pressure. If these
two schools are mutually exclusive, then fault zones are either all
very weak, or all almost as strong as intact rocks.

Geological evidence, however, suggests that both high- and low-
stress faulting may occur at shallow crustal levels, although absolute
values of the tectonic shear stress, τ , in fault zones cannot be
measured directly (Brune, 1970).

There are two important factors that suggest the stress level is
low. Firstly, heat flow studies around the San Andreas Fault (Brune
et al., 1969) imply an upper limit of a few tens of MPa for the time-
averaged shear stress along the fault. Secondly, earthquake stress
drops, which provide a minimum estimate of the shear stress in fault
zones, have surprisingly consistent values between 1 and 10 MPa,
apparently independent of magnitude (Kanamori and Anderson, 1975).
This leads to the theory that the shear stress in all fault zones is of
a similar magnitude and that total stress release occurs on faulting.

Evidence that the shear stress may be high also comes from two
sources: the frictional strength of rock surfaces recorded in many
experiments (Chapter 3) is high ($\simeq$ 100 MPa); theoretical calculations,
based on known stress configurations around faults, yield the minimum
shear stress required to overcome friction and cause slip at a given
depth (Stesky and Brace, 1973). If λ_v (the ratio of fluid pressure
to overburden pressure, P/σ_v) equals 0.36 (hydrostatic pressure) and

the coefficient of static friction equals 0.75 (an approximation derived from the compiled friction data of Byerlee (1978)), the stresses around a thrust fault should be four times as high as those around normal faults at a given depth (Sibson, 1974). Calculated shear stresses under these conditions are 110 and 30 MPa at 5 Km depth, respectively. Transcurrent faults have intermediate values (Fig. 4.1).

Estimates of the tectonic shear stress derived from in-situ and
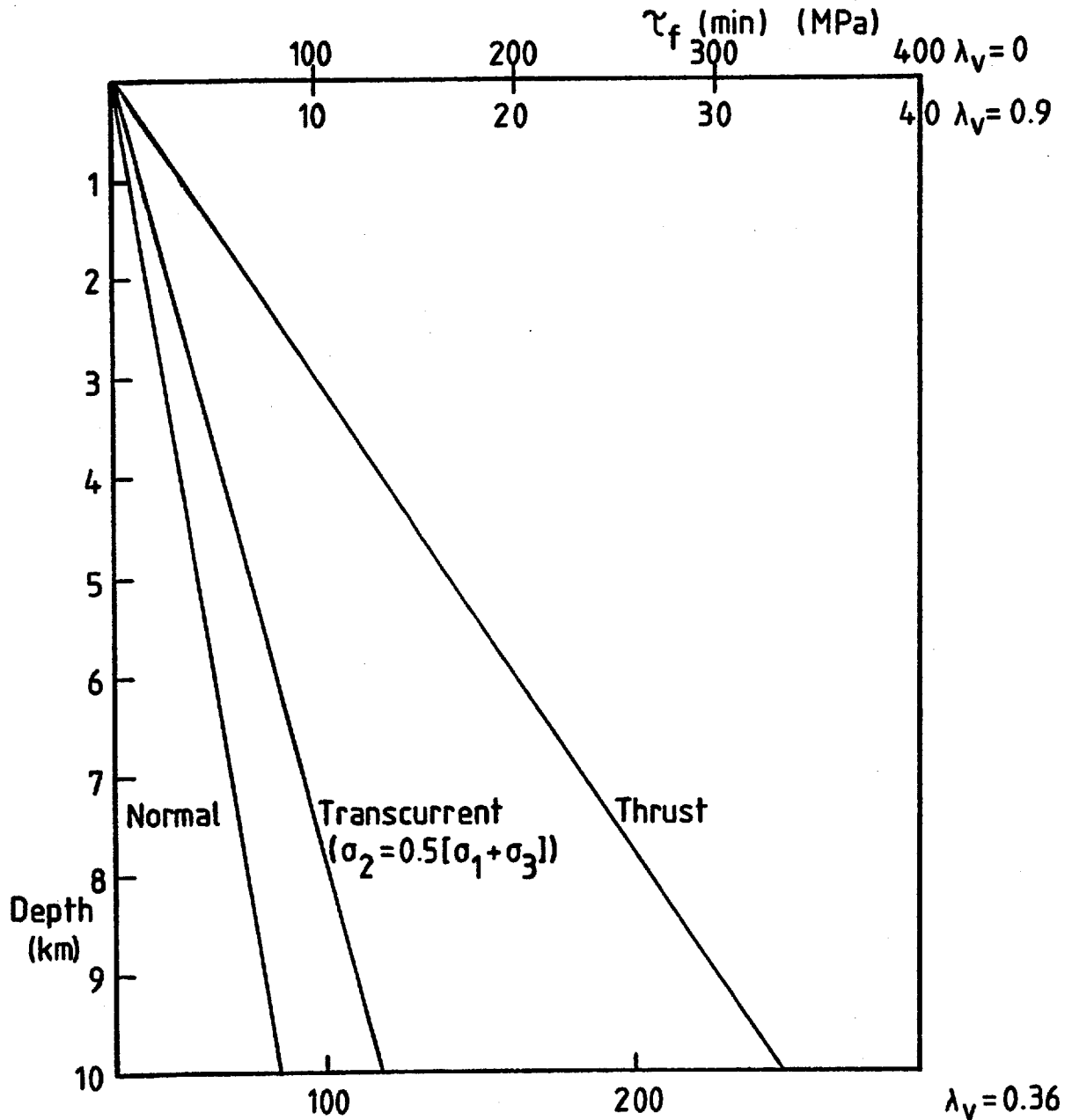
Fig. 4.1. Minimum shear stress required to overcome friction, versus depth. $\mu_s = 0.75$ $\rho_{rock} = 2800$ Kg m^{-3} g = 9.8 ms^{-2} (after Sibson, 1974).

palaeostress measurements show great variation. In-situ stress measurements have rarely been made at depths greater than 1 km (McGarr and Gay,

1978). Their extrapolation to greater depths is debatable and its
relevance to deeper-level faulting is, therefore, questionable.
McGarr and Gay (1978) show that shear stresses of up to 70 MPa exist
in deep mines in South Africa, in a region where average stress drops
during small seismic events fall between 0.5 and 5 MPa. This suggests
that there is only partial stress release during faulting and that
ambient stress levels may characteristically be an order of magnitude
greater than the stress drops.

Palaeostress measurements have been made in mylonites from intra-
crystalline features such as recrystallised grain size, sub-grain size
and dislocation density. There is controversy over the reliability of
these measurements (White, 1979). In addition, direct application of
these data, from rocks of the quasi-plastic regime to frictional
faulting, should be made with care. Palaeo-shear stresses of between
1 and 100 MPa have been recorded at levels in which mylonites form
(Etheridge and Wilkie, 1979; White, 1979).

4.1.1. Apparent Stress

The concept of apparent average stress (Wyss and Brune, 1968)
illustrates the problems in interpreting seismological information with
respect to the shear stress level. The apparent average stress is
derived from the definitions of seismic moment, seismic efficiency
and the equation expressing the extracted work, E, resulting from
shear on a dislocation (Wyss, 1970).

The extracted work, E, is given by:

$$E = \bar{\tau} . \bar{u} . A \tag{4.1}$$

where $\bar{\tau}$ = average shear stress during slip

$\bar{u}$ = average displacement

A = area undergoing slip

The seismic moment, M_o, is defined as:

$$M_o = G . \bar{u} . A \tag{4.2}$$

where G = shear modulus of rigidity

The proportion of the extracted work that is radiated from the fault
as seismic waves, E_s, depends upon the seismic efficiency, η :

$$E_s = \eta E \tag{4.3}$$

Both E_s, M_o and G can be measured seismologically. By combining equa-
tions (4.1), (4.2) and (4.3) the apparent average shear stress, $\eta \bar{\tau}$,

is given by:

$$\eta \bar{\tau} = \frac{GE_s}{M_o}$$

(4.4)

Measured values for the apparent average shear stress vary between 0.1 and 10 MPa (Kanamori and Anderson, 1975). The actual stress level is indeterminable unless the seismic efficiency is known, and vice versa. If η is low ($\leqslant 0.1$) the shear stress is high (about 100 MPa). If the efficiency is high (about 0.9), the shear stress is low (about 10 MPa).

4.2. Energy Balance in Faulting

Distortional elastic strain energy accumulates around fault zones as a result of regional shearing displacements. In the case of steady, aseismic faulting, the level of stored energy remains constant as a result of continuous dissipation. In seismic faulting, cyclic accumulation occurs with intermittent and catastrophic release of all, or part of the stored energy. Released energy is partitioned into a variety of sinks, but the proportions vary for different faulting modes.

The four main energy sinks are: heat, radiated seismic energy, fracture surface energy, and work done against (or by) gravity.

$$E = E_H + E_s + E_\delta + E_g$$

(4.5)

where
E_H = energy converted to heat.
E_s = radiated seismic energy.
E_δ = fracture surface energy.
E_g = work done against gravity.

The amount of energy available for dissipation into these sinks depends upon E and thus the average shear stress, $\bar{\tau}$, in the fault zone (equation 4.1). The work done against or by gravity in reverse and normal faulting respectively, may be high. The energy released in this manner is the difference between large changes in the potential energy of the elastic and gravitational fields (Savage and Walsh, 1978). The gravitational term is usually considered to be negligible in the case of transcurrent faulting.

4.3. Energy Sinks in Seismic Faulting

In the following sections energy sinks during seismic slip are
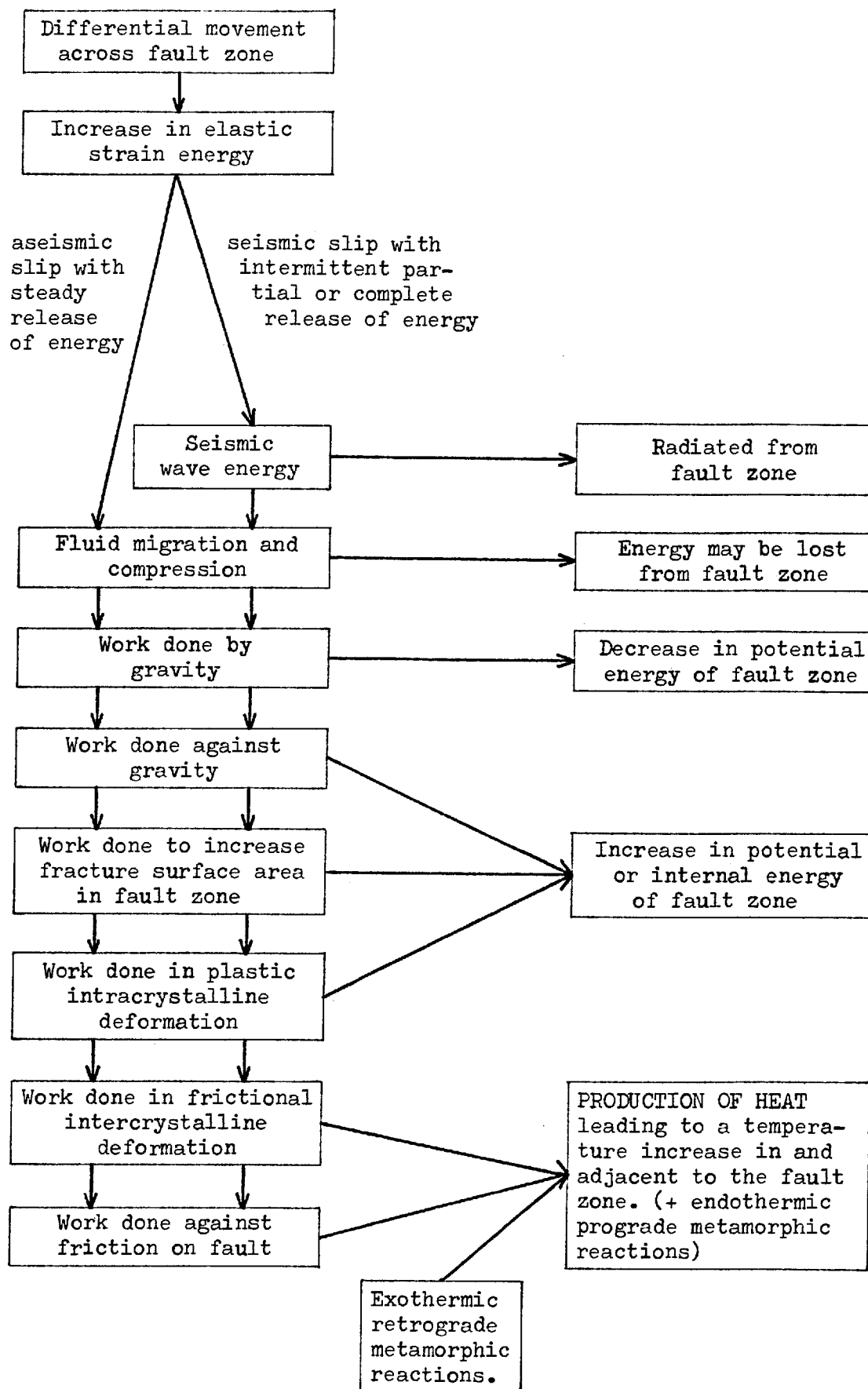
Fig. 4.2. Energy sinks in faulting.

considered in detail. A summary of the energy sinks is given in Fig. 4.2.

4.3.1. Seismic Wave Energy

Crude estimates of seismic wave energy, E_s (in joules) can be obtained from the empirical Gutenberg-Richter relationship (Richter, 1958):

$$\log_{10} E_s = 4.8 + 1.5 M_s \qquad (4.6)$$

where M_s = surface wave magnitude.

Values of E_s obtained in this manner are based on an assumption that total wave energies for earthquakes of different size and type, can be derived by sampling their frequency spectra at one particular period (Kanamori and Anderson, 1975). Compiled data of $E_{s/A}$, derived from published earthquake source data by Sibson (1978) using the Gutenberg-Richter relationship, show that values of between 10^5 and 10^8 $J.m^{-2}$ are common.

4.3.2. Fracture Surface Energy

The exact definition of the term "fracture energy" varies. It is most commonly defined in the seismological literature as the energy associated with the passage of the rupture front (Husseni et al., 1975; Sibson, 1980). This, then, is the energy used in creating new surface at the tip of the propagating rupture and includes the energy required for crack branching and any comminution occurring at the rupture front. With this definition the fracture energy term presumably also includes heating at the rupture front. Such heating effects are often ignored as their value is hard to estimate and their significance is not clear (Richards, 1976).

Here, the fracture surface energy is defined as the energy required to create all new surface area including that of the fault and its associated fracture zone, whether such surface area is produced by the passage of the rupture front or by subsequent frictional sliding. The specific fracture, or surface energy, γ, exists because work must be done to a material to fracture it. The potential energy of the material increases as a result of the increase in its surface area. For a single, tensile fracture (Fig. 4.3):

$$W = 2A\gamma_g \qquad (4.7)$$

where W = work done to create the extra surface

A = surface area produced on one side of the fracture

γ_g = Griffith surface energy of the material.
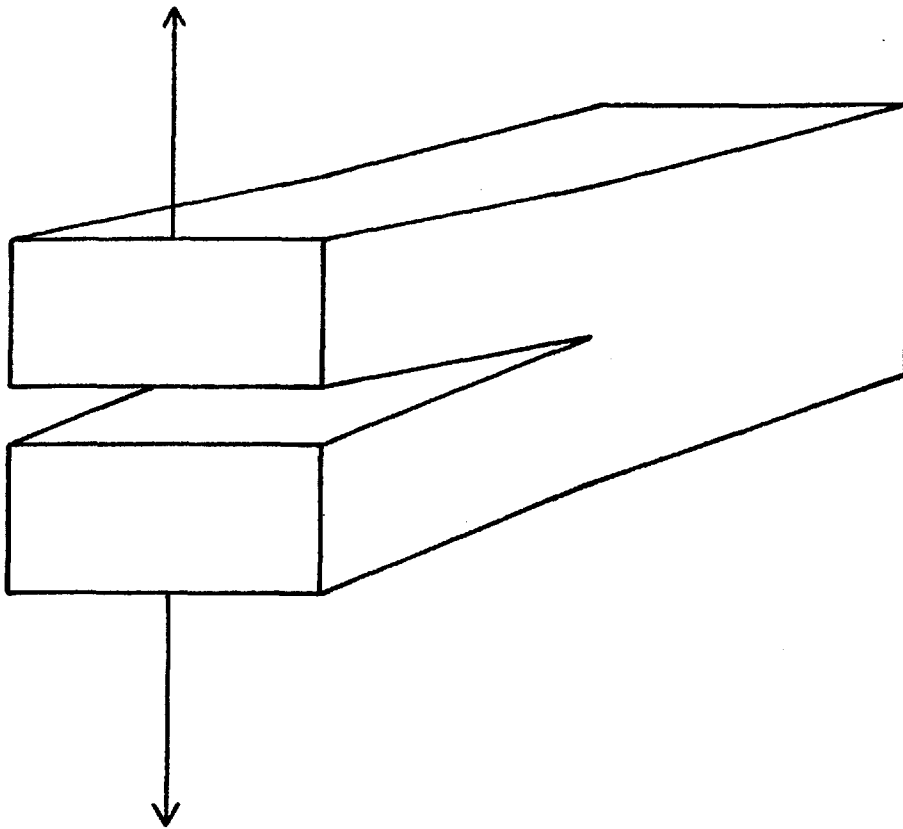
Fig. 4.3. Simple pull-apart model from which the Griffith surface energy is calculated.

In a series of experiments, Brace and Walsh (1962) obtained values for γ_g of 0.1 $J.m^{-2}$ for quartz and 1 $J.m^{-2}$ for orthoclase. With natural faulting, where failure does not occur under tension but by shear, and where the new surface area is not created isothermally, these values must be used with caution (Lawn and Wilshaw, 1975).

A first approximation to the fracture surface energy of a fault can nevertheless be obtained by considering it equal to the sum of the Griffith surface energy of all fragments within the fault zone. In a unit mass of fragmented rock:

$$W_m = S\gamma_g \tag{4.8}$$

where W_m = work done per unit mass in creating the surface area

S = surface area per unit mass

S can be estimated from the particle size distributions (Herdan, 1953):

$$S = \frac{K}{\rho}\sum\frac{m_i}{x_i} \tag{4.9}$$

where K   = geometrical shape factor of the particles

m_i = proportion by mass of particles of size x_i

ρ = density of the material.

Substituting the values of S presented by McGarr et al. (1977) for comminuted material generated by crushing experiments, gives W_m values between 6 and 8 $J.kg^{-1}$. When multiplied by the mass of comminuted material this yields a fracture surface energy of between 0.01 and 0.03 J, which is less than 0.1% of the energy supplied to the apparatus. The quantity of heat produced was not measured. This agrees with the gouge deformation experiments of Engelder et al. (1975) where an estimated 0.13% of the energy supplied to their experimental apparatus is required to generate the surface area.

Multiplying the work per unit mass, W_m, by the density converts it to the work done per unit volume, W_v. W_v then has values between 1.6 x 10^4 and 2.2 x 10^4 $J.m^{-3}$ for a density of 2700 $kg.m^{-3}$. If these experimental results can be scaled up to natural faulting they imply that the fracture surface area per unit area of the fault, E_γ, is given by:

$$E_\gamma = W_v.w \qquad\qquad (4.10)$$

where w = width of fault zone

Thus for a fault zone, say 0.1 m wide E_γ is 2 x 10^3 $J.m^{-2}$, considerably higher than the Griffith surface energy for a single fracture.

4.3.3. Heating Energy

The heating energy term is made up of two components; heat production at the rupture front and heat produced in overcoming frictional traction on the fault's surface. As discussed in Section 4.3.2, the value and significance of the first of these is unclear. Whether or not the temperature rise at the rupture front is large, as a heat source it is very short lived at any given location since the rupture velocity approaches the shear-wave velocity of about 3 $km.s^{-1}$. In contrast, the heating induced by frictional traction behind the rupture front will last for periods of several seconds (the typical rise-time for moderate to large events, Section 2.3) and will have more influence on the surrounding rock. It is this frictional heating alone, that is considered in this section.

The frictional energy, E_F, may be expressed in terms of the mean value of the kinetic shear resistance, $\tilde{\tau}_{fk}$ acting across the fault

during slip

$$E_F = \bar{\tau}_{fk} \cdot \bar{u} \cdot A \tag{4.11}$$

where from Amontons' Law

$$\tau_{fk} = \mu_k (\sigma_n - p) \tag{4.12}$$

This frictional energy is partitioned between the frictional heating, and fracturing associated with sliding. The previous section suggests that the total fracture surface energy is a small percentage of the expended energy. This is supported by the findings of industrial comminution processes where grain size is reduced by mechanical wear and frictional sliding of particles. In most machines used, the fracture surface energy of the grains produced is only 1 to 2% of the input energy (Hukki, 1975; Marshall, 1975). Between 95 and 99% of the expended energy is converted to heat.

If these results can be applied directly to natural faulting, almost all of the frictional energy is dissipated as heat. E_F is therefore approximately equal to the heat produced in overcoming friction on the fault and in the ensuing argument it is generally assumed that $E_F \simeq E_H$.

The kinetic shear resistance, τ_{fk}, is often assumed to stay roughly constant during stick-slip, although this may not always be the case. In the standard stick-slip model (Sibson, 1977a), the kinetic shear resistance is assumed to stay fixed at a high proportion of the initial shear stress. In this case $\bar{\tau}_{fk}$ is almost equal to the average tectonic stress level. This gives likely values for the shear resistance of 1 to 100 MPa which, with average seismic slip of 0.01 to 10 m, gives an upper limit to the frictional energy dissipated per unit area of about 10^9 Jm^{-2}. It is also worth pointing out that such a model with τ_{fk} constant and close to the initial shear stress at failure implies low efficiency faulting.

From the rise times of earthquake faults (typically around 1-10 seconds, Section 2.3), the power dissipation per unit area may be calculated. The maximum expected power level is in the order of 100 MW.m^{-2}. Such rates of power dissipation should lead to considerable temperature increases adjacent to the fault (Section 4.4).

4.3.4. Aseismic Slip

The principal energy sinks are similar for seismic and aseismic

slip, but in the latter no energy is radiated from the fault zone and since movement across the fault stays constant, no energy is associated with the propagation of a rupture front.

From equation (4.11) the frictional power dissipation per unit area on a discrete plane may be expressed as:

$$\dot{E}_F = \bar{\tau}_{fk} . v \qquad (4.13)$$

where   v = slip velocity

With aseismic slip velocities typically between 0.01 and 0.1 m yr^{-1} (Sibson, 1977b) and shear resistances between 1 and 100 MPa the power dissipation is at maximum, 0.3 Wm^{-2}.

If slip is uniformly distributed through a zone of finite width, the power dissipation per unit volume, E_{F_v} from equation (4.13) becomes:

$$\dot{E}_{F_v} = \bar{\tau}_{fk} . \frac{v}{w} \qquad (4.14)$$

or $$\dot{E}_{F_v} = \bar{\tau}_{fk} . \dot{\gamma} \qquad (4.15)$$

where   w = width of slipping zone

$\dot{\gamma}$ = rate of shear straining.

4.3.5. Summary

The remaining energy sinks in Fig. 4.1., such as those involving fluid flow etc. are likely to be of only minor importance. Ancillary energy sinks resulting from transient electrical and chemical effects in the fault zone will also be small.

Thus for seismic slip on most transcurrent faults, much of the energy released in the fault zone is divided between fracture surface energy, radiated seismic energy and the production of frictional heat. If the frictional shear resistance remains approximately constant during slip, much of the energy released during seismic slip is dissipated as frictional heat. Resulting power dissipations may reach up to 100 MW_m^{-2}. Much lower levels of power dissipation are expected for aseismic slip.

4.4. Temperatures Resulting from Fault Slip

4.4.1. Theoretical Approaches

Likely temperature rises adjacent to faults undergoing seismic

slip have been calculated by several theoretical methods.

Richards (1976), discusses a general earthquake model where fault motions are assumed to nucleate at a point on the fault's surface, in an infinite, pre-stressed elastic medium. The rupture grows at sub-sonic speeds, maintaining the shape of an ellipse. His analysis shows that in the special case of a steadily expanding circular rupture, the temperature on the fault plane, T, is given by:

$$T = \frac{8(\pi kt)^{1/2} \bar{\tau}_{fk} \cdot a}{K} \cdot f\left(\frac{v}{R \cdot \sin \Theta}, \frac{kt}{R^2 \sin^2 \Theta}, \cos \Theta\right) \qquad (4.16)$$

where k = thermal diffusivity

t = time from nucleation of crack

K = thermal conductivity

$\bar{\tau}_{fk}$ = average kinetic shear resistance

a = particle velocity ($= \frac{1}{2} \times$ slip velocity)

v = rupture velocity

$R, \emptyset, \Theta$ = Spherical polar coordinates

This equation yields, $T \simeq 1100 \times t^{1/2}$ °C, for a point on the fault's surface, halfway between the rupture front and the point of nucleation, when the shear resistance is constant at 10 MPa and the particle velocity, 0.1 ms^{-1} at nucleation. Substitution of more representative values for k and K (1×10^{-6} m^{2}s^{-1} and 3 J.m^{-1}. °C^{-1}. s^{-1} respectively, Clarke (1966)) gives $T \simeq 875 \times t^{1/2}$ °C. The values for the shear resistance and particle velocity are both high. The temperature rise predicted by this method is therefore the maximum expected.

Analogous results were presented by McKenzie and Brune (1972) using a similar model. In this infinite model, heat flows only perpendicular to the fault's surface to which slip is restricted. The real area of contact of the sliding surface is assumed to equal the apparent contact area. With this model the temperature increase on the fault's surface is given by:

$$T = \frac{\bar{\tau}_{fk} \cdot u}{\rho c_p (\pi kt)^{1/2}} \qquad (4.17)$$

where u = fault displacement

ρ = density

c_p = specific heat at constant pressure

This equation predicts that the temperature rise exceeds 1000°C after 1 mm displacement if the shear resistance is 100 MPa. Slip

velocities implied by this model (which has an infinite rupture velocity) are high, which in turn means that the rise in temperature will be over-estimated.

Cardwell et al. (1978) used the model of McKenzie and Brune (1972) but considered slip to be distributed throughout a zone of finite width. The temperature rise on the fault's surface is then given by:

$$T = \frac{\bar{\tau}_{fk} \cdot u}{c_p w} \qquad (4.18)$$

where w = width of the fault.

This analysis assumes that thermal conduction is unimportant during slip, the fault width is at least 0.01 m and that frictional heat is generated uniformly across the width of the zone. The width effect on the temperature rise is shown in Fig. 4.4.
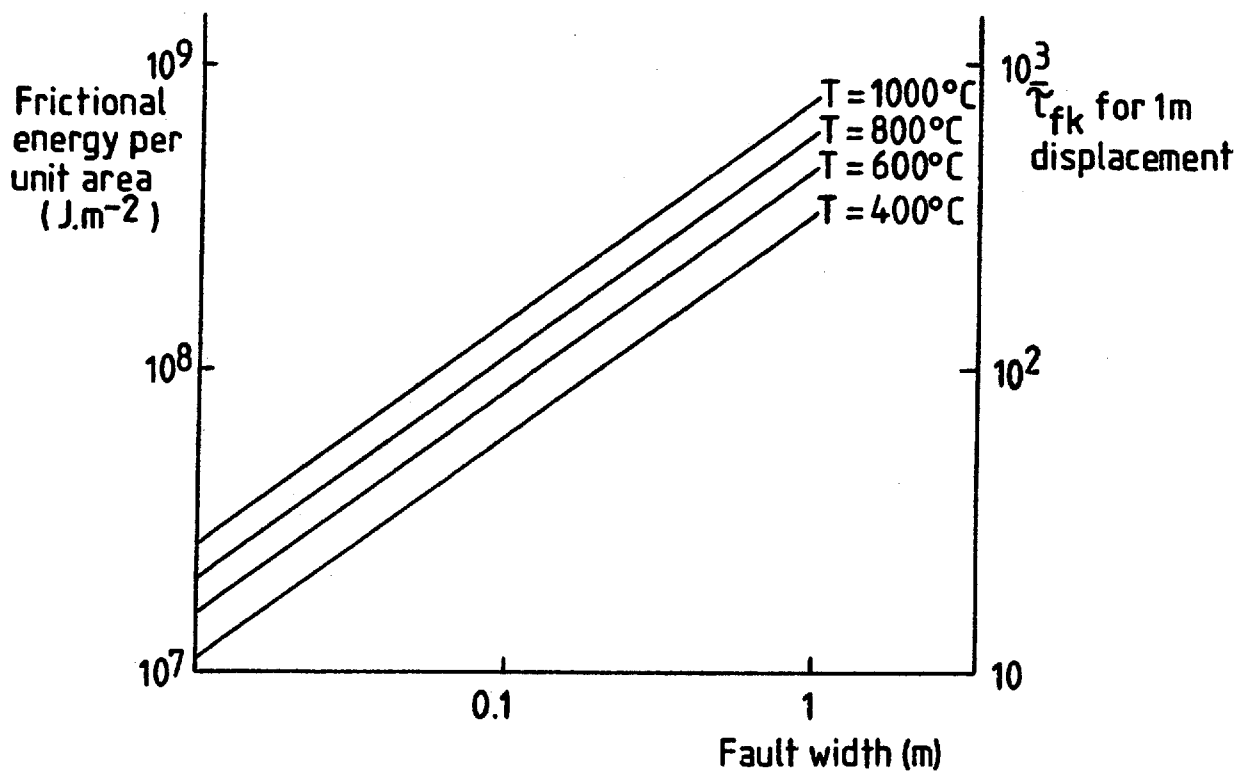
Fig. 4.4. Effect of fault zone width on temperature rise during fault slip (after Cardwell et al., 1978).

Theoretical studies suggest that elevated temperatures on and adjacent to faults will develop during seismic slip. The actual temperature rise is strongly dependent upon the physical conditions of faulting; shear resistance, slip velocity and fault width and the thermal characteristics of the host rock. Most models assume τ_{fk} remains constant and that faults are dry which may be unusual in natural faulting.

4.4.2. Experimental Slip

Studies of metals have shown that during frictional sliding heat is generated at the points of contact of the sliding surfaces. Heat flows from these points and raises the average temperature of the entire surface. During sliding, frictional bonds at asperity contacts are continually created and destroyed. As a consequence, the location of the "hot-spots" changes. Hot-spot temperatures in metals were measured from their thermo-electric emf's (Bowden and Tabor, 1967). Temperatures may locally be very high but are limited by the melting point of the solid. Despite the relatively high thermal conductivities of metals, most of the body remains cold.

Sliding experiments on rocks show that during stick-slip, patches of glass may form on the sliding surface (Section 6.2). In a recent series of experiments, Teufel and Logan (1978), used thermally sensitive dyes to measure the temperatures on sliding surfaces in sandstone. Their results show that although hot-spots with temperatures above $1000^{\circ}C$ may exist locally during stick-slip, the average surface temperatures lay between 115 and $135^{\circ}C$. These experiments used relatively smooth, sawcut surfaces in room dry samples, deformed at room temperature at 50 MPa confining pressure. The overall surface temperatures of 115 to $135^{\circ}C$ which resulted from very small slip increments are expected to be smaller than those developed on faults. In addition the behaviour of the rmodyes under the conditions found on a sliding surface is not fully understood and may have led to mis-estimates of temperature. Pore fluid effects were not considered during these experiments.

4.4.3. Fault Zones

While most faults show no evidence for a history of elevated temperatures or melting, there is some field evidence that fault temperatures have sometimes been high enough to cause partial or complete melting. Sibson (1975) has demonstrated that pseudotachylyte, which is sometimes associated with faulting, has been though a melt phase. He

considers that friction-melts may form under relatively high-stress seismic faulting with zero pore-fluid pressure. These conditons explain why pseudotachylyte is absent on the majority of faults.

Evidence, within fault zones, for transient increases in temperature less than those required for melting may be difficult to recognise. Such thermal cycling may play an important role in the deformation within and adjacent to the fault plane (Chapter 6).

4.5. Summary

Theoretical, experimental and field studies all show that under certain conditions frictional heating may lead to large temperature rises on and adjacent to faults undergoing slip. For this to occur, sliding must be restricted to a narrow zone, with rapid-slip rates. If these conditions of slip are satisfied, the temperature rise during seismic slip is ultimately dependent upon the stress levels under which faulting occurs, and therefore the seismic efficiency (Fig. 4.5).

	$\bar{\tau}$ high, $\geqslant$ 100 MPa	$\bar{\tau}$ low $\leqslant$ 10 MPa
Seismic Efficiency	LOW	HIGH
Earthquake stress drop	PARTIAL	ALMOST COMPLETE
Possible temperature rise on fault	HIGH	MODERATE TO HIGH

Fig. 4.5. Relationship between stress levels, seismic efficiency and possible temperature rise on faults undergoing seismic slip.

If the average tectonic shear stress, $\bar{\tau}$, is high (about 100 MPa) then seismic efficiency is low, there is partial release of the shear stress during faulting and under the right conditions temperature rises on the fault plane may be high. If the average tectonic shear stress is low ($\leqslant$ 10 MPa), then seismic efficiency is high and shear stress is almost completely relieved by slip. In the latter case, temperature rises will be less marked irrespective of fault type.

CHAPTER 5

SIMULATION OF THERMAL STRESSES ASSOCIATED WITH SEISMIC SLIP

5.1. Introduction

Frictional heating may lead to large temperature rises adjacent to slipping faults. Friction melts have been considered (McKenzie and Brune, 1972; Sibson, 1975; Richards, 1976; Cardwell et al., 1978) but to date little attention has been paid to possible deformation resulting from transient high temperatures and their associated thermal gradients when the temperature increase is insufficient to cause melting. In this case, the temperature gradients may be high enough to cause thermal fracturing adjacent to the fault plane.

Although some thermal deformation may be present in samples that have undergone experimental frictional sliding, it is impossible to distinguish it from fracturing and attrition arising from the actual shearing. A series of experiments has been devised to investigate possible deformation resulting from frictional heating on a fault without the effects of shear (Chapter 9). In this way, the degree of fracturing could be studied under varying simulated conditions of slip and the role of thermal processes in the overall deformation adjacent to fault planes assessed.

5.2. Faulting Model

The model of seismic faulting used here (case "A" of McKenzie and Brune, 1972), consists of two semi-infinite half-spaces which slide past each other at constant velocity for a period t'. This corresponds to the "slip model" of Nur (Section 4.2.2.) where the displacement is achieved by an instantaneous acceleration and deceleration (Fig. 5.1.).

It has been demonstrated (Chapter 4) that with this model the work done per unit area against friction is given by:

$$E_{Fa} = \bar{\tau}_{fk} \cdot \bar{u} \tag{5.1}$$

This model assumes slip is achieved with constant velocity. If τ_{fk} is also assumed to stay constant, the power dissipation on the fault during slip is constant and given by:

$$\dot{E}_{Fa} = \tau_{fk} \cdot v \tag{4.13}$$

where $\dot{E}_{Fa}$ = power dissipated per unit area

v = slip velocity.
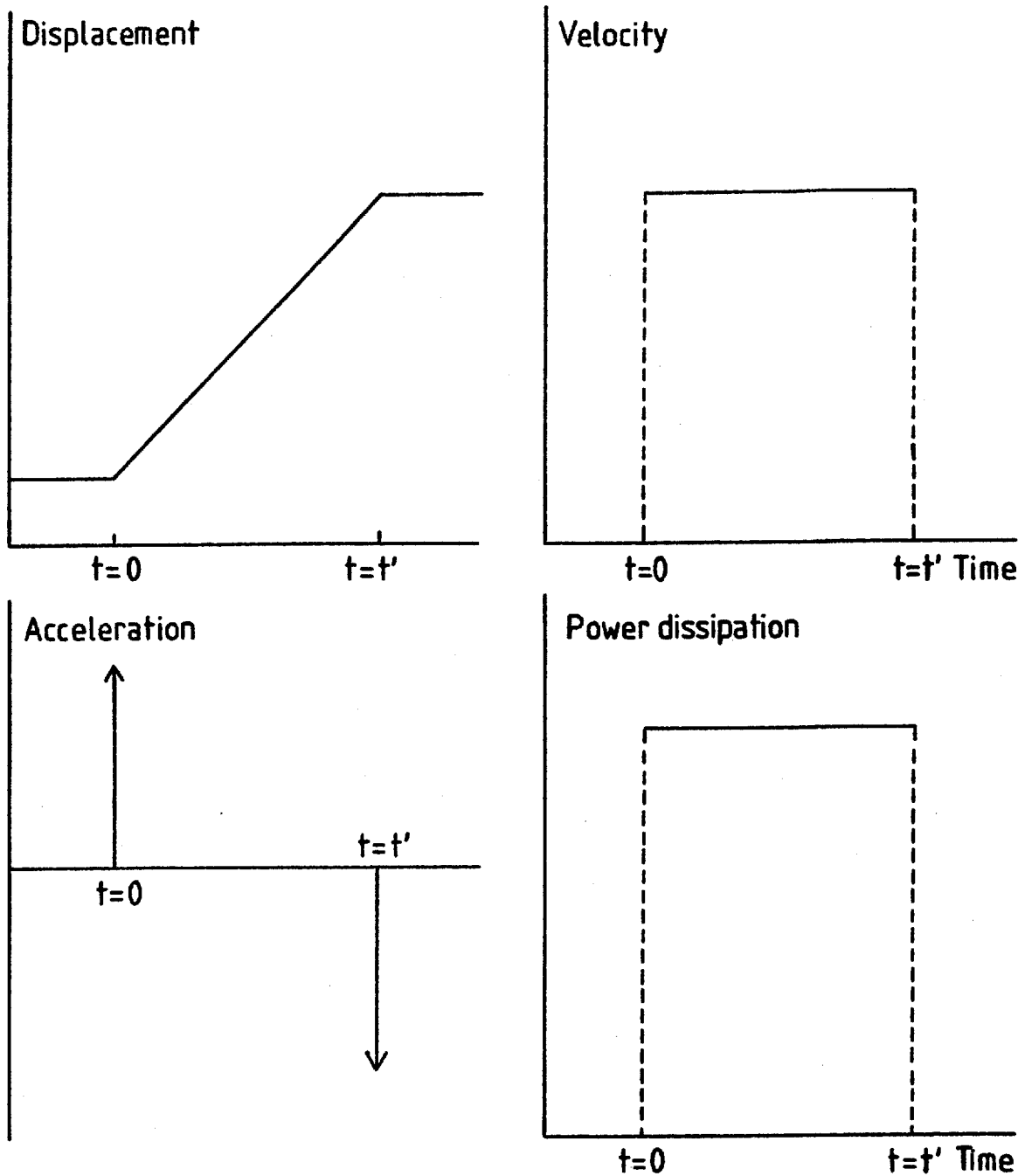
Fig. 5.1. Variation of displacement, velocity, acceleration and power
dissipation in the faulting model used.

5.3. Temperature Achieved Adjacent to the Fault

The medium containing the fault is assumed to be infinite, isotropic
and homogeneous. Heat therefore flows at right angles to the fault's sur-
face, and the problem becomes essentially one dimensional. Under the
boundary conditions imposed by the faulting model, the equation govern-
ing the temperature in either half-space is found in Carslaw and
Jaeger (1959):

$$T = \frac{\dot{E}_{Fa}}{K}\left\{\left(\frac{kt}{\pi}\right)^{\frac{1}{2}} \exp\left(-\frac{x^2}{4kt}\right) - \frac{x}{2}\, erfc\left(\frac{x}{2(kt)^{\frac{1}{2}}}\right)\right\} \qquad (5.2)$$

when $t \leqslant t'$, or:

$$T = \frac{\dot{E}_{Fa}k^{\frac{1}{2}}}{K}\left\{t^{\frac{1}{2}}\, ierfc\left(\frac{x}{2k^{\frac{1}{2}}\,t^{\frac{1}{2}}}\right) - (t - t')^{\frac{1}{2}}\, ierfc\left(\frac{x}{2k^{\frac{1}{2}}\,(t - t')^{\frac{1}{2}}}\right)\right\}$$

$$(5.3)$$

when $t > t'$ (after slip).

where k = thermal diffusivity

      T = temperature increase in either half space

      x = perpendicular distance from the fault plane

      t = time

      K = thermal conductivity

      $erfc(x)$ = $(1 - erf(x))$

      $erf(x)$ = Gaussian error function

$$= \frac{2}{\pi^{\frac{1}{2}}} \int_{0}^{x} \exp(-\xi^2)\,d\xi$$

      $ierfc(x)$ = $\dfrac{1}{\pi^{\frac{1}{2}}} \exp(-x^2) - x\, erfc(x)$

The temperature at any given distance from the fault, at any given time after the initiation of heating, may be calculated for given values of power dissipation provided the thermal constants of the material are known.

5.4. Model Limitations

Clearly there are many drawbacks involved in the application of this model to natural fault zones. The analysis is only valid for isotropic, homogeneous rocks. The fault must be a single, narrow feature and the presence of fluids is ignored. The possible effects of fluids in fault zones are complex. Their mechanical effect may reduce the frictional shear resistance τ_{fk} (in accordance with equation 4.12) and thus the amount of frictional heat generated. The migration of large volumes of hot fluid from the fault zone during or following slip will also reduce the heat available for conduction into the surrounding rock. Only in the absence of fluids will the heat convection term be zero. These factors lead to an over-estimation of the calculated temperatures associated with natural faulting.

If temperatures are calculated using room temperature values for

the thermal material constants (thermal conductivity, K, and thermal diffusivity, k) they may be underestimated. This is because both K and k decrease in value over the measured range (up to $400°C$), a trend that may continue over the entire temperature range associated with faulting.

It has so far been assumed that all of the heat generated on the fault's surface is conducted into the rock. No allowance is made for any resistance to thermal conduction which may result from the small area of real contact across a fault, the presence of shattered aniso-tropic material or conduction through a film of fluid. These factors combine to mean that temperatures calculated with this faulting model are only sensibly applicable to dry faults where slip occurs on a single, narrow surface.

5.5. Resistance to Thermal Conduction

The problems introduced by the concept of the real contact area across a natural fault are complex. Measurements of the real contact area, between two sides of a sawcut block in friction experiments performed at 50 MPa confining pressure, vary between 5 and 14 percent of the apparent area (Teufel and Logan, 1978). The real contact area of natural faults is not known and cannot be measured directly. Asperity creep and the presence of gouge will both increase it. Brock and Engelder (1977) present evidence that gouge may be very mobile. If this is true for gouge-filled faults, the real contact area may approach the apparent contact area. In this case slip will only occur on a narrow surface if it is localised either within the gouge layer or at the gouge-rock interface.

If heat is only generated at the isolated points of real contact between the two sides of a fault, the overall temperatures achieved during slip will be lower, since heat is used to raise the temperature of those areas of the fault's surface not in contact. This effect cannot be stated in simple mathematical terms since during slip the locations of the points of real contact are continually changing due to the frictional wear processes. It is simpler to include a general term for the thermal contact resistance of the fault, whatever its origin, in the power dissipation expression (equation 4.13), which becomes:

$$\dot{E}_{Fa} = \bar{\tau}_{fk} \cdot v \cdot (1 - R_c) \qquad (5.4)$$

where E_{Fa} = power dissipated on fault's surface per unit area

$\bar{\tau}_{fk}$ = frictional shear resistance

v = slip velocity

R_c = thermal contact resistance of the fault.

When the thermal contact resistance is zero, there is perfect thermal conduction across the fault and the power dissipated on it depends upon $\bar{\tau}_{fk}$ and v. R_c cannot be related directly to the percentage real area of contact without modifying the stress term to account for the stress concentration around the points of real contact. Equation (5.4) uses an average value for the overall stress acting on the fault plane. The use of an average stress value may to some extent cancel out the surface area effect. However, since the temperature at the points of real contact is limited by the rock's melting point this will not happen. The value of R_c will be lower than if the actual stresses acting at the points of real contact were used but will have a finite value. Its precise level will vary between individual faults.

Temperature profiles have been calculated for various values of $\dot{E}_{Fa}$. The fault parameters, $\bar{\tau}_{fk}$ and v, that these relate to are shown in Fig. 5.2. for various values of R_c. For likely values of shear resistance, 0.1 to 100 MPa and seismic slip rates of 0.01 to 1 ms^{-1}, power dissipation on faults at rates up to 100 MWm^{-2} for periods of seconds may be inferred if the thermal contact resistance is zero.

5.6. Temperature Distribution.

Solution of equations (5.2) and (5.3) shows that a power dissipation of only 2 MWm^{-2} for 10 seconds is sufficient to raise the temperature of the fault by between 1400° and $1500^\circ C$. This will lead to surface melting in most rock types at which point the frictional resistance and the further heat generating capacity of the fault will decrease abruptly. Indeed lower temperature rises of between 800° and $1000^\circ C$ might be expected to bring about partial melting. It is unlikely, in the time over which slip is accomodated ($\leqslant 10$ seconds), that metamorphic equilibrium is attained between the rock-forming minerals and therefore it seems reasonable to assume that minerals will melt when their individual melting temperatures are reached (Table 5.1). A low temperature equilibrium granitic melt is therefore unlikely to form. Instead a melt consisting of the minerals with the lowest individual melting temperatures may be expected. This appears to be the case for pseudo-tachylyte friction-melts (Sibson, 1975).

The melting temperatures of quartz and feldspar lie between 1400°

48
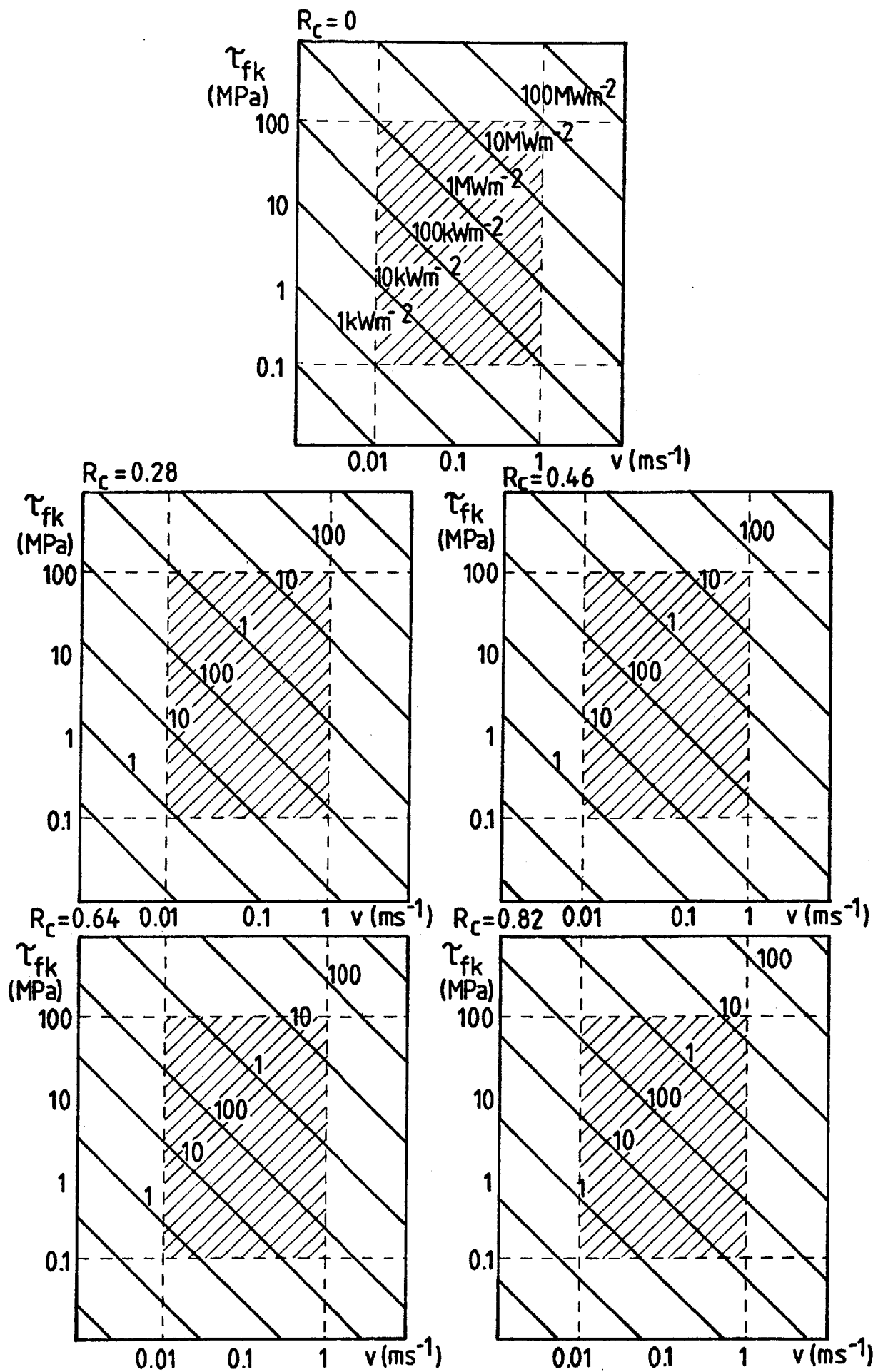
Fig. 5.2. The relationship between power dissipation and fault slip parameters

and 1500°C and since these are the dominant constituents of quartzo-feldspathic crust, the temperatures adjacent to faults are unlikely to exceed this value. Once the melting temperature has been reached, further energy is required to overcome the latent heat of fusion.

Table 5.1.

Approximate melting temperatures for common constituents
of quartzo-feldspathic crust at atmospheric pressure

Mineral	Melting Temperature (°C)	
[1] Quartz	1713	
[1] Albite	1118	
[1] Anorthite	1553	(1) Ehlers (1972)
[1] Orthoclase	1540	(2) Clarke (1966)
[2] Olivine	1205-1890	(3) Spry (1969)
[3] Biotite	950	
[2] Enstatite	1557	
[2] Diopside	1391	
[2] Amphibole	950-1050	

Thus the temperature distribution resulting from a power dissipation of 2 MWm^{-2} where the fault's surface is at the maximum likely temperature after a 10 second heating pulse, shows the maximum temperatures that can be achieved during seismic slip at shallow crustal levels. For power dissipations of 2 MWm^{-2} or greater, similar temperature distributions result (Fig. 5.3) and the maximum thermal stresses will develop.

5.6.1. Relationship Between Power Dissipated and Fault Parameters

A power dissipation of 2 MWm^{-2} would, for example, be achieved by a slip velocity of 0.02 ms^{-1} against a shear resistance of 2 MPa if R_c = 0. Reference to Fig. 5.2 supplies the slip velocities and shear resistances when R_c has finite values. For example, when R_c = 0.28 slip at a velocity of 0.028 ms^{-1} against a shear resistance of 100 MPa will dissipate about 2 MWm^{-2}.

5.6.2. Maximum Fault Temperature

Maximum temperatures on the fault are reached at the end of the
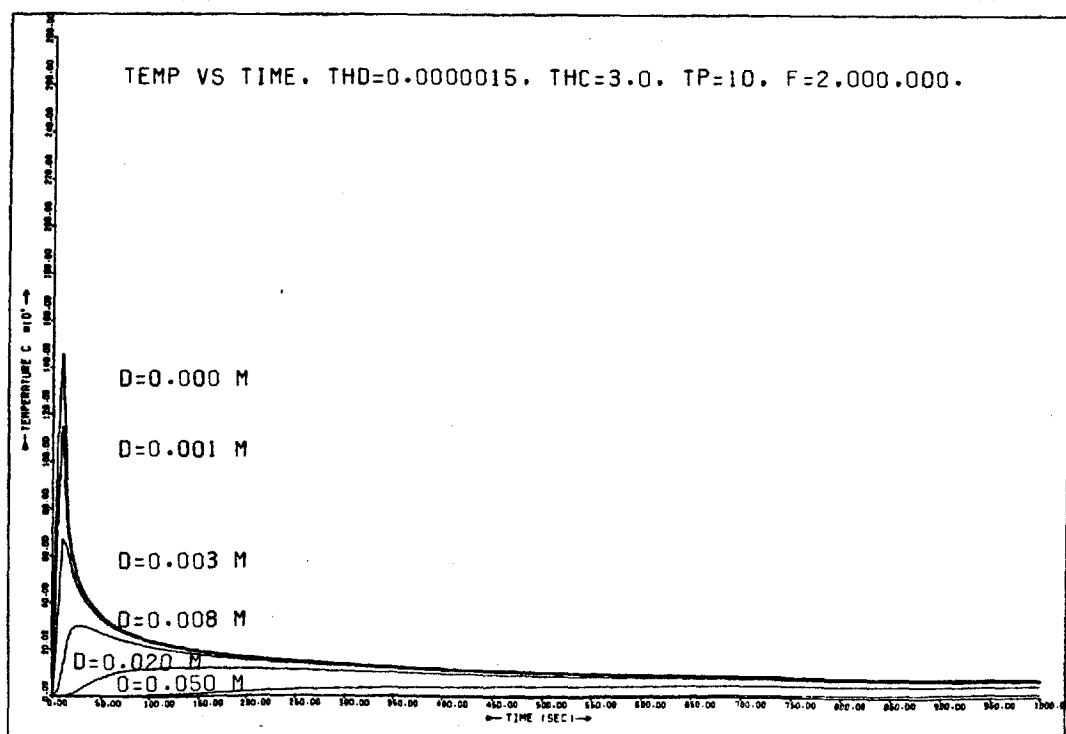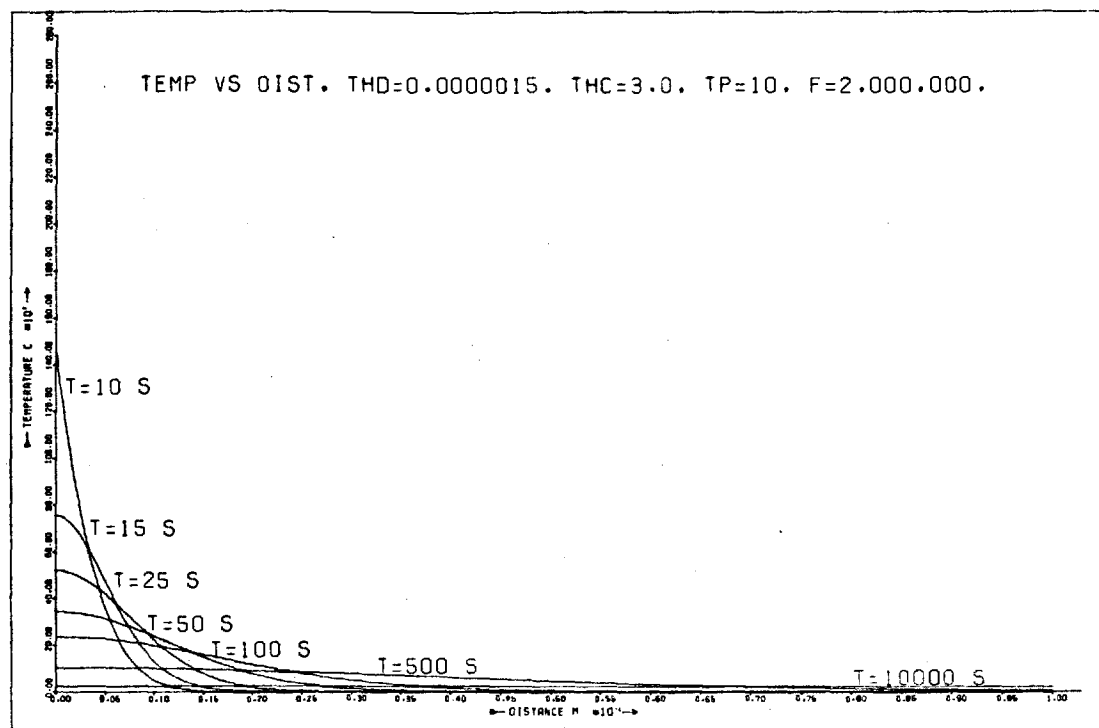
Fig. 5.3. Temperature distribution for a power dissipation of 2 MWm^{-2} (or greater).

(N.B. In this and all similar diagrams, the variables given in the graph heading are in MKS units; THD is thermal diffusivity ($m^2 s^{-1}$), THC is thermal conductivity ($Wm^{-1} {}^{\circ}C^{-1}$), TP is the rise time (s) and F is the power dissipated on the fault plane per unit area ($W.m^{-2}$). The values of these variables used are average ones for crystalline quartzo-feldspathic rock (Clarke, 1966). Temperatures refer to temperature increase due to slip.)
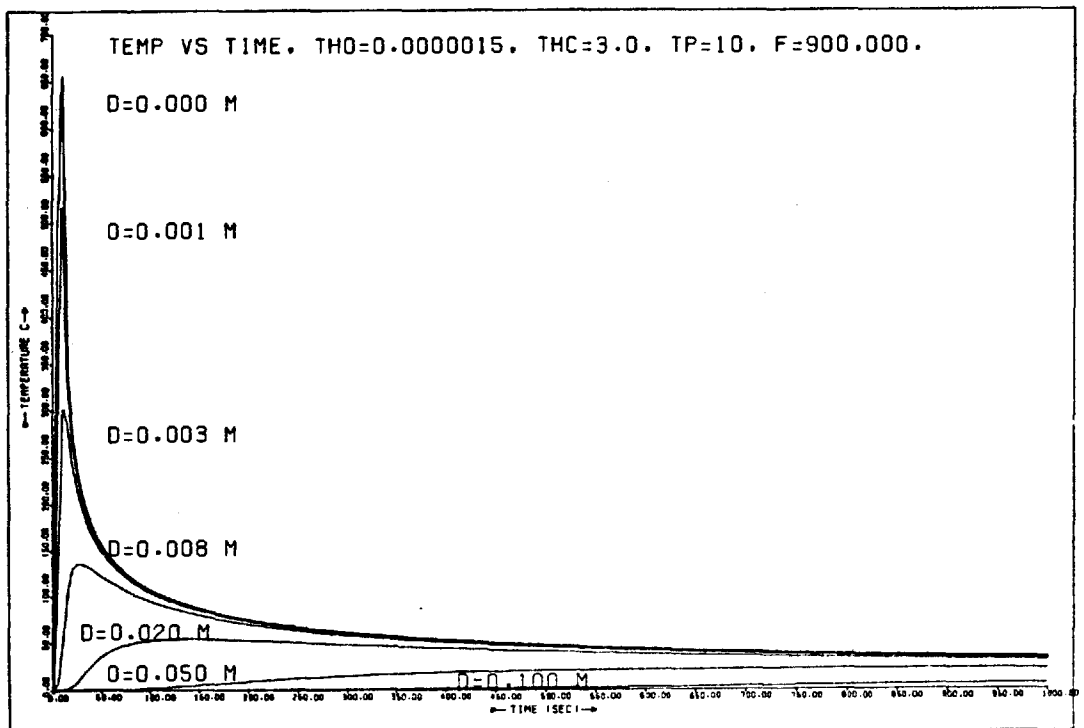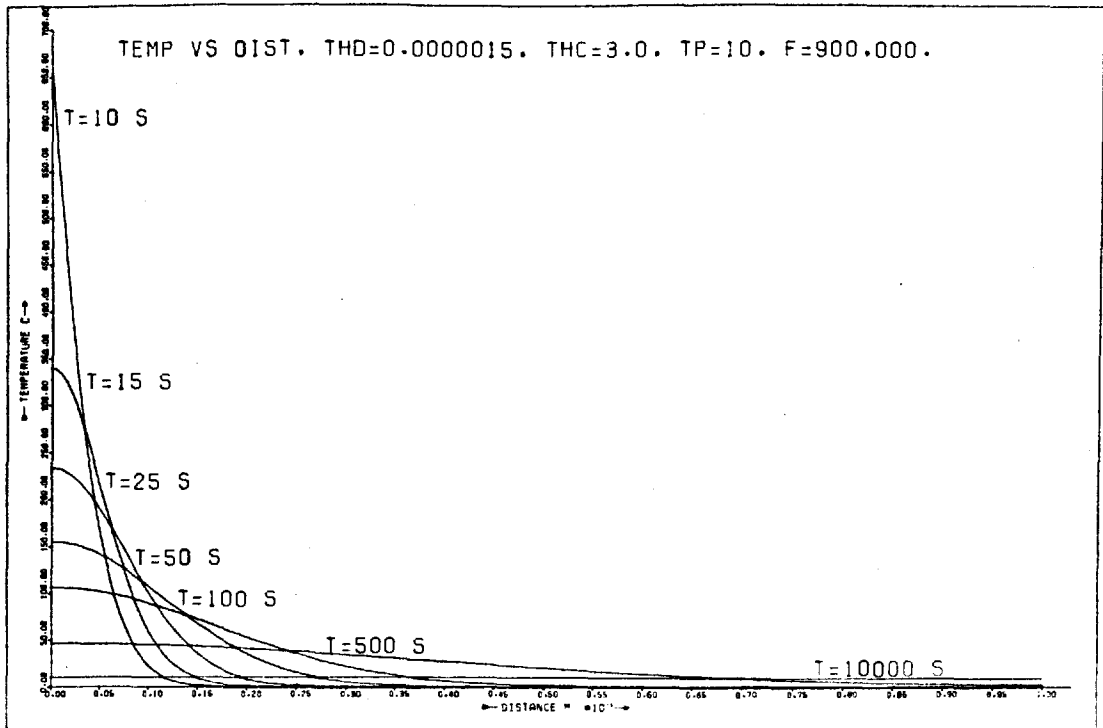
Fig. 5.4. Temperature distribution for a power dissipation of $900kWm^{-2}$.
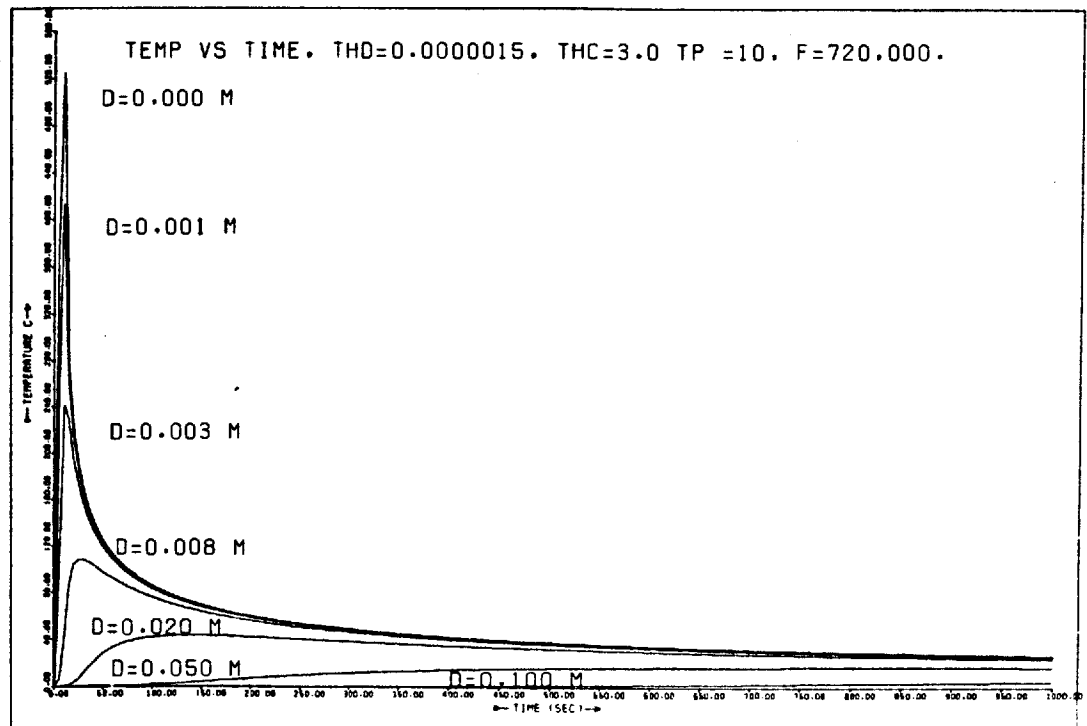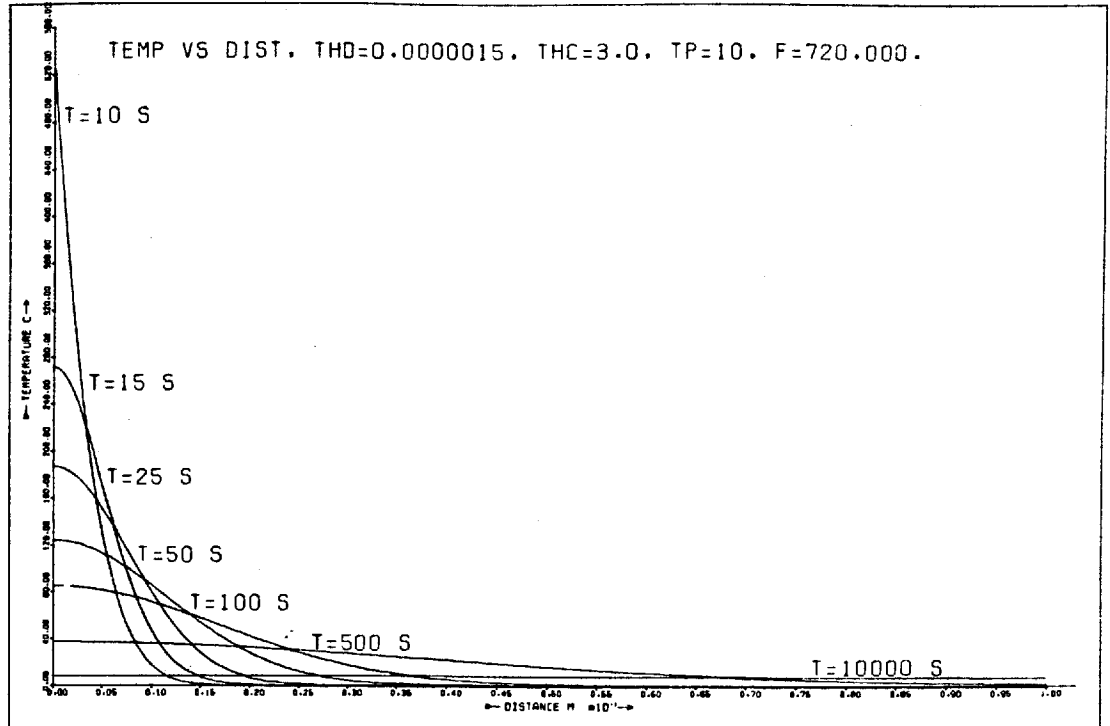
Fig. 5.5. Temperature distribution for a power dissipation of 720 kWm^{-2}.

TEMP VS DIST. THD=0.0000015. THC=3.0. TP=10. F=540.000.

T=10 S

T=15 S

T=25 S

T=50 S

T=100 S

T=500 S

T=10000 S

←— DISTANCE M ×10⁻¹ —→

TEMP VS TIME. THD=0.0000015. THC=3.0. TP=10. F=540.000.

D=0.000 M

D=0.001 M

D=0.003 M

D=0.008 M

D=0.020 M

D=0.050 M

←— TIME (SEC) —→
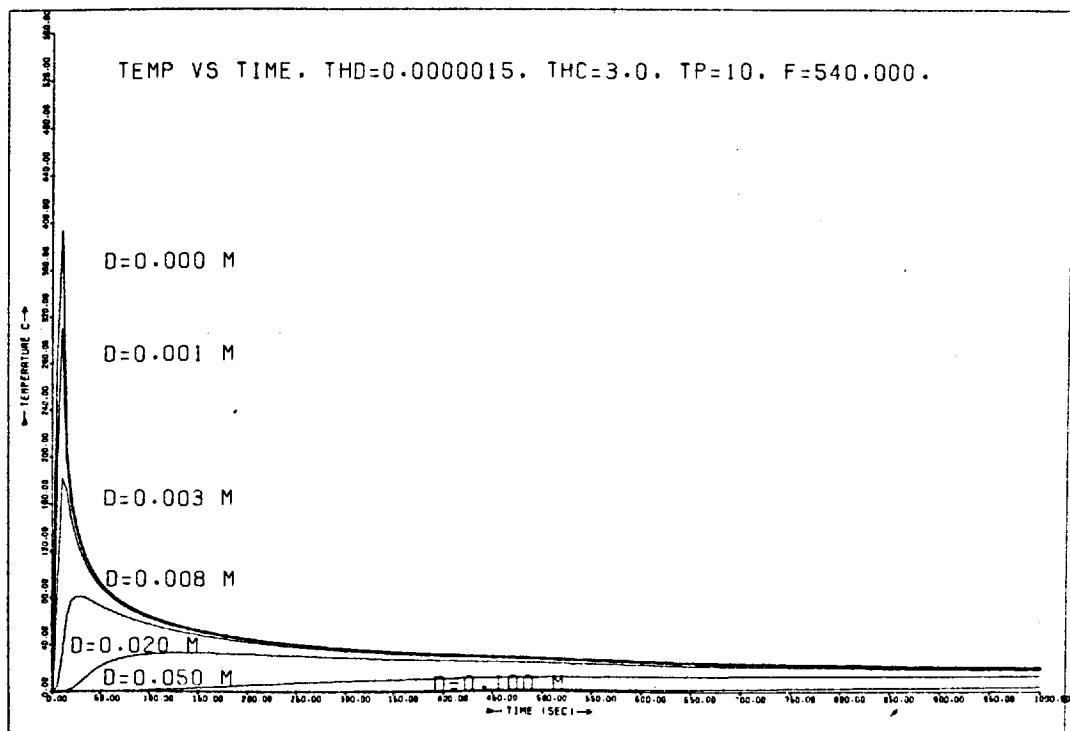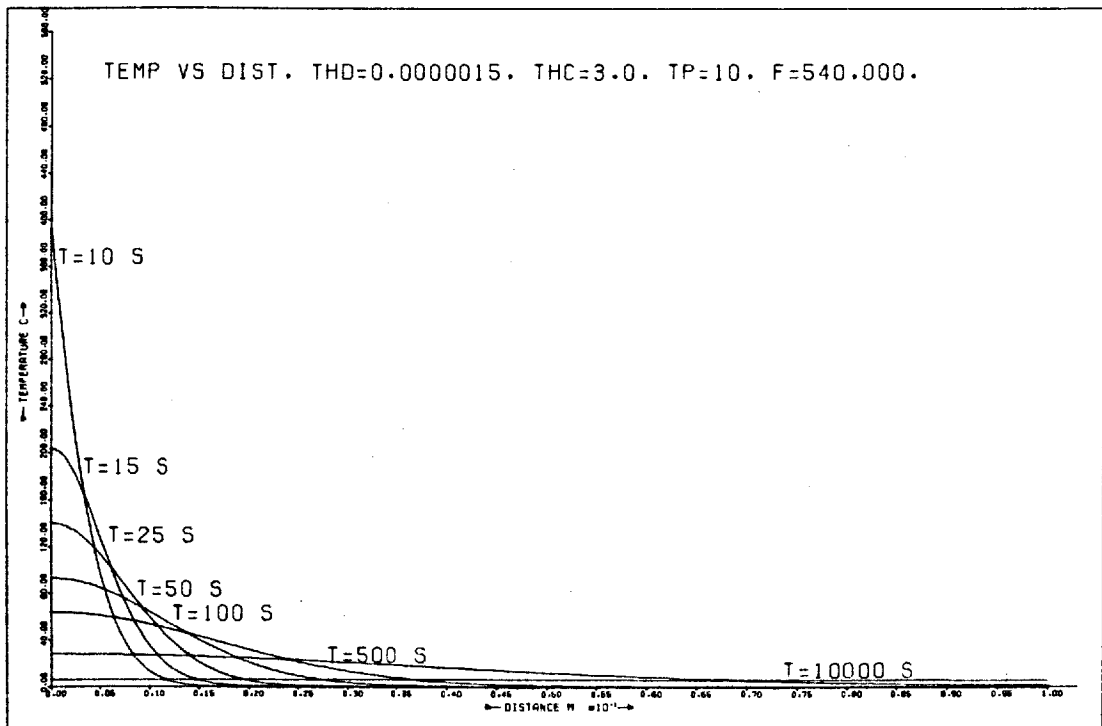
Fig. 5.6. Temperature distribution for a power dissipation of 540 kWm^{-2}.

TEMP VS DIST. THD=0.0000015. THC=3.0. TP=10. F=360.000.

T=10 S

T=15 S

T=25 S

T=50 S

T=100 S

T=500 S

T=10000 S

TEMP VS TIME. THD=0.0000015. THC=3.0. TP=10. F=360.000.

D=0.000 M

D=0.001 M

D=0.003 M

D=0.008 M

D=0.020 M

D=0.050 M

D=0.100 M
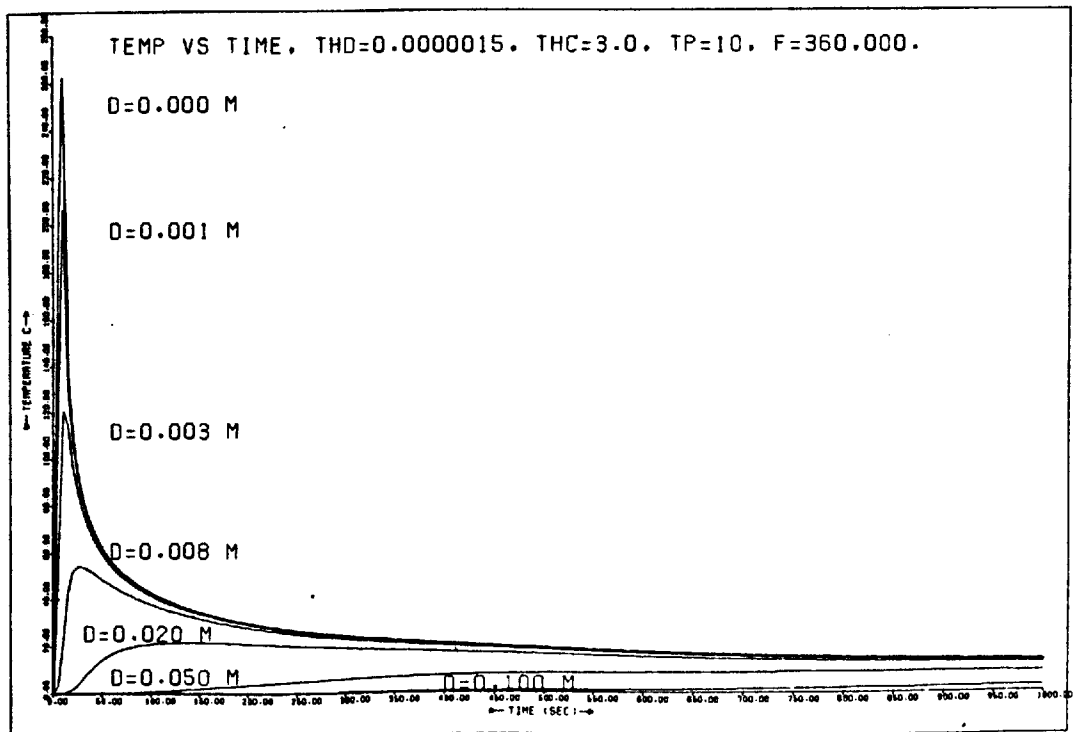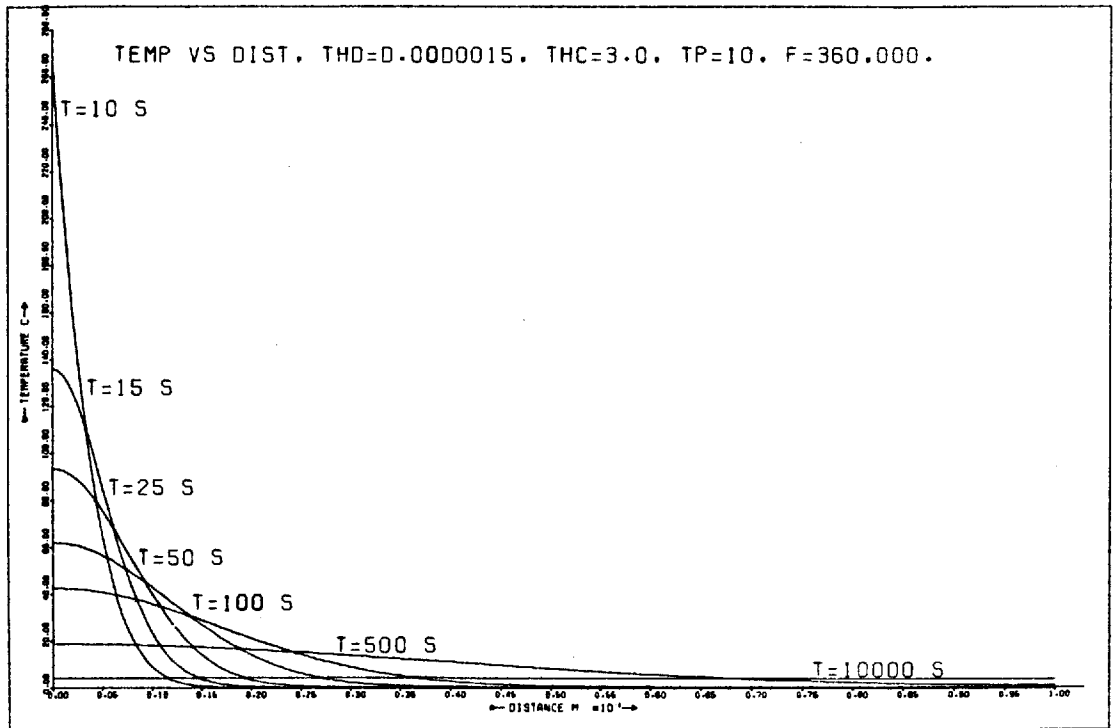
Fig. 5.7. Temperature distribution for a power dissipation of 360 kWm^{-2}.
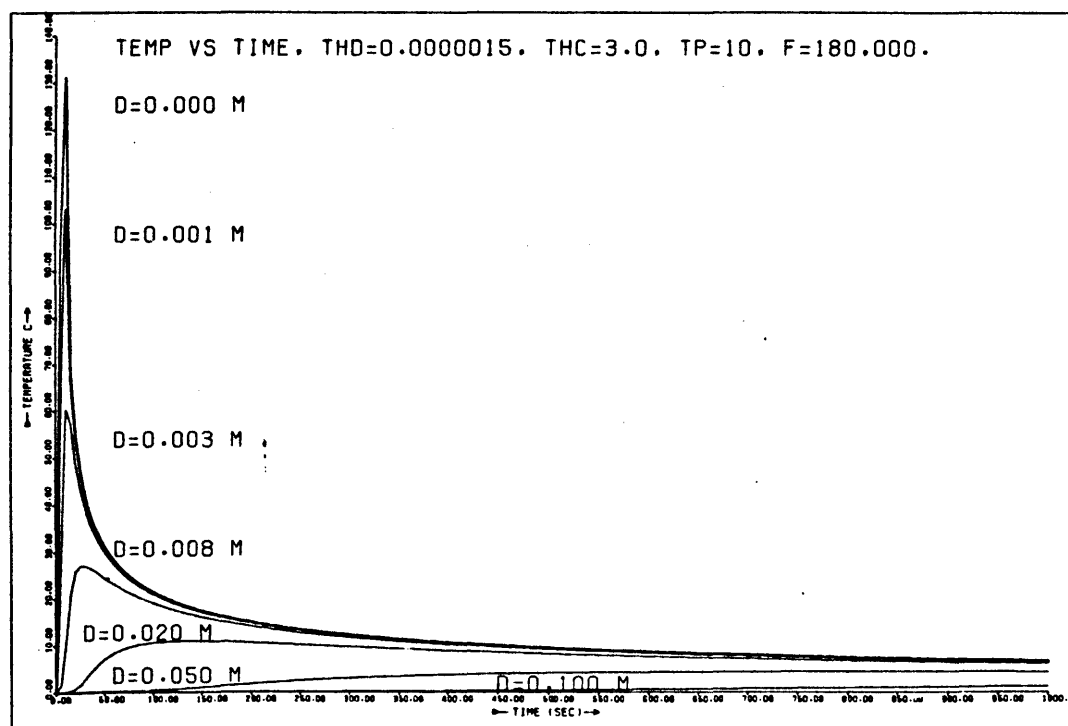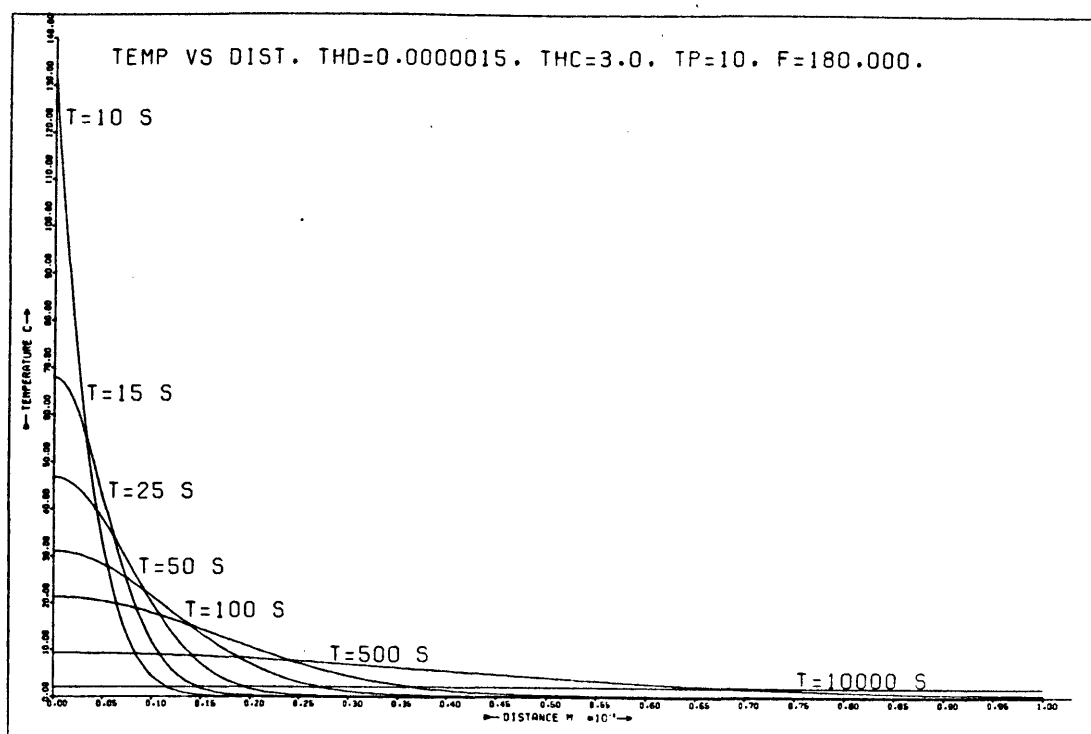
Fig. 5.8. Temperature distribution for a power dissipation of 180 kWm^{-2}.

slip event. Temperatures rapidly decrease with distance from the fault plane (Fig. 5.3a) and at any given distance, with time (Fig. 5.3b and Table 5.2).

Table 5.2.

Decrease in surface temperature of fault with time.
Duration of slip event is 10 seconds.

Time (s)	Surface Temperature (°C)
10	1460
100	236
1,000	73
10,000	24
100,000	7.3
1,000,000	2.4
10,000,000	0.7

5.6.3. Temperatures Achieved with Lower Power Dissipations

Figs. 5.4 to 5.8 show the temperature distributions resulting from lower power dissipation over the same 10s period. Again reference to Fig. 5.3 gives the relevant slip parameters for a given value of R_c.

5.7. Thermal Stresses

Thermal stresses are likely to arise as a result of frictional heating because of the transient high temperatures and steep thermal gradients adjacent to the fault plane. The anisotropy of thermal expansion in non-isometric crystals (Rosenholz and Smith, 1949; Kuszyk and Bradt, 1973) and variations in the coefficients of thermal expansion for different mineral grains (Kingery, 1957; Boas and Honeycombe, 1947) both cause thermal stresses even with uniform heating. The development of steep, non-linear thermal gradients across both individual crystals and crystalline aggregates (Lauriello, 1974; Richter and Simmons, 1974) adds to this effect. Detailed accounts of thermal stress theory may be found in Nye (1976), Boley and Weiner (1960) and Timoshenko and Goodier (1951). A brief summary is given here.

5.7.1. Thermal Stress Theory

The thermal expansion, on heating, of any homogeneous, isotropic, elastic material can be described by considering the body to consist of a number of small cubical elements. If the temperature of the body is

uniformly raised and its bounding surface is unrestrained, each element will expand in all directions and no internal stresses will develop. The body has then undergone a homogeneous strain given by:

$$E_{ij} = \alpha_{ij} \Delta T \qquad (5.5)$$

where α_{ij} = coefficient of thermal expansion
ΔT = a small change in temperature.

The thermal expansion tensor, α_{ij} is a symmetrical second rank tensor and so may be referred to its principal axes. Thus, the strain equations simplify to:

$$\begin{matrix} E_1 & = & \alpha_1 \Delta T &) \\ E_2 & = & \alpha_2 \Delta T &) \\ E_3 & = & \alpha_3 \Delta T &) \end{matrix} \qquad (5.6)$$

If the elements expand by unequal amounts, as would be the case in polymineralic rock where the thermal expansion coefficient depends upon the mineralogy, or if they do not expand uniformly in all directions, as with common minerals where the expansion coefficient varies with the crystallographic orientation, or if there is a thermal gradient across the body, then the expanded elements will not fit together. If the body is to remain continuous throughout, each element will restrain adjacent elements and thus internal stresses develop.

Similar arguments apply to cooling. In general, compressive stresses arise from heating and tensile stresses from cooling. If the differential stresses are high enough compressive, shear failure will occur during heating and tensile failure during cooling.

Determining the full configuration of stresses during seismic slip is complex because faulting is a dynamic process during which the external stress field changes rapidly. It is, however, possible to gain some idea of thermal stress effects, including the volume of rock likely to be affected.

5.7.2. Effect of Thermal Gradients

The stresses resulting from the thermal gradients may be usefully considered separate from those arising from other causes. They may be calculated by considering the thermal stresses which arise in an elastic, homogeneous, thick plate (Fig. 5.9) when one side of it is insulated and the other is subject to a sudden, uniform heat flux . Although the plate is unrestrained, its internal stresses are identical

to those of a constrained body when heat flow is perpendicular to the heated surface (Geller, 1970). Under these conditions the thermal stresses are proportional to the coefficient of expansion and the temperature gradient represents the stress distribution (Norton, 1949).
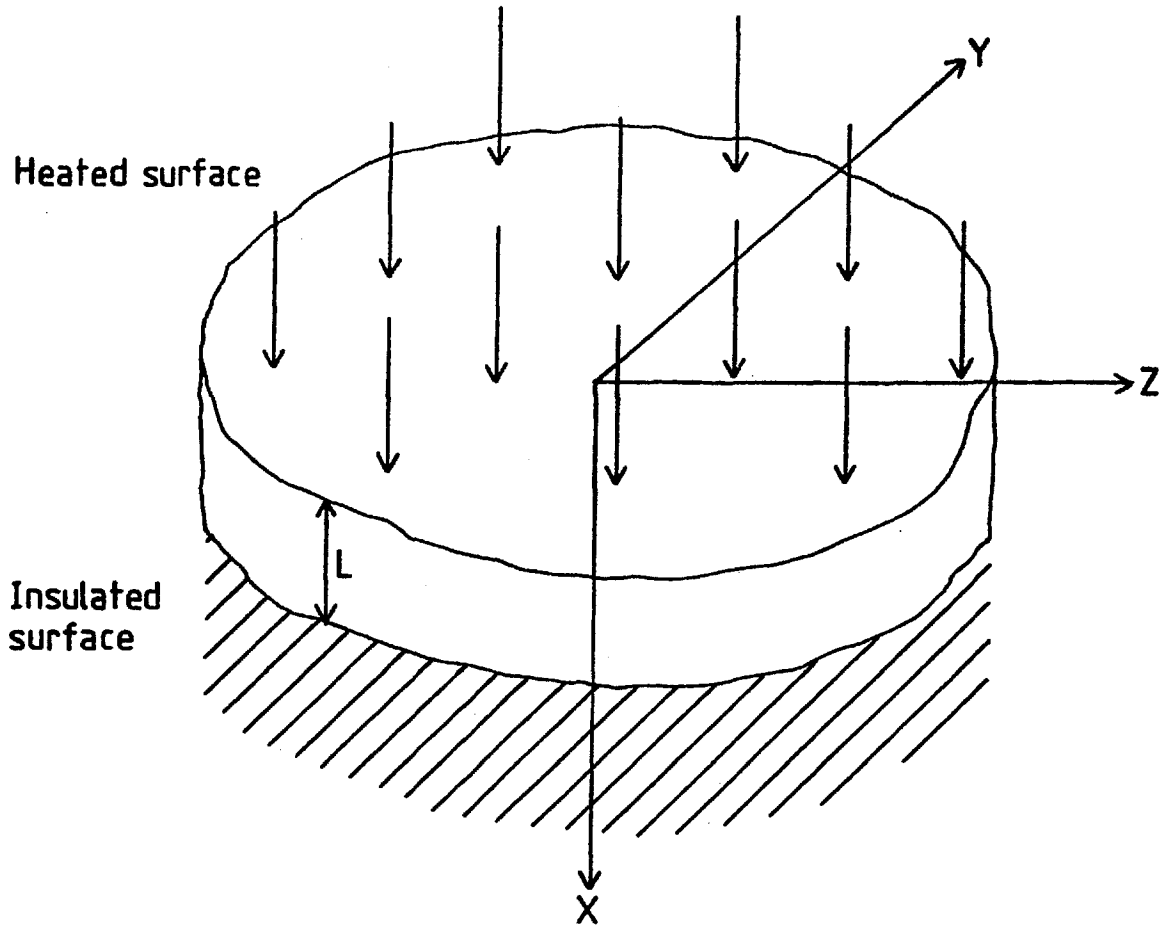
Fig. 5.9. Flat plate uniformly heated on one side and insulated on the opposite face.

Biot's number, m, is given by:

$$m = \frac{HL}{K} \qquad (5.7)$$

where H = surface heat transfer coefficient
   L = plate thickness
   K = thermal conductivity

Boley and Weiner (1960) show that when $m = \infty$, the case when the plate has infinite thickness, the maximum stress occurs at the heated surface. Since the isothermal lines are everywhere parallel to the heated surface the principal thermal stresses are either parallel or perpendicular to the heated surface and are given by:

$$\left. \begin{array}{rcl} \sigma_{yy} & = & \sigma_{zz} & = & \dfrac{\alpha E \Delta T}{1-\upsilon} \\[2mm] & & \sigma_{xx} & = & 0 \end{array} \right\} \qquad (5.8)$$

where α = thermal expansion coefficient

E = Young's modulus

T = Temperature rise

υ = Poisson's ratio.

Substituting average values for the material constants ($\alpha = 1 \times 10^{-5}\,{}^{\circ}C^{-1}$, $E = 4 \times 10^{4}$ MPa, $\upsilon = 0.2$, Clarke (1966)) gives a differential stress ($\sigma_{zz} - \sigma_{xx}$) of $0.5\ \Delta T$ (MPa). On the basis of short term laboratory experiments the differential stress required for failure is assumed to be about 250 MPa for intact quartzo-feldspathic rock under shallow crustal conditions. Thus a surface temperature rise of about 400° or $500^{\circ}C$ is sufficient to initiate fracture adjacent to the heated surface. In the absence of any external stress field, compressional shear factures would be expected at about 30° to the fault's surface.

Young's modulus and Poisson's ratio decrease and the thermal expansion coefficient increases with increasing temperature. This will lead to an underestimation of the actual thermal stresses if the room temperature values for these parameters are used. The underestimation is likely to be small (Lehnhoff and Scheller, 1975). The pressure dependence of these variables is not fully understood but its effect is also likely to be small.

These stresses result from the thermal gradient at the heated surface. When the surface of an infinite or thick block is heated to about $400^{\circ}C$ (Fig. 5.6b) this thermal gradient is $65^{\circ}C\ mm^{-1}$. The thermal stresses will be large enough to initiate fracture at any point in heated rock where this thermal gradient is exceeded. For the faulting model considered, this gradient exists within a maximum of 10 mm of the fault's surface, where it is reached 5 seconds after initiation of slip. The direct effect of the thermal gradient is, therefore, limited to a very narrow band each side of the fault. Even if the thermal gradient required for the initiation of compressive thermal fractures has been overestimated by a factor of 3, fractures would only initiate within 15 mm of the fault.

5.7.3. Effect of Thermal Expansion Anisotropy

Investigation of the deformation resulting from the crystallographic

anisotropy of thermal expansion and its variation between minerals has been experimental rather than theoretical. Thermal anisotropy effects are very localised and generally cause microcracking of the sample (Thirumalai and Cheung, 1972). On a microscopic scale, where the material cannot be considered elastic, isotropic and homogeneous, fracture initiation results from stress concentration around flaws and defects (cleavage planes, grain boundaries, intergranular pores etc.). Experiments performed at low heating rates (less than $2^{o}C$ per minute) to minimise thermal gradients (Richter and Simmons, 1974) show permanent strain in samples whose temperature exceeds $350^{o}C$. This is attributed to the formation of intergranular microcracks which develop only when this critical temperature is exceeded.

Surface fracture morphology suggests that these microfractures commonly lead to macroscopic intergranular fracture in some ceramics (Kuszyk and Bradt, 1973) and that in rocks, tensile cracks typified by rubble-free fractures containing step-like conchoidal rills on quartz grains, are common (Thirumalai and Cheung, 1972).

With reference to Fig. 5.3 (in which the maximum possible temperatures are attained), $350^{o}C$ is exceeded only within 7 mm of the fault plane. This suggests that microfracturing due to thermal anisotropic effects will also be restricted to a narrow strip adjacent to the fault.

5.7.4. Other Factors

One frequently observed experimental phenomenon is that thermal fracture is more widespread in rocks with a high quartz content (Richter and Simmons, 1974; Geller, 1970). This is attributed to the sudden increase in volume of quartz at the α/β transition at $573^{o}C$ (Fig. 5.10). In the faulting model used, only rocks within 5 mm of the fault plane pass through this transition.

An alternative explanation was given by Moore and Sibson (1978). They proposed that fracturing of quartz grains may be brought about by the overpressuring of internal fluid inclusions on heating. They suggest that failure would be in tension and that temperature rises of between 50° and $100^{o}C$ would be sufficient to initiate fracture. Rock temperatures exceed $100^{o}C$ at distances up to 22 mm from the fault and $50^{o}C$ at 42 mm.

Another factor that influences thermal fracture is the rate of heating. The experimental work of Richter and Simmons (1974) suggests that microfracturing results from fast ($\geqslant 0.03^{o}$ s^{-1}) heating rates.
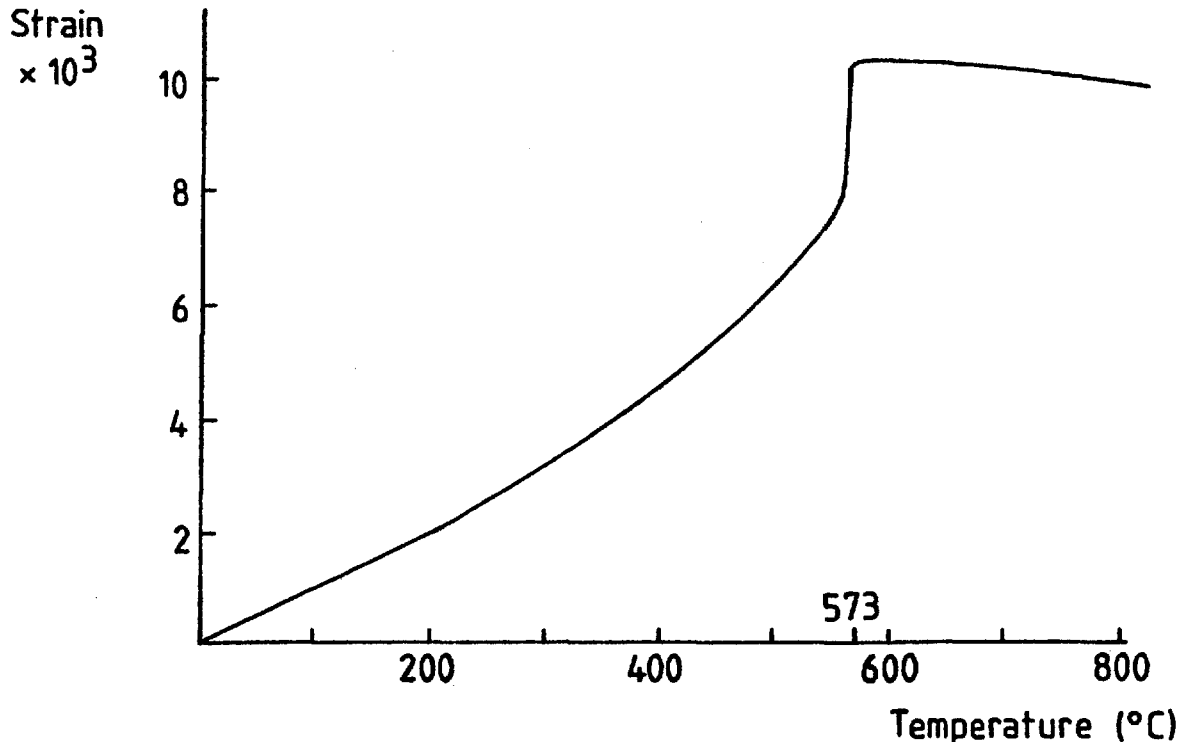
Fig. 5.10. Thermal expansion of quartz parallel to the c-axis (from Richter and Simmons, 1974)

This effect is caused essentially by the thermal gradients but should not be confused with the macroscopic fracturing discussed in Section 5.7.2. Instead it depends upon the stress concentrations developed in an anisotropic, inhomogeneous medium. Heating rates above this critical value of $0.03^{\circ}C\ s^{-1}$ exist within a maximum of 0.1 m of the fault plane.

5.7.5. Extent of Thermal Damage

The preceding sections suggest that even if melting temperatures are attained on the fault's surface and if the rock is considered to be ideally elastic, isotropic and homogeneous, any initiation of large thermal fractures is restricted to within 10 mm of the fault. The combined effects of fluids and shearing in a natural fault zone would be expected to bring about fracture propagation out of this zone. If the micro-structural inhomogeneities of rock are considered, a more realistic estimate of the zone likely to undergo thermal damage can be obtained. Although microstructural damage resulting from the heating rate may

then occur up to 0.1 m (100 mm) from the fault's surface when it is
at melting point, the zone is reduced to less than 50 mm when the power
dissipated on the fault is only 180 kW m^{-2} and the surface temperature
reaches about 130°C (Fig. 5.8). The effect of this microfracturing, which
is associated with grain boundaries, cleavage planes or intracrystalline
flaws, will be to weaken the rock adjacent to the fault plane. This
in turn will facilitate mechanical wear resulting from shear.

If only 20 kW m^{-2} is dissipated on the fault (Fig. 5.11), the surface
temperature reaches almost 15°C after 10 seconds and the microstructural
damage is then restricted to within 20 mm of the fault. In this case,
with low finite temperatures the level of damage within this zone
would be expected to be slight and macroscopic fracturing will not
occur. This can be considered the lower limit of significant thermal
damage. Slip parameters for this level of power dissipation are shown
in Fig. 5.12. which gives the parameters of slip for which thermal
effects will be important.
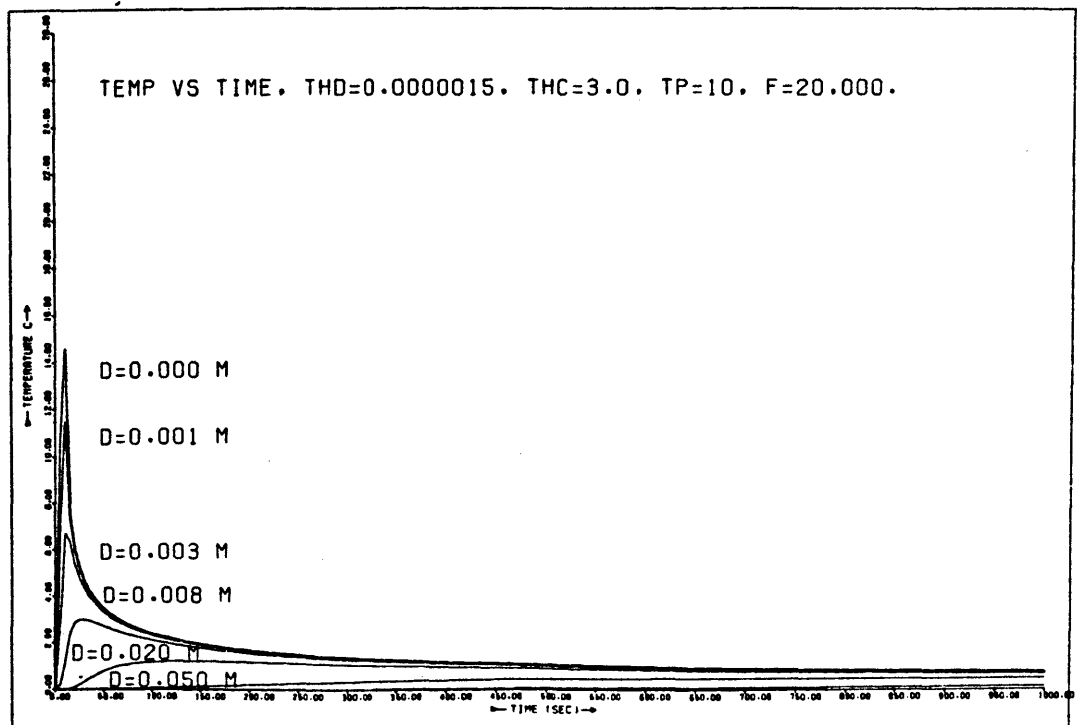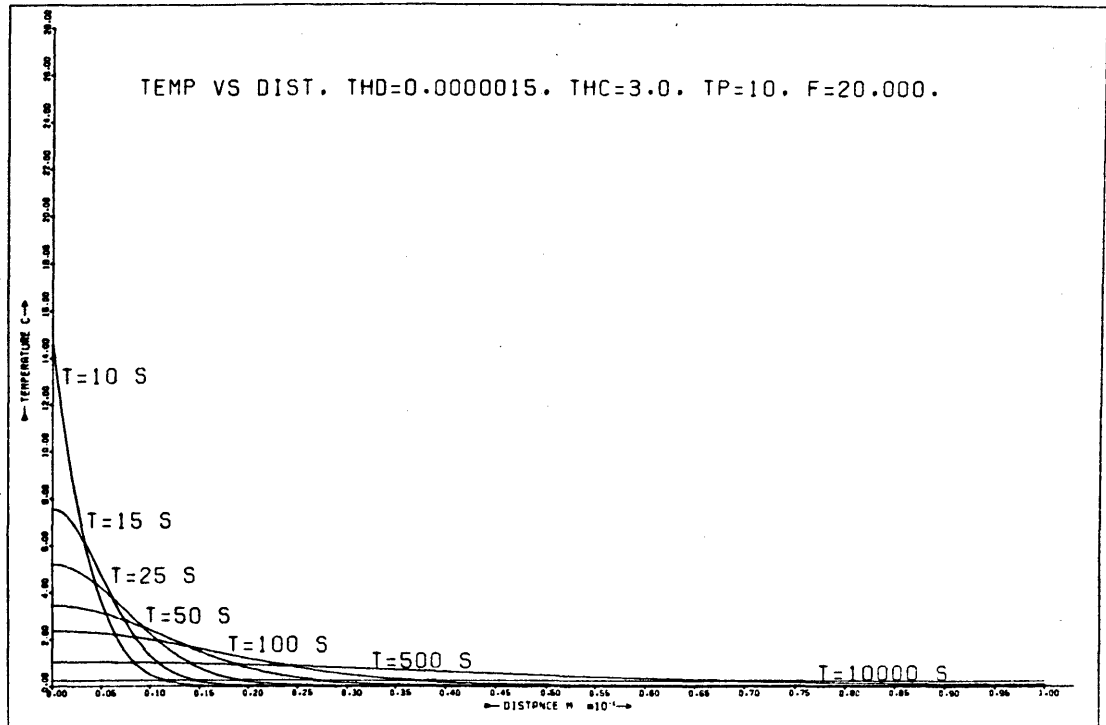
Fig. 5.11. Temperature distribution for a power dissipation of 20 kW m^{-2}.
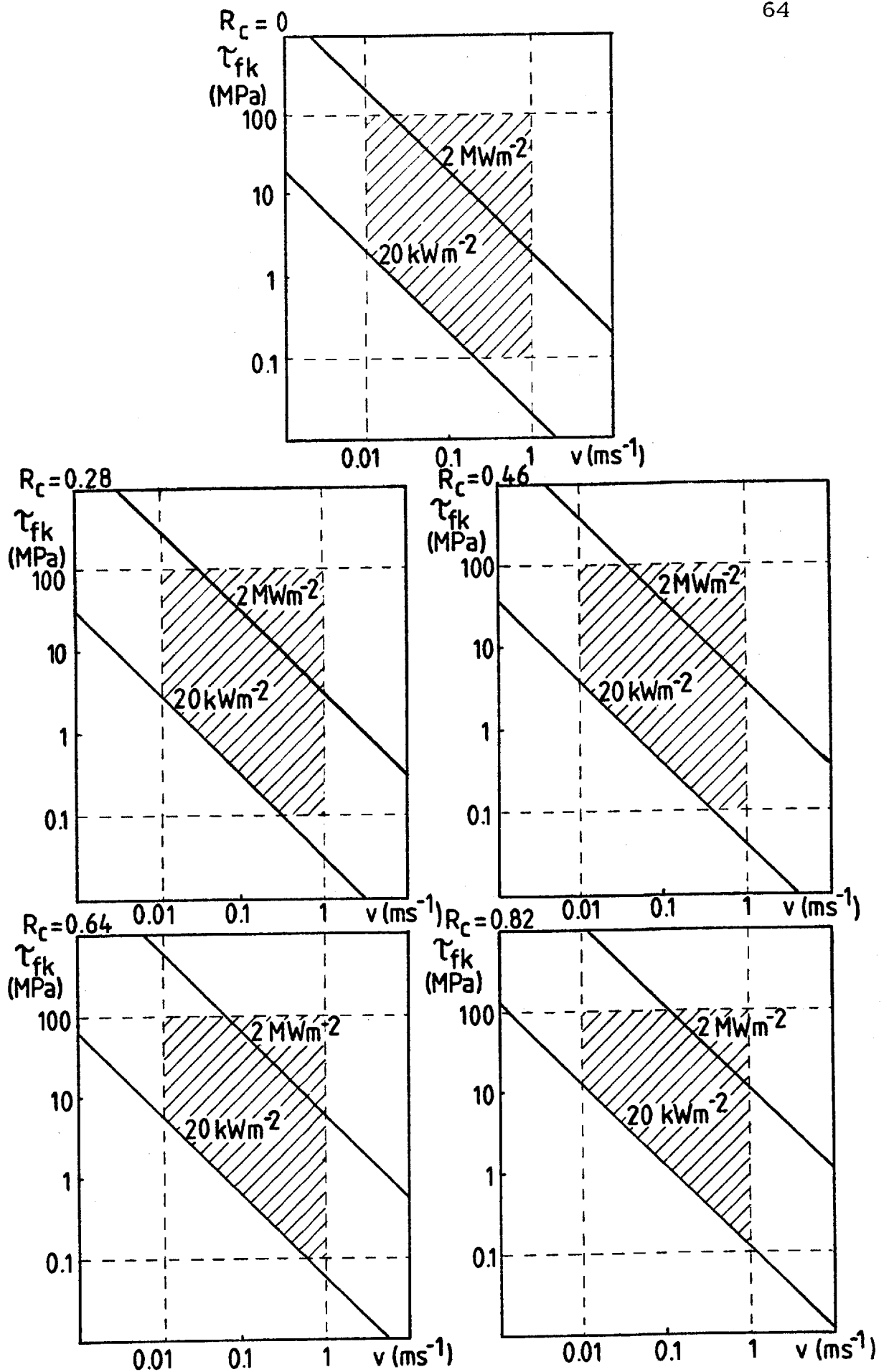
Fig. 5.12. Shaded area represents the parameters of fault slip for which thermal effects are significant. 2 MW m^{-2} line represents the conditions for which melting will occur.

CHAPTER 6

ROCK DEFORMATION ASSOCIATED WITH FAULTING

6.1. Fault Rocks

Texturally distinctive rock types are found associated with many zones of shear dislocation. Their texture arises either directly or indirectly from the shearing process and the textural character depends upon the physical conditions under which shearing occurred. Sibson's (1977b) definition of the term "fault rock" for this suite of rocks is used here in preference to the term "cataclasitic" rock introduced by Waters and Campbell (1935), which is restricted here solely to rocks that have developed by cataclasis; i.e. brittle fracture and rigid body rotation of mineral grains accompanied by dilatation.

Several attempts have been made to classify fault rocks on a descriptive rather than a genetic basis and although such classifications are useful, problems arise since many rocks are the result of polyphase deformation and/or have been modified by later events on the fault plane; fluid flow, fracture, veining and recrystallisation. The classification given here (Fig. 6.1) is based upon those of Spry (1969), Higgins (1971), and Sibson (1977b) and is used as a basis for discussion rather than as a rigid structure into which all fault rocks fit.

In the two main suites of fault rock, the cataclasite and mylonite series, mechanisms which reduce the grain size are dominant over grain growth and the fault rock usually has a finer grain size than the host rock into which it grades. In the cataclasite series, cataclasis is the dominant deformation mechanism and the rock shows no marked crystallographic or shape-preferred orientation. With progressive cataclasis an ultra-fine-grained, structureless rock is produced. In the mylonite series, recovery and recrystallisation are dominant and are responsible for the reduction in grain size, the development of a foliation and the development of shape and crystallographic preferred orientations. Members of this series commonly develop penetrative L-S tectonite fabrics.

The second fundamental division arises from whether or not the rocks possess cohesion. The term "primary cohesion" was introduced by Higgins (1971) without precise definition. He considered fault rocks with primary cohesion to be metamorphic rocks and excluded secondary

		PROPORTION OF MATRIX			
		0 - 70 %		70 - 100 %	
INCOHESIVE		Fault breccia		Fault gouge (sometimes foliated)	RANDOM FABRIC
COHESIVE	Crush breccia fragments ⩾ 0.5cm Fine crush breccia 0.5cm > frags. > 0.1cm	◄──────── CATACLASITE SERIES ────────►			RANDOM FABRIC
		Proto-cataclasite	Cataclasite	Ultra-cataclasite	
	Crush microbreccia fragments ⩽ 0.1cm	Proto-mylonite	Mylonite	Ultra-mylonite	FOLIATED
		◄──────── MYLONITE SERIES ────────►			
	0 - 10 %	10 - 50 %	50 - 90 %	90 - 100 %	
		PROPORTION OF MATRIX			

Fig. 6.1. Fault rock classification.

cementation from the undefined processes leading to primary cohesion. It is implied that these processes include recrystallisation, grain growth and the growth of new phases.

6.1.1. Cohesion of Fault Rocks

Higgins' distinction between primary and secondary cohesion (that brought about by later cementation) is not used here since it is often difficult to distinguish between them. Processes bringing about cohesion of a fault rock may occur during and/or after the deformation which reduces their grain size. At near surface levels, late cementation alone is likely to occur while with increasing depth, pressure solution, the growth of hydrothermal minerals and metamorphic reactions of increasing grade become progressively more important both during and after each episode of deformation. In effect, this means that there will be a continuous series of random-fabric fault rock types which vary from incohesive (gouge) at near surface levels, to cohesive (cataclasite) at depth.

6.1.2. Relationship Between Cohesive and Incohesive Fault Rocks

During the development of mylonite series rocks, quasi-plastic ductile deformation is dominant with thermally activated dislocation processes responsible for intracrystalline plasticity. Macroscopic cohesion of this type of fault rock is retained during deformation while recovery and recrystallisation modify the texture.

In rocks of the cataclasite series, intracrystalline plastic deformation is largely absent and the rock responds to deformation by brittle, friction-controlled processes. In this series, grain size reduction results from fracture and mechanical wear of particles during frictional sliding. This suggests that cohesion may be lost from time to time in rocks of the cataclasite series while they are undergoing deformation but may be subsequently regained.

To some extent the question of cohesion is related both temporally and spatially to that of scale. Mylonites are cohesive on all scales and deformation probably takes place continuously throughout the mylonite band. Cataclasites, on the other hand, show abrupt textural changes within the rock as a whole. A cataclasite unit may be cohesive even though on a smaller scale it is seen to be made up of many fractures and fine-grained bands in which most of the deformation occurs and

across which there is presumably no cohesion during slip. Between
deformation episodes, healing of these bands may occur(from the growth
of new phases from solution for example) and the rock becomes cohesive
at all scales.

6.1.3. Distribution of Fault Rocks in Fault Zones

Models describing the structure of fault zones at depth are based
on the inferred distribution of fault rocks within the zone and knowledge
of the physical conditions required for their formation. In quartzo-
feldspathic crust temperature is thought to be the most important
parameter in determining whether quasi-plastic (mylonite-forming) or
frictional (cataclasite-forming) deformation will occur (Sibson, 1977b).
The effects of confining pressure, pore fluid pressure and strain rate
for example are considered to be of secondary importance.

Any fault zone model must either explain or allow for the depth
to which seismic slip on major faults is commonly recorded and the
observed juxtaposition of different fault rock types in exhumed fault
zones.

Focal depth determinations suggest that intermittent seismic slip
on well established faults in continental crust commonly occurs to
depths of between 10 and 15 km (Eaton et al., 1970). Slip on faults at
deeper levels does also occur especially during larger magnitude earth-
quakes, but is less common.

Juxtaposition of different fault rock types in major fault zones is
common. Gouge-filled faults are observed in cataclastic rocks and in
mylonites, although in the latter case the gouge can invariably be attributed
to a later deformation episode. Mylonites that have undergone cataclasis
are also relatively common in fault zones. The reverse is not true; that
is gouges or cataclasites that have undergone mylonitisation are not seen.
However, evidence for polyphase deformation of this kind is unlikely to
be preserved since the intracrystalline processes of deformation accom-
panying mylonitisation will destroy the original texture of the rock at
a very early stage.

6.1.4. Fault Zone Model

A three-tiered fault zone model proposed by Sibson (1977b) adequately
describes the features mentioned above (Section 6.1.3.). A brittle,
friction-controlled regime, producing incohesive fault gouge and breccias
to depths of between 1 and 4 km. and cataclasites at intermediate
levels, passes downwards into a zone where deformation is controlled

by quasi-plastic processes and rocks of the mylonite series develop
(Fig. 6.2). He proposes that this transition occurs at the point at
which quartz begins to exhibit intracrystalline plasticity when lower
greenschist conditions are attained at temperatures of between 250° and
$350^{\circ}C$. Under normal geothermal gradients, this corresponds to depths
of between 10 and 15 km.

6.1.5. Juxtaposition of Fault Rocks

The juxtaposition of gouge and cataclasite and the occurrence of
mylonites that have undergone cataclasis (Section 6.1.3) can be explained
in at least two ways using Sibson's model.

It may result from progressive uplift and unroofing of a fault
zone (Grocott, 1977) or reverse shear across the zone elevating mylonites
to levels where cataclasis takes place. Cataclasites may similarly be
elevated to levels where shear is accomodated by slip on discrete
planes accompanied by gouge or breccia production. In the case of a
mylonite, the original texture is only preserved if the subsequent
deformation is not extreme.

Alternatively, some instability may extend slip on a single fault
or cataclasis to depths where cataclastic flow and quasi-plastic mechanisms
are normally responsible for deformation. This suggests that fluctua-
tions in some other parameter, perhaps strain rate or pore fluid pressure
may alter the dominant style of faulting at any given crustal level.

6.1.6. Occurrence of Fault Gouge

Fault gouge frequently occurs in narrow planar zones associated
with a sharp fault break. This association may have two causes. The
first is that gouge is the incohesive fault rock which forms only at
very shallow crustal levels where displacements are localised on
individual faults. The second possibility is that fault gouge is the
incohesive member of a series of rocks that develop on fault planes at
various crustal levels from the mechanical wear resulting from frictional
sliding. Where discrete fault surfaces extend to greater depths, either
momentarily or for longer periods, a cohesive cataclasite may develop on
the fault. Even though this series of rocks is restricted to discrete
slip zones, their textures are described by the classification given in
Fig. 6.1.

FAULT ZONE MODEL

	FAULT ROCK TYPE	DISPLACEMENT
1-4 km	Incohesive fault gouge and breccia associated with fracture zones	Displacement is accommodated by slip on individual faults at near surface levels.
1-15 km	Cohesive rocks of the cataclasite series.	At intermediate depths cataclastic flow becomes progressively more important but may be localised. At deeper levels displacement is accommodated by cataclastic flow throughout the width of the fault zone.
	Cohesive rocks of the mylonite series.	Displacement by intracrystalline plastic yield across a single shear zone which may widen with depth.

Fig. 6.2. Fault zone model (modified from Sibson, 1977b)

6.2. Rock Products of Frictional Sliding

Debris produced on sliding surfaces during experiments has been equated with naturally occurring fault gouge recognised in the field for many years. Control of the parameters affecting frictional sliding in laboratory experiments (Chapter 3) has led to an understanding of how sliding debris accumulates and what factors affect its structure. Problems in applying the following results to natural faulting resemble those encountered when scaling experimental frictional laws to the natural environment. Additional problems arise from the very different movement histories of natural and experimental faults. Not only is the rock deformation in natural fault zones the result of large overall displacements involving many slip increments and many stress cycles, but the finite deformation may result from the superposition of tex-

tures induced by faulting under differing environmental conditions throughout the fault's history.

Detailed observation of debris and wear on experimental sliding surfaces, using optical and scanning electron microscope techniques, has led to some understanding of the mechanisms by which gouge forms. Three approaches have been used by experimentalists; a detailed study of asperity deformation during sliding, debris development on clean sliding surfaces and the study of gouge deformation itself using artificial gouge layers or cylinders of granular material.

6.2.1. Deformation of Asperities

Slider experiments (Engelder and Scholz, 1976; Scholz and Engelder, 1976) and triaxial tests using highly polished surfaces (Engelder, 1974; Ohnaka, 1975) have shown that the deformation of the asperities and the surface they slide on depends upon their relative scratch hardness (Engelder, 1976). Three types of wear track are seen:

1. Asperity softer than the flat (e.g. feldspar asperity sliding on quartz). Here, adhesion of the asperity occurs. Subsequent shearing leaves a trail of feldspar on the quartz flat. Brittle fractures at a high angle to the wear track are usually seen in the quartz.

2. Asperity harder than the flat (e.g. quartz asperity sliding on feldspar). The asperity ploughs a groove in the softer flat. In this case brittle fractures of both the asperity and flat occurs leaving loose debris in the groove.

3. Asperity and flat of the same hardness. The wear track for these conditions consists of a series of scratches and fractures at high angles to the direction of slip, suggesting sliding of the asperity over the surface of the flat rather than ploughing.

Swain and Jackson (1976) describe similar fractures in wear tracks which they postulate formed by Hertzian-like fractures caused by indentation of the asperity. Continued shearing of the surface leads to the coalescence of these cracks and the eventual formation of flaky wear particles.

Two distinct mechanisms, then, produce debris from an asperity: brittle fracture of the asperity itself, and the fractures it causes in the flat which may coalesce. Adhesion of the softer material also occurs with the debris coating the harder surface.

6.2.2. Experimental Gouge Development

Little systematic experimental work has been done to determine the parameters (effective normal stress, temperature, mineralogy, grain size, displacement etc.) which affect the development of gouge. It is generally agreed that gouge results from the interaction of the two sliding surfaces where they are in contact.

At low confining pressure and at room temperature the debris that forms around the areas of contact consists of loose, fine grained angular fragments which may have cleavage faces (Friedman et al., 1974). When a sufficient volume of this debris has accumulated, it is transported by the sliding to form clumps (Jackson and Dunn, 1974; Ohnaka, 1975). These consist of poorly sorted, randomly oriented, finely comminuted material which is cohesive, very weak but brittle. With further sliding, the clumps break up to form a striated, relatively thick layer of loose gouge whose fragments have been modified by cataclasis and are no longer angular. There is some debate as to whether glass forms the matrix of these lumps, or whether it is an aggregate of ultra-fine particles (Friedman et al., 1974; Jackson and Dunn, 1974).

Friction sliding experiments have been performed at high ambient temperatures (Stesky, 1978a) and show that, at high strain rates, brittle fracture is dominant in the development of gouge up to temperatures of 700°C. However, the relevance of these high temperature, fast strain rate tests is doubtful (Section 3.4.1).

6.2.3. Sidewall Fracturing

Three common types of fracture in the sidewall of the faults have been described in experiments. Hertzian fractures caused by asperity indentation were recognised by Swain and Jackson (1976). Riedel-type fractures also thought to be caused by an asperity (Jackson and Dunn, 1974) and microscopic feather fractures (Conrad and Friedman, 1976) have also been recognised. Riedel shears in the sidewalls form at low angles to the sliding surfaces (Fig. 2.2.), whereas microscopic feather fractures are extension fractures parallel to σ_1 (Fig. 6.3). Grains damaged by any or all of these fractures are more easily plucked from the sidewall and rotated into the gouge layer. Sidewall fractures provide a means to develop the very thick gouge layers that have been observed on natural faults since microscopic feather fractures and
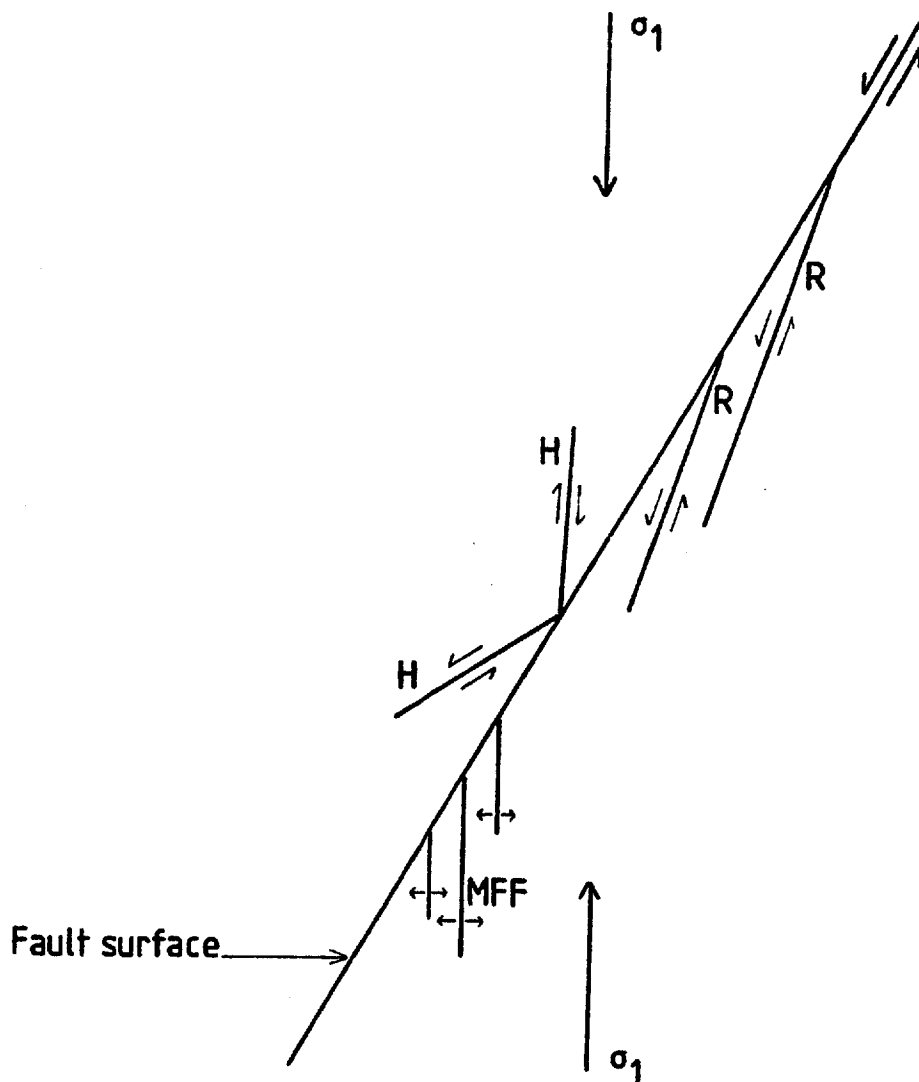
Fig. 6.3. Schematic representation of the three common fracture types seen in the sidewall of experimental sliding surfaces.

R = Riedel shears

MFF = Microscopic feather fractures

H = Hertzian fractures

possibly Riedel-type shears do not require an asperity. If all gouge resulted from wear caused by asperities the maximum gouge thickness would be that required to blanket the largest asperity. It is possible that large particles embedded in the gouge may behave in a similar manner to asperities. Asperities in the laboratory are generally similar in size to the grain size of the rock, whereas in the field the surface roughness has a larger scale, which may lead to wide gouge zones.

6.2.4. Frictional Behaviour of Granular Material

Initially, it was thought that fault gouge would prove to be weak under shear. However, experiments using simulated gouge layers

(Section 6.2.5) and granular samples have shown that when compacted, the frictional strength of crushed rock almost equals that of an intact sample of the same material (Zoback and Byerlee, 1976). When deformed in a triaxial deformation rig, granular samples deform by pervasive cataclasis and by the formation of through-going fractures (Engelder et al., 1975).

6.2.5. Deformation of Gouge Layers

To overcome the problems of creating an experimental gouge layer by sliding, artificial gouge is often used. This is usually the material of the sliding blocks crushed, sieved and washed. Occasionally a different material, such as quartz sand, is used (Byerlee et al., 1978).

The grain size reduction with sliding in an artificial gouge layer depends primarily upon displacement, effective confining pressure, layer thickness and the presence of pore fluids. Although increasing displacement reduces the mean grain size in the gouge (Byerlee and Summers, 1976; Engelder, 1974) the sorting of the aggregate becomes progressively poorer. That is, the grain size reduction is by no means uniform, with some grains remaining relatively undamaged. Engelder (1974) proposes two stages of grain size reduction by brittle, cataclastic processes during gouge deformation. The first consists of fracture and grinding of the grains throughout the gouge layer. Fractures showing no preferred orientation are seen at the contacts of the quartz sand grains (Byerlee et al., 1978). With displacement, these fragments are repeatedly rotated, new contacts formed and more fractures developed, Engelder's second stage is dominated by translation and rotation of the finer fraction relative to the coarse fragments. Increased confining pressure decreases both median grain size and sorting.

Structures also develop within the layer as a whole. Byerlee et al. (1978) report that at low confining pressures, the gouge layer deforms stably by pervasive cataclastic flow, but at higher confining pressures the deformation is unstable and localised. At the high confining pressures, shear zones developed both oblique and parallel to the sliding surfaces (Fig. 6.4). Shearing in the oblique zones, at about 20° to the sliding surfaces, was found to precede sudden, stick-slip which was confined to the intact rock-gouge boundary.

These experiments, and those on granular material, suggest that both aseismic and seismic slip may occur on gouge-filled faults. They
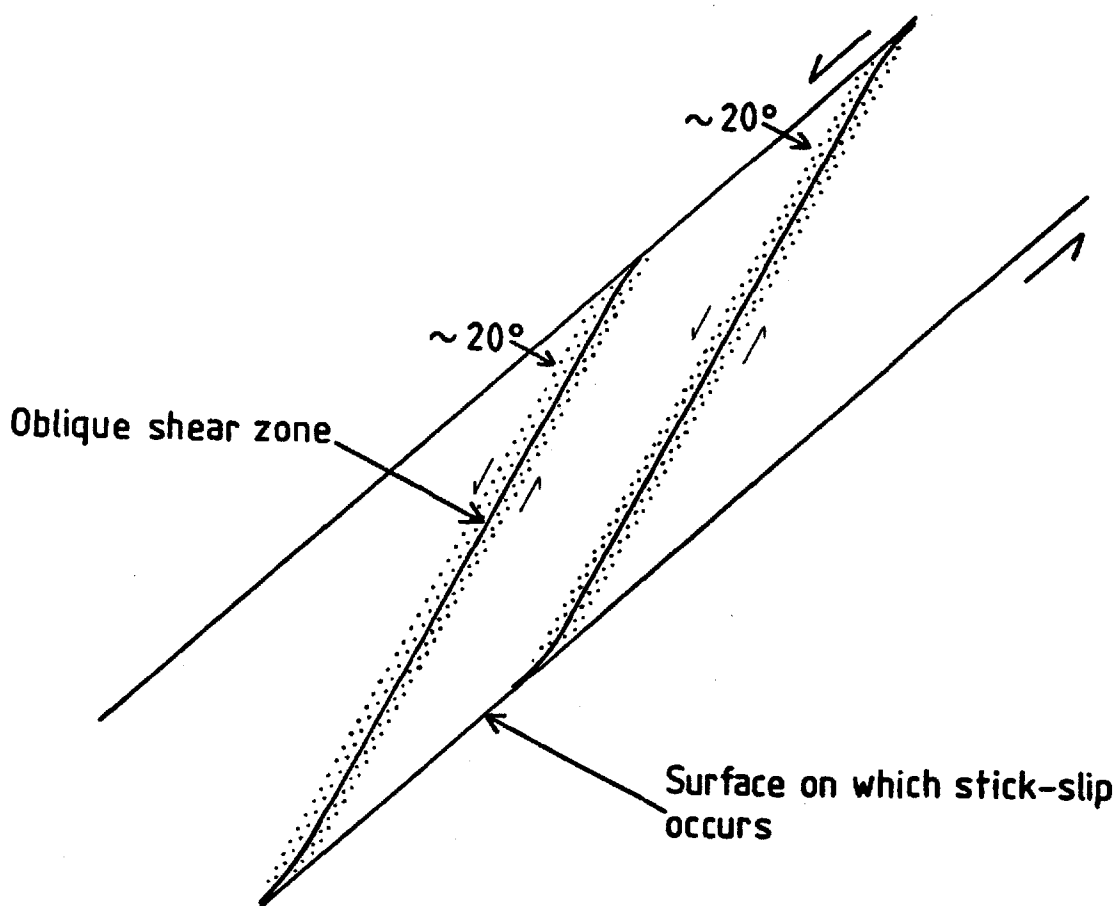
Fig. 6.4. Oblique shear zones across which shearing occurs before
seismic slip, which is confined to the intact rock-gouge
interface.

are consistent with a model put forward by Engelder et al. (1975),
whereby during stable sliding the two sides of the fault ride on a layer
of gouge which flows cataclastically, while during stick-slip, localised
slip occurs at the interface between the intact rock and the gouge layer.

There does not seem to be a single deformation mechanism charac-
teristic of either stable sliding or stick-slip. Fracture, adhesion,
ploughing and cataclastic flow have all been recognised in both sliding
modes and the transition from stable sliding to stick-slip appears to
be due, not to a change in deformation mechanism, but in the degree to
which each is developed. It is in this context that evidence for localised
thermal effects becomes particularly important as it may provide a
means for discriminating the products of stick-slip and stable sliding.

6.2.6. Natural Fault Zones

Work is just beginning on the problem of relating these experimental features to those seen in natural fault zones. Slickensides which are fairly common on shallow faults often show striations, grooves and step-like protuberances which bear a remarkable resemblance to experimental wear features (Engelder, 1974).

Fracture and cataclasis adjacent to a dominant fault is seen on many natural faults as in experiments. Brock and Engelder (1977) report a decrease in median grain size and an increase in both microfractures and macrofractures in the country rock approaching the Muddy Mountain thrust. Cataclasis is more widespread in the field than in experiments where it is limited to a distance of a few grain diameters from the fault.

The most striking similarity of natural and experimental fault zones is the presence of gouge. The end members of a series of different gouge types are; granular gouge consisting of country rock with subsidiary clay and clay gouge with subsidiary rock fragments.

Granular gouge has been found to possess foliated layers (Brock and Engelder, 1977), thought to be small-scale shear zones. There is also evidence that gouge (or its finest portion) is very mobile. Brock and Engelder (1977) describe injection of fine material into cracks in the upper plate of the Muddy Mountain overthrust and tentatively suggest that the gouge may act as a fluid in producing extension fractures. The characteristic fracture orientations described from laboratory studies (Fig. 2.2) have been recognised in fracture zones both with and without gouge layers (Logan et al., 1979). Of these fractures (Section 2.2), R_1, R_2, P, X, and Y types were recognised, with Y fractures developed more in the field, probably because of the larger displacement, than in the laboratory. R_2 fractures are less well developed in the field and T fractures have not yet been identified.

Other fault gouges in a wide variety of country rocks contain large amounts of clay minerals, the most common of these being montmorillonite, kaolinite and illite. Other clay minerals occurring in smaller quantities are vermiculite, mixed phase montmorillonite-illite and chlorite-vermiculite mixed layer. Chlorite is common in some gouges. The densities of these gouges vary with their depth from about 2200 kgm^{-3} to the range 2600 — 2800 kg m^{-3} at 300 m which is close to the density of intact granite rock. Thus, the clay and other particles are closely packed and may show slickensides (Wu, 1978). Internal structures within

clay gouge have not been described. Experiments have shown that small quantities of montmorillonite and vermiculite may promote stable sliding and that the presence of water, at low confining pressures drastically lowers the strength of many clays.

CHAPTER 7

MESOSCOPIC DEFORMATION IN NATURAL FAULT ZONES

7.1. Introduction

Two contrasting fault zones were chosen for detailed microstruc-
tural study. The first was the Walls Boundary Fault zone, a major,
dextral transcurrent fault in the Shetland Islands and the second, a
series of thrusts in the Moine Thrust Zone at Loch Eribol, Sutherland.
These areas were chosen as they offered good exposure along with rela-
tively easy access to the fault zones. In addition, the fault style in
each zone was different (transcurrent and thrust), with different finite
displacements across each zone, and different host lithologies affected
by the faulting. This last point is important since the Loch Eribol
faults occur in a pure quartzite and as discussed in Chapter 6, the
presence of quartz in a deforming rock is one of the most important
factors in determining the resulting rock deformation under given
environmental conditions. In the Walls Boundary Fault zone the rock
type studied was granitoid and the contrasting response of both quartz
and feldspar to deformation could be studied.

Both areas have previously been mapped geologically on a scale of
1:10560. The field work undertaken for this study consisted primarily
of sampling, with some detailed structural investigation of important
regions within the fault zones.

7.2. Shetland Islands

7.2.1. Regional Geology

The Shetland Islands are composed of a series of ancient sedimentary
rocks, variably metamorphosed and intruded by igneous rocks during the
Caledonian Orogeny, together with sedimentary and volcanic rocks of Old
Red Sandstone (Devonian) age. The latter were laid down and deformed
during the final phases of the Caledonian Orogeny. Shetland is separated
into two distinct geological parts by the Walls Boundary Fault, a major
dextral transcurrent fault trending north-south across Mainland, the
largest island of the group (Fig. 7.1).

No Geological Survey Memoir is available covering the entire
Shetland Islands but adequate accounts of the stratigraphy and geological
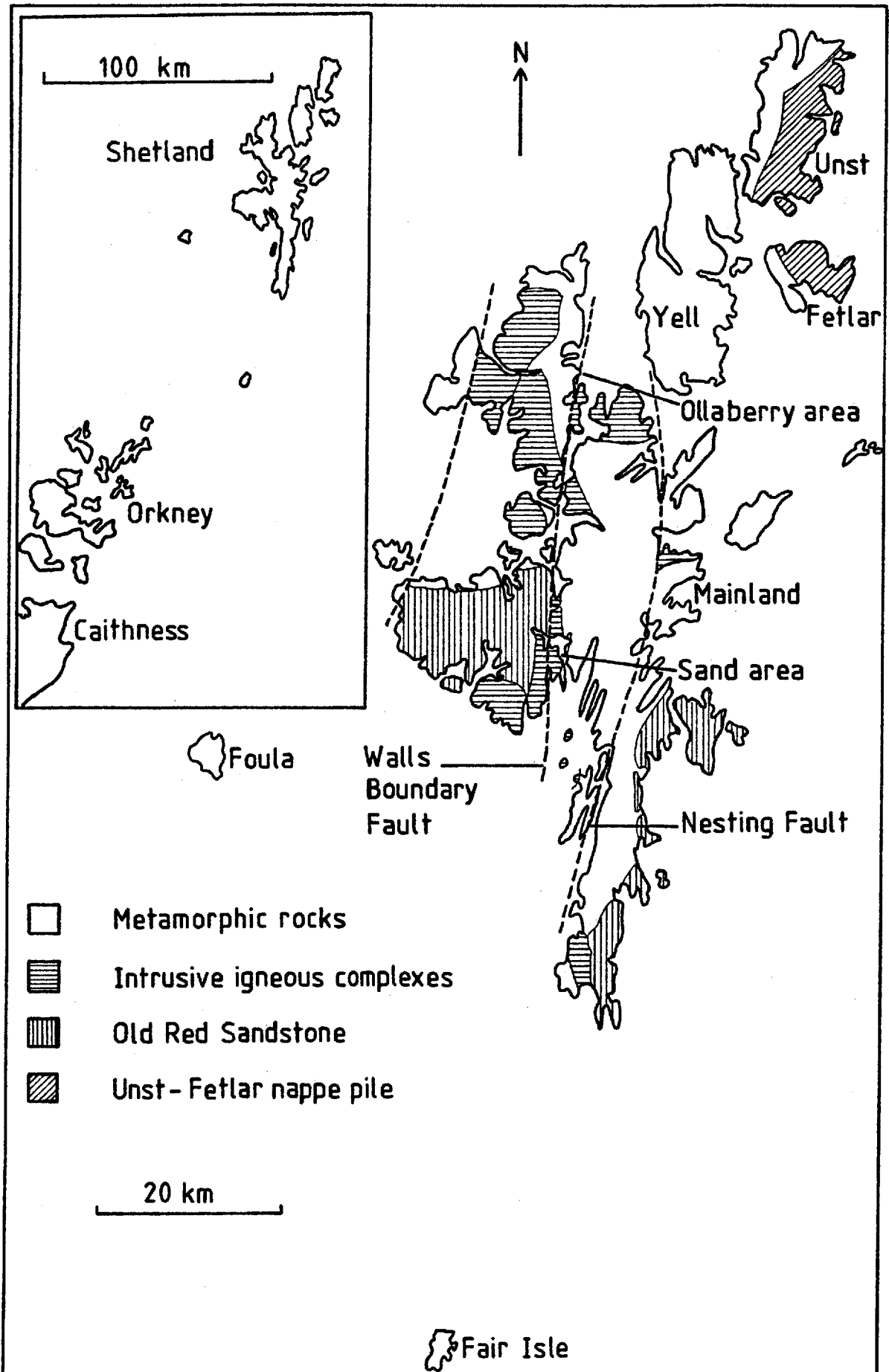history are available in Mykura and Phemister (1976) and Mykura (1976).

Fig. 7.1. General geology of the Shetland Islands.

More detailed work on specific aspects of Shetland geology can be found
(Flinn, 1954, 1958, 1959, 1961, 1967, 1969, 1977; Miller and Flinn, 1966;
Flinn et al., 1972).

7.2.2. Walls Boundary Fault

The Walls Boundary Fault can be traced across Mainland for a distance
of about 35 km, intersecting the coastline at 14 localities, in 12 of
which it is exposed (Fig. 7.1). Inland, exposure of the fault zone is
rare and along the coastal sections weathering is severe.

The Walls Boundary Fault zone is a complex, locally branching dis-
location zone consisting of a number of sub-parallel faults within a
crush belt whose width varies from a few hundred metres at Bixter Voe
(HU 336 506) to almost 3 km at Seli Voe (HU 335 480). Its average width
is 1-1.5 km although the eastern margin is often beneath the sea. Within
this crush belt, the fault planes of the Walls Boundary Fault and
associated minor faults are everywhere sharp and clearly defined.

There is no direct evidence on the direction and amount of movement
across the zone, but from indirect evidence, post Old Red Sandstone
movement of 60-80 km in a dextral sense has been postulated (Flinn,
1969; Mykura, 1972a, 1972b; Mykura and Young, 1969). While Tertiary
activation of this and parallel faults cannot be discounted, the bulk of
the movement is probably Mesozoic in age (Flinn, 1977). As a result of
the large offset and the diversity of lithologies in the Shetland Islands,
marble, granite, hornblende-gneiss and schist, psammites, pegmatites,
phyllites, diorite and dolerite. It is common to find several of these
in juxtaposition at any given locality within the crush zone.

Two areas, at Ollaberry and Sand (Fig. 7.1) were selected for micro-
structural study. In both areas, a continuous sequence of a single,
uniform rock type could be traced into the crush zone and up to a major
fault within it.

7.2.3. Ollaberry Area.

At the Back of Ollaberry (HU 372 810) (Fig. 7.2), the Walls Boundary
Fault is exposed in a vertical cliff, 30 m in height (Plate 1a,b).
Remnants of a band of maroon-coloured ultracataclasite, 0.5 m in width,
can be seen on the fault plane. In this area, the Walls Boundary Fault
separates a granite of the Graven Complex from rocks of the Lunnister
Metamorphic Group and occurs within a crush zone which is at least 0.5 km
in width although its eastern margin is covered by the sea. Although
considerable deformation of the rocks adjacent to the Walls Boundary
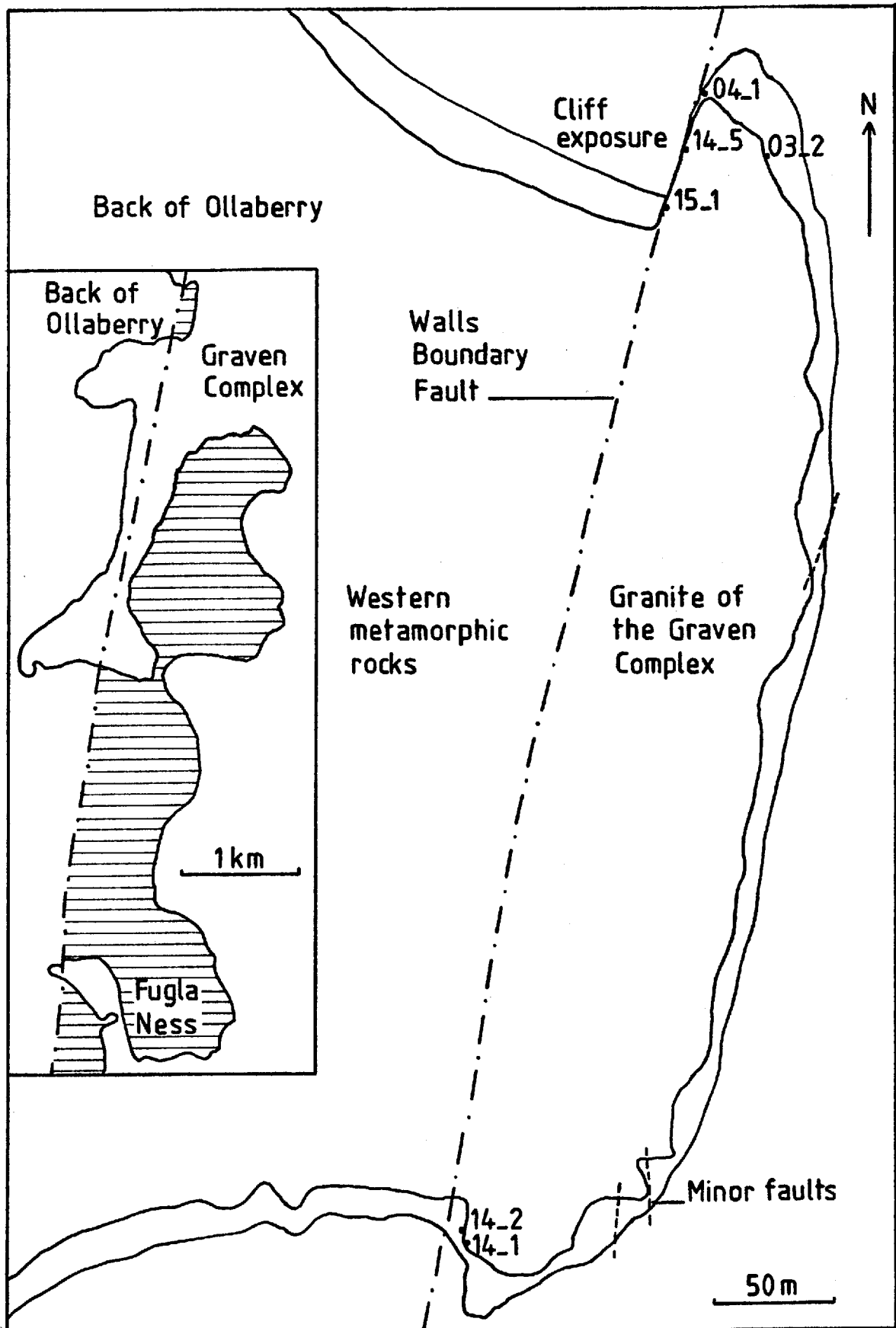
Fig. 7.2. Locality map of the Ollaberry area, Shetland Islands.

Fault is seen, everywhere in Shetland, this main fault controls the major lithological break within the crush zone.

The metamorphic rocks to the west of the Walls Boundary Fault consist of 4 groups which are, from west to east: 1. the Western Unclassed Group, 2. the Green Beds Assemblage, 3. the Calcareous Group, and 4. the Banded Gneiss Group (Mykura, 1976). These rocks are shattered and deeply weathered within 300 m of the Walls Boundary Fault. Their distribution suggests that they occupy a tight, northward plunging synform with a nearly vertical axial plane.

The granite to the east of the Walls Boundary Fault is part of a complicated intrusive complex containing large enclaves of country rock. At the Back of Ollaberry, the granite within the crush zone is continuously exposed along the coastline to a distance of 100 m from the main fault plane. Seven samples of the deformed granite were taken for microstructural analysis at increasing distances from the fault (Fig. 7.2).

In this region the granite is pale pink in colour, deeply weathered and somewhat knobbly in appearance. It is cut by several small faults seen only on the rocky foreshore which lie sub-parallel to the Walls Boundary Fault. Bands of maroon-coloured ultracataclasite, up to 10 mm in thickness, are seen on these faults. There appears to be a slight decrease in the intensity of deformation with increasing distance from the Walls Boundary Fault. The deformation at the margins of the crush zone consists of a series of fractures which separate roughly equidimensional blocks of intact rock. 100 m to the east of the Walls Boundary Fault, the intact granite blocks are about 0.2 m in diameter but their size decreases progressively to less than 0.1 m about 40 m east of the fault. Within these intact blocks, although the larger quartz and feldspar crystals are fractured, there appears to be little disruption of the original granitic texture.

It is only within 10 m of the Walls Boundary Fault that the granite loses its igneous texture. Within this zone the intact blocks are disrupted internally until at about 5 m from the fault the granite becomes a fractured mass of mineral fragments in which only very small remnants of the original granitic texture remain.

At the intersection of the Walls Boundary Fault and the southern coastline of the Back of Ollaberry (HU 371 806) the maroon ultracataclasite is absent. However, in line with the projected trace of the fault across the beach there is a small exposure of fractured
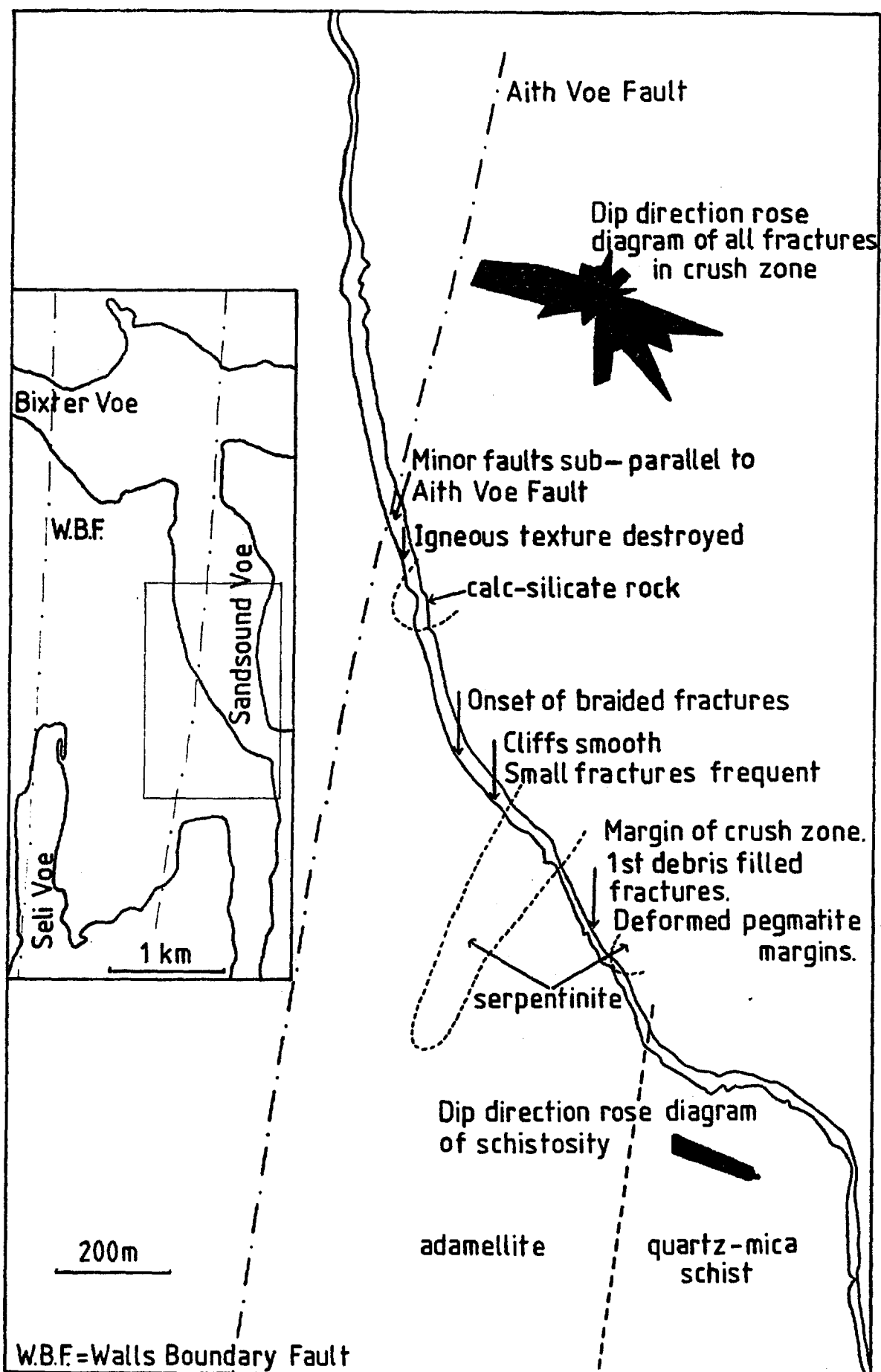
Fig. 7.3. Map of the fault zone in the Sand area, Shetland Islands.

84

Plate 1

a   Cliff exposure of the Walls Boundary Fault on the northern coastline
    of the Back of Ollaberry. Scale bar = 10 m.

b   Cliff exposure of the Walls Boundary Fault on the northern coastline
    of the Back of Ollaberry. Photograph taken looking east.
    Scale bar = 5 m.

c   Aith Voe Fault crossing the coastline of Sandsound Voe.

d   Aith Voe Fault crossing the coastline south of Sand. Scale bar = 1 m.

e   Jointed adamellite in the Sand area. Scale bar = 0.5 m.

f   Adamellite crossed by fractures in the Sand area.
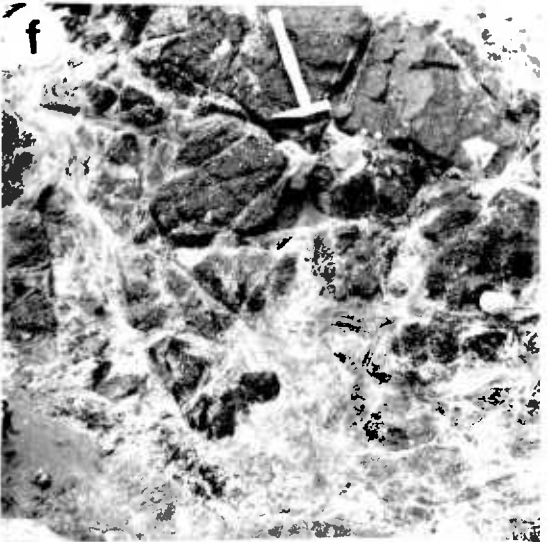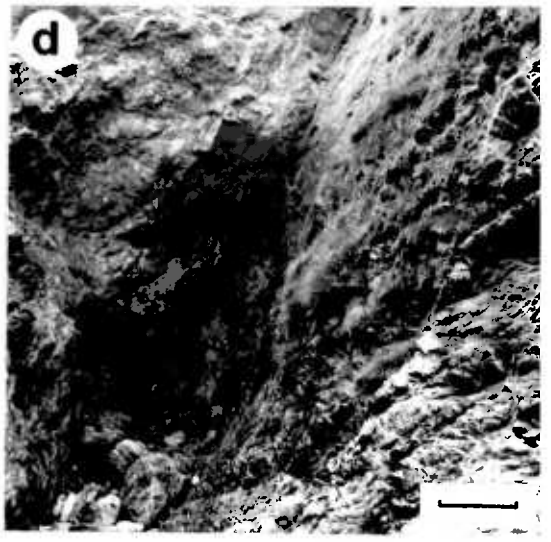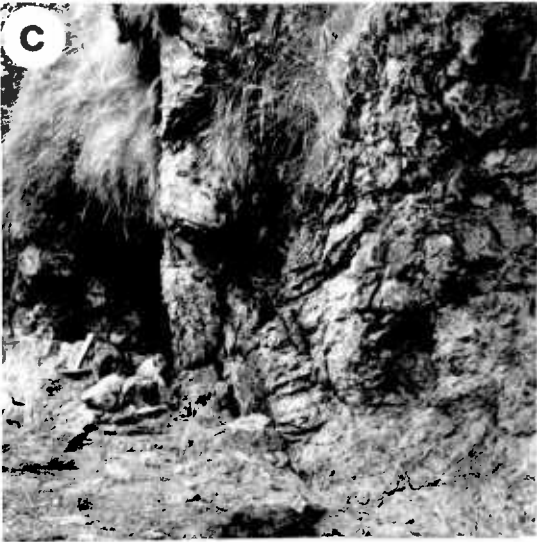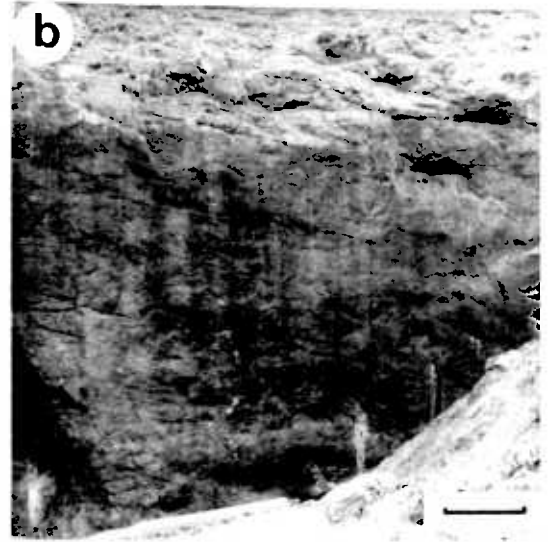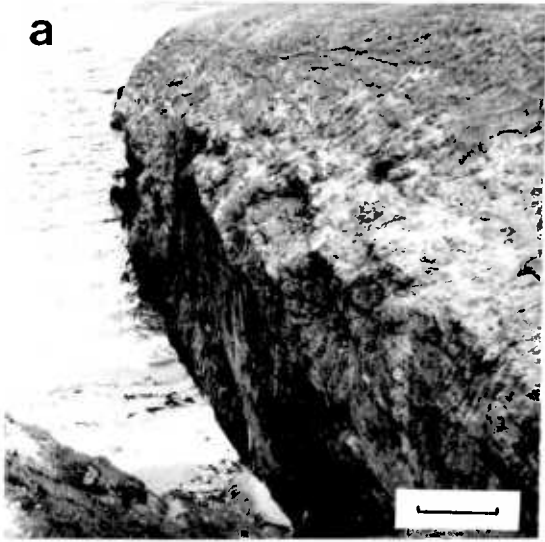
quartz-rich rock, which in thin section appears to be a mylonite that has undergone late cataclasis.

7.2.4. Sand Area

The second area studied within the Shetland Islands forms part of the western coastline of Sandsound Voe from Saltness (HU 346 504) to Innersand (HU 356 479), (Fig. 7.3). This coastal section is cut at an acute angle, by the Aith Voe Fault (HU 347 495) (Flinn, 1977).

In this region, the Aith Voe Fault strikes 020° and is almost vertical (Plate 1c). Evidence for dextral transcurrent movement across it comes from the sense of overturning of late folds to the north of this area (Flinn, 1977). Its actual displacement is unknown, but is small (Probably < 1km) since adamellite, a marginal facies of the Spiggie Complex (Mykura, 1976), is present to both sides of it. On the coastline to the south of Sand (HU 343 467) the fault strikes 175° and dips 58°E (Plate 1d).

7.2.4.1. Deformation of the Adamellite

Within the adamellite fracturing increases progressively as the Aith Voe Fault is approached (see summary, Fig. 7.4). The undeformed adamellite is cut by a series of curved joints, giving it a blocky appearance, each block being 0.3-1 m across (Plate 1e). A stereographic plot of poles to the joints (Fig. 7.5a) confirms that the joints are non-systematic and almost randomly orientated. The adamellite is cut by pegmatite veins and the rock as a whole weathers to a grey colour.

In the following section, all given distances to the fault are measured perpendicular to its projected trace. Uncertainty in the position of the fault inland leads to errors of ± 100 m when distances over 500 m are given. The error is much reduced as the fault is approached.

Mesoscopically detectable deformation begins 500 m from the Aith Voe fault, to the east, and takes 3 forms. First, crushing of the adamellite occurs in bands 10-20 mm wide which margin the pegmatite veins. In these bands, the igneous texture of the adamellite is destroyed and a foliation lying parallel to the pegmatite walls, sometimes develops. Secondly, the adamellite is cut by minor faults (Section 7.2.4.3) and finally by small fractures containing up to 4 mm thickness of fine grained cataclastic detritus. This detritus appears to be derived from the adamellite and contains small recognisable fragments of it.

Distance from Aith Voe Fault	Deformation within the Adamellite
> 500m	Undeformed. Grey in colour. Jointed. Pegmatites undeformed.
500m	Minor faults. Small single fractures containing crushed material. Joints seen between faults and fractures. Pegmatite margins deformed.
300m	Pink/red colour overall. No joints, cliffs smooth. Small single fractures containing crushed material seen about every 10m.
200m	Braided fracture zones consisting of fractures with and without crushed material.
150m	Igneous texture between the braided fractures is disrupted by microscopic fractures.
100m	The number of barren fractures has increased and equals those with cataclastic detritus. Together they cut the adamellite into blocks about 0.1m across.
50m	The igneous texture of the adamellite is lost and it appears as a jumbled mass of mineral fragments.
20m	Many minor faults sub-parallel to the Aith Voe fault.

Fig. 7.4. Deformation of the adamellite at Sand

87

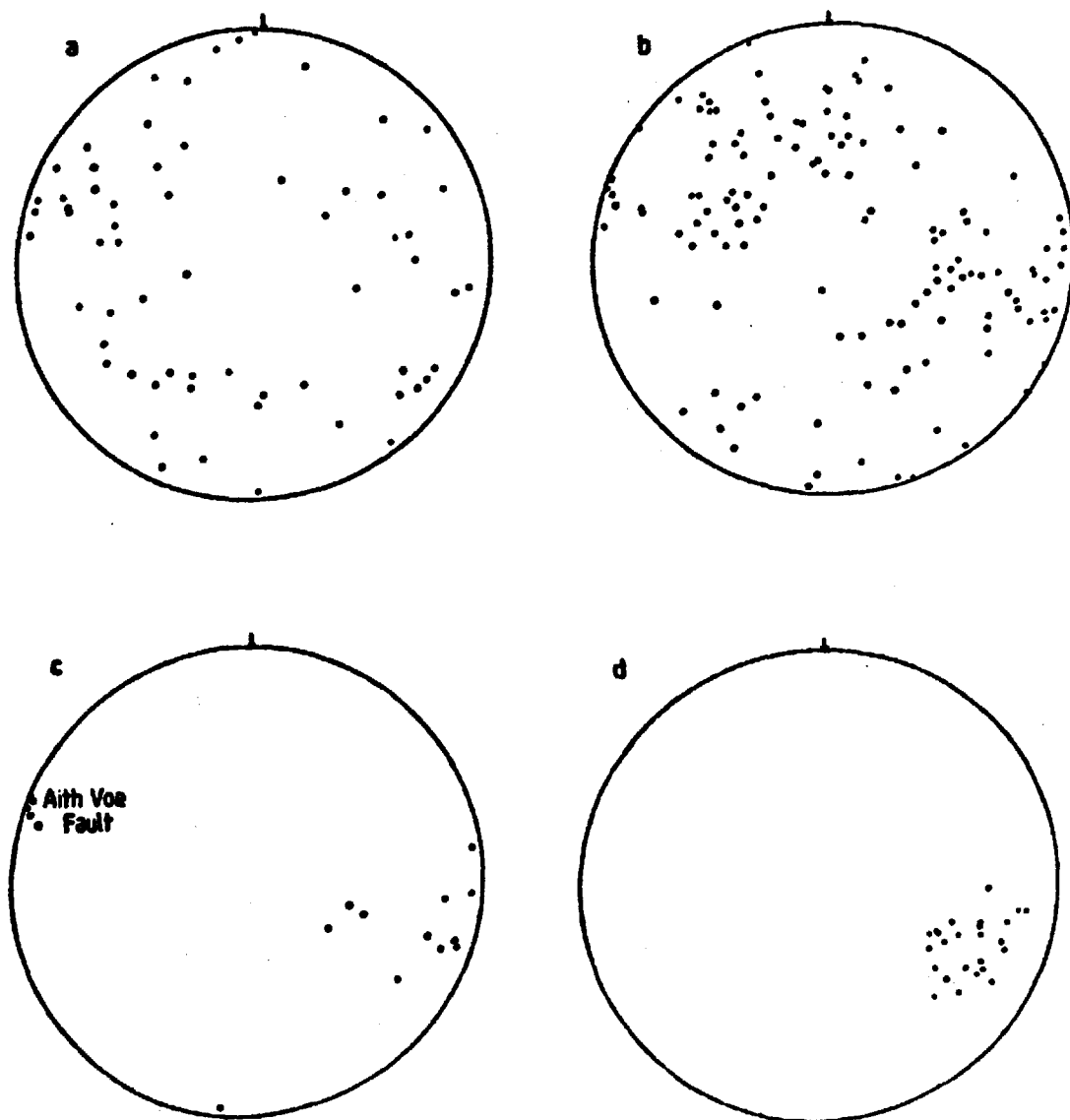

Fig. 7.5. Stereographic plots of field data from the Sand area, Shetland Islands.

a. Poles to joints in undeformed adamellite.

b. Poles to minor faults within the fault zone at distances greater than 20 m from the Aith Voe Fault.

c. Poles to minor faults within 20 m of the fault.

d. Poles to foliation of the quartz-mica schist of the Scatsta Quartzitic group.

As the Aith Voe Fault is approached from both sides the colour of the adamellite changes to red and the cliffs become smooth. The fractures containing the cataclastic detritus increase irregularly in frequency until at 300 m from the fault they occur about every 10 m.

Still closer to the Aith Voe Fault (200 m), complex arrays of braided fractures are seen. These consist of both fractures containing cataclastic detritus and similar barren fractures (devoid of detritus) which are described fully in Section (7.2.4.2). From this point, the frequency of the barren fractures increases until at about 100 m from the fault, the adamellite is divided into blocks only 0.1 m in diameter (Plate 1f).

At a distance of about 150 m from the Aith Voe Fault, the igneous character of the adamellite between these fractures begins to break down. Microscopic fracturing reduces the size of the feldspar porphyroclasts to less than 10 mm. At only 50 m, the rock has become a jumbled mass of mineral fragments in which remnants of the original texture are only occasionally visible (Plate 2a).

The Aith Voe Fault itself has a very different character. It forms a sharply banded zone, 2 m thick of yellow cataclastic material through which there is a sharp break. This material is foliated with the fine ground mass wrapping around rounded fragments of shattered adamellite which are rarely larger than 5 mm across.

7.2.4.2. Braided Fractures

Braiding occurs when an individual fracture splits into anastomosing branches which may be cut and perhaps offset by one or more sets of fractures (Fig. 7.6a,b). In many cases the fractures containing cataclastic detritus are offset by barren fractures. Along a single fracture of the braided network, the cataclastic detritus may thicken to about 15 mm and thin or even be absent for part of its length. Shear displacements across some of these fractures undoubtedly occur since they displace pegmatite veins. On others it is impossible to determine whether or not shear displacements have occurred, as it is sometimes possible to match feldspar porphyroclasts across them. The overall width of the braided zones varies from 1 m or less to a maximum of about 3 m.

7.2.4.3. Minor Faulting

Small faults of variable slip-sense cross the coastline with a fairly uniform frequency throughout the fault zone. Their frequency

0.5m   Beach

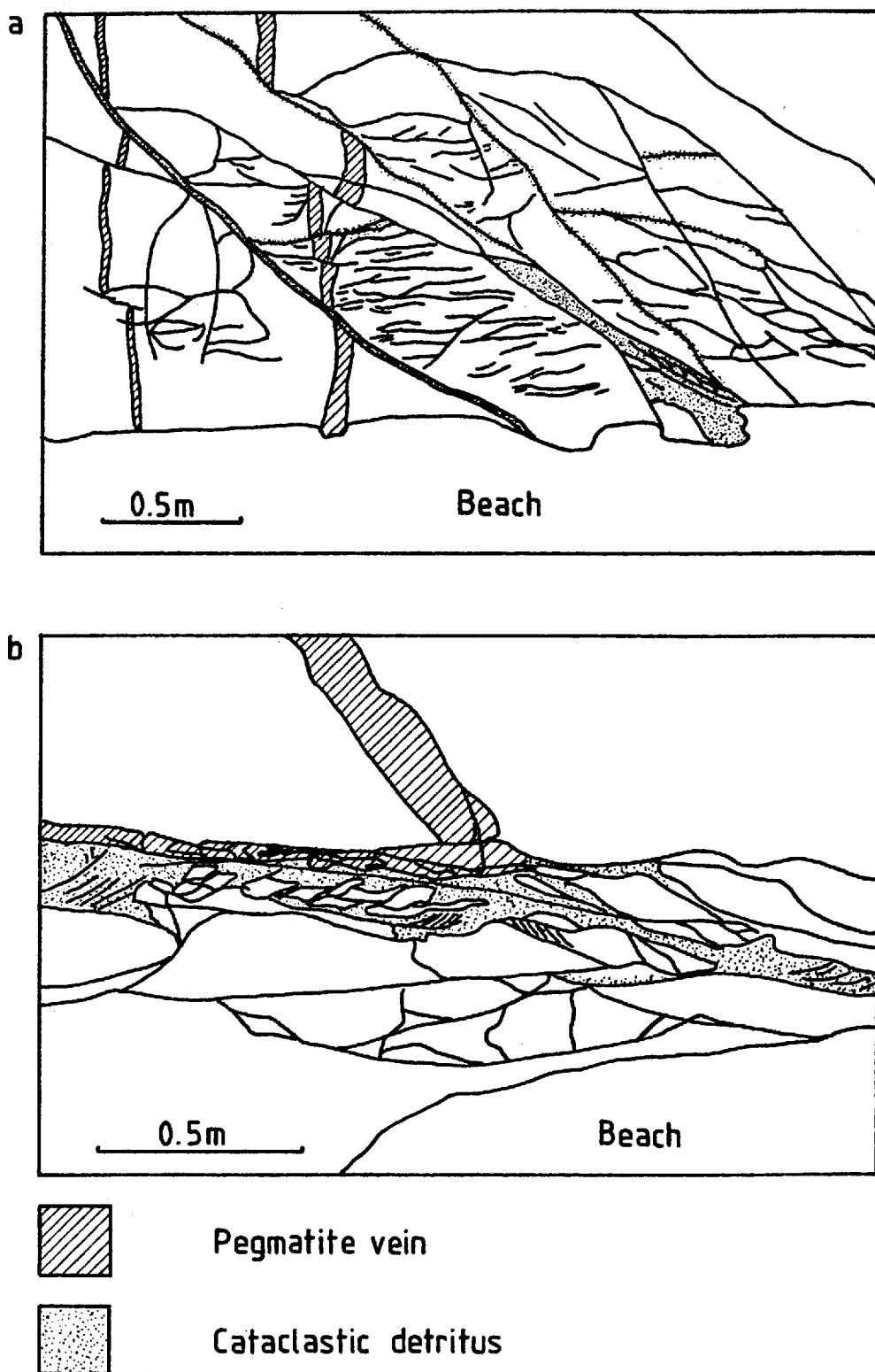0.5m   Beach

Pegmatite vein

Cataclastic detritus

Fig. 7.6. Diagrams showing the structure of the braided fracture networks.

does, however, increase within 20 m of the Aith Voe Fault, where they occur about every 4-5 m as opposed to every 20-30 m elsewhere. Away from this zone immediately adjacent to the Aith Voe Fault, the minor faults have no marked preferred orientation but their dips are restricted to between 20° and 65° (Fig. 7.5.b). The majority of minor faults, barren fractures and fractures containing cataclastic detritus strike between 0° and 100° (Fig. 7.3, rose diagram) and have dips exceeding 30°.

All but one of the 12 minor faults within 20 m of the Aith Voe Fault, strike between 170° and 032° and with 3 exceptions they dip more steeply than 75°. This means that within this area, minor faults are generally sub-parallel to the Aith Voe Fault and lineations on the fault surfaces indicate they have a dip-slip sense of displacement (Fig. 7.5c).

The foliation of the quartz-mica schist of the Scatsta Quartzitic group, which occurs south-east of the adamellite (Fig. 7.3), lies sub-parallel to the dominant orientation of minor faults and fractures within the Aith Voe Fault zone (excluding the strip to each side of the fault itself). The foliation strikes $0-040^\circ$ and dips $40-75^\circ$ north-west (Fig. 7.5.d). This foliation is thought to pre-date the faulting (Mykura, 1976). The coincidence in orientation of these features may be unconnected. Alternatively, the deformation (thought to be late Caledonian, Mykura, 1976) that rotated the schistosity into sub-parallelism with the margins of the Spiggie complex, may also have introduced fractures within the intrusion. The later deformation associated with the large scale faulting in this region may then have reactivated them.

An alternative origin for these fractures is not readily available. With the exception of the strip to each side of the Aith Voe Fault, the orientations of the minor fractures and faults do not appear to be directly related to the fault. There is no systematic orientation of minor fractures corresponding to those expected from the sense of slip on the main fault from the work of Logan et al. (1979). There are, however, very few fractures striking at high angles to the Aith Voe Fault and the strike of the minor fractures is more consistent with dextral than with sinistral slip on the fault.

No systematic differences in the orientation or age of the barren fractures and those containing cataclastic detritus can be found. They appear to be contemporaneous having formed under a similar stress field. It seems probable that the orientation of all the minor features was

controlled by pre-existing structures within the adamellite, which, when favourably oriented, were reactivated by later fault movement. Thus, in this area, many planes of weakness striking at less than 65° to the Aith Voe Fault were reactivated.

7.3. Loch Eribol

The second area selected for study lies within the Moine Thrust Zone on the north-eastern slopes of Conamheall (NC 376 515), lying south-west of Loch Eribol, Sutherland (Fig. 7.7).

7.3.1. Regional Geology

The strata affected by the thrusting consists of Cambrian members of the Sole or Heilem Nappe (Geikie, 1888; Soper and Wilkinson, 1975). The succession is:

> Durness Limestone
>
> Serpulite Grit
>
> Fucoid Beds
>
> Pipe Rock
>
> Basal Quartzite

On this hillside the beds are the right way up and, in the faulted area, dip consistently to the south-east at about 25°. The lithologic unit is disrupted by at least 4 listric thrusts which curve up from the Sole Thrust, which is itself exposed south-west of Conamheall (NC 345 498). Where they are exposed, the listric thrusts dip 35°-40°S and strike parallel to bedding (Fig. 7.7). Fault surface lineations confirm a dip-slip sense of movement.

There is some associated small scale open folding with fold axes invariably striking sub-parallel to the fault strike. Drag folds are common adjacent to both the major listric thrusts and parallel minor faults (Plate 2c). Usually, only the faulted anticline is seen and its size is related to the scale of the fault and possibly also to its displacement.

Fault displacement (probably Lower to Mid Ordovician in age (Soper and Wilkinson, 1975)) thickened the Cambrian strata significantly. After the faulting the thickness of the Pipe Rock (measured perpendicular to bedding) is at least 300 m, compared with a sedimentary thickness of about 180 m (Phemister, 1948). The thickening is caused by repetition of the sequence by the thrusting. As no beds are inverted, the displace-ment of one of the thrusts (fault B on Fig. 7.7) may be estimated from a knowledge of the amount of thickening, the dip of the fault and strata
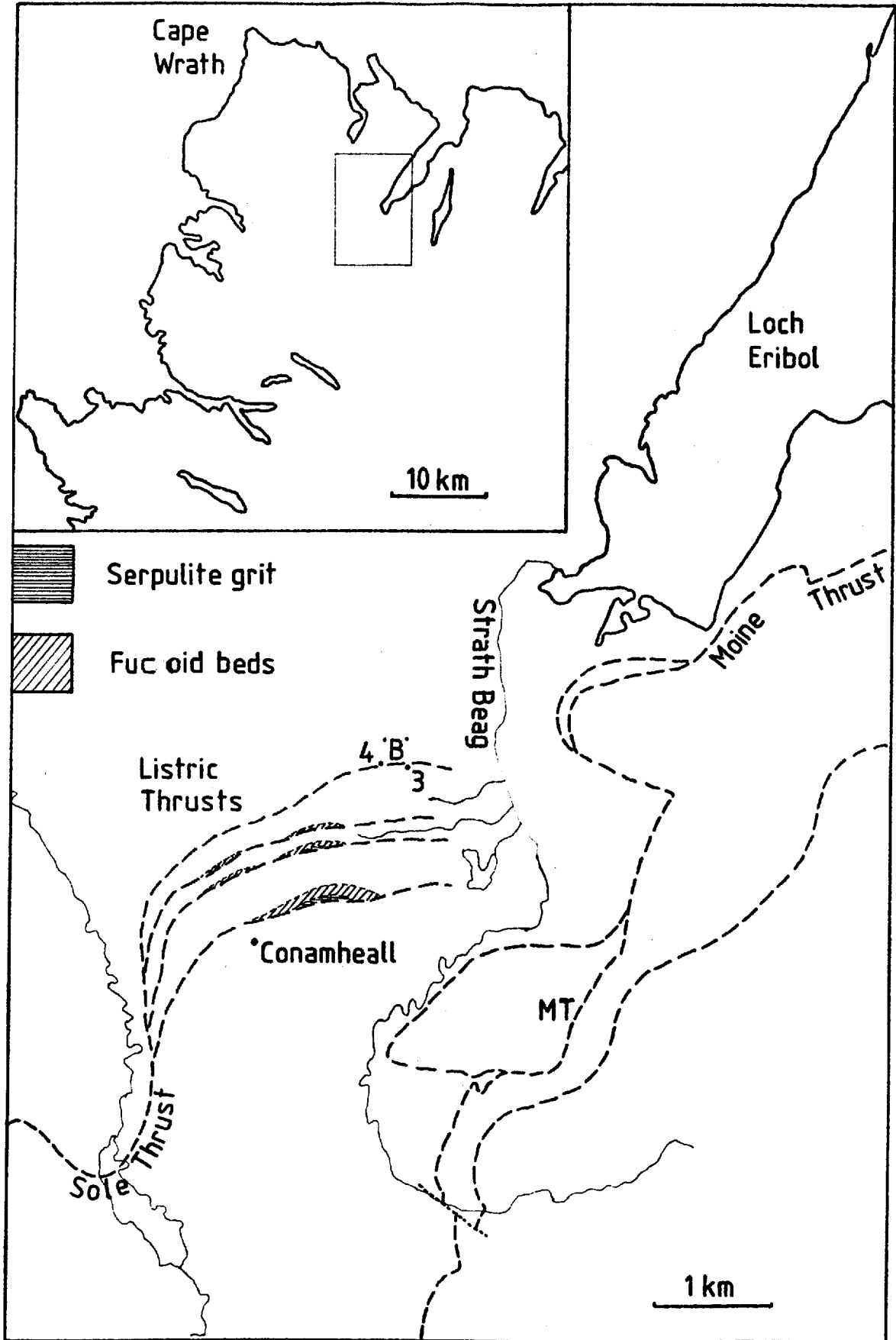
Fig. 7.7. Map of the Loch Eribol area.

Plate 2

a   Highly deformed adamellite appearing as a jumbled mass of mineral
fragments. Sand area.

b   Braided network of minor fractures containing cataclastic debris.
Sand area. Scale bar = 0.5 m.

c   Minor fold in centre of photograph associated with listric thrust
'B', lower right hand side. Loch Eribol area.

d   Rubble-filled gully in which Serpulite Grits and Fuc oid beds are
exposed below the southern thrusts. Loch Eribol area.

e   Surfaces marked 'A' accommodate slip parallel to listric thrust
'B'. Loch Eribol area.

f   Curved minor fault plane. Loch Eribol area.
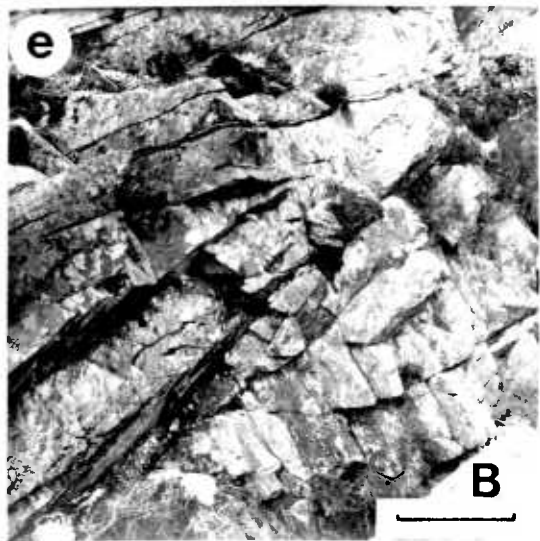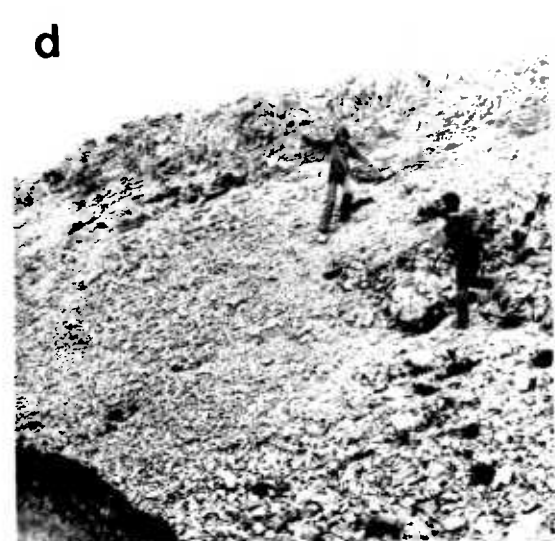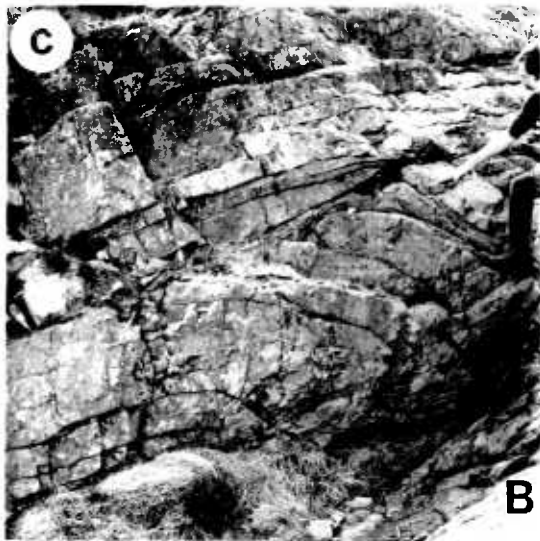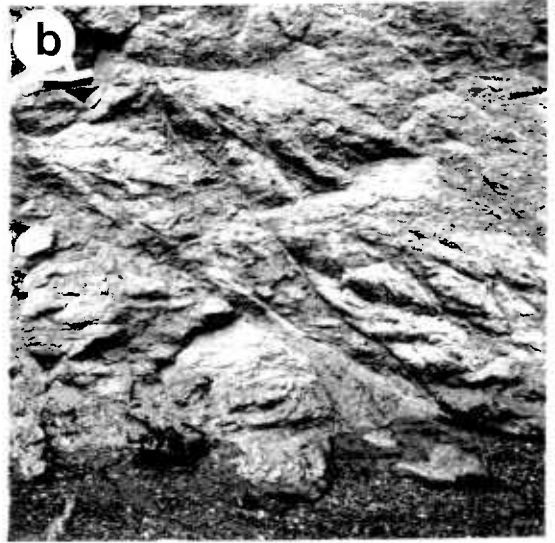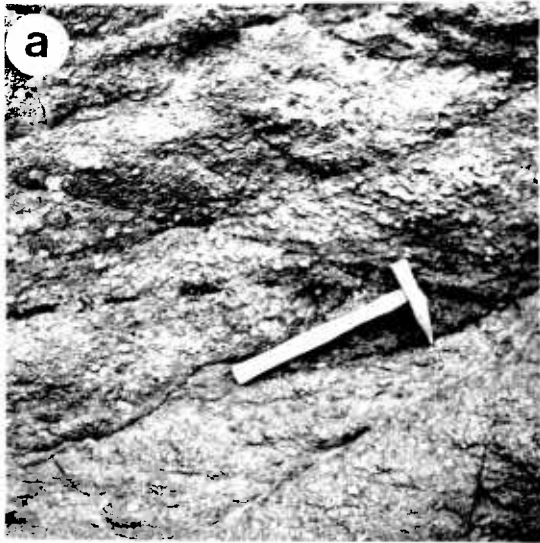
and the sense of movement across the faults. This calculation is possible since the Serpulite Grit and Fuchoid Beds are exposed below the three southern faults in deeply eroded gullies (Plate 2d). A displacement of between 200 and 390 m is thereby estimated, the uncertainty arising from 5°-10° variations in the dips of the fault and strata. Thickening of the Pipe Rock units implies a total displacement of at least 1700 m across all thrusts (assuming it is all achieved by dip-slip movement).

Some thickening will also be accommodated by the folding, but since all the folds are minor and open, usually with large interlimb angles ($>120^{\circ}$), their contribution to the overall thickening cannot be great and will probably be less than 20%. Thus, the thickening is thought to arise mainly from thrust repetition and stacking of the sequence, with the implication that several hundred metres of slip has occurred on each of the main listric thrusts.

7.3.2. Fault Structure

In addition to the four listric thrusts shown in Fig. 7.7., the hillside in this area is also crossed by several minor thrusts which parallel the listric faults. Usually, details of the structure and deformation associated with the main listric thrusts are obscured by rubble filling the gullies in which they are exposed. Fault B (listric thrust, Fig. 7.7), and several adjacent minor thrusts are, however, well exposed. It is on rocks from these faults that the microstructural study is centred.

As well as being associated with drag folding (Section 7.3.1), the listric thrusts commonly consist of several sub-parallel surfaces across which movement has occurred (Fig. 7.7, location 3; Plate 2.e.), which are occasionally curved on the scale of the outcrop (Fig. 7.7, location 4; Plate 2.f).

The minor thrusts adjacent to fault B can be traced for up to 100 m (Plate 3.a). Individual faults both follow and cut across the bedding as "ramps" (Fig. 7.8). Slightly more than 50% of their length forms the "ramp" sections. The surfaces of almost all faults are polished with quartz slickensides on both the ramp and bedding plane sections (Plate 3.b).

7.3.3. Fault Rock

Adjacent to the minor faults, and fault B, the white host quartzite

96

Plate 3

a   'Ramp' section of a minor thrust stepping across the bedding. Loch
     Eribol area.

b   Slickensides on the 'ramp' section of a minor thrust. Loch Eribol
     area.

c   Greenish-black, flinty fracture-fill adjacent to movement surface
     ('A'). Loch Eribol area.

d   Quartzite block showing the fracture vein network containing the
     greenish-black material. Loch Eribol. Scale bar = 25 mm.

e   As 3d. Scale bar = 50 mm.

f   Sharp sided band of opaque-black fracture-fill containing haematite.
     Veinlets extending into parent quartzite are marked 'A'. Scale bar
     = 10 mm.
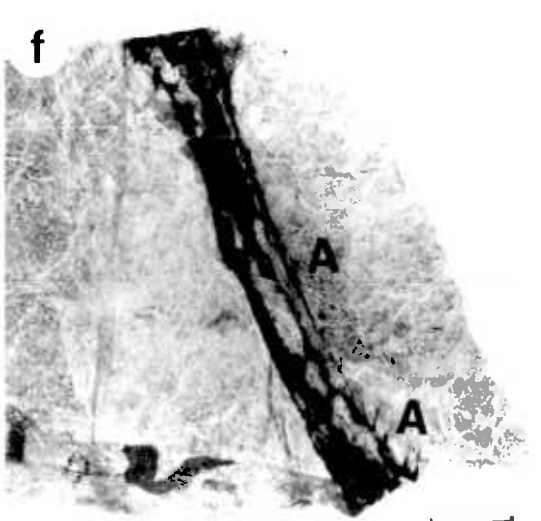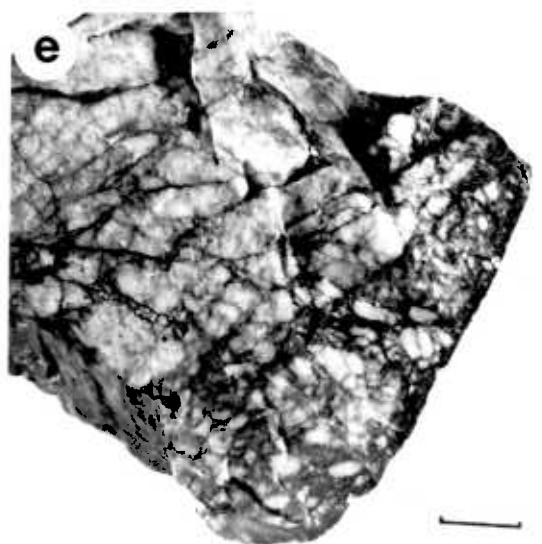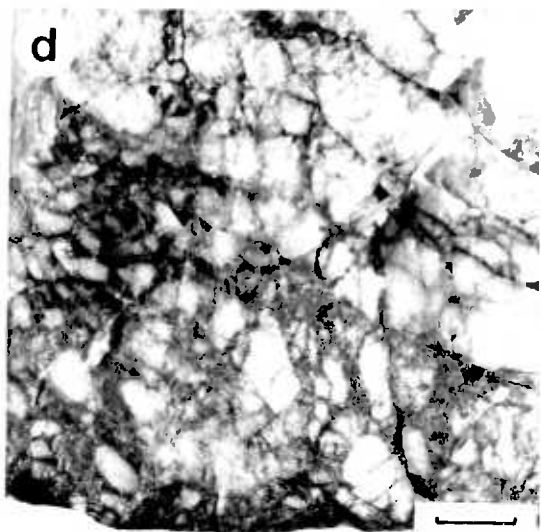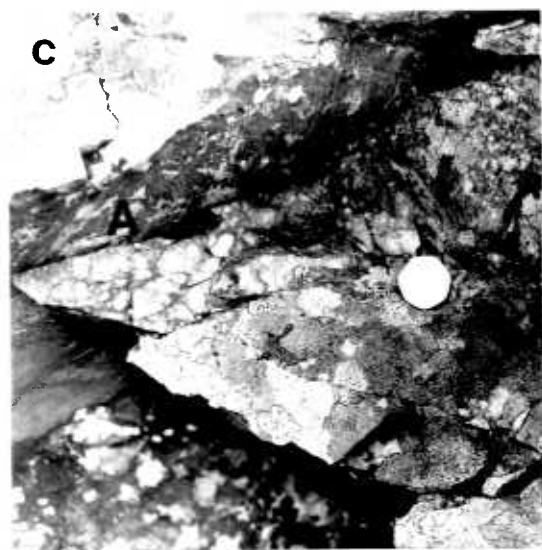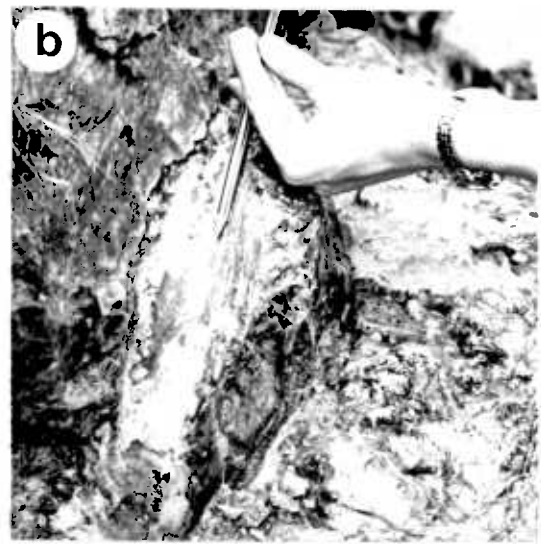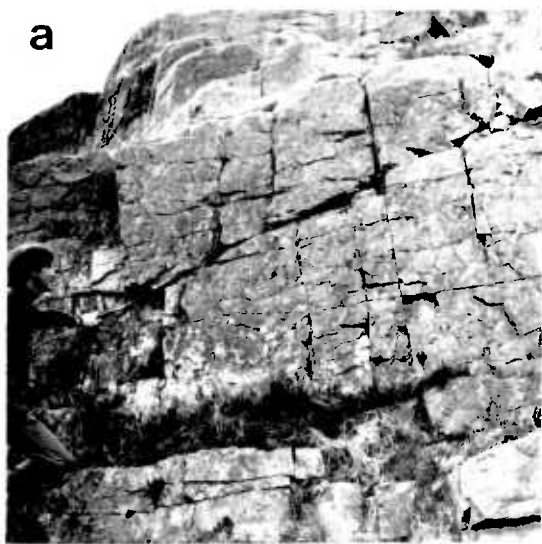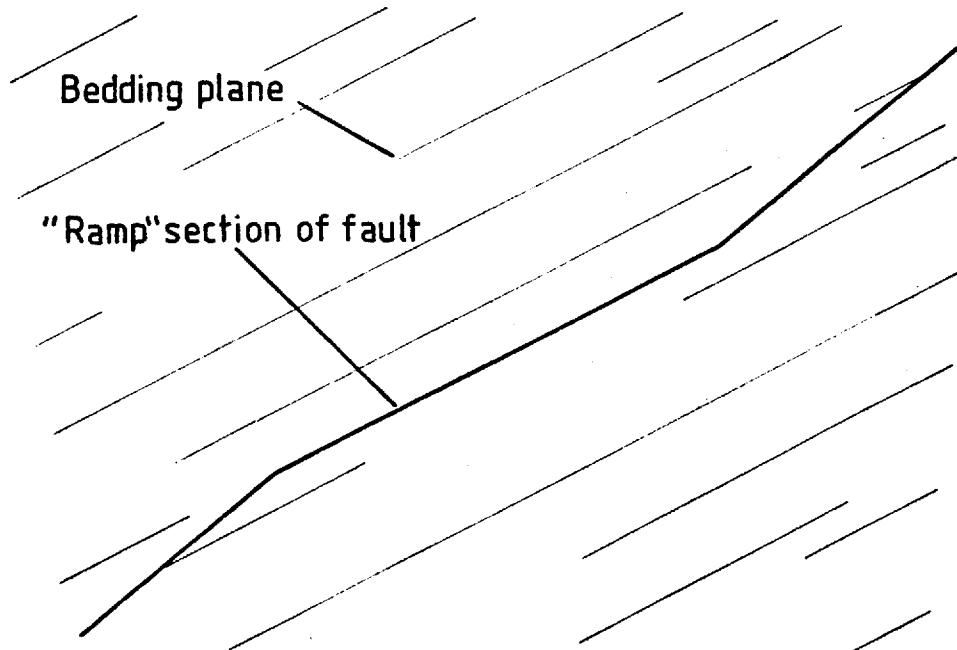
Fig. 7.8. Minor thrust stepping across and following bedding planes.

is divided into angular fragments by a number of healed fractures filled with fine grained, greenish-black flinty material (Plate 3.c). This material is best developed next to the listric thrust (fault B) where it extends 0.3 m from the fault. On the minor thrusts a limit of 0.1 m is more common.

Immediately adjacent to fault B, this flinty material occupies about 50% by volume of the rock and forms a matrix containing rounded white quartzite fragments between 2 and 5 mm in diameter. Away from the fault, there is a steady decrease in the volume of the flinty material which then begins to form a fracture-vein network (Plate 3.d,e) surrounding larger angular fragments. These fractures do not at the present time form zones of weakness in the fault rock.

The matrix/fracture-vein patterns described above, have not developed next to the minor thrusts. Instead, small bands of the flinty material are seen within 30 to 50 mm of the fault. These bands are generally sub-parallel to the fault but occasionally form at high angles to it (Plate 3.f). The boundaries between the flinty material and quartzite are diffuse. Microstructural characteristics of this material are described in detail in Chapter 8.

CHAPTER 8

MICROSTRUCTURES

8.1. Introduction

The textures and microstructures described here, developed in
zones across which shear displacements are believed to have occurred.
They record the physical response of the rock to internal stresses
induced by this movement. The primary feature of these rocks is that
they have undergone varying amounts of grain size reduction and are
members of the cataclasite series of fault rocks (Section 6.1). The
4 most important factors controlling the character of the resultant
microstructure are:

1. Metamorphic environment.
2. Host lithology.
3. Finite displacement.
4. Style of faulting.

From a detailed investigation of the microstructure, including
the use of a high voltage transmission electron microscope (HVEM),
which makes it possible to study individual grains and the grain to
grain relationships, information on the metamorphic environment of
faulting can be obtained. This includes interpretation of the internal
deformation features of the rock and the mineral assemblage. It will
be shown in this chapter that the fault rocks studied in the Shetland
Islands developed in a shallower crustal environment than those studied
from Loch Eribol (Sections 8.2.5, 8.4.4).

The response of quartz to shear displacements has been studied
at Loch Eribol where a fairly pure quartzite is faulted. The contrasting
granitoid rock types studied in the Shetland Islands show how this
response is modified by the presence of other minerals. In addition,
the contrasting effects of deformation in what is essentially a closed
chemical system (Loch Eribol) and an open one (Shetland Islands) can
be studied.

Although a much greater finite displacement has occurred across
the Walls Boundary Fault in Shetland than across the faults studied
at Loch Eribol, and although the movement sense is transcurrent on the
former as opposed to reverse dip-slip on the latter, the microstructures
from both areas do show some similarities. The most important of these
is that significant amounts of recrystallisation and growth of new

phases have occurred in both zones. These features are discussed fully in Section (8.5).

8.2. Ollaberry Area

The Ollaberry area was chosen in order that microstructural variations across the wide crush-zone adjacent to the Walls Boundary Fault might be studied in a region where the intensity of deformation varied considerably in a uniform host rock. This granite was sampled at irregular intervals across the crush-zone (Fig. 7.2) with each sample showing a different intensity of deformation. A completely undeformed member of the series was not present at the Back of Ollaberry, where the margin of the crush-zone lies below the sea. For the purpose of comparison, a sample of a very similar granite from the same intrusive complex was collected from the margin of the crush-zone 1 km from the Walls Boundary Fault at Fugla Ness (HU 369 740), some 6 km to the south. This granite appeared identical to the deformed rock studied at the Back of Ollaberry but textural comparisons between them were made with care because of the possibility of at least some initial compositional and textural variation. The sample numbers are shown in Fig. 7.2.

With the exception of samples 03-2 and 14-5, where the thin-sections were oriented perpendicular to the Walls Boundary Fault, thin-sections were not specifically oriented. This was because for all samples other than 14-5, no differences in the mesoscopic fracture patterns could be seen on sawn surfaces perpendicular and parallel to the main fault. As in sample 03-2, this lack of preferred orientation in the mesoscopic fractures was echoed in the microstructure; thin-section orientation was not considered worthwhile for the remaining samples. Samples were not impregnated with Araldite before sectioning.

The microstructures of the deformed samples from the crush-zone are summarised in Fig. 8.1 and described in detail below. Descriptions are listed from the crush-zone margins, with a very low level of cataclasis (sample 01-2, 1 km from the Walls Boundary Fault), towards the centre of the crush-zone at the Walls Boundary Fault itself. Thus an increase in the intensity of cataclasis is recorded for each successive sample described.

8.2.1. Optical Microstructures

Sample O1-2, 1 km from the Walls Boundary Fault

The granite involved in the Walls Boundary Fault crush zone consists almost entirely of plagioclase (of oligoclase composition) and quartz, with biotite showing some alteration to chlorite. Rare crystals of muscovite and opaque ores are also seen. The original granitic texture of this sample, which shows very slight cataclasis, has been slightly modified by ductile deformation. This may have resulted from uplift and erosion or may have arisen during the late stages of the Caledonian Orogeny. As a result, undulatory extinction, deformation bands and sub-grains are seen in quartz and mechanical twins, which may be kinked, in plagioclase (Plate 4.a,b). Many biotite crystals are also kinked. A small number of quartz-filled, healed fractures cross the sample (Plate 4.a). All these intra-crystalline features are seen within the larger fragments throughout the fault zone.

In this sample, the low level of cataclasis takes the form of a number of closed inter- and intra-granular fractures. They are invariably cleavage cracks in feldspar but there is no crystallographic control of their orientation in quartz. No shear displacements have been observed across these fractures, which are therefore assumed to be dominantly extensional in origin.

Sample O3-2, 40m from the Walls Boundary Fault.

At this position within the crush zone, the granite is not only cut by closed fractures but also by open fractures which contain mineral fragments (Plate 4.c). These fractures divide the rock into rough equidimensional or lenticular areas between 2 and 50 mm in diameter, within which the original granitic texture is preserved. Across the fractures, small shear displacements (in the plane of the section) of up to 0.5 mm are visible. The width of individual fractures varies but they are generally wider (up to 0.5 mm) than in sample O3-2. In the less intensely deformed regions of this sample, the lenticular areas are themselves crossed by small closed fractures. Offsets across these reach 0.5 mm in the plane of the section, and the sub-fragments they produce are rotated by up to 10° (Plate 4.d). The size of these sub-rounded, roughly equidimensional sub-fragments varies between 0.2 and 3 mm in diameter.

The overall intensity of cataclasis is heterogeneous with the sample possessing more strongly deformed regions where the fracturing

101

Plate 4

All photographs are the same scale. Scale bar = 8 mm.

a   Sample 01-2, 1 km from the Walls Boundary Fault. Kinked mechanical
     twins in oligoclase crossed by infrequent, closed fractures. An
     early, quartz-filled fracture also crosses the crystal.

b   Sample 01-2, 1 km from the Walls Boundary Fault. Cleavage cracks
     in orthoclase.

c   Sample 03-2, 40 m from the Walls Boundary Fault. Large fracture
     filled with cataclastic detritus. Sub-fragments show very little
     rotation or displacement.

d   Sample 03-2, 40 m from the Walls Boundary Fault. Heterogeneous
     cataclasis with a fine grained matrix between the undeformed remnants
     beginning to develop.

e   Sample 03-2, 40 m from the Walls Boundary Fault. Reduction in size
     of unfractured blocks which also show greater misorientations. The
     fine grained matrix is better developed.

f   Sample 04-1, 1 m from the Walls Boundary Fault. Fine grained matrix
     now forms more than 50% of the total volume.

h   Sample 14-5, 0.25 m from the Walls Boundary Fault. Onset of a
     further episode of fracturing in a well developed cataclasite.

i   Sample 15-1, fault plane ultracataclasite.

     About 70% of the visible porphyroclasts are analcime. The remainder
     are quartz, feldspar or have a cataclastic texture. All porphyroclasts
     are rounded and are surrounded by a maroon-coloured ultra-fine grained
     matrix.
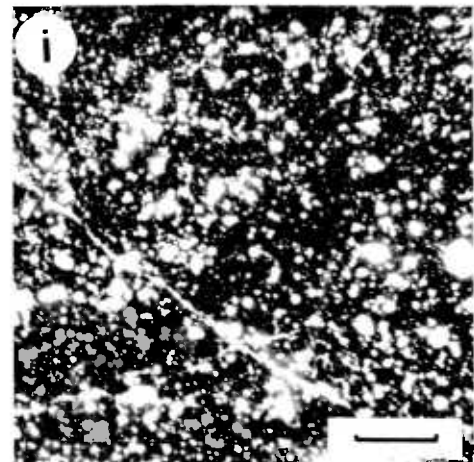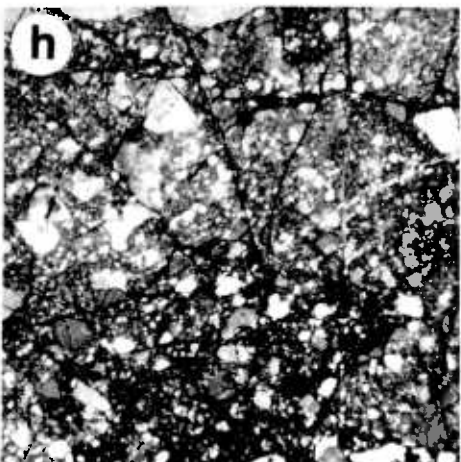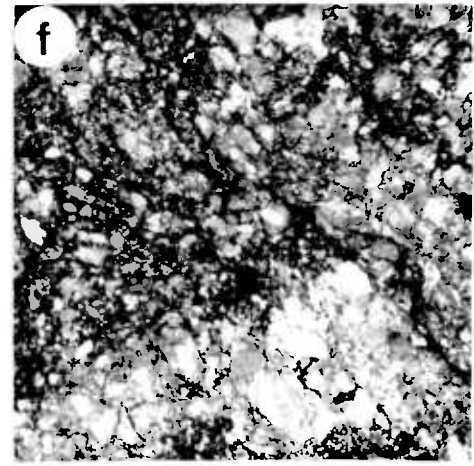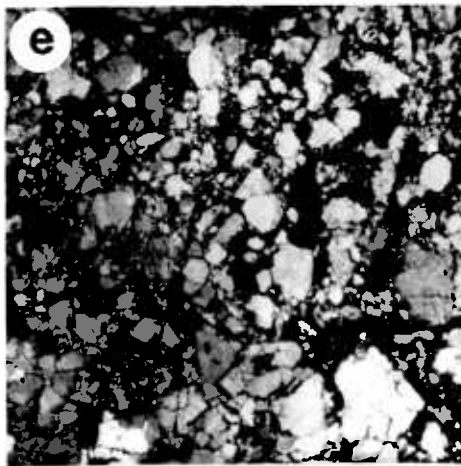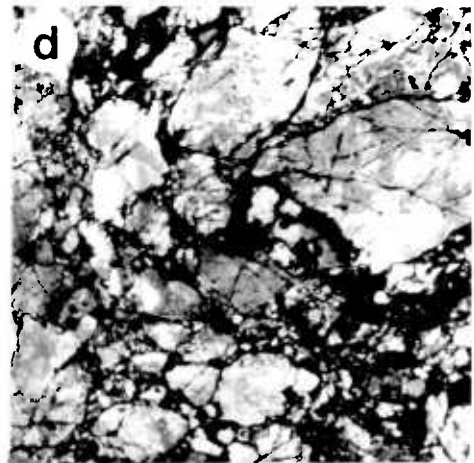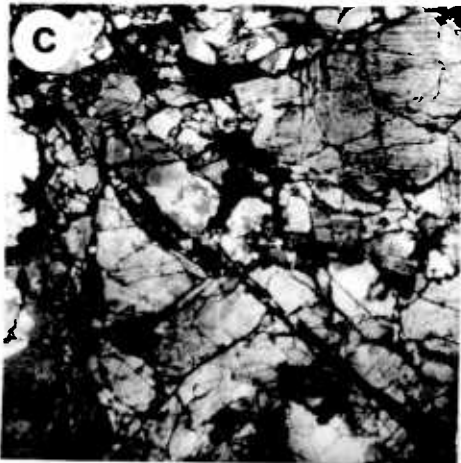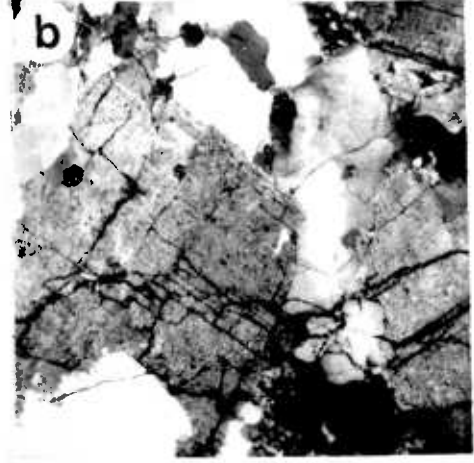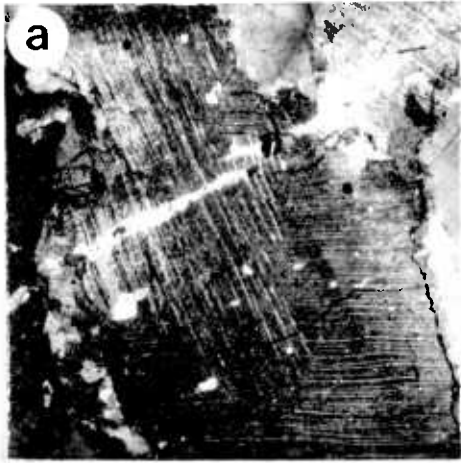
of the lenticular areas between the large debris filled fractures is more severe (Plate 4.e) and a fine grained matrix with many fragments smaller than 0.1 mm is beginning to develop. In these areas, all of the sub-fragments are small (between 0.2 and 1 mm) and rounded, with a big spread in their orientations such that they no longer appear to have been derived from a single crystal, as is often the case in the less deformed regions of the same sample. No original mica crystals remain in these regions although small phyllosilicate crystals can be identified in the matrix.

Sample 14-2, 7m from the Walls Boundary Fault

This sample is again texturally heterogeneous and resembles sample 14-1. Fewer debris filled fractures are seen and the sample is made up of a matrix surrounding small porphyroclasts ($\leqslant 2$ mm) in which the original igneous texture can still be recognised. Occasional larger remnants of the lenticular areas described in samples O3-2 and 14-1, remain.

Sample O4-1, 1m from the Walls Boundary Fault

Very few textural changes are seen in this sample when compared to sample 14-2. As in the previous sample, the fine grained matrix forms about 50% of the total volume. The rock is altered and its matrix contains chlorite in addition to small grains of quartz and feldspar (Plate 4.f).

Sample 14-5, 0.25m from the Walls Boundary Fault

Two major features are seen in this sample alone: it has a coarse, diffuse banding of cataclasite and ultracataclasite, and some of the fragments within the matrix have a cataclastic rather than granitic internal microstructure. These features, alone, are non-random and are oriented sub-parallel to the Walls Boundary Fault.

In the ultracataclasite bands, the matrix forms about 90% of the total volume and porphyroclasts are rounded with diameters between 0.15 and 2 mm. No remnants of the granitic texture can be recognised in these bands. In the cataclasite bands, the matrix forms about 50% of the total volume, the porphyroclasts are sub-angular or rounded and have diameters up to 10 mm. Texturally, these bands closely resemble samples 14-2 and O4-1.

The presence of porphyroclasts with an internal cataclastic texture is important since it indicates that the rock at this locality has undergone more than one episode of cataclasis. This feature is also

Sample	Distance from Walls Boundary Fault	Prominent microstructural features of cataclastic deformation
01-2	1000 m	Both inter- and intragranular, closed fractures cross the original granitic texture. There are no visible shear displacements across them.
03-2	40 m	Closed fractures are still seen and the rock is divided into lenticular areas 2-50 mm in diameter by open fractures 0.01-0.15 mm in width which contain mineral debris. Small offsets are seen across these fractures.
14-1	10 m	The cataclasis is very heterogeneous. In parts, the texture is similar to 03-2, with the lenticular areas only 2-6 mm in diameter and the open fractures 0.5 mm in width. The resulting sub-fragments rotated. Elsewhere, rotation of the sub-fragments (by cataclastic flow) has been great and a matrix with porphyroclasts structure is developing.
14-2	7 m	A structure consisting of a matrix with porphyroclasts is well developed with each occupying 50% of the total volume. Quartz and feldspar make up the porphyroclasts.
04-1	1 m	As 14-2.
14-5	0.25 m	A diffuse banding of cataclasite and ultracataclasite has developed. In the ultracataclasite the matrix makes up about 90% of the total volume and the porphyroclast diameter varies between 0.15 and 2 mm. In the cataclasite the matrix makes up 50% of the total volume and the porphyroclast diameters reach up to 10 mm. In both bands the porphyroclasts are quartz, feldspar or cataclasite.
15-1	on the fault	The ultracataclasite on the fault plane is stained a deep maroon. Porphyroclasts of quartz, feldspar, analcime and cataclasite reach up to 7 mm in diameter.

Fig. 8.1. Summary of the microstructures associated with the Walls Boundary Fault.

seen immediately adjacent to a minor fault within the crush zone
about 20 m from this sample where the latest episode of cataclasis
has not involved much fragment rotation (Plate 4.g). It may be that
further fracturing and fragment rotation of this sample (Plate 4.g)
could lead to a texture similar to that of the ultracataclasite bands
of 14-5 in which the porphyroclasts are themselves cataclasites.

Sample 15-1, on the Walls Boundary Fault

The material on the fault itself is a deep maroon-coloured ultra-
cataclasite in which only the porphyroclasts can be identified (Plate
4.h). These are quartz, feldspar, analcime and cataclasite. They
are all rounded and vary in size from a diameter of 7 mm downwards.
Late calcite veins cross both matrix and porphyroclasts.

8.2.2. Grain Size Distribution.

From the thin-sections described above, measurements of grain and
fragment sizes were made. These data from each sample were compared
directly without converting to sieve analysis (Folk, 1968). The grain
size data were obtained, for each sample, by superimposing a grid on
the thin-section, with a spacing greater than the largest dimension of
the largest grain in that sample. The longest apparent dimension of
the grain or fragment under each node of the grid was measured. Thus
for the less deformed samples, the grain size distribution was largely
related to the original igneous texture, but for the more highly
fractured samples more fragments were counted and the grain size dis-
tributions reflected the intensity of cataclasis. A minimum of 300
counts spread over the entire section (Table 8.1) were taken to ensure
consistent results (Friedman, 1958).

The smallest grain that could be measured optically was 8 µm. To
extend the analysis to the finest fraction (almost 35% by volume of
sample 15-1 are below 10 µm in size), electron microscope photomicro-
graphs were used in addition to the thin-section data for sample 15-1.
Some errors were introduced by reducing the grid size over the finest
fraction, but these did not have a significant effect on the shape of
the cumulative frequency curves. Cumulative frequency curves obtained
by this thin-section procedure and by sieve analysis have been found
to correspond closely (Engelder, 1974a).

Cumulative frequency curves (Fig. 8.2) were constructed by
plotting the cumulative percentage of grains (by volume) against grain

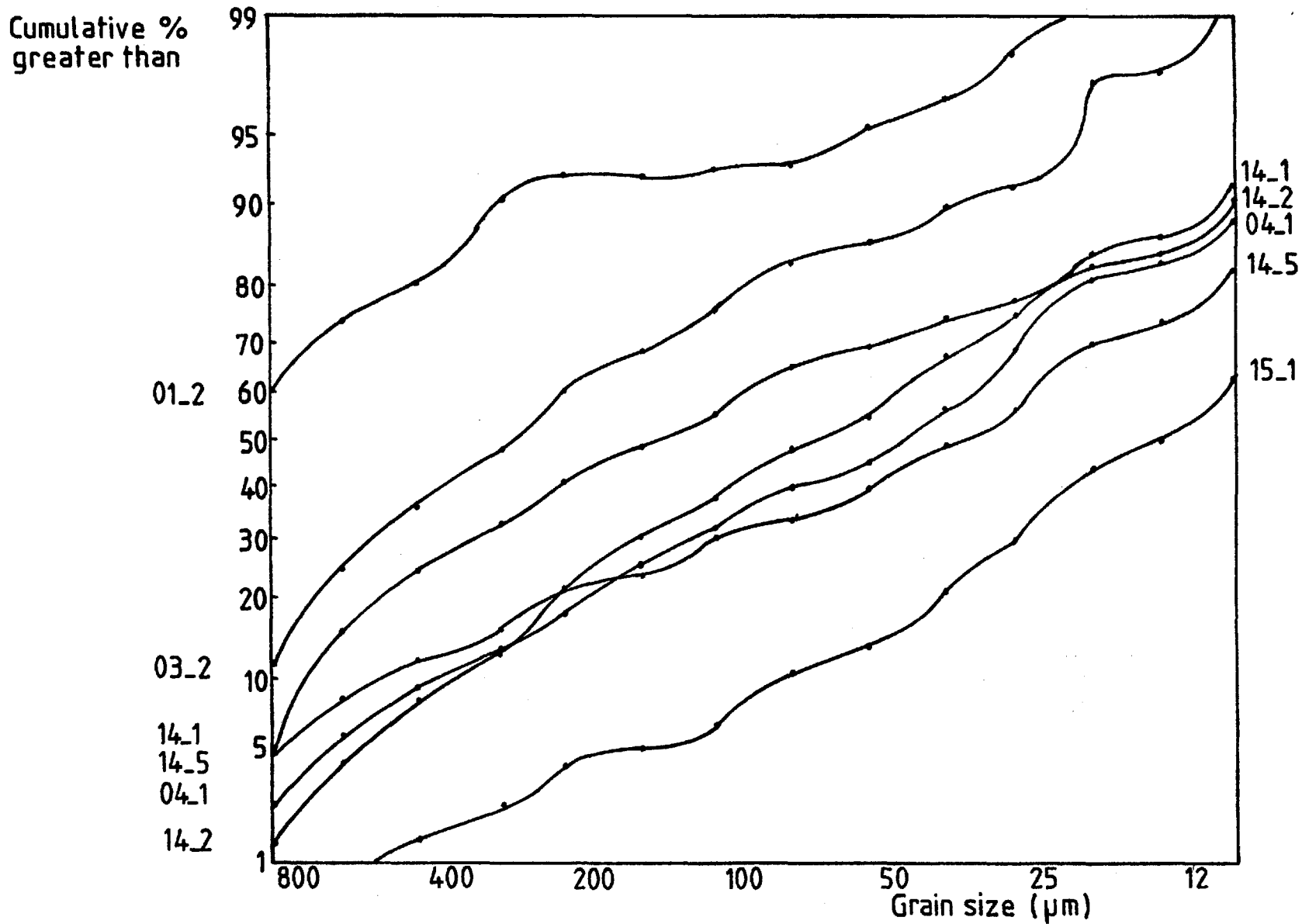Fig. 8.2. Cumulative frequency curves for rocks from the Ollaberry area.

Table 8.1.

Number of counts taken per sample and derived grain size data

Sample Number	Distance from *W.B.F. Fault (m)	Number of Counts	Median Grain Size (μm)	Graphic Standard Deviation (μm)	Graphic Mean (μm)
15-1	0	574	12.3	59	4.25
14-5	0.25	299	36	188	51.5
04-1	1	305	49	232	55
14-2	7	378	65	234	64
14-1	10	335	144	164	115
03-2	40	507	300	296	250
01-2	1000	158	1130	404	1032

*W.B.F. = Walls Boundary Fault

size. These data were plotted with cumulative percentage (ordinate) represented in a probability scale and the grain size (abscissa) with a logarithmic scale. A normal distribution forms a straight line at some angle to the abscissa.

8.2.2.1. Calculation of Median, Graphic Mean and Standard Deviation

The cumulative frequency curves were used to calculate the median grain size, graphic standard deviation and graphic mean for each sample.

The median grain size, the grain size in the centre of the distribution, were read directly from the cumulative frequency curves. The graphic standard deviation and graphic mean were calculated from the value of the grain size (in phi units) that 16, 50 and 84% of the grains are greater than

$$\text{Graphic mean} = \frac{\emptyset_{16} + \emptyset_{50} + \emptyset_{84}}{3} \tag{8.1}$$

$$\text{Graphic standard deviation} = \frac{\emptyset_{84} - \emptyset_{16}}{2} \tag{8.2}$$

where $\emptyset_{16}$ = grain size, in phi units, that 16% of the grains counted are larger than.

etc.

Data from the ultracataclasite on the fault plane was plotted at a distance of 0.01 m from the fault although there is, in fact, an abrupt textural change between this rock and the adjacent cataclasites.

Fig. 8.3.   Plot of graphic mean, median grain size and graphic standard deviation against distance from the Walls Boundary Fault.
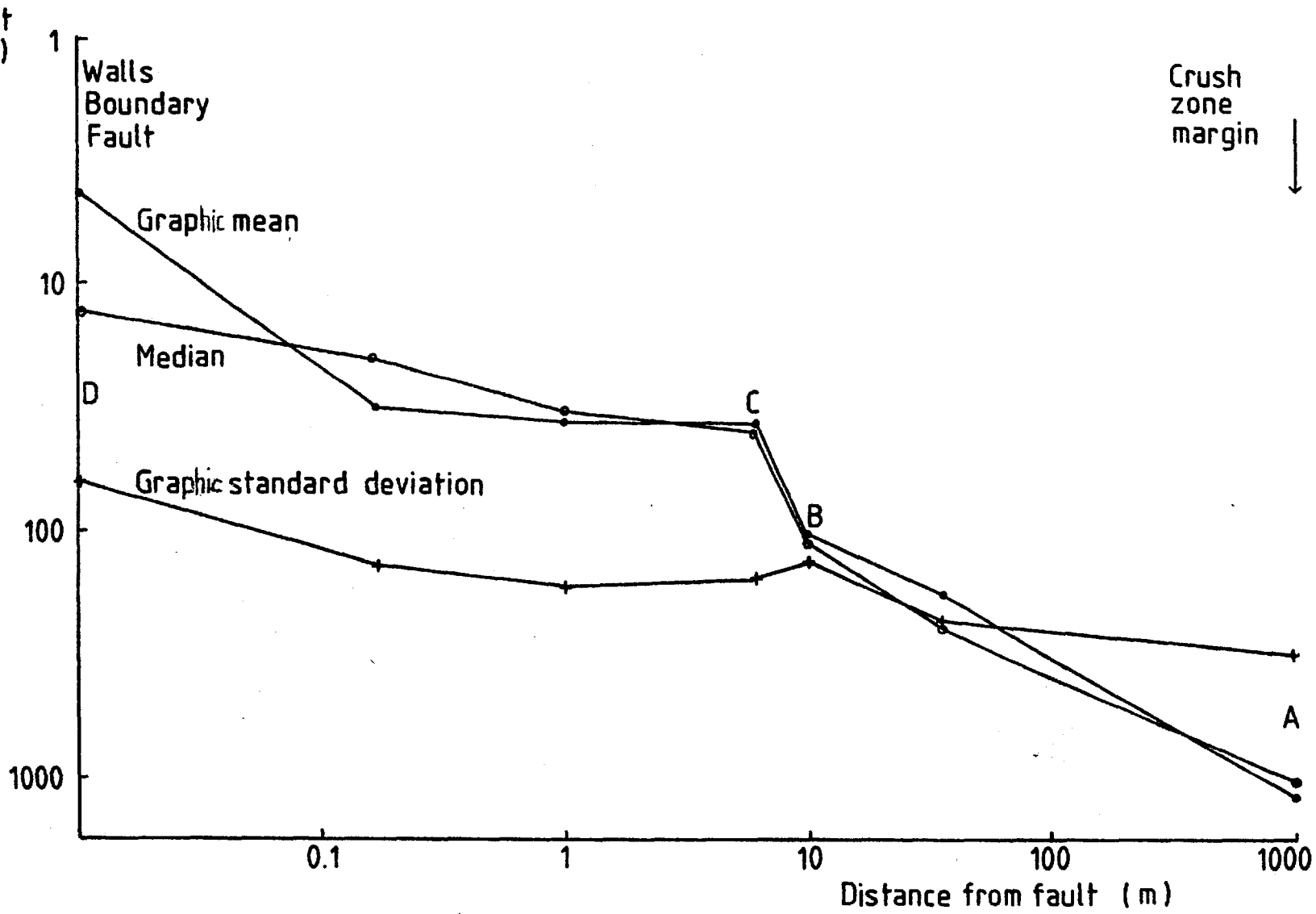
Both the average grain size (mean) decreases and the number of fine grains increases as the fault is approached (Fig. 8.3). This effect is fairly steady from the margins of the crush zone (A to B on Fig. 8.3) but increases rapidly about 10 m from the Walls Boundary Fault (B to C on Fig. 8.3), that is the mean and median grain sizes decrease more rapidly.

The graphic standard deviation is a more sensitive measure of sorting. Small values (in μm) indicate poor sorting (a large variation in the grain size). There is a slight but fairly steady decrease in the value of the graphic standard deviation as the fault is approached with only the fault plane ultra-cataclasite having a significantly lower value (D on Fig. 8.3).

From these results a slight but steady increase in the degree of cataclasis from the outer margins of the fault zone to a point about 10 m from the Walls Boundary Fault may be inferred. At this locality, values of the median grain size, and graphic mean decrease rapidly. This appears to correlate with the onset of cataclasis of the fragments between the large fractures seen in the field (Section 7.2.3). Between this point and the Walls Boundary Fault, the intensity of cataclasis, as represented by the median, graphic standard deviation and graphic mean, increases slightly but does not reach that of the material on the fault plane itself.

8.2.3. High Voltage Electron Microscopy

8.2.3.1. Sample Preparation

Electron microscope foils were prepared following the standard procedure outlined by Barber (1970). This involves mounting (with water based glue) copper discs on the required areas of uncovered thin sections made with Lakeside cement. The rock slice was removed from the glass by immersion in alcohol and the copper grid with the attached area of thin-section was lifted from the slide. Unwanted areas of the rock slice were broken from around the edges of the copper disc. Rock samples were not impregnated with Araldite before sectioning .

The rock slices mounted on the copper discs were then thinned by ion beam bombardment (Barber, 1970). As the thinning time for different minerals varied, extreme care was needed in the preparation of poly-mineralic cataclasites. In these rocks the thinning time for the porphyroclasts was invariably several hours less than that required

for the matrix (15 to 25 hours). By using a low angle of ion beam
impingement (about 11°) it was possible to thin both at a similar
rate and produce a foil in which the structure of the contact between
matrix and porphyroclast could be examined. For study of one or the
other, it was more satisfactory to prepare separate foils.

8.2.3.2. Microstructures

Sample 01-2, 1 km from the Walls Boundary Fault

The internal dislocation structure of this sample is thought to
have developed during an early episode of intracrystalline, plastic
deformation and is seen in many of the porphyroclasts and larger
fragments within the matrix of the cataclasites throughout the fault
zone.

Quartz has a well developed sub-grain structure indicating sub-
stantial recovery (Plate 5.a). The sub-grains are fairly small (about
4 μm in diameter) and commonly equidimensional. The dislocation walls
between adjacent sub-grains are usually straight and often contain bubbles.
Within the sub-grains, dislocations are occasionally pinned and prismatic
dislocation loops are common. The density of unbound dislocations in
quartz grains of this sample is about 9×10^{11} m^{-2}.

Feldspar has also undergone recovery. Unbound dislocations are
commonly straight and some dislocation walls have developed. These
are usually discontinuous and occur in segments which are less than
3 μm in length (Plate 5.b). Both mica and chlorite crystals are found
within the feldspar.

Sample 14-1, 10 m from the Walls Boundary Fault

Although most of the cataclasis of this sample is contained
within the optically visible, debris-filled fractures, in places
there is some modification of the characteristic intragranular features
of the granite along the margins of the lenticular areas next to these
fractures. In these areas, diffuse equidimensional cells with indis-
tinct margins have developed (Plate 5.c). The cells contain high
densities (about 5×10^{12} m^{-2} in quartz) of tangled, unbound disloca-
tions and are about 2 μm in diameter in quartz and 1-2 μm in feldspar.
The splitting of the spots of diffraction patterns from these areas
indicates that the cells in any given region have variations of up to
10° in their orientation.

There is a sharp boundary between the cellular areas and the cataclastic bands (which form the optically visible, debris filled fractures) in which the grain size has been reduced to between 0.04 and 0.6 μm (Plate 5.d). It is difficult to identify the smallest fragments, but the larger ones are feldspar and quartz, the latter being equidimensional and sub-rounded. Occasional grains (usually the smallest) have a crystalline shape and may be new. A few small, slender ($<$ 0.1 μm in width) phyllosilicate crystals also occur in these bands and may be new.

Localised zones within the cataclastic bands have a high phyllosilicate content (Plate 5.e). The phyllosilicates in these zones are coarser grained and are dominantly chlorite, with subordinate mica. The lath shaped crystals are 0.2-0.5 μm in width and 1-2.5 μm in length, and form zones up to 5 μm in thickness in which aligned phyllosilicates surround rare, rounded porphyroclasts of quartz and feldspar about 1 μm in diameter. There are no very small grains within these zones.

Sample 14-2, 7 m from the Walls Boundary Fault

Although this sample has the same basic structure as sample 14-1, there is an increase in the number and width of the cataclastic bands and the cellular structure at the margins of the porphyroclasts is more widespread. The cellular structure is most strongly developed in feldspar grains where the cell size may be as small as 0.2 μm. In this sample, there is usually a gradational margin between these cellular zones and the cataclastic bands, and the cataclastic fragments are usually similar, in size, to the cells within the porphyroclasts. There is a progressive increase in the cell misorientation as the cataclastic bands are approached until, with a 17° spread within a 30 μm^2 area, new grains can be distinguished. At this stage new, slender phyllosilicate crystals are also visible between grains. Again the cataclastic bands contain zones with a very high phyllosilicate content and no very small fragments.

Sample 04-1, 1 m from the Walls Boundary Fault

The microstructure of this sample is similar to that of samples 14-1 and 14-2, but differs in that there has been widespread recrystallisation of the cellular areas of both feldspar and quartz. The cataclastic bands, although more extensive, are unchanged and the central portions of the porphyroclasts have a similar microstructure to the undeformed

Plate 5

a   Sample 01-2, 1 km from the Walls Boundary Fault. Dislocation
    structure in quartz. Note pinned and bowed dislocations, occa-
    sional prismatic dislocation loops and bubbles in the sub-grain
    walls. Scale bar = 1 μm.

b   Sample 01-2, 1 km from the Walls Boundary Fault. Dislocation
    structure in oligoclase. Note discontinuous segments of dislocation
    walls. Scale bar = 1 μm.

c   Sample 14-1, 10 m from the Walls Boundary Fault. Diffuse equidimen-
    sional cells with indistinct margins which form the edges of the
    lenticular areas between cataclastic fractures. Splitting of the
    spots in the diffraction pattern shows that these cells have 10°
    misorientations. Scale bar = 1 μm.

d   Sample 14-1, 10 m from the Walls Boundary Fault. Material within the
    optically visible detritus filled fractures. Most fragments are
    equidimensional and sub-rounded. The larger fragments are quartz and
    feldspar. Scale bar = 0.4 μm.

e   Sample 14-1, 10 m from the Walls Boundary Fault. Localised area of
    the cataclastic bands (3d) with a high phyllosilicate content. These
    are chlorite and surround rounded quartz fragments. Scale bar =
    0.5 μm.

f   Sample 14-5, 0.25 m from the Walls Boundary Fault. Small porphyro-
    clasts of quartz and feldspar in a fine grained phyllosilicate-rich
    matrix. Scale bar = 1 μm.

h   Sample 14-5, 0.25 m from the Walls Boundary Fault. Defect-free growth
    rum on albite porphyroclast. Scale bar = 0.4 μm.

i   Sample 15-1, fault plane ultracataclasite. Ultra-fine matrix particles
    surrounding small porphyroclasts of varying shape. Note crystal
    form of many of the tiny matrix fragments. Scale bar = 1.6 μm.
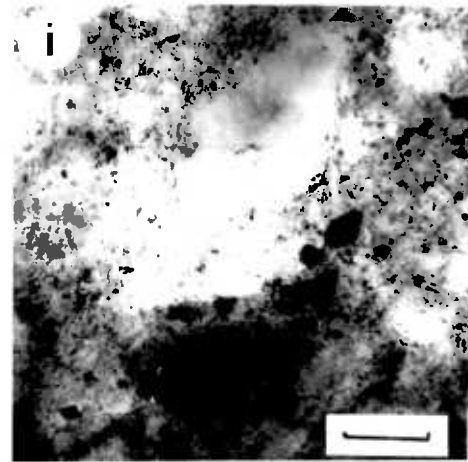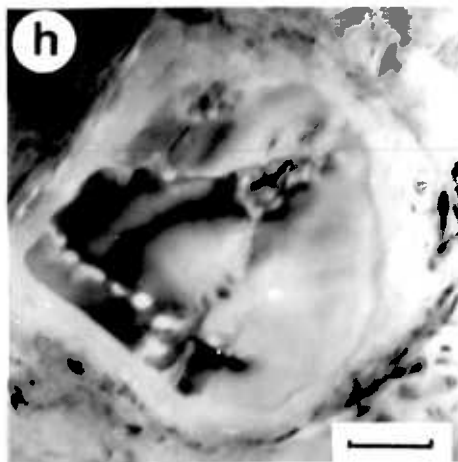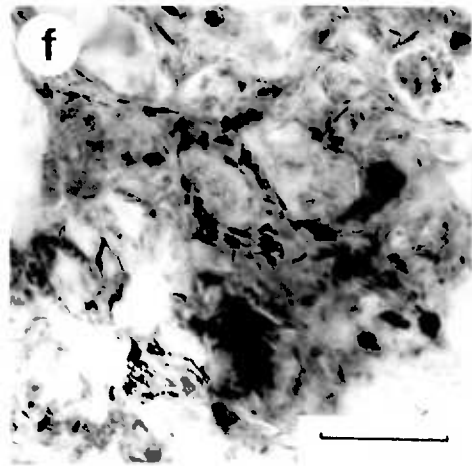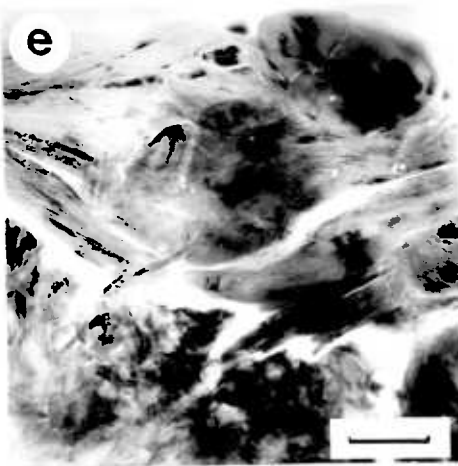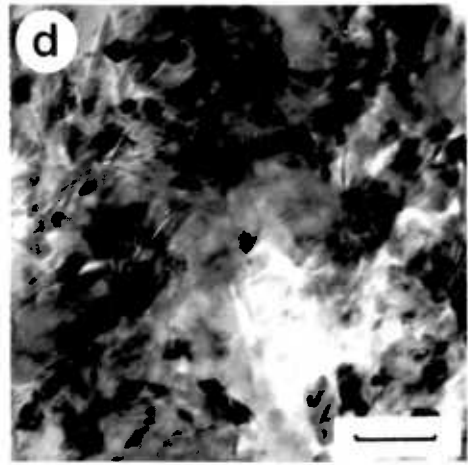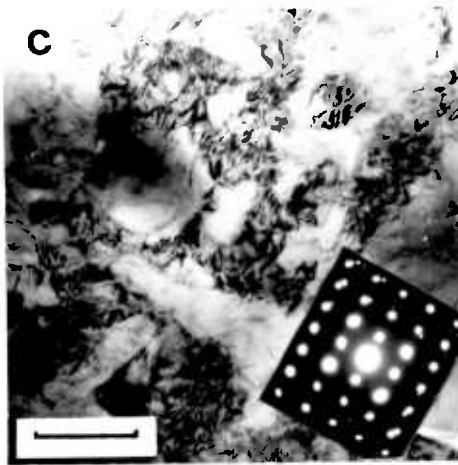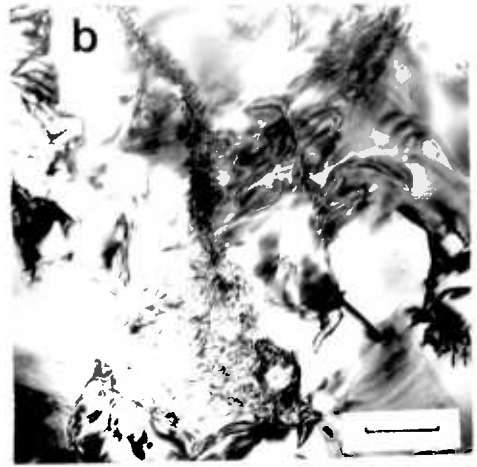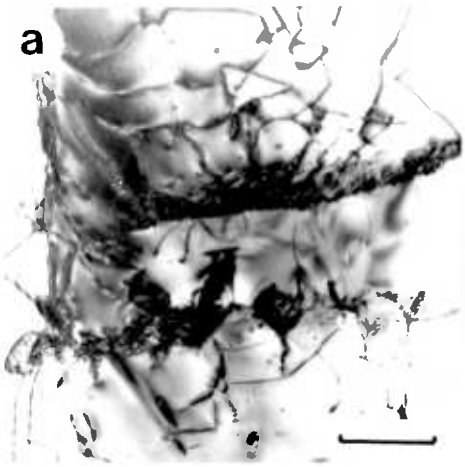
granite.

Sample 14-5, 0.25 m from the Walls Boundary Fault

Microstructurally, the optically visible cataclasite bands in this sample are similar to sample 04-1. The ultracataclasite bands, which appeared similar optically are, however, quite distinct on a finer scale. In these bands, the porphyroclasts have recrystallised margins but the matrix between them consists of smaller rounded porphyroclasts (usually $\leqslant 3$ µm) within a very fine grained, phyllosilicate-rich matrix (Plate 5.f).

The matrix is heterogeneous, consisting in part of regions in which the phyllosilicates form about 50% of its volume, whereas elsewhere, the phyllosilicate content of the matrix may approach 100%. The phyllosilicates are too fine for easy identification. Individual crystals have lengths of about 0.3 µm and widths of only 10 nm (100 Å). This extreme fineness also leads to imaging problems, as it is impossible to find areas where crystal overlap does not occur. The phyllosilicates have no overall preferred orientation, although they lie parallel to the porphyroclast boundaries.

In these bands, occasional defect-free rims surround small plagioclase porphyroclasts (Plate 5.g). The absence of deformation of these rims, reinforced by the lack of deformation of the phyllosilicates (fracturing, kinking, etc.), suggests these features may be post deformational in age.

Sample 15-1, on the Walls Boundary Fault

On a fine scale the fault plane ultracataclasite is inhomogeneous. Although all of the optically visible porphyroclasts were rounded, there are many smaller ones whose shape varies from angular to rounded. The size of the porphyroclasts is variable with diameters ranging continuously up from 1.5 µm (Plate 5.h). Analcime, quartz, peristerite and intermediate plagioclase all form porphyroclasts but their shape appears to be independent of mineralogy. Quartz and analcime porphyroclasts contain sub-grains and unbound dislocations, but the latter mineral damaged too rapidly under the electron beam for a study of the internal dislocation structure to be made. Feldspar porphyroclasts commonly contain dislocations and occasional sub-grain walls. Rare peristerite porphyroclasts were also present and may have developed during the faulting as none were seen in the parent granite.

The matrix is also heterogeneous and has an average grain size of

less than 0.5 μm with many grains less than 0.1 μm in diameter. Most matrix grains are equidimensional and many have a good crystalline shape, suggesting that they may be new (Plate 5.h). In contrast, the larger of the matrix grains (usually plagioclase) are more commonly angular and appear to be fragments. Many of the matrix grains are too small for identification. The larger ones, however, proved to be quartz, plagioclase and analcime. In most parts of the matrix phyllosilicate crystals are rare, but when they occur they are small and slender. Preferred orientation of the phyllosilicates is only seen in localised in regions where these crystals make up about 25% of the matrix volume. More commonly, phyllosilicates are randomly oriented or are aligned parallel to the boundaries of the porphyroclasts. Scanning-transmission electron microscopy (STEM) and detailed diffraction pattern analysis show that the phyllosilicate assemblage contains both chlorite and mica which may be muscovite. These minerals are indistinguishable morphologically.

8.2.4. Microstructural Summary.

Optical microscopy, including the grain size analysis (Section 8.2.2.)   , shows that rocks in the Walls Boundary Fault zone undergo a sudden textural change about 10 m from the fault itself. This results from the onset of deformation and fracturing within the stable blocks that are surrounded by large scale fractures. At greater distances from the fault, the level of cataclasis is roughly constant and is confined to individual fractures, many of which are filled with cataclastic material. Within 7-10 m of the fault these cataclastic bands widen and cease to have sharp margins. There is a gradational contact between the zones of cataclasite and the remaining porphyroclasts, each of which make up about 50% of the whole. It seems likely that rocks within 7-10 m of the Walls Boundary Fault have been subject to pervasive cataclastic flow at some point in the history of movement of the fault zone. It is also at this distance from the fault that the first evidence of grain growth, both of new phyllosilicates and of the smaller fraction of the cataclastic matrix is seen. It is impossible to determine whether the latter arises from the nucleation and growth of new phases, or whether it is in part recrystallisation of the finest cataclastic particles.

The cataclastic matrix of these rocks contains phyllosilicate rich bands about 5 μm in width. These bands consist of aligned chlorite

and muscovite crystals surrounding occasional, rounded porphyroclasts of quartz and feldspar which are about 1 μm in diameter. The cause of the phyllosilicate concentration and lack of ultra-fine grains, which are seen in the rest of the cataclastic bands, is not clear. One explanation may be that fluid flow was concentrated in these zones in which pressure solution was then concentrated. Consequently, the finest grains, which are most susceptible to solution processes, were removed. Some mechanism leading to growth of the phyllosilicates is also needed, as these crystals are comparatively coarse grained. The quartz and feldspar fragments in these bands show no evidence for growth.

Within 7-10 m of the Walls Boundary Fault, there is no appreciable change in the cataclastic texture, although there is a slight increase in the volume percentage of the matrix and decrease in porphyroclast diameter as the fault is approached. Within 1 m of the fault, recrystallisation of the cellular structure in the margins of the quartz and feldspar porphyroclasts has occurred. This recrystallisation may have occurred as the result of a greater strain leading to larger cell misorientations in this region, which should in turn enhance recrystallisation.

Alternatively (or additionally), the recrystallisation may have been driven by higher ambient temperatures which could have resulted from frictional heating. Frictional heating produced by intermittent seismic slip on the Walls Boundary Fault would be localised and is unlikely to have had a significant effect on rocks at a distance of 1 m.

Within 1 m of the Walls Boundary Fault, the rock consists of layers of cataclasite (with a microstructure identical to that found 1-10 m from the fault) and ultracataclasite. The ultracataclasite layers have a high volume percentage of phyllosilicate crystals which appear to have grown at the expense of the finest fraction of the matrix. It is not clear whether this is due to concentrated fluid flow or increasingly effective chemical activity because of the ultra-fine grain size.

The ultraclasite on the fault is texturally distinct but heterogeneous, and is the only rock containing analcime and peristerite. The analcime, which is thought to have grown from hydrothermal solution at an intermediate stage in the movement history of the fault, is itself

broken by later cataclasis and forms smaller porphyroclasts and grains within the matrix.

8.2.5. Metamorphic Environment of Faulting

The small matrix grain size of these cataclasites makes modal analysis impossible. It is not therefore possible to determine whether the cataclasites are chemically as well as mineralogically distinct from the parent granite. The growth of new phases does indicate that chemical processes were active within the fault zone and metamorphic processes other than cataclasis have been active.

Limits on the depth at which the fault plane ultracataclasite developed can be obtained from its mineral assemblage. Analcime is generally not thought to grow below about 7 km (Boles and Coombs, 1977) if the geothermal gradient is taken as 30°C/km, and a quartz-analcime assemblage will not be stable at temperatures above $190^{\circ}-200^{\circ}$C (Thompson, 1971). With the same geothermal gradient, this corresponds to depths of between 6 and 7 km. Thus the fault plane ultracataclasite must have developed at shallower crustal levels than these.

The mineral assemblage of the cataclasites within 10 m of the Walls Boundary Fault differs. In these rocks, growth of chlorite, muscovite and plagioclase (thought to be albite) has occurred. This does not provide a complete metamorphic assemblage, but if the plagioclase is albite as indicated by the diffraction pattern analysis, the assemblage may have developed under lower greenschist conditions (around 300°C, Turner, 1968), that is deeper than the texturally distinct fault plane ultracataclasite. This implies that the deeper level cataclastic flow recorded by the cataclasites within 10 m of the Walls Boundary Fault, occurred across a wider zone than the localised shallow fault slip that led to the development of the fault plane ultracataclasite. Thus there is some evidence that even within the frictional regime of the crust fault zones may widen with increasing depth in line with the experimental work of Griggs and Handin (1960), Fig. 2.2., where slip becomes localised at low confining pressures.

8.3. Sand Area

All samples taken from the Sand area proved to be highly weathered and as a result no detailed microstructural studies or HVEM work were attempted. Rocks from this area showed very similar optical features

to those from the Ollaberry area. The deformation was restricted to
fractures (in this case two sets, one barren and one containing cata-
clastic debris) thoughout most of the fault zone. The fragments in
these fractures were primarily quartz and feldspar and ranged in size
from sub-microscopic to 0.5 mm.

Within 20 m of the Aith Voe Fault, the igneous texture of the
adamellite between these fractures broke down completely and the whole
rock developed a cataclastic texture. Unfortunately, the level of
weathering in these rocks in particular was severe and the phyllosilicate
alteration products widespread; most details of the cataclastic micro-
structure were lost. Similarly, the rock found on the fault itself
appeared as a few fragments of quartz and altered feldspar in a
matrix of mixed phyllosilicates.

8.4. Loch Eribol

8.4.1. Introduction

In contrast to the wide fault zone in the Shetland Islands, the
rocks studied at Loch Eribol occur immediately adjacent to individual
faults. In the field, the deformation is represented by a single set
of fractures which are greenish-black in colour and contrast strikingly
with the white parent quartzite. It was hoped that microscopic
examination would reveal:

1. The processes involved in the healing of the fractures.
2. The cause of the colouration.
3. The environmental conditions under which faulting and
   the associated fracturing took place.

In the deformed rocks, sections were, whenever possible, cut
perpendicular to the fault plane they were associated with and
perpendicular to and parallel with any lineation on this surface. In
the samples for which this was possible, there were no obvious differences
in the fracture patterns for either orientation. Elsewhere sections were
merely cut perpendicular to their associated fault plane.

On the sawn surfaces of the quartzite a second series of fractures
containing opaque-white fracture-fill can be seen. These fractures
are hard to distinguish from the transluscent, white host quartzite,
especially on weathered surfaces. It was also possible to distinguish
a third fracture type filled with black material. Detailed micro-

structural descriptions of the parent quartzite and these three sets of fractures are given below.

8.4.2. Optical Microstructures

8.4.2.1. Host Quartzite

The Cambrian Pipe Rock cut by the faults, is a pure quartzite consisting almost entirely of slightly elongate, sub-rounded quartz grains, with occasional grains of plagioclase and K-feldspar together making up less than 2% of the total volume (Plate 6.a). Most quartz grains exhibit undulatory extinction and many contain deformation bands. Optically visible, well developed sub-grains are infrequent. Minor recrystallisation has occurred on phyllosilicate-free grain boundaries. Phyllosilicates on the grain boundaries are relatively common and inter-crystalline spaces are invariably filled with a phyllosilicate matrix. The Pipe Rock has occasional dirty bands in which well rounded quartz grains are entirely surrounded by the phyllosilicate matrix. There is very little grain boundary recrystallisation in these layers. Occasional bands of the Pipe Rock are pinkish in colour as a result of haematite in addition to the phyllosilicates along the quartz-quartz grain boundaries (Plate 6.b).

### 8.4.2.2. Opaque-white Fracture-fill

The opaque-white fracture-fill forms bands up to 5 m thick with associated fracture-vein networks. The bands usually lie parallel to the adjacent fault but the fracture-veins (fractures containing debris-like material) usually make high angles with the bands from which they extend. The fracture-veins are made up of relative l y straight segments with abrupt changes in orientation similar to those of the greenish black fracture-fill (Plate 3.c-e).

On a microscopic scale, the opaque-white fracture-fill is clean, recrystallised quartz with an average grain size of less than 0.1 mm. The bands contain rounded porphyroclasts of the host quartzite and, more commonly, individual quartz grains from it.

There are very few phyllosilicate crystals (Plate 6.c) and localised regions within the bands have a crystallographic preferred orientation. The boundaries of the bands and fracture veins are indistinct because they are made up of many small recrystallised grains (Plate 6.d). The material in the fracture veins is, microstructurally, identical to that of the bands and has the appearance of a recrystallised quartz

118

Plate 6

a   Undeformed Pipe Rock. Quartz grains exhibiting undulatory extinction with phyllosilicates on the grain boundaries. Note the plagioclase grains. Scale bar = 1 mm.

b   Haematite crystals in addition to phyllosilicates on the grain boundaries of an impure layer of Pipe Rock. Scale bar = 1 mm.

c   Low phyllosilicate content of the opaque-white fracture-fill. Scale bar = 60 μm.

d   Recrystallised nature of the boundary between the parent quartzite and opaque-white fracture-fill. Scale bar = 1 mm.

e   Recrystallised vein of opaque-white material showing low crystallographic misorientations between adjacent recrystallised grains and, in the centre, the parent quartz crossing the vein without misorientation. Scale bar = 0.5 mm.

f   Deformed quartz grain with a deformation band parallel to the opaque-white fracture vein. Scale bar = 0.2 mm.
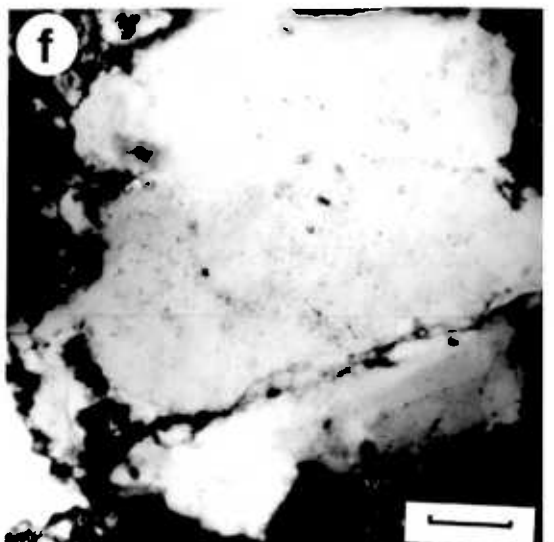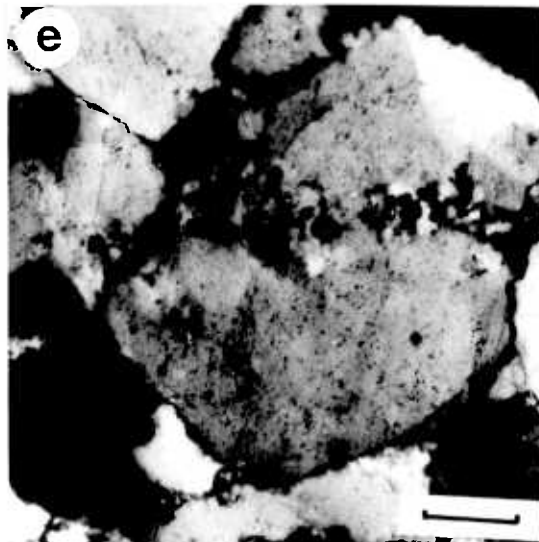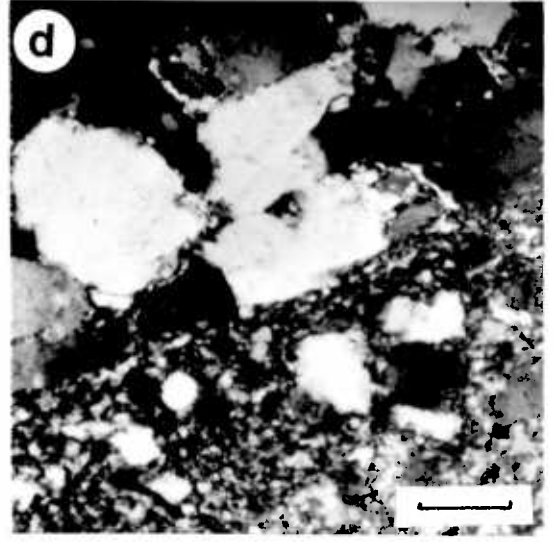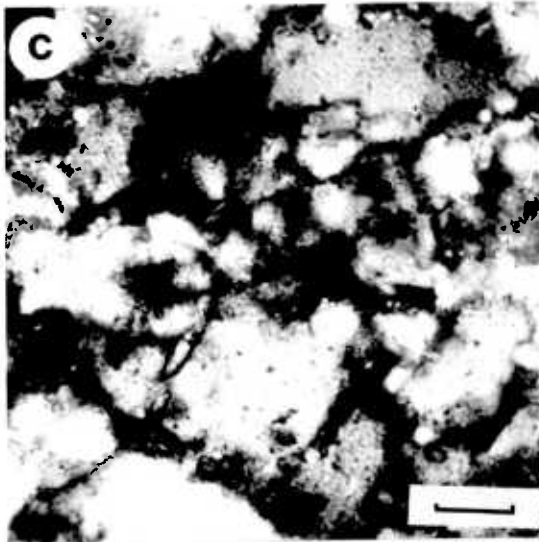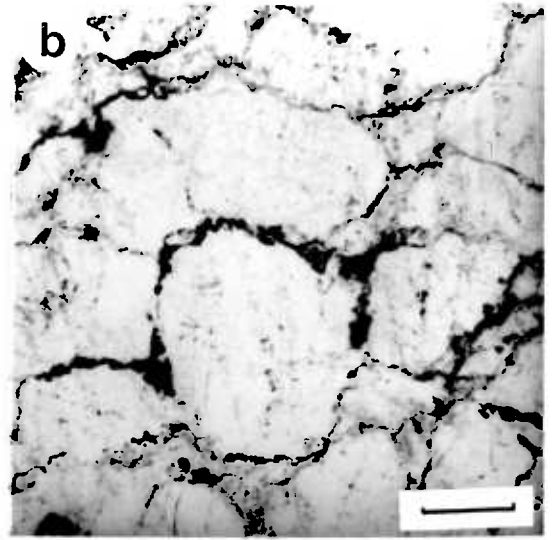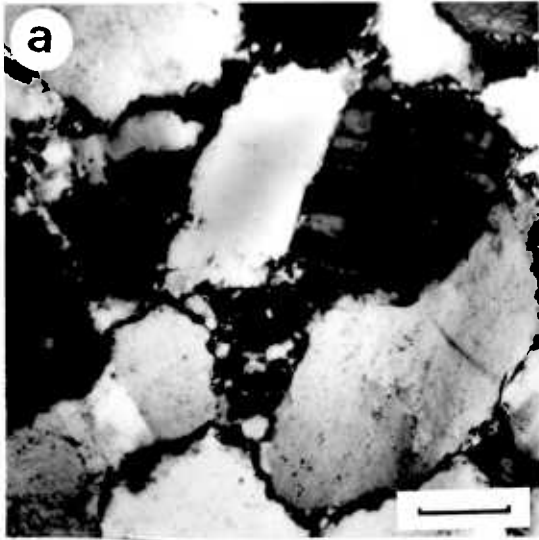
debris. Several features of the fracture-veins indicating that this is not the case are described below:

1. Shear displacements are rarely seen across the fracture-veins and where they do occur, rarely exceed 0.2 mm (in the plane of the section). In addition, the character of the veins varies along their length from a band of recrystallised grains, several grains wide, to a single, planar fracture. Although this vein thickening could result from frictional wear it is rarely seen in friction experiments.

2. There are invariably small crystallographic misorientations between the recrystallised grains of the fracture-veins and the host. In some cases, the host crystal can be traced through the recrystallised vein without undergoing any misorientation (Plate 6.e). Large misorientations between individual recrystallised grains and between grains of the veins and parent rock would be expected if the veins resulted from the recrystallisation of fault debris.

3. The phyllosilicate content is approximately equal to that of the parent, but the phyllosilicates are disseminated. There appears to have been no material added to, or removed from the veins. This alone does not preclude a cataclastic origin but does suggest the fractures have not acted as channels for fluid flow.

4. Some quartz grains of the parent have deformation bands adjacent to, and parallel with the fracture veins (Plate 6.f). This suggests that there may be some link between the internal deformation features of the host grains (of intracrystalline plastic origin) and the deformation producing the opaque-white material.

8.4.2.3. Greenish-black Fracture-fill

Structurally this flinty material resembles the opaque-white fracture-fill. It forms both bands, usually parallel to minor faults, up to 10 mm in width and also fracture vein networks (Plate 3.c-e). The bands are roughly parallel sided and may have small off-shoots that extend a few millimetres into the host at a high angle to the boundary of the band (Plate 3.f). The macroscopic pattern of the fracture-veins is described in Section 7.3.3.

The boundaries between the host quartzite and this flinty fracture-fill are both diffuse (Plate 3.c-e; 7.a) and sharp (Plate 3.f; 7.b). In thin section, the material is pale brown in colour because of its

high phyllosilicate content (Plate 7.c). There has been localised
recrystallisation with rare, indistinct, elongate areas of the bands
developing a crystallographic preferred orientation. The phyllosilicate
content of such areas is always low. This material forms a matrix
around rounded or occasionally sub-angular fragments of both the parent
quartzite and the opaque-white fracture-fill (Plate 7.b). An anasta-
mosing network of thin ($<$ 0.1 mm), dark brown lines crossing the
bands of this flinty fracture-fill are opaque and appear to be entirely
composed of phyllosilicates. They are usually sub-parallel to the
margins of the band they cross.

Although recrystallisation is rare in the fracture-vein network
it occurs in phyllosilicate-free regions where the veins as a result
have indistinct boundaries. It is more common for the fractures to
be sharp and show offsets of up to 0.5 mm in the plane of the section
(Plate 7.d). These fractures contain small rounded quartz fragments
in an ultra-fine matrix (with most grains $<$ 0.1 mm in diameter).
This small grain size makes the grain-to-grain structure within the
veins impossible to determine optically, although it appears to be
cataclastic in nature.

The greenish-black bands and fracture-veins cross-cut the opaque-
white fracture-fill in all samples studied. In places they partially
surround fine grained opaque-white areas which have not been completely
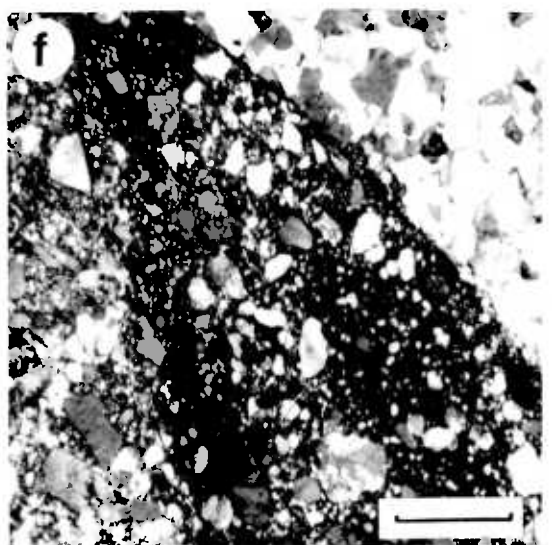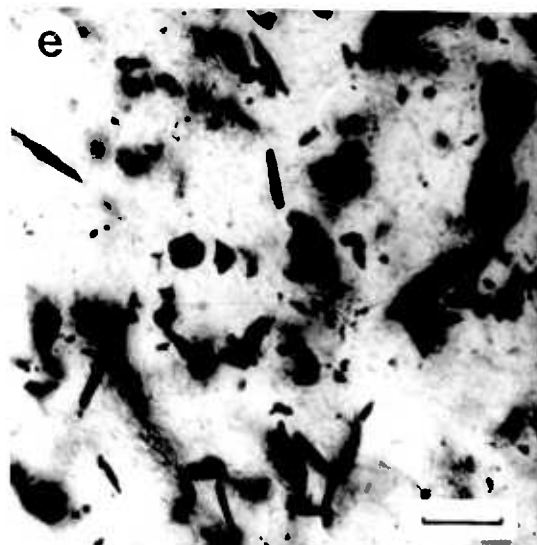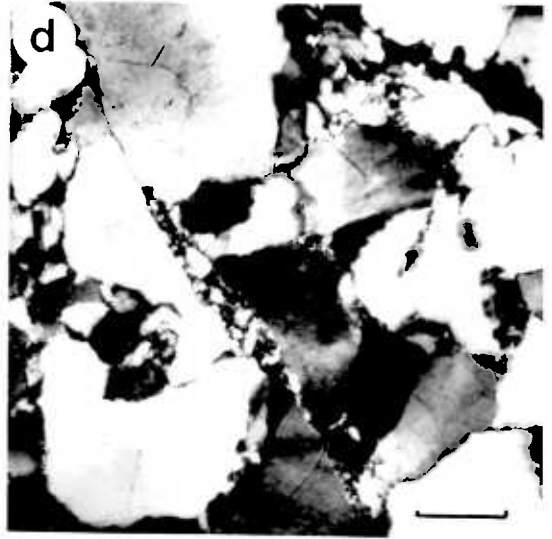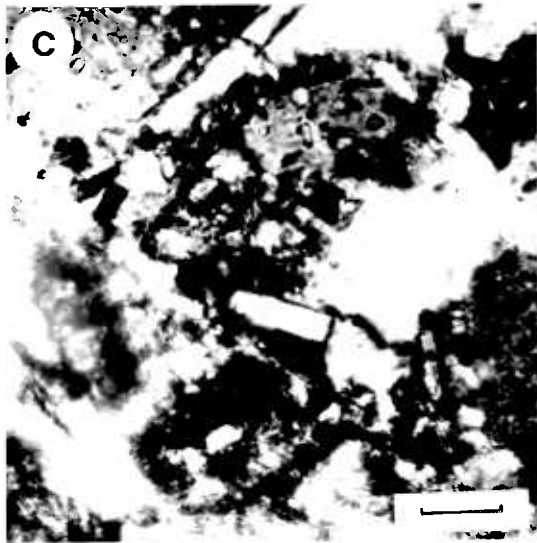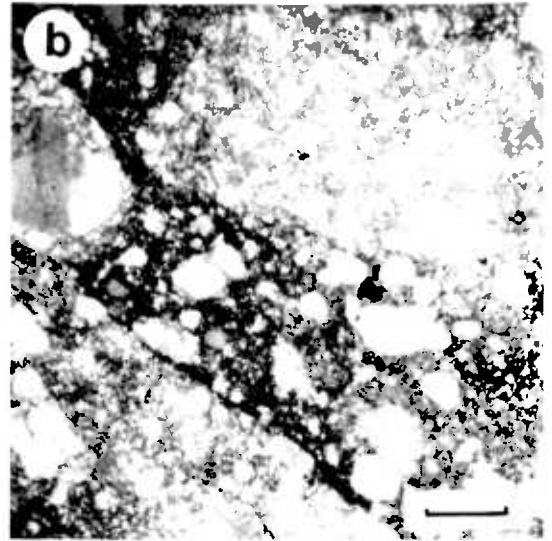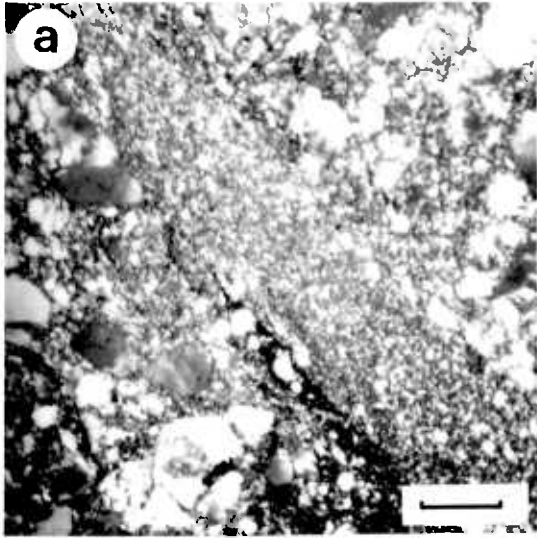detached from the band they belong to.

8.4.2.4. Black Fracture-fill

These veins are easily distinguished from the host quartzite but
may be confused with the greenish-black fracture-fill that they
frequently cut. This material forms sharp sided bands between 0.5 and
5 mm in width which are black and opaque. Offshoots at a high angle
to the main band, which extend for a few millimetres into the parent
quartzite before pinching out, are common (Fig. 8.4).

These bands contain many small haematite crystals (Plate 7.e) and
are only seen in and adjacent to haematite-rich layers of the Pipe
Rock. The wider bands contain rounded fragments of both other types
of fracture-fill, with occasional fragments of the host quartzite
(Plate 7.f). Shear displacements across the fracture-veins are not
visible and there has been no recrystallisation of the fragments or
fine grained matrix within the veins.

Plate 7

a   Band of greenish-black fracture-fill with a crystallographic preferred orientation. This region has diffuse boundaries. Scale bar = 0.4 mm.

b   Sharp boundary to a band of greenish-black fracture-fill. This band contains rounded fragments of the opaque-white fracture-fill. Scale bar = 0.4 mm.

c   High phyllosilicate content of greenish-black fracture-fill. Scale bar = 60 μm.

d   Sharp-sided, barren segment of a greenish-black fracture-vein. Scale bar = 1 mm.

e   Haematite crystals within the opaque-black fracture-fill. Scale bar = 60 μm.

f   Opaque-black band (centre) cutting parent quartzite and greenish-black fracture-fill. Scale bar = 1 mm.

transluscent host quartzite

sharp but undulating boundary

greenish-black fracture-fill

indistinct boundary

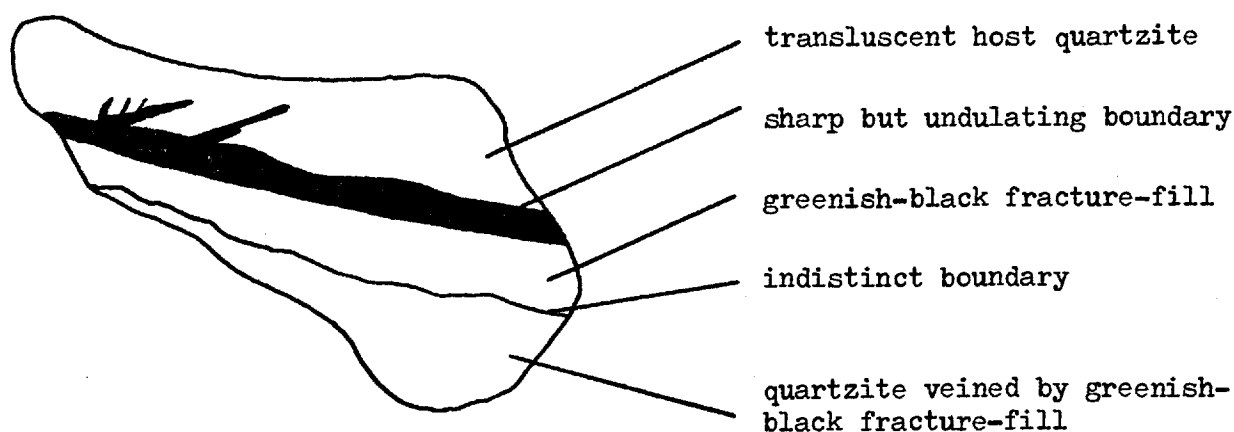quartzite veined by greenish-black fracture-fill

Fig. 8.4. Structure of the opaque-black fault rock.

These bands have a purely cataclastic texture and appear to have formed at shallow crustal levels where quartz behaved in a wholly brittle manner. They are later than the other two types of fracture-vein which they cross-cut. Their counterpart in non-haematite rich layers is unknown.

8.4.3. High Voltage Electron Microscopy

During sample preparation, up to 10 hours of thinning were required for foils of the parent quartzite and the opaque-white fracture-fill. The thinning rate was related to the phyllosilicate content and the greenish-black fracture-fill took between 25 and 30 hours to be thinned sufficiently.

8.4.3.1. Undeformed Quartzite

Away from any fracture-veins, the quartz grains within the Pipe Rock have well developed sub-grains which are commonly but not always elongate (Plate 8.a). In this region a sub-grain in sub-grain structure is fairly common (White, 1973). That is, the sub-grains visible with the electron microscope have a smaller size than those visible optically and occur in groups within which the sub-grain misorientation is low.

It is these groups of sub-grains, between which there is a higher misorientation, that are visible with the optical microscope. Elsewhere, sub-grains with low misorientations contribute to the optically visible

undulatory extinction.

Bubbles are rarely present on sub-grain walls but small inclusions are common within the grains. These latter features are thought to be a second phase and appear as strain centres or prismatic dislocation loops. The unbound dislocation density is variable, especially in the elongate sub-grains where, in occasional sub-grains, the dislocation density is too high for individual dislocations to be clearly resolved ($>10^{13-14}$ m^{-2}). Elsewhere the dislocation density is generally high (about 9×10^{11} m^{-2}). Many of the unbound dislocations are bowed and may be pinned by inclusions within the crystal (Plate 8.a).

Within the parent quartzite are localised areas where a cellular structure has developed (Plate 8.b). The unbound dislocation density in these cells is generally high (about 4×10^{12} m^{-2}) which makes individual dislocations difficult to resolve. The cells are roughly equidimensional with diameters similar to the sub-grain width (4-8 μm) and walls consisting of tangles of dislocations. These cellular areas are most common adjacent to the fine grained fracture-veins.

The development of a sub-grain structure, along with the existence of dislocation walls and loops indicates that in these regions recovery has occurred. In contrast, there has been very little recovery in the cellular areas. Here the dislocations are difficult to image and, where their density is high, they are tangled (Plate 8.c). In these areas the microstructure is similar to that resulting from cold-working of metals (Section 8.4.4.).

8.4.3.2. Opaque-white Fracture-fill

Under the electron microscope, recrystallised grains are easily resolved. Usually they are roughly equidimensional (Plate 8.d), but some elongate crystals occur. Their diameter varies between 1 and 8 μm with an average of about 4 μm (from 56 measured grains). Grain boundaries are straight and commonly meet at 120° triple junctions. Small, new, strain-free grains often occur at the triple junctions.

The recrystallised grains contain unbound dislocations and occasional simple dislocation walls (Plates 8.e,f). These are usually of the picket-fence type and are only seen in the larger crystals. The unbound dislocation density of the new grains is variable. The smallest grains are probably also the newest. Many of these are practically unstrained with low dislocation densities ($<10^{11}$ m^{-2}).

124

Plate 8

a   Elongate sub-grain in quartz from the parent Pipe Rock. Note
     prismatic dislocation loops, pinned and bowed dislocations and
     "picket-fence" type sub-grain walls. Scale bar = 1 μm.

b   Cellular structure in quartz adjacent to opaque-white bands of
     fracture-fill. Note the indistinct margins of most cells. Scale
     bar = 1 μm.

c   Dislocation structure within the cellular areas of 86.
     Scale bar = 1 μm.   /

d   Equidimensional quartz grains that make up the opaque-white
     fracture-fill. These are relatively unstrained and have low dis-
     location densities. Scale bar = 1 μm.

e   Rare chlorite crystals within the opaque-white fracture-fill. These
     are both on and parallel to the grain boundaries. Scale bar = 1 μm.

f   Recrystallised quartz grains within the opaque-white fracture-fill
     containing several "picket-fence" type walls of dislocations.
     Scale bar = 0.5 μm.
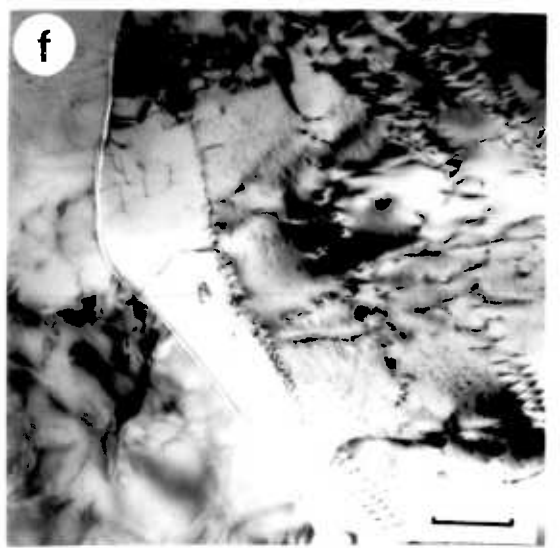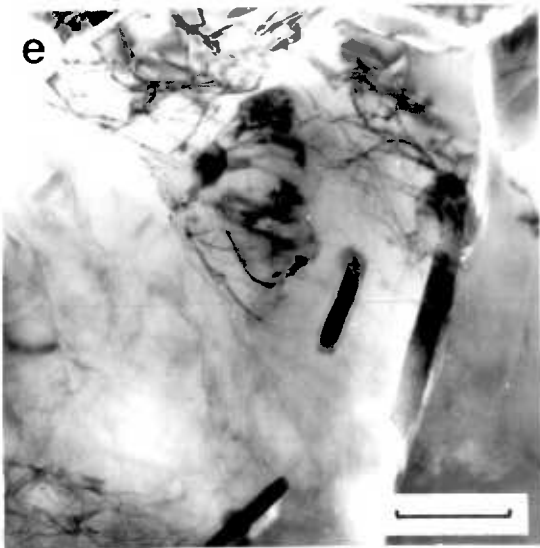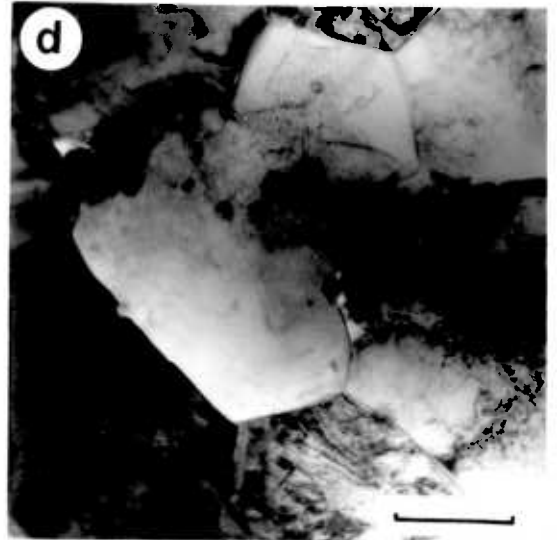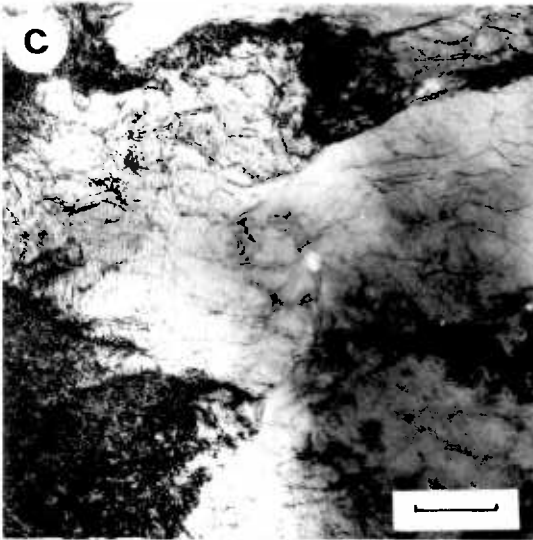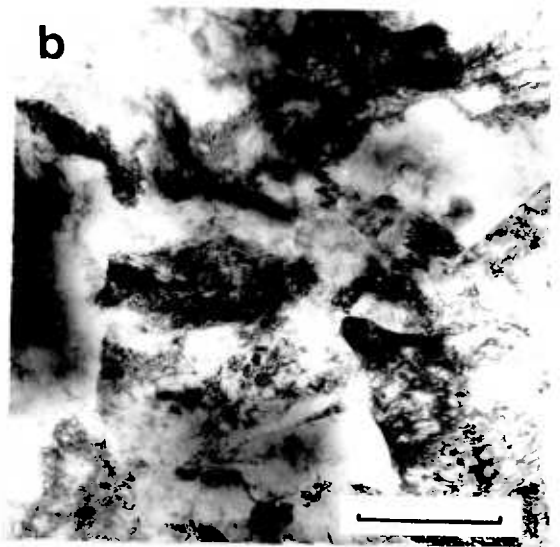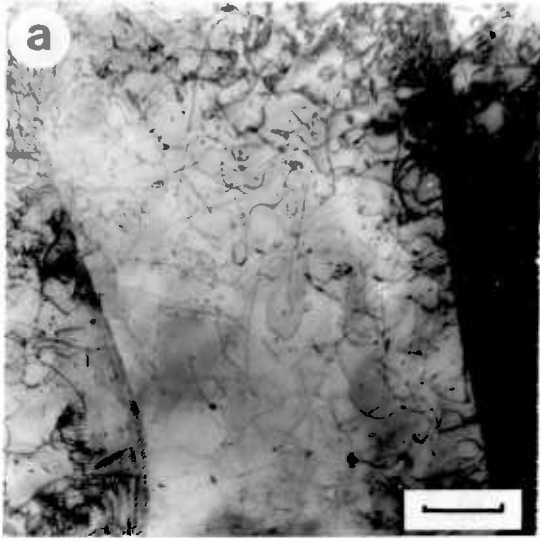
The larger grains have variable densities (10^{11} - 2 x 10^{12} m^{-2}) which are generally lower than those recorded in the cellular areas of the host quartzite (Section 8.4.3.1).

Some grain boundaries contain phyllosilicate crystals which also, more rarely, occur within the grains where they lie parallel to the crystal boundaries (Plate 8.e). The phyllosilicates are new and usually small ($\leqslant$ 3 µm in length). Diffraction patterns show that there are two types of phyllosilicate, chlorite and mica, which are morphologically identical. The mica shown by STEM "finger-printing" to be muscovite, may be dominant over chlorite in these bands.

In the larger recrystallised grains, very small crystal nuclei are seen (Plate 9.a). They resemble those seen in the Pipe Rock at a similar structural level 3 km to the east, which have been identified as chlorite by STEM analysis (White, 1979, pers. comm.). Their size varies from less than 0.1 µm to 0.5 µm.

The junction between the original quartzite grains and the fracture-veins is diffuse and occurs over a distance of 5-50 µm. In this strip there is a transition from quartz with a dominant sub-grain structure through to a dominant cellular structure at the fracture vein margins. As the recrystallised quartz of the fracture-veins is approached, new grains appear in the cellular areas. It is not clear whether these develop from the growth of small strain-free nuclei or from the progressive rotation of the cells. There is a rapid increase in the number of new grains with sharp, straight grain boundaries over a distance of a few microns into the fracture-veins.

8.4.3.3. Greenish-black Fracture-fill

There are three distinct microstructures within these bands each of which can be distinguished optically: the areas with crystallographic preferred orientation, the common "dirty" areas, and the narrow phyllo-silicate bands which cross the other two types.

(i) Areas with a crystallographic preferred orientation

Microstructurally, the areas with a crystallographic preferred orientation are very similar to the opaque-white fracture-fill (Plate 9.b). There has been complete recrystallisation but they have higher phyllosilicate content and smaller average grain diameter (about 3 µm). Again, the smaller crystals have a lower dislocation density than the larger ones and phyllosilicate crystals are most commonly seen on the

Plate 9

a   Small crystalline nuclei within the larger recrystallised quartz
    grains of the opaque-white fracture-fill. Scale bar = 1 μm.

b   Recrystallised area within a region of the greenish-black fracture-
    fill showing crystallographic preferred orientation. Chlorite and
    muscovite are common on grain boundaries. Scale bar = 1 μm.

c   More common cataclastic texture within the greenish-black fracture-
    fill. Scale bar = 1 μm.

d   Cataclastic parts of the greenish-black fracture-fill commonly con-
    tain small equidimensional crystals of albite and chlorite.
    Scale bar = 1 μm.

e   Phyllosilicate-rich layers within the greenish-black fracture-fill
    contain clay minerals and small epidote crystals. Scale bar = 1 μm.

· f Within the phyllosilicate-rich layers of the greenish-black fracture-
    fill the small epidote crystals are invariably equidimensional and
    have a good crystalline outline. Scale bar = 0.5 μm.
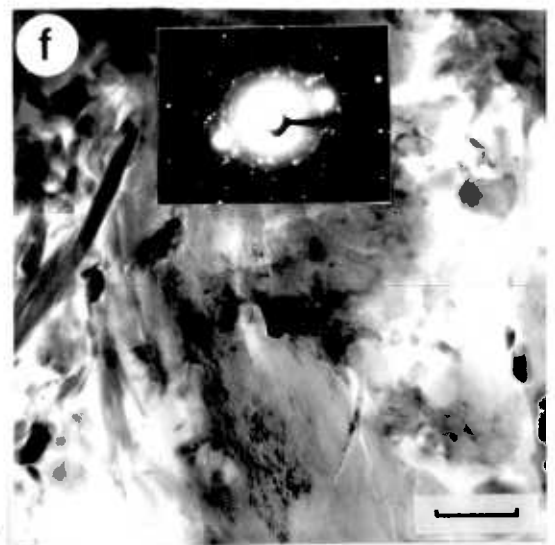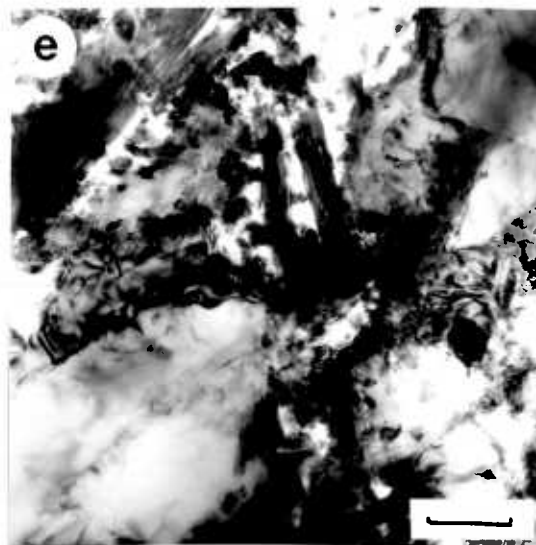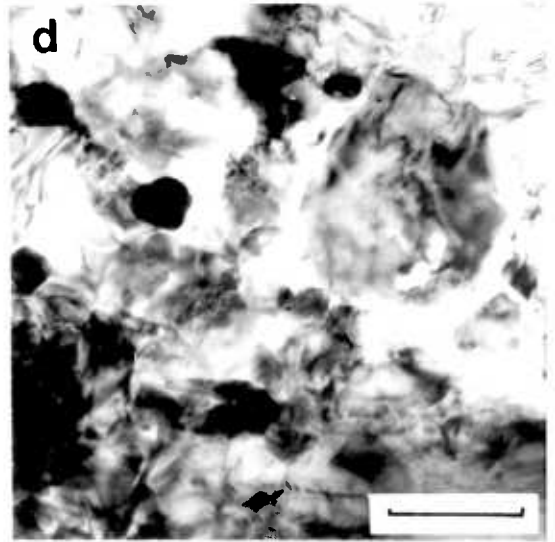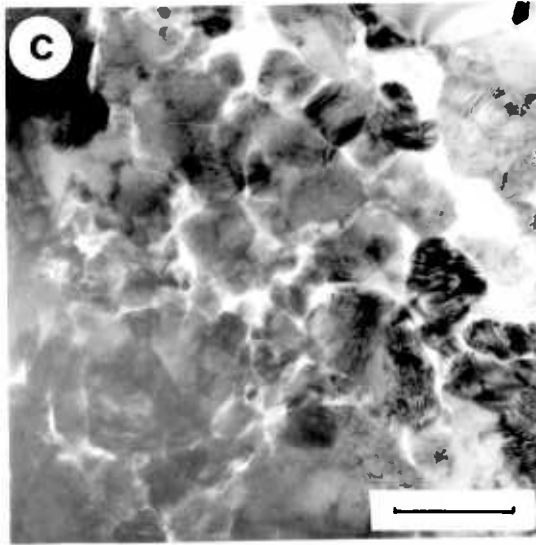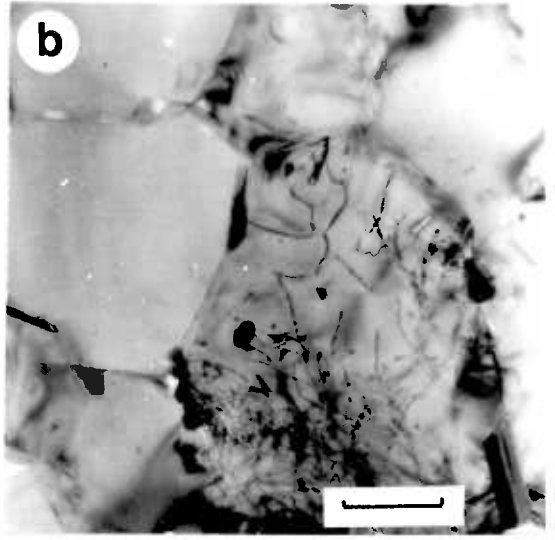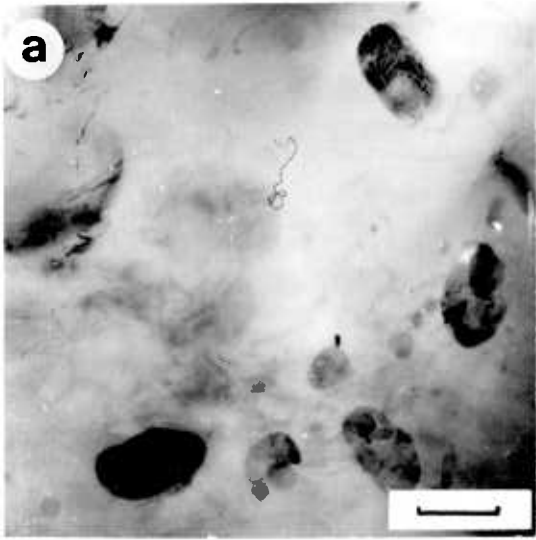
grain boundaries although they occasionally occur within the crystals.

(ii) "Dirty" areas

The bulk of these fracture-veins, which are pale-brown in colour optically, have a cataclastic texture. Occasional rounded quartz fragments are surrounded by a matrix of much smaller grains. The size of these fragments varies but they are rarely larger than 6 μm in diameter. The dislocation sub-structure is similar to that in the original quartzite. They contain both unbound dislocations (with a density of about 9×10^{11} m^{-2}) and occasional dislocation walls.

The matrix grain size is commonly between 0.2 and 1 μm (Plate 9.c,d). Most of the grains are equidimensional but their shape varies. The larger grains appear to be old, often contain dislocations and are invariably rounded (Plate 9.c). The misorientation between adjacent grains is large. In contrast, the small grains often possess crystalline faces and may be new. They are strain free and have been identified as albite, muscovite and chlorite (Plate 9.d). The chlorite may be partly responsible for the dark optical colour.

(iii) Thin phyllosilicate rich bands

These bands have a cataclastic texture but contain a high percentage of clay minerals (Plate 9.e,f). There are no large fragments in these bands, where the average grain size is less than 0.5 μm. They consist almost entirely of clay minerals (perhaps the product of late alteration) and epidote. The epidote crystals invariably show well developed crystal faces but have random crystallographic orientation. From the experimental work of Rutter and White (1979), crystal faces in such zones may indicate that pressure solution has been concentrated in these narrow bands.

8.4.4. Microstructural Summary and Metamorphic Environment of Faulting

The three sets of fractures described above, that occur adjacent to the faults studied, show consistent cross-cutting relationships which indicate that there have been at least 3 episodes of side wall fracturing. These are thought to be related to 3 distinct episodes of movement across the faults themselves.

Both the opaque-white and the greenish-black fracture-fill contain features which indicate that their origin cannot be directly attributed to cataclasis adjacent to a slipping fault. In the opaque white fracture-fill the following features are inconsistent with a

cataclastic origin; the variation of the width and character of the
fracture veins along their length, the small misorientations between
adjacent grains, the unchanged mineralogy between the host quartzite
and opaque-white fracture-fill, and the relationship between internal
deformation features (deformation bands) in some host quartz crystals
and the fracture veins (Section 8.4.2.2).

From the optical evidence it appears that strain was concentrated
in the fracture-veins. If movement across the listric faults occurred
at levels where a certain amount of dislocation glide could take place
but where environmental conditions did not allow recovery processes
involving the climb of dislocations, then high dislocation densities
could have developed in the rocks adjacent to the fault. With little
recovery taking place, large grain misorientations would result and could
have led to the formation of strain-free nuclei (White, 1976a). In
areas where the strain could not be accommodated by dislocation controlled
flow, brittle failure occurred and led to the formation of a single
fracture. All of the optically observed features listed above can be
explained with this model. If it is correct, the opaque-white fracture-
fill formed primarily by solid-state dislocation controlled flow near
the brittle-ductile (intracrystalline-plastic) transition.

Under the high voltage electron microscope, the opaque-white
fracture-fill appears, microstructurally, almost identical to a mylonite
from the same region described by White (1979b). The boundary
between the host quartzite and the opaque-white bands is gradational
over a width of between 5 and 50 μm. In this transition zone, the
microstructure changes from the well developed sub-grain structure
of the Pipe Rock, through a cellular region into the equant, recrystallised
grains of the opaque-white fracture-fill.

The existence of this cellular region is important because,
when compared to the microstructures observed in metals, it closely
resembles the structure produced by warm-working. In materials
science, cold-working refers to low temperature (<0.3 Tm, melting
temperature), high strain rate deformation. The resulting micro-
structure is one of cells containing a high dislocation density and
with indistinct boundaries made up of tangles of dislocations (Nutting,
1974). Hot working, or creep, occurs at higher temperatures (>0.5 Tm)
and produces a characteristic dislocation structure with dislocation
walls, sub-grains and, eventually, recrystallisation at high strains

(Nicolas and Poirier, 1976).

At intermediate temperatures, warm-working may produce a mixture of the two microstructures with co-existing cells and sub-grains. By analogy with the microstructures produced in metals, the dominantly cellular areas of the host quartzite appear to have undergone a type of warm-working which has modified the original sub-grain structure that resulted from an earlier deformation episode.

The temperatures and strain rate appropriate for the warm-working of quartzite are hard to estimate. In general, hot-working, or creep, results from deformation at greenschist and greater metamorphic grades when temperatures are sufficient to allow dislocation climb ($>250^{\circ}$-$300^{\circ}C$). Cold-working will occur at supra-metamorphic crustal levels (White, 1976b). Warm-working would be expected between these two levels.

The cellular areas of the host quartzite appear to be the regions in which strain has been concentrated. It seems likely that the opaque-white fracture-fill resulted from strain induced recrystallisation of the parts of these areas that underwent most strain. The mechanism of recrystallisation has not been determined but could be by the development and growth of strain-free nuclei, or by the progressive rotation of the cellular areas, or by some combination of both mechanisms.

Thus, the coexistence of the cellular and sub-grain microstructures associated with the opaque-white fracture-fill suggests that the observed deformation occurred in a warm-working environment slightly deeper than lower greenschist metamorphic conditions. The microstructure developed by solid-state processes with subsequent grain growth.

The mineralogy of this material (quartz, chlorite and muscovite) is consistent with deformation in a closed system. No material needed to be added or subtracted from the zone since the breakdown of the alkali-feldspar would have been sufficient to provide material for the growth of the phyllosilicates.

In contrast, the other two fracture-vein types both have essentially cataclastic textures, although localised regions of the greenish-black fracture-fill closely resemble the opaque-white fracture-fill described above. These rock-types consist of a fine grained matrix surrounding rounded fragments of the host quartzite and the products of earlier deformation episodes. In both, the matrix fragments are

Fracture-fill	Mineral Assemblage	Microstructural Features	Depth of Formation
Black, opaque	Quartz, haematite, muscovite, chlorite.	Purely cataclastic resulting from a cold-working type deformation.	Above lower greenschist metamorphic conditions.
Greenish-black	Quartz, muscovite, chlorite, albite, epidote.	Essentially cataclastic with localised regions exhibiting a warm-working type microstructure (see below)	At lower greenschist metamorphic conditions.
Opaque-white	Quartz, muscovite, chlorite.	Warm-working type microstructure consisting of recrystallised grains adjacent to regions of the parent quartzite with a dominantly cellular microstructure.	Marginally below lower greenschist metamorphic conditions.

Fig. 8.5. Mineralogical and microstructural summary of the 3 fault rock types in the Loch Eribol region.

between 0.2 and 1 μm in diameter with shapes varying from rounded to sub-angular. The boundary between these fracture-veins and the host is generally sharp with no modification of the sub-grain structure of the parent as the fracture veins are approached.

The greenish-black fracture veins and bands formed at higher crustal levels than the earlier opaque-white fracture-fill. However, the existence of the small recrystallised patches indicates that the difference in levels was not great. The overall microstructure of the greenish-black fracture-fill is cataclastic with very little evidence for dislocation controlled deformation. Deformation has been primarily by brittle fracture followed by rotation and attrition of the fragments. The growth of albite, epidote, chlorite and muscovite in these bands, which appears to be contemporaneous with the deformation, pins the crustal level at lower greenschist conditions. This is marginally shallower than the depths at which the oldest deformation is thought to have occurred.

The textures within the narrow phyllosilicate-rich layers inside the bands of the greenish-black fracture-fill are thought to have resulted from pressure solution accompanying cataclasis. If this is so, these bands developed in an open chemical system in the presence of fluids, which must have been restricted to the cataclastic zones since the parent quartzite is unaltered. In the black-opaque bands, haematite crystals are present in the cataclastic bands within pure quartzite but only within a few 10's of metres of an impure band. This may indicate that the passage of fluids through the fracture zones was not extensive and it is concluded that fluid flow was localised.

The microstructures and mineralogy of these zones are consistent with a history of deformation where the older fracture-veins developed at deeper crustal levels than the later ones. This is consistent with the progressive uplift and unroofing of the fault, as a consequence of reverse shear across the entire zone. The sequence of structural events in the Moine Thrust zone in this region has not yet been fully established although Soper and Wilkinson (1975) have proposed a provisional scheme. It is likely that the listric thrusts are con-temporaneous with the imbrication of the Heilem nappe, a D_4 event dated at about 430 Ma (van Breemen et al., 1979). Indeed, it is possible that the progressive decrease in depth indicated for the deformation associated with these faults may have occurred during the passage

of the nappe over a large ramp. Interpretations of this kind cannot
be based on a study of small scale features and must await fuller
large scale field studies.

8.5. Comparison of the Fault Rocks from the Shetland Islands and Loch Eribol

The two fault zones studied differ in many features, but the
majority of these differences may be explained by the contrasting
rock types that were faulted and the dissimilar environmental con-
ditions under which the shear displacements and associated rock
deformation occurred. In addition, the displacement across the trans-
current Walls Boundary Fault (60-80 km, Flinn, 1969) is several orders
of magnitude greater than the displacement estimated for each thrust
at Loch Eribol (200-400 m).

The Walls Boundary Fault zone (Shetland Islands) is complex and up to
3 km in width. Within this zone a series of minor faults lie sub-
parallel to the Walls Boundary Fault and there is widespread fracturing
of the country rock on a variety of scales. It is not generally poss-
ible to pick out sets of fractures with consistent age relations. Most
of the shear displacement across the fault zone was accommodated by
slip on the faults and perhaps at greater depths by pervasive cata-
clastic flow of the cataclasites immediately adjacent to them.

In contrast, the deformation of the rock adjacent to the faults
at Loch Eribol is localised, rarely extending beyond 0.3 m. In each
case the deformation can be related to an individual fault, either
major or minor. Again, most of the shear displacement across the zone
was accommodated on the faults and, to a small extent, by cataclastic
flow within the narrow (< 10 mm) bands of cataclasite found adjacent to
them. In these fault zones, 3 distinct sets of fractures can be iden-
tified throughout the region. Each is related to deformation under
progressively shallower depths and each set of fractures is likely to
represent an episode of deformation rather than a single slip increment
across the fault. In this region, the first recognised episode of
deformation associated with the faulting occurred marginally below
lower greenschist metamorphic conditions, the second at lower
greenschist conditions and the third may have been marginally
shallower (Fig. 8.5).

These depth estimates are based upon mineral assemblage and the

microscopic texture of the fault rock. At Loch Eribol this estimation
is relatively easy since the country rock is a fairly pure quartzite
and the rocks have not been deeply weathered.

The fault zone in the Shetland Islands is not such a simple
system. The country rock varies along strike and weathering of the fault
zone is deep. There are many open fractures which weaken the country
rock and the growth of new phases in the fault rocks do not give enough
information to determine the precise depth at which the cataclasites
were generated. The coexistence of fractured analcime and quartz in
the fault plane ultracataclasite indicates that, although it is now at
the surface, it was produced at depths not greater than 6-7 km. This
is somewhat shallower than the depths at which the Loch Eribol fault
rocks developed, if the two areas are assumed to have had similar
geothermal gradients.

The restriction of analcime to the fault plane ultracataclasite
of the Walls Boundary Fault and some minor faults suggests that the
circulation of hydrothermal fluids was restricted to channel flow along
the faults. The subsequent cataclasis of the analcime indicates that
fluids were circulating at an intermediate stage in the deformation
history of the faults. Indeed the fact it forms porphyroclasts and
matrix fragments and rare euhedral crystals strongly indicates that
it was deposited in several stages separated by slip events.

Although mass balancing calculations were not made because of the
fine matrix grain size it is unlikely that sufficient sodium was
available in the parent granite for the growth of analcime. In addition,
the rocks on all the faults are haematite stained. These factors almost
certainly indicate an open chemical system with the possibility of
material derived from the nearby Old Red Sandstone units having been
added to the fault zone. In contrast, the fault rocks at Loch Eribol
have had little or no material added or subtracted, though there is
evidence for some localised transportation of haematite.

CHAPTER 9

EXPERIMENTAL THERMAL FRACTURING OF GRANITE

9.1. Introduction

A series of experiments were devised to assess the degree of thermal damage resulting from the dissipation of frictional heat, without the effects of shearing. A fault was modelled by two blocks of rock, sandwiched across a flat electrical element through which energy, equivalent to that associated with seismic shear on a fault, could be dissipated as heat.

Theoretical considerations (Chapter 5), were related to natural faulting where the rock adjacent to the fault plane extends to infinity in both directions. In the majority of these experiments the fault is modelled by two granite cylinders 38 mm in diameter and 40 mm in length. The thermal relaxation time (Shimazu, 1961) for a slab with thickness, l, equal to the samples used in the experiments and with a thermal diffusivity, $k = 1.5 \times 10^{-6}$ $m^2 s^{-1}$ is given by:

$$tr = \frac{l^2}{k} = 1067 \text{ sec} \qquad (9.1)$$

During the heating pulse, samples of these dimensions will, therefore, behave thermally as semi-infinite solids since the thermal relaxation time is two orders of magnitude greater than the duration of each heating episode.

9.2. Apparatus and Sample Configuration

The apparatus and sample configuration (Fig. 9.1) falls into four sections; sample assembly, uniaxial rig, power supply and recording apparatus. Pairs of sample blocks were held under uniaxial pressure across the element. The normal stress on this plane, the energy supplied to the element and the duration of the energy pulse could all be varied independently.

9.2.1. Sample Preparation and Assembly

Two sample geometries were used: right circular cylinders (of diameter 38 and 54 mm and length 40 mm) and cuboid blocks of varying sizes. Each sample pair was cut and ground until opposed faces were parallel to within 0.5°. The two faces to be held against the element were ground
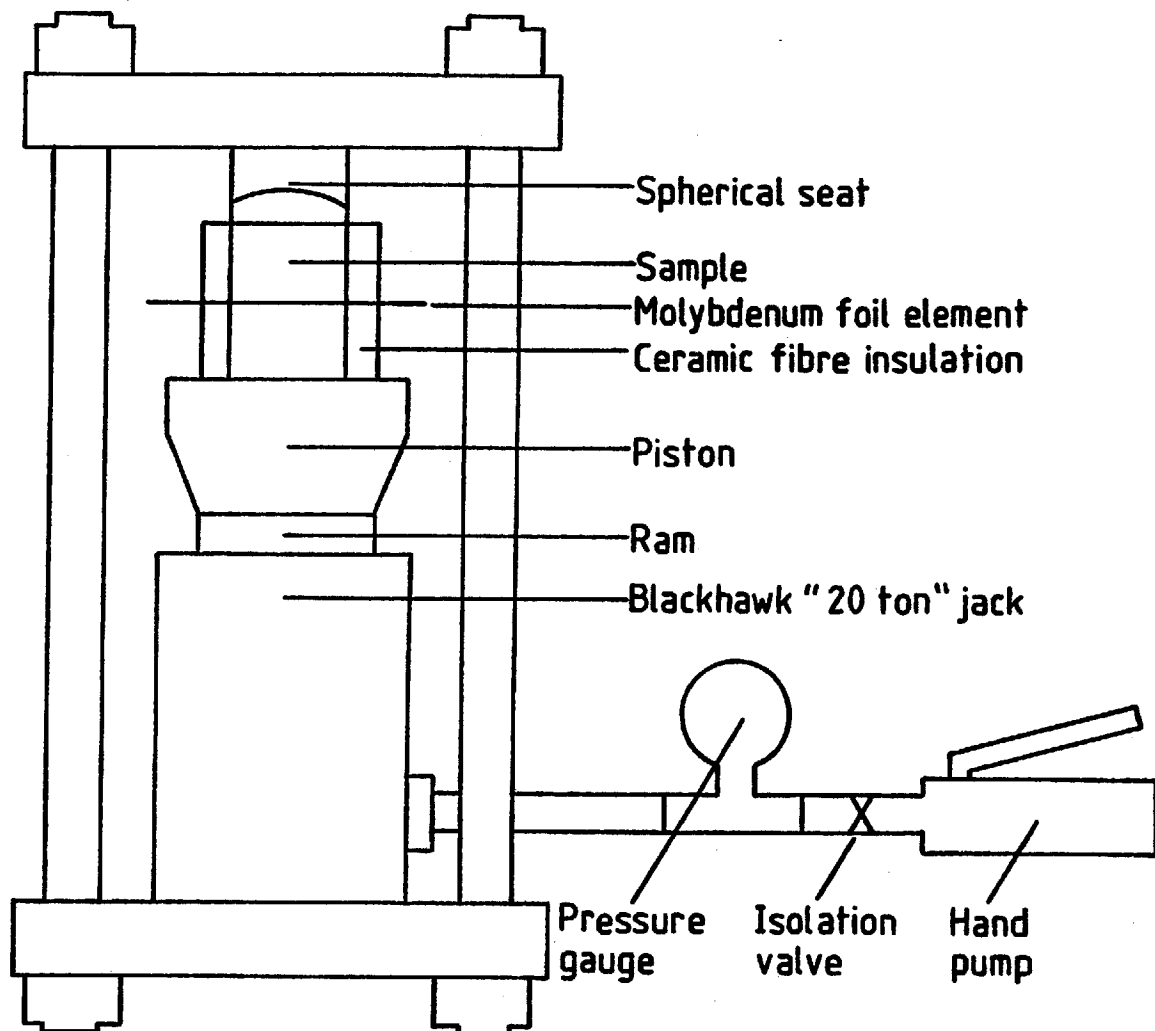
Fig. 9.1. Apparatus used in heating experiments

with progressively finer carborundum powder down to $\#$ 600 , to ensure uniform and constant contact area with the element in each experiment. In ten of the samples, two narrow grooves were cut in these ground surfaces to accommodate platinum / 13% platinum-rhodium thermocouples.

In each experiment the element (Fig. 9.2) was a molybdenum foil strip 0.1016 mm thick. The tapering of the width of the strip ensured approximately uniform heat dissipation over the central portion. The

-10
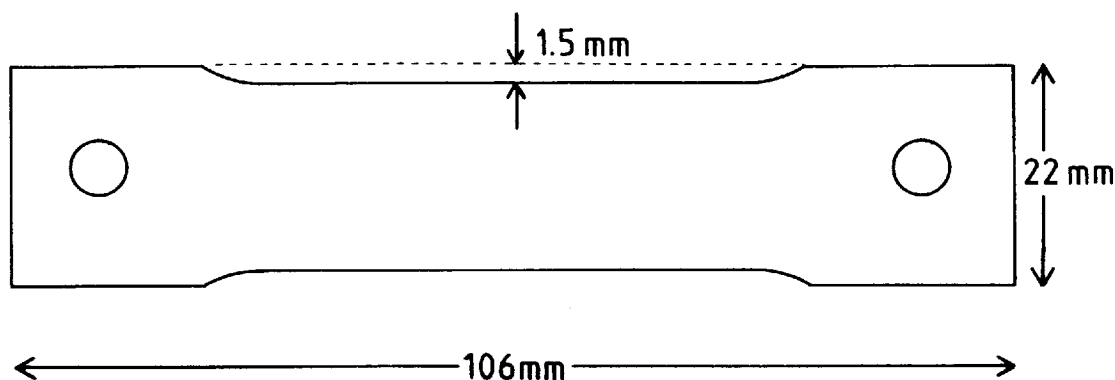
Fig. 9.2. Shape of element used in heating experiments.

ends of the element were clamped in brass blocks through which connections to the copper bars supplying current from the power supply were made.

Before assembly, ceramic fibre insulation was secured laterally around each sample to reduce heat loss from the sample sides. The insulated, paired blocks were assembled across the element with "end-pieces" of the same granite covering the element to each side of the sample (Fig. 9.3.). These were used to reduce the oxidation of the molybdenum during heating. If oxidation was severe this led to both element breakage and variation in electrical resistance along its length.

9.2.2. Uniaxial Rig

The uniaxial rig consisted of a "20 ton" Blackhawk jack in a uniaxial frame (Fig. 9.1). The sample was loaded through a spherical seat via an oil filled hand pump. Pressure in the loading line was measured on a Budenburg "16,000 psi" gauge. This rig has very low stiffness.

9.2.3. Power Supply

The power dissipated in the heating assemblage during each cycle was controlled by a 3 kW Variac (auto-transformer) and could reach a
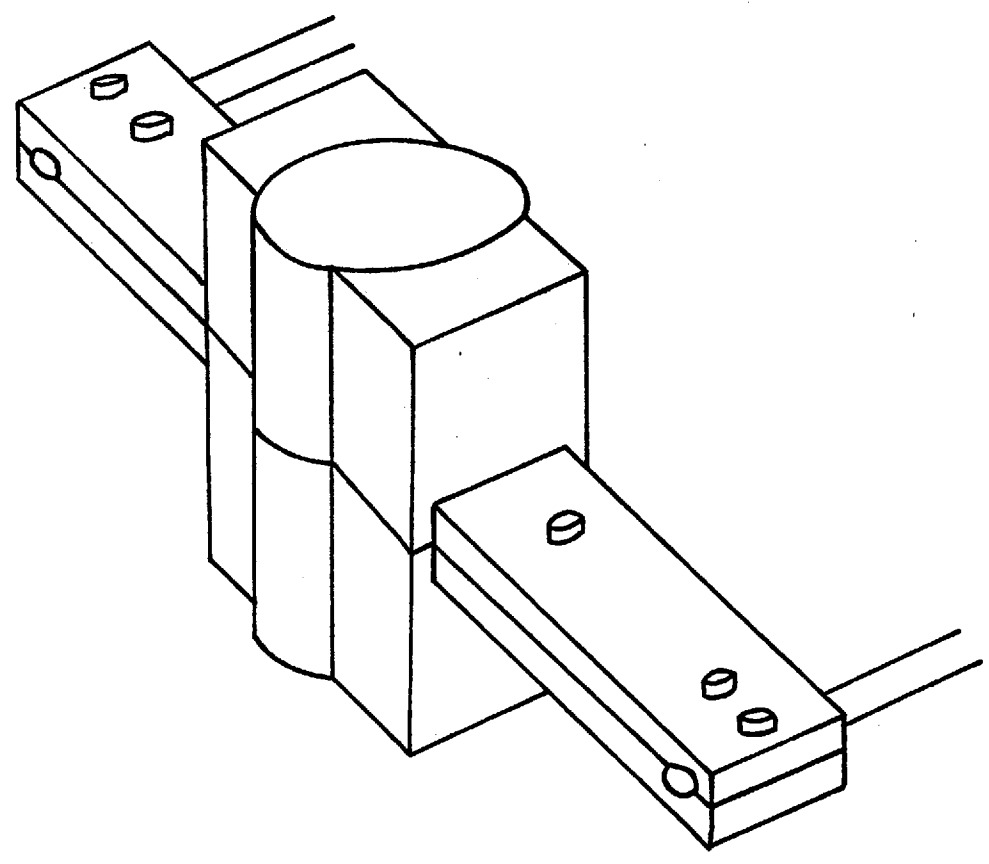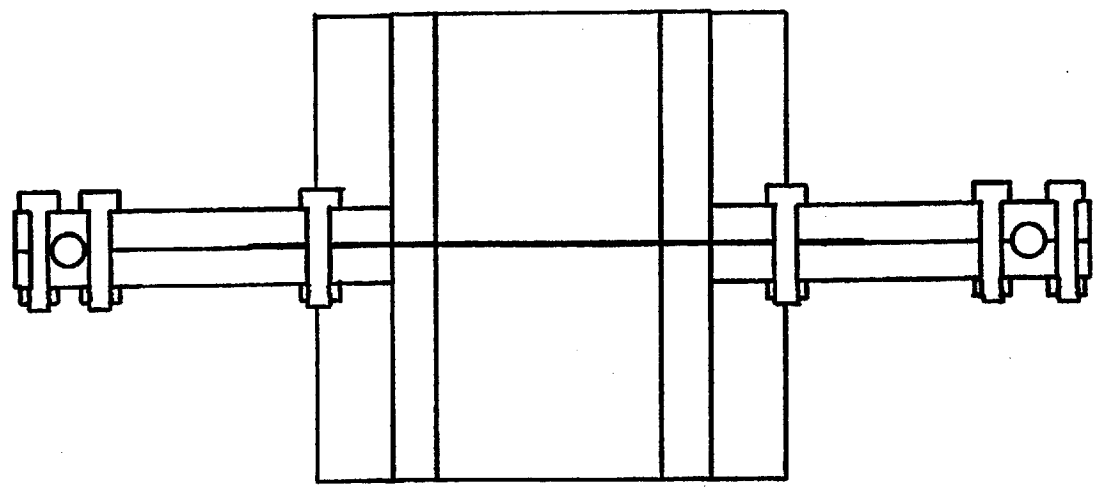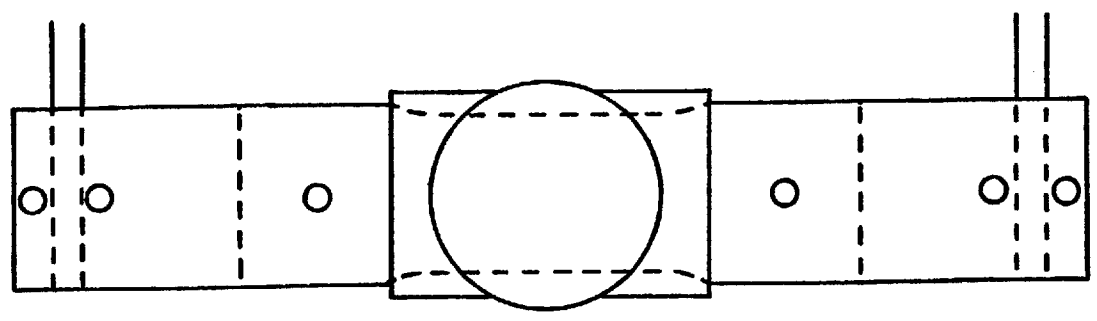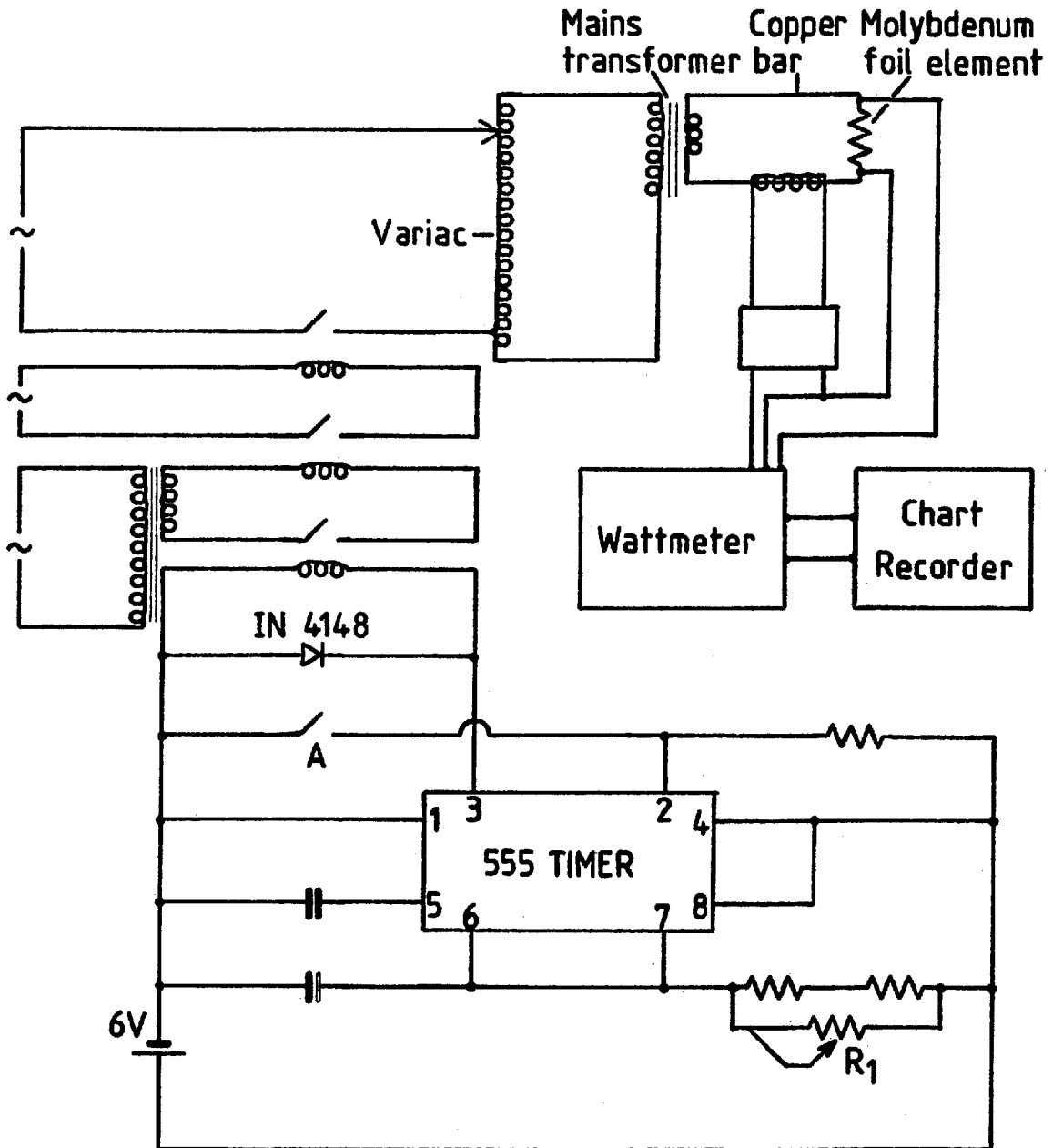
Fig. 9.3. Sample assembly

Fig. 9.4. Circuit diagram of power supply.

maximum of 1.14 MWm^{-2}. The length of timed pulse was controlled by
the potentiometer, R_1. The Variac and potentiometer were set before
the start of a heating cycle, each of which was triggered by closing
switch A in the timing circuit. Mains voltage was stepped down to
about 6 volts AC with a current of about 200 amps. To minimise power
loss, electrical connection between the transformer and heating element

were made through short (0.15 and 0.20 m) lengths of copper bar 9.5 mm in diameter and thick brass clamps.

9.2.4. Recording Apparatus

Two chart recorders were used to record data during each test. The power dissipated was measured by a Vaw meter (wattmeter). The voltage channel was connected across the element, via a current transformer which reduced the current measured by 50:1. The energy pulse was recorded on an Oxford Instruments Series 300 chart recorder, on which the time period and the shape and size of the energy pulse could be measured.

In ten experiments, platinum / 13% platinum-rhodium thermocouples were placed in grooves in the rock adjacent to the element and insulated electrically from it by a thin (less than 0.1 mm) mica flake. The cold junction of the thermocouple was at ambient temperature and the emf produced during each test was recorded on a Honeywell chart recorder. Both chart recorders used had been calibrated using standard cells and were accurate to within 1% in the range used. The Vaw meter and Variac were calibrated before use according to the procedure described in Appendix B.

9.3. Experimental Procedure

The time and size of the energy pulse were preset before each test. The two sample blocks were carefully aligned across the element and placed in the uniaxial rig and loaded to a few tenths of a MPa. The connections between the element and the heating circuit through the brass clamps were then made. This procedure minimised the risk of disturbing the sample alignment while the brass clamps were tightened. In all tests, the sample was loaded before the heating pulse and the pressure was maintained for 20 minutes after heating to allow cooling. The sample was then rapidly unloaded.

9.4. Tests Performed

Four series of experiments were performed to determine the effect of sample size and geometry, normal stress, quantity of energy dissipated and the number of heating cycles, on the overall deformation resulting from the heating pulses.

9.4.1. Sample Size and Geometry

Eleven tests were performed to assess the effect of sample size

and geometry. Five tests used cuboid samples (Table 9.1), and one
test used right circular cylinders 54 mm in diameter. The remaining
five tests were performed on right circular cylinders with diameter,
38 mm, and varying thicknesses (Fig. 9.5). The experimental conditions
for each test are given in Table 9.2.

9.4.2. Normal Stress

Thirteen tests investigated deformation resulting from constant
energy dissipation with the samples held at different normal stresses
(Tables 9.3 and 9.4). In these, and all subsequent tests, the samples
were right circular cylinders of a standard size (38 mm in diameter and
40 mm in thickness).

9.4.3. Power Dissipation

Six tests were performed at 40 MPa normal stress to determine the
effect of variation of the level of power dissipated (Tables 9.5 and
9.6). The shear resistance and slip velocity for earthquake faulting
modelled by these tests are shown in Fig. 9.6.

9.4.4. Thermal Cycling

The final series of tests, again performed at a normal stress
of 40 MPa, studied the effect of repeated thermal cycling. As a
result of the inevitable oxidation of the molybdenum element during
each cycle it was necessary to use power levels of around 0.8 MWm^{-2}.
Maximum power dissipation (around 1 MWm^{-2}) led to element breakage
after between 3 and 10 cycles. Each sample was kept under load through-
out each test and allowed to cool for 10 minutes between cycles.

9.5. Experimental Problems and Sources of Error

9.5.1. Sample Error

Errors resulting from the sample preparation were minimised but
not completely eliminated. As shown in Table 9.1 the cuboid sample
size varied considerably and the paired blocks were not parallel
sided but deviated up to 3° from it. This led to stress concentra-
tions within the samples and variation in load stresses for different
tests. Errors of this sort were considerably reduced in the cylindrical
samples for which preparation was easier.

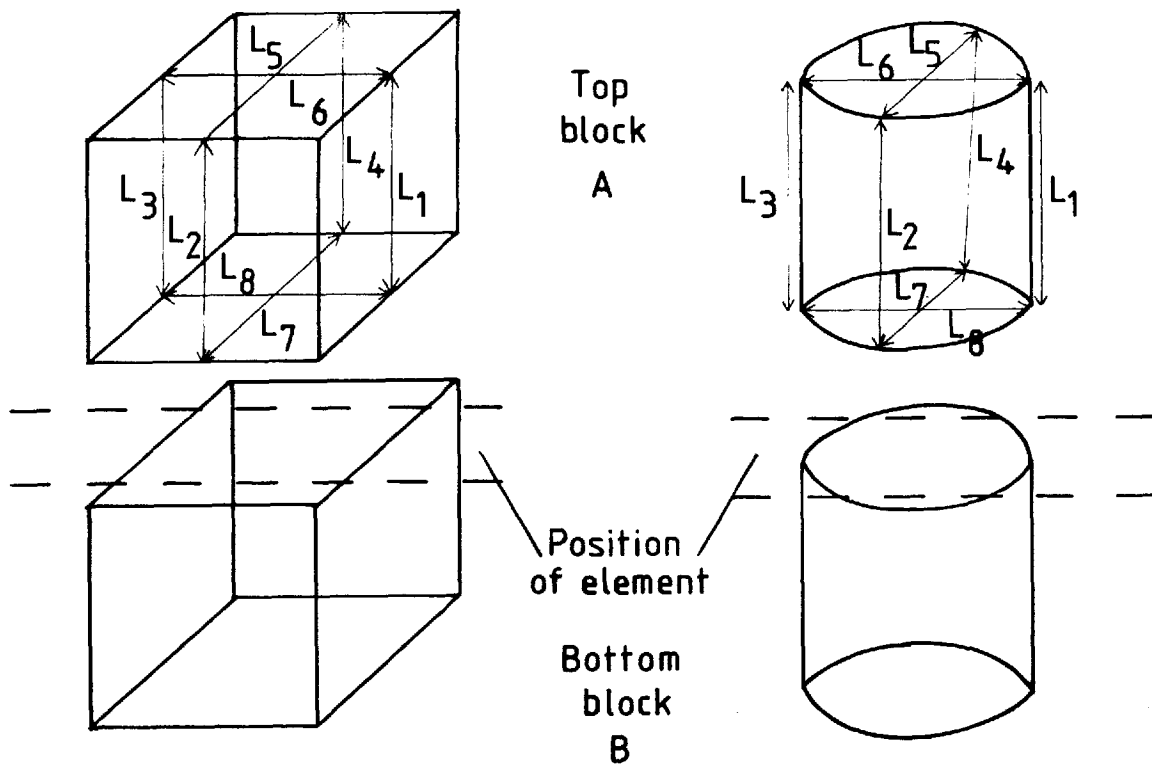The surface finish was constant for different samples, but the

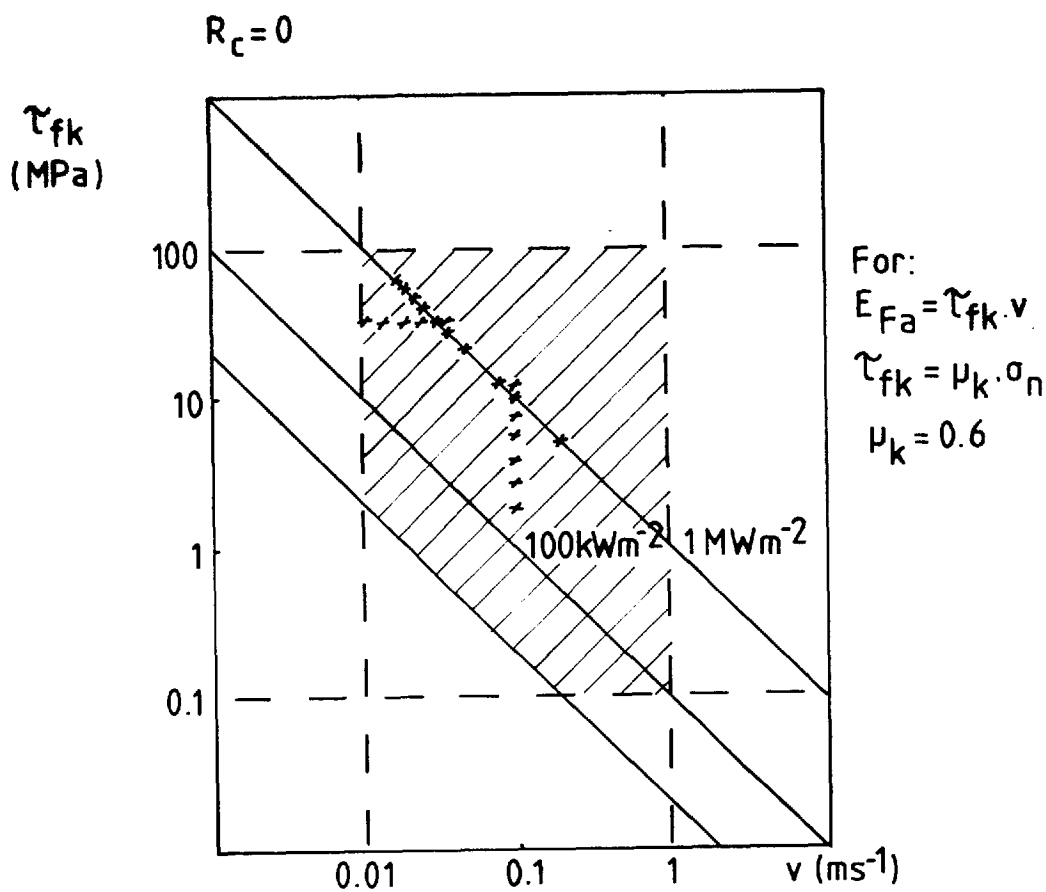Fig. 9.5. Orientation of sample dimensions listed in Tables 9.1, 9.3, 9.5 and 9.7.

Fig. 9.6. Fault slip parameters modelled in these experiments.

Table 9.1.

Sample measurements used in the study of the effect of
sample size on the thermal fracture pattern.

Test Number	Sample Number	Thickness(mm) $\frac{L_1+L_2+L_3+L_4}{4}$	Average cross sectional area (mm^2) $\frac{(L_5 \times L_6)+(L_7 \times L_8)}{2}$
Cuboid Samples			
1	C1 A	40.0	62.5
	C1 B	38.8	65.0
2	C2 A	35.5	135.0
	C2 B	36.5	135.0
3	C3 A	34.0	179.0
	C3 B	39.5	198.0
4	C4 A	38.8	255.0
	C4 B	35.8	255.0
5	C5 A	37.4	294.0
	C5 B	36.6	294.0

Test Number	Sample Number	Thickness(mm)	$\frac{(L_5+L_6+L_7+L_8)^2}{8} \times \pi$
Cylindrical Samples			
6	C6 A	39.7	231.0
	C6 B	40.7	231.0
35	T35 A	34.8	112.5
	T35 B	34.8	112.5
36	T36 A	29.8	112.7
	T36 B	29.9	112.5
37	T37 A	24.8	112.6
	T37 B	24.7	112.7
38	T38 A	19.8	112.5
	T38 B	19.8	112.6
39	T39 A	14.8	112.4
	T39 B	14.5	112.2

Table 9.2.

Experimental conditions used in the study of the effect of
variation of sample size on the thermal fracture pattern.

Test Number	Stress (MPa)	Duration of energy pulse, TP, (sec)	Average power dissipated (MWm^{-2})
1	Failed on loading between 60 and 64 MPa.		
2	40	10.8	0.86
3	Failed on loading between 33 and 35 MPa.		
4	28.4	10.2	0.68
5	29.5	10.8	0.77
6	40.2	No data recorded	
35	40.0	9.6	1.02
36	40.0	6.6[*]	0.92
37	40.0	11.4	0.95
38	40.0	9.6	0.87
39	40.0	No data recorded	

[*]element broke during the heating cycle.

Table 9.3.

Sample measurements used in the study of the effect of
normal stress on the thermal fracture pattern.

Test Number	Sample Number	Average thickness(mm) $\dfrac{L_1+L_2+L_3+L_4}{4}$	Average cross sectional area $\dfrac{(L_5+L_6+L_7+L_8)^2}{8} \times \pi$
7	T7 A	39.8	112.5
	T7 B*	40.0	112.2
8	T8 A	39.9	112.6
	T8 B*	39.9	112.5
9	T9 A	39.9	112.5
	T9 B*	39.8	112.5
10	T10 A	39.9	112.5
	T10 B*	40.0	112.6
11	T11 A	39.8	112.5
	T11 B*	39.9	112.5
12	T12 A	40.0	112.5
	T12 B	40.0	112.5
13	T13 A	40.0	112.2
	T13 B	39.9	112.6
14	T14 A	40.1	112.7
	T14 B	39.9	112.5
15	T15 A	40.0	111.2
	T15 B	40.0	112.5
16	T16 A	40.0	112.6
	T16 B	40.2	112.5
17	T17 A	40.1	111.9
	T17 B*	40.0	112.7
18	T18 A	39.9	112.5
	T18 B*	40.0	112.5
19	T19 A	40.0	112.2
	T19 B	39.9	112.5

* signifies sample with groove for thermocouple

Table 9.4.

Experimental conditions used in the study of the effect of
normal stress on the thermal fracture pattern.

Test Number	Stress (MPa)	Duration of energy pulse, TP, (sec)	Average power dissipation (MWm^{-2})	Temperature (°C)
8	0.1	10.8	1.14	423
17	5.2	12.0	1.04	490
9	10.3	11.0	1.10	293
14	15.4	12.0	0.99	
10	19.3	9.6	1.03	225
15	24.6	9.0	1.03	
11	29.7	10.5	0.96	480
16	34.7	12.0	0.98	
13	39.9	12.0	0.96	
7	41.2	10.2	0.96	185
18	45.0	12.0	0.96	235
12	49.9	10.2	0.96	220
19	55.4	12.0	0.92	

Table 9.5.

Sample measurements used in the study of the effect of power dissipation on the thermal fracture pattern.

Test Number	Sample Number	Thickness(mm) $\frac{L_1+L_2+L_3+L_4}{4}$	Cross sectional area (mm^2) $\frac{(L_5+L_6+L_7+L_8)x \, \pi}{8}$
7	T7 A	39.8	112.5
	T7 B*	40.0	112.2
13	T13 A	40.0	112.5
	T13 B	39.9	112.5
20	T20 A	39.8	112.5
	T20 B*	40.0	111.9
21	T21 A	40.0	111.9
	T21 B*	40.0	112.2
22	T22 A	40.0	112.2
	T22 B	40.0	112.5
23	T23 A	40.0	112.5
	T23 B	39.9	112.2

* signifies sample with grooves for thermocouple

Table 9.6.

Experimental conditions used in the study of the effect of power dissipation on the thermal fracture pattern.

Test Number	Stress (MPa)	Duration of energy pulse, TP, (sec)	Average power dissipated (MWm^{-2})	Surface Temperature($^{\circ}$C) (if measured)
13	39.9	12.0	0.96	
7	41.2	10.2	0.96	185
20	40.0	12.0	0.82	170
21	40.1	12.0	0.59	135
23	39.9	12.0	0.53	
22	39.9	12.0	0.33	

Table 9.7.

Sample measurements used in the study of the effect of
thermal cycling on the thermal fracture pattern.

Test Number	Sample Number	Thickness (m) $\frac{L_1+L_2+L_3+L_4}{4}$	Cross sectional area (m^2) $\frac{(L_5+L_6+L_7+L_8)}{8} \times \pi$
24	T24 A	40.0	112.5
	T24 B	40.1	112.5
25	T25 A	40.0	112.5
	T25 B	40.0	112.7
26	T26 A	40.1	112.8
	T26 B	39.9	112.2
27	T27 A	40.0	112.5
	T27 B	40.0	112.6
28	T28 A	40.0	111.0
	T28 B	40.0	112.5
29	T29 A	40.0	112.5
	T29 B	40.0	122.2
31	T31 A	40.0	112.6
	T31 B	40.0	112.5
32	T32 A	40.0	112.4
	T32 B	39.8	112.7
33	T33 A	39.9	112.5
	T33 B	39.9	112.4

Table 9.8.

Experimental conditions used in the study of the effect of
thermal cycling on the thermal fracture pattern.

Test Number	Stress (MPa)	Average duration of energy pulse (sec)	Average power dissipated (MWm^{-2})	No. of cycles
29	39.9	10.0	0.89	2($\frac{1}{2}$)
33	39.9	10.3	0.80	6
25	39.9	10.2	0.71	6($\frac{1}{2}$)
28	40.1	10.0	0.73	10
31	39.9	9.8	0.88	10($\frac{1}{2}$)
26	39.9	10.2	0.83	15
27	39.9	10.0	0.71	20
24	39.9	10.6	0.50	50
32	39.9	9.8	0.89	49*

* During this test the sample was unloaded and the element
replaced 8 times.

heterogeneity and relatively coarse grain size of the granite meant that the areal proportions of different minerals varied. All surfaces were thoroughly washed and air-dried before the paired blocks were assembled.

Internal stress concentrations could not be avoided around the thermocouple grooves and at the edges of the element. In the first case, the block containing the grooves was not used in the ensuing microstructural analysis. In the second case, a crack appeared in the rock parallel to the element edge in the samples deformed at the highest normal stresses. Again, these blocks were not used for fracture analysis. It should be possible to overcome this problem by using a more powerful power supply and a wider, low resistance element which would cover the entire rock surface. Alternatively, if the lateral thermal insulation could be improved, a finer grained rock would allow smaller sample sizes to be used.

9.5.2. Heat Losses

Heat losses from the sample sides were minimised by ceramic fibre insulation which suppressed radiation and convection. The steel piston and spherical seat, at each end of the rock assembly, provided a heat sink and ensured that the isotherms remained parallel to the heated surface, at least in the central part of the block.

Although the granite end-pieces inhibited radiation from the ends of the element, some heat was unavoidably radiated from its sides. Heat losses from this edge, which was 0.1 mm thick were considered to be small.

9.5.3. Electrical Circuit

Two problems arose with the element. The first was its progressive oxidation on heating. The problem could have been eliminated were it possible to perform the tests in an inert atmosphere. Provided the entire element was covered by rock, the oxidation effects were not important for a single, 10 second heating pulse. In the cyclic tests, oxidation invariably led to the eventual breakage of the element. The element was also liable to break if it was stressed by bending or twisting as the sample was loaded (Fig. 9.7).

Between each test the brass clamps were cleaned of the deposit of molybdenum oxide (MoO_3) which built up during each heating cycle. Failure to do this increased the contact resistance between the element and clamps and reduced the power dissipated across the element. The
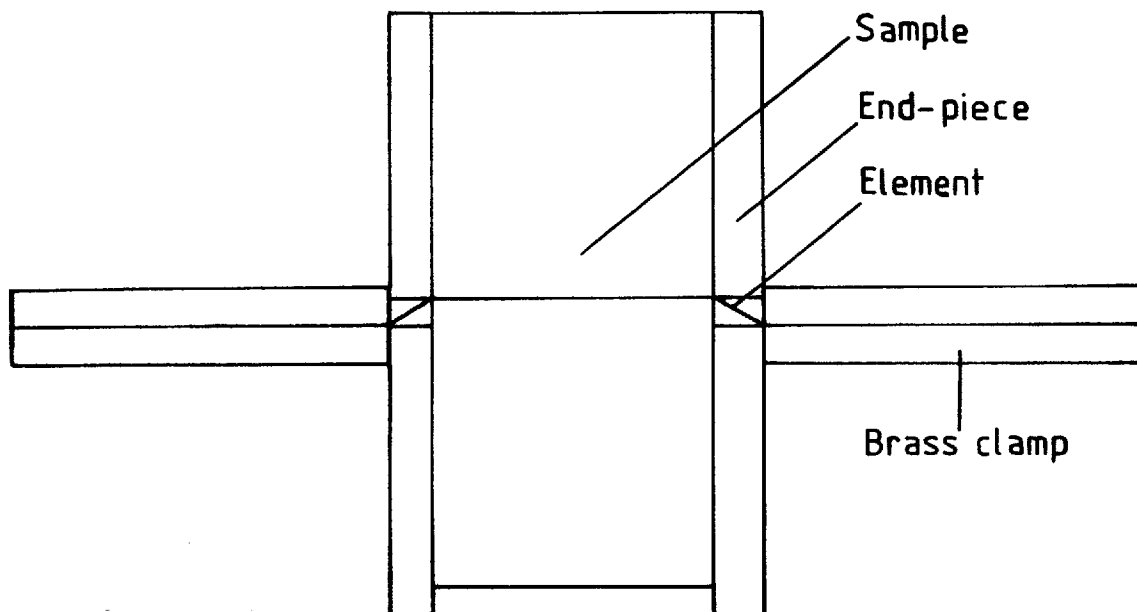
Fig. 9.7. Bending of the element by loading the sample, which led
to its breaking during a single heating pulse.

measured power dissipation in the circuit was shared between the brass
clamps and the element. The respective resistances of these were
8×10^{-5} and 150×10^{-5} Ω which meant that 95% of the power measured
was dissipated across the element, assuming the contact resistance
between the clamps and the element to be small. This is a valid
assumption for a clamped metal to metal contact.

Switching spikes were recorded on both wattmeter and chart recorder
at the start and end of each energy pulse. A storage oscilloscope
showed these to be the response of the wattmeter to switching and not
true power spikes. The actual shape of the energy pulse is shown in
Fig. 9.8. The power attained its maximum value after 0.5 seconds and
decayed in less than 0.04 seconds.
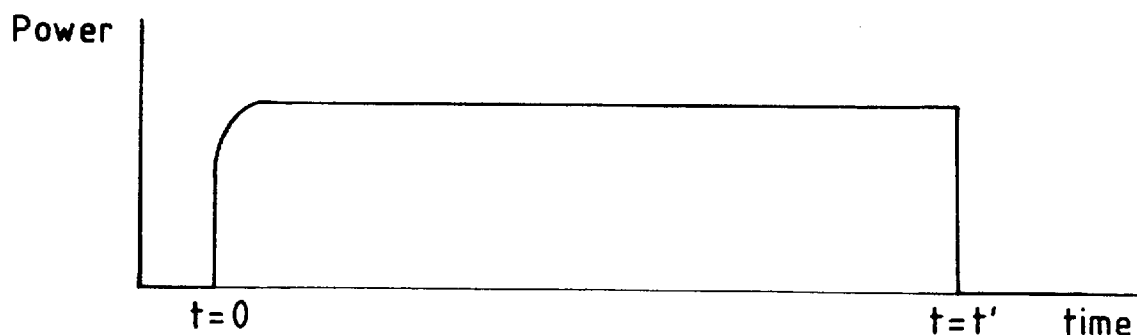
Fig. 9.8. Shape of energy pulse in each heating cycle

The maximum power attainable was low because of large copper losses in both the primary and secondary windings of the transformer, which was only 50% efficient at maximum power.

9.6. Macroscopic Fracture Analysis

Two types of fracture, not relevant to faulting were produced by the heating tests. They resulted from block geometry and stress concentrations in the rock around the edges of the element.

Position
of element
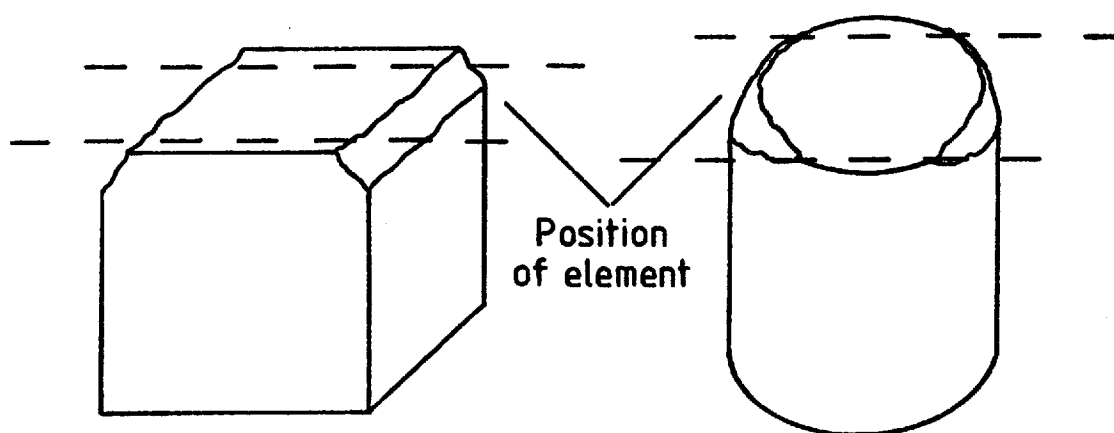
Fig. 9.9. Fractures caused by block geometry in both cuboid and cylindrical samples.

The first of these led to partial spalling of the corners in the cuboid samples, with fractures forming at about 50° to the heated surface (Fig. 9.9). In the cylindrical samples, these spalls occurred at each end of the element. These fractures are irregular, partly cutting through crystals and partly following grain boundaries.

Fractures of the second type are planar and wholly transgranular. They cut the heated surface along the edge of the element and are oriented almost perpendicular to the surface. They are only visible in samples heated at normal stresses greater than 30 MPa and become more pronounced at higher loads (Fig. 9.10). They result from a combination of the sudden lateral temperature change on the heated surface and the stress concentrations at the edge of the element.
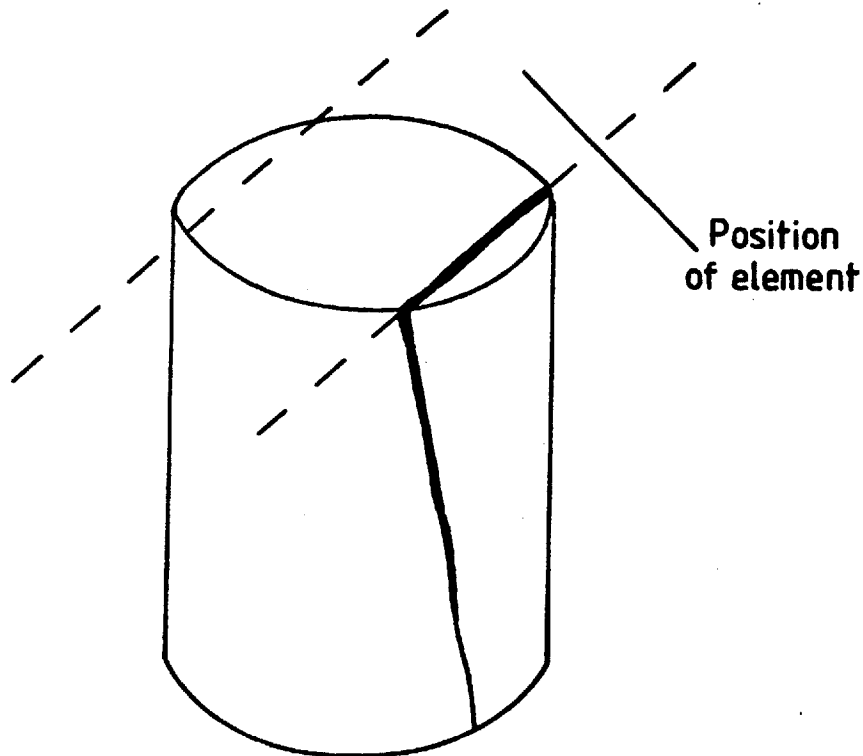
Fig. 9.10. Fracture type resulting from the edge of the element.

9.6.1. Comparison of Fracture Patterns

The following sections describe the fracture patterns resulting from thermal shock. From Tables 9.2, 9.4, 9.6 and 9.8, it is apparent that there is some variation in the experimental parameters for individual tests of each series. For example in tests 7 to 19, where the normal stress is varied between 0.1 and 55.4 MPa, there is $\pm 11\%$ variation in the power dissipated and $\pm 14\%$ variation in the duration of the energy pulse. The question then arises, to what extent the deliberately varied parameter is responsible for the observed variations in the fracture pattern.

For each test, the energy pulse duration and power values (Table 9.4) may be combined to obtain an estimate of the maximum surface temperature (equation 5.2 and Table 9.9). The amount of thermal damage is theoretically related to this temperature which could, for example, be used in a statistical check of comparability. For this check, the mean maximum calculated surface temperature and its 90% confidence interval are calculated. Only tests with temperatures falling within this interval should then be compared.

If this statistical check is applied, the mean surface temperature is $727^{\circ}C$ with a 90% confidence interval of $\pm 31^{\circ}C$. This indicates that

Table 9.9.

Theoretical maximum surface temperature in
each test in which the normal stress is varied.

Test	Normal stress (MPa)	Maximum surface temperature °C
8	0	820
17	5.2	788
9	10.3	798
14	15.4	750
10	19.3	698
15	24.6	676
11	29.7	681
16	34.7	743
13	39.9	728
7	41.2	671
18	45.0	728
12	49.9	671
19	55.4	697

N.B. Temperatures are calculated here and in
Table 9.10 assuming that 95% of the power
measured is dissipated across the heating
element.

tests 8, 17, 9, 15, 11, 7 and 12 should be discarded. For these experiments, this treatment of results is artificial since the physical effects that result from rapid surface heating to a temperature of 730 ± 100°C (which includes the whole series of tests) are similar. Instead, in the subsequent sections, the effects of variations in the level of power dissipation (and hence surface temperature) will first be characterised as an aid to the description of variations in the fracture pattern brought about by variation of the other experimental parameters (normal stress and number of heating cycles undergone).

9.6.2. Effect of Sample Size and Geometry on the Macroscopic Fracture
Pattern

These tests were performed to determine the sample size and shape least likely to be affected by geometrically controlled fractures. The cuboid samples, possibly as a result of irregularities from sample

preparation, developed more geometrically controlled fractures than the cylindrical samples. Tests T1 and T3 (Table 9.2) failed on loading and through-going fractures were seen in all the remaining blocks after heating (Fig. 9.11). These fractures, which widen towards the base of

Side surface of block C5 A.
Element width shown by
arrows.

Lower surface of block C5 A.
Element was placed in
direction of arrow.
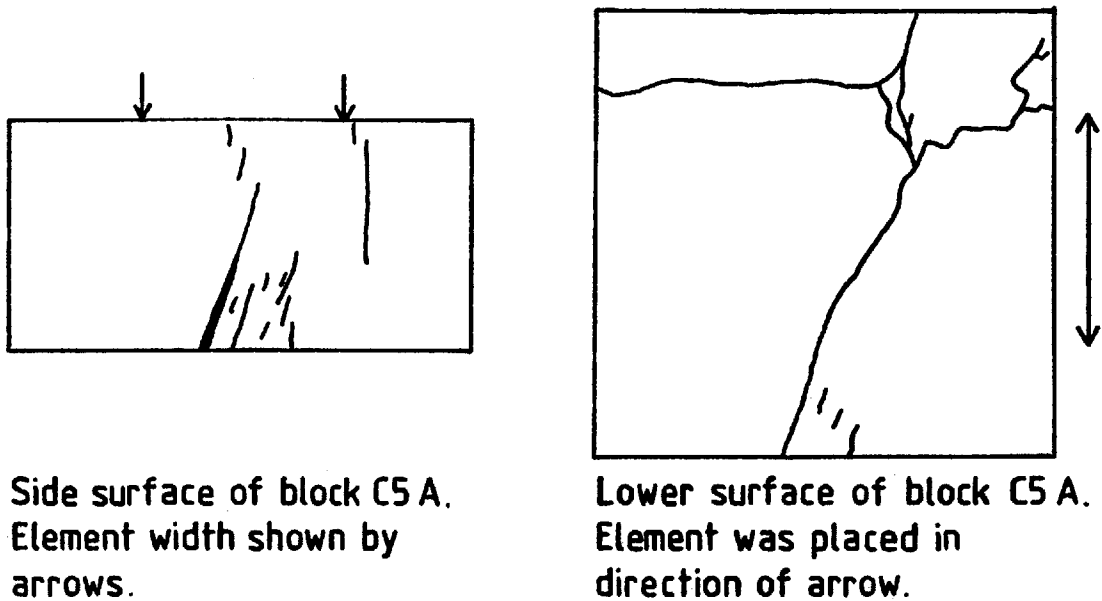
Fig. 9.11. Typical thermal fractures seen in all cuboid samples.

the block (away from the heated surface), probably resulted from uneven lateral heating on the upper surface. This is caused by the relative narrowness of the strip covered by the element. In the cylindrical samples with diameters of 38 mm, 69.5% of the circular faces of the cylinders was heated and this fracture type did not develop.

Tests nos. 35 to 39 determined the optimum sample thickness. The blocks should effectively represent semi-infinite masses of rock, and must be thick enough to contain macroscopic thermal fractures. An upper limit of 41.3 mm was imposed by the uniaxial rig.

The results of these heating tests showed that fractures crossed the entire block when it was less than 30 mm thick. In thicker samples, the majority of fractures were restricted to the upper 25 mm, although a few closed cracks did cross the block completely (Fig. 9.12).

Cylindrical samples 40 mm thick and 38 mm in diameter were chosen for the remaining tests. In these samples, the effects of block geometry were minimised and the fracture pattern in the central parts
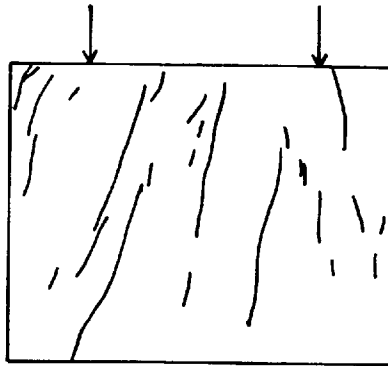
Fig. 9.12. Fractures in the axial section of block 35A. The upper
surface was heated and all fractures are closed.

of the block, away from stress concentrations resulting from the
cylinder edges should be equivalent to the thermal deformation associated
with seismic slip.

9.6.3. Macroscopic Fracture Types

In this and following sections, a comparison of macroscopic
thermal fracturing is made based on analysis of sections cut through
the damaged samples. After each experiment, one of the paired blocks
was impregnated with Araldite to preserve it for thin-sectioning and
the other was stored carefully. The impregnated block was cut as in
Fig. 9.13 and fractures intersecting the cut surfaces were recorded and
compared.

In the other block, the damage to the heated surface was assessed
and the number of fractures cutting the edge of the cylinder immediately
below the heated surface counted. There is a relationship between the
number of these fractures and the interior damage seen in the cut
blocks. The thermal fracturing in the three series of experiments
where power, normal stress and number of cycles were varied, is
compared pictorially in Figs. 9.14 - 9.16.

The damage to the heated surface itself comprises two types of
fracturing. One consists of a network of tiny fractures similar to
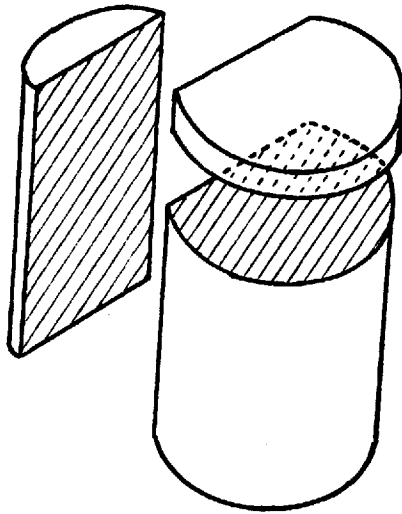
Fig. 9.13. Cut surfaces on which fractures are compared in the
Araldite impregnated blocks.

cracks in a ceramic glaze. These are only seen when the block is
impregnated with Araldite which is absorbed into the fractures (Plate
10a). The other type of fracturing is seen in the unimpregnated
block, where the quartz grains appear white and opaque. This effect
results from intense microfracturing which, by increased scattering of
light, lightens the colour of the pink feldspar grains (Plate 10b).

All fractures on the sawn surfaces and cylinder sides appear as
light lines which are difficult to see when they intersect the surface
at a high angle (Plate 10c-f).

9.6.4. Effect of Power Dissipation on the Macroscopic Fracture Pattern

For purposes of comparison, the theoretical maximum surface tempera-
ture in each test has been calculated (Table 9.10). With decreasing
power dissipation, the area of surface damage characterised by micro-
cracks in quartz grains, decreases in size. It is effectively absent
in tests T22 and T23 where the theoretical surface temperature was
below about $400^{\circ}C$. The pattern of the larger fractures on this
surface (Fig. 9.14) is similar in all tests, but the fractures which
form a radial pattern decrease in both number and length with decreasing
levels of power dissipation. The fractures which cut the axial section
also decrease in number with decreasing power dissipation, but show no

154

Plate 10

All photographs are the same scale. Scale bar = 10 mm.

a   Glaze-like fractures on the heated surface.

b   Surface damage caused by the heating that results in lightening of
the colour of the granite.

c   Fractures on the outside surfaces of the granite cylinders.

d   Fractures on the surface cut parallel to the heated surface.

e   Fractures on the axial sawn surface.

f   Fractures on the axial sawn surface.
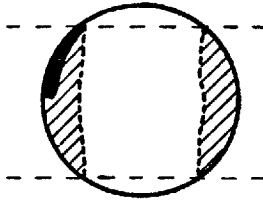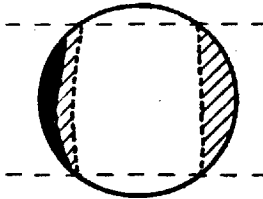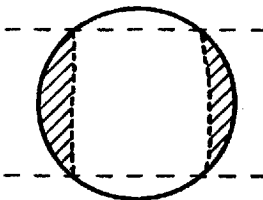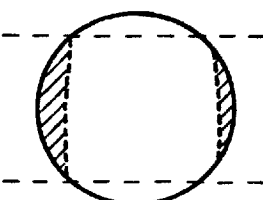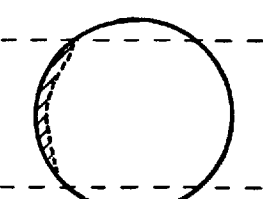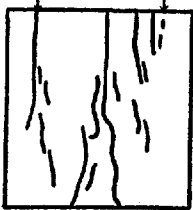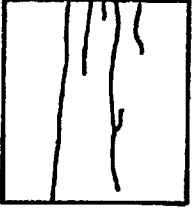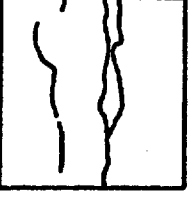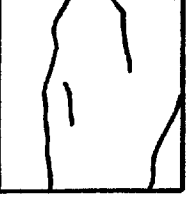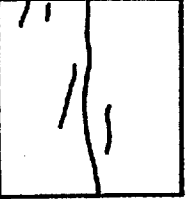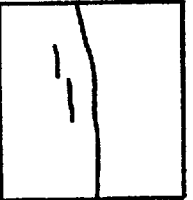
Test Number	Calculated maximum surface temperature(°C)	Area of heated surface affected by intense microfracturing	Number of fractures on cylinder sides		Thermocouple groove	Corner spalls, angle of intersection with heated surface and depth to which they extend
			at edge of heated surface	reaching to cylinder base		
13	728		15	6	No	1 side 45°, 2.5 mm
7	671		10	1	Yes	1 side 42°, 2.7 mm
20	622		10	3	Yes	No
21	447		7	1	Yes	No
23	402		7	1	No	No
22	250	No surface damage	1	0	No	No

Fig. 9.14. Variations in the thermal fracture pattern due to variation of power dissipation.

a. un-impregnated block.

Normal stress	Fractures on vertical sawn surface	Number at edge of heated surface	Number reaching to cylinder base	Fractures on horizontal sawn surface (ticks indicate fractures cutting the cylinder sides)	Number of thermal cycles
39.9		5	2		1
41.2		5	2		1
40.0		4	2		1
40.1		2	1		1
39.9		3	1		1
39.9		1	1		1

b. impregnated block
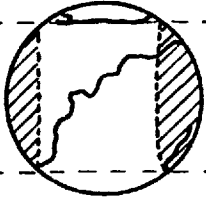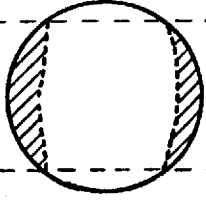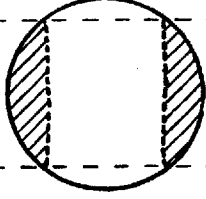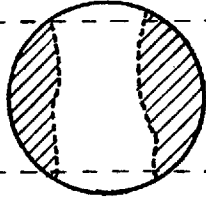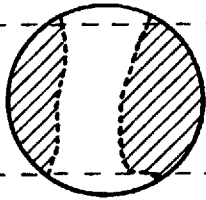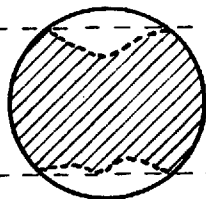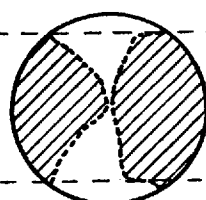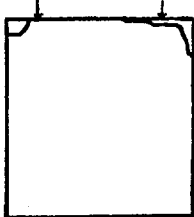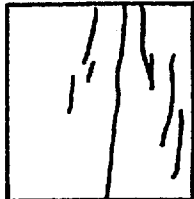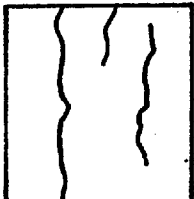
Test Number	Calculated maximum surface temperature($^{\circ}$C)	Area of heated surface affected by intense microfracturing	Number of fractures on cylinder sides at edge of heated surface	reaching to cylinder base	Thermocouple groove	Corner spalls, angle of intersection with heated surface and depth to which they extend
8	820		5	0	Yes	Both sides 23°, 3 mm 28°, 5 mm
17	788		1	0	Yes	Both sides 25°, 6 mm 35°, 8 mm
9	798		11	0	Yes	Both sides 45°, 3 mm 40°, 2 mm
14	750		8	0	No	Both sides 50°, 1.5 mm 82°, 10.5 mm
10	698		4	0	Yes	Both sides 43°, 6 mm 45°, 2 mm
15	676		6	1	No	Both sides 50°, 1 mm 83°, 24 mm
11	681		5	2	No	Data not available

Fig. 9.15. Variation in the thermal fracture pattern due to variation of normal stress.

a. un-impregnated block

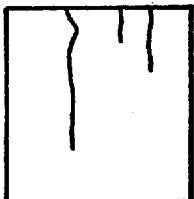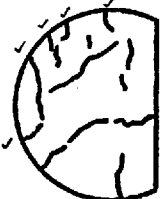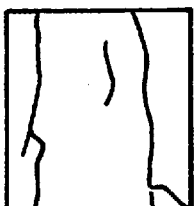| Normal stress	Fractures on vertical sawn surface	Number at edge of heated surface	Number reaching to cylinder base	Fractures on horizontal sawn surface (ticks indicate fractures cutting the cylinder sides)	Number of thermal cycles
0.1		2	0		1
5.2		2	0		1
10.3		2	0		1
15.4		3	1		1
19.3		3	1		1
24.6		3	0		1
29.7		2	2		1

b. impregnated rock
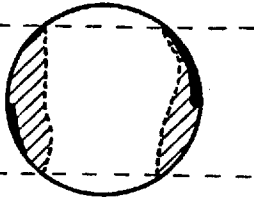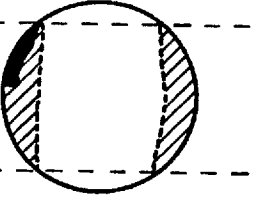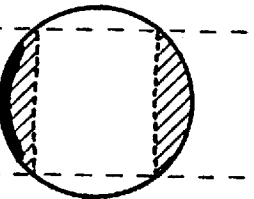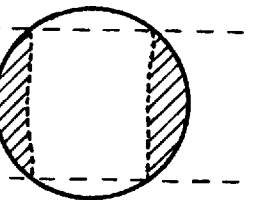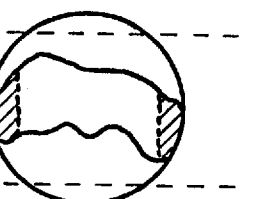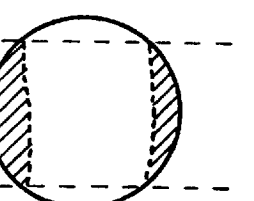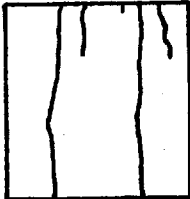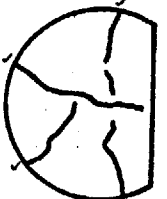
Test Number	Calculated maximum surface temperature(°C)	Area of heated surface affected by intense microfracturing	Number of fractures on cylinder sides at edge of heated surface	reaching to cylinder base	Thermocouple groove	Corner spalls, angle of intersection with heated surface and depth to which they extend
16	743		9	3	No	Both sides 80°, 5.5 mm 68°, 5 mm
13	728		16	6	No	Both sides 51°, 2 mm 75°, 9 mm
7	671		6	3	Yes	1 side 48°, 2.5 mm
18	728		15	4	Yes	1 side 48°, 1 mm
12	671		Block failed while cooling		Yes	data not available
19	697		10	5	No	None

Fig. 9.15. a. un-impregnated block (continued)

Normal stress	Fractures on vertical sawn surface	Number at edge of heated surface	Number reaching to cylinder base	Fractures on horizontal sawn surface (ticks indicate fractures cutting the cylinder sides)	Number of thermal cycles
34.7		4	1		1
39.9		3	1		1
41.2		5	2		1
45.0		3	1		1
49.9	Block failed while cooling				1
55.4		2	2		1

b. impregnated block (continued)

Table 9.10.

Calculated maximum surface temperature

Test	Normal stress (MPa)	Maximum surface temperature(^{o}C)
13	39.9	728
7	41.2	671
20	40.0	622
21	40.1	447
23	39.9	402
22	39.9	250

systematic variation in the depth to which they extend from the heated surface.
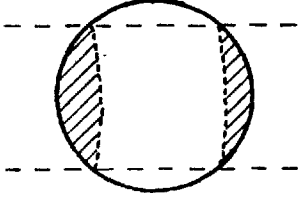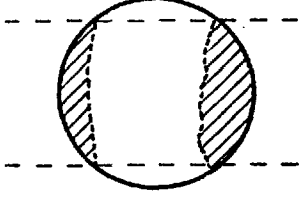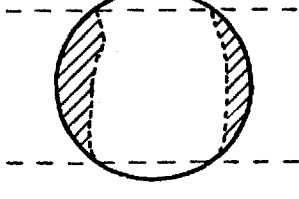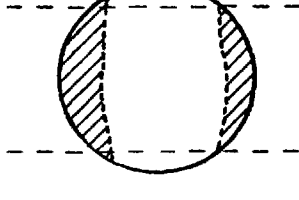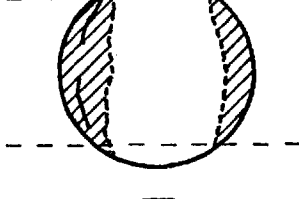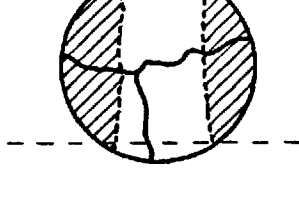
9.6.5. Effect of Normal Stress on the Macroscopic Fracture Pattern

The area of the heated surface showing microcracks in the quartz grains is considerably greater in the samples held at 0 and 5.2 MPa (Fig. 9.15) where it covers almost all of the surface beneath the element. With increasing normal stress, the extent of this area decreases to a constant size in samples heated at stresses above 15 MPa. In addition, the sample heated at zero load stress alone developed a low-angle fracture which caused lifting of the entire microfractured surface.

The variation in the pattern of the larger fractures on this surface (Fig. 9.15) is less clear. In the samples heated at and below 10.3 MPa, the fractures lie sub-parallel to the curved edge of the cylinder. At, and above 15.4 MPa, the intersection of these fractures with the cylinder sides is at a high angle and their pattern approximates to a radial distribution. There is no systematic variation in their number with increasing normal stress.

The number of fractures in the cylinder sides shows a general increase with increasing normal stress. Above a normal stress of 30 to 35 MPa, the number of fractures reaching the base of the cylinders increases from zero or one, to three or more.

A similar increase in fracture density with increasing normal stress, is seen in the axial section cut through the cylinders. This

162

Test Number	Calculated maximum surface temperature(°C)	Area of heated surface affected by intense microfracturing	Number of fractures on cylinder sides		Thermocouple groove	Corner spalls, angle of intersection with heated surface and depth to which they extend
			at edge of heated surface	reaching to cylinder base		
20	622		10	3	Yes	No
29	616		6	2	No	1 side 45°, 2.5 mm
33	562		7	3	No	1 side 55°, 5.0 mm
31	603		6	4	No	1 side 56°, 3.5 mm
26	580		5	3	No	1 side 53°, 4 mm
*32	610		10	7	No	1 side 45°, 2 mm

*during this test the sample was unloaded and the element replaced 8 times.

Fig. 9.16. Variations in the thermal fracture pattern due to variation in the number of heating cycles.

a. un-impregnated block

Normal stress	Fractures on vertical sawn surface	Number at edge of heated surface	Number reaching to cylinder base	Fractures on horizontal sawn surface (ticks indicate fractures cutting the cylinder sides)	Number of thermal cycles
40.0		4	1		1
39.9		4	1		2($\frac{1}{2}$)
39.9		5	1		6
39.9		8	1		10($\frac{1}{2}$)
39.9		6	2		15
39.9		6	2		49

b. impregnated block

164

Test Number	Calculated maximum surface temperature(°C)	Area of heated surface affected by intense microfracturing	Number of fractures on cylinder sides		Thermocouple groove	Corner spalls, angle of intersection with heated surface and depth to which they extend
			at edge of heated surface	reaching to cylinder base		
21	447		7	1	Yes	No
25	497		5	4	No	No
28	505		9	3	No	1 side 40°, 2.5 mm
27	491		10	3	No	No

Fig. 9.16. a. un-impregnated block (lower level of power dissipation), (continued).

Normal stress	Fractures on vertical sawn surface	Number at edge of heated surface	Number reaching to cylinder base	Fractures on horizontal sawn surface (ticks indicate fractures cutting the cylinder sides)	Number of thermal cycles
40.1		2	1		1
39.9		8	1		6($\frac{1}{2}$)
40.1		8	3		10
39.9		8	3		20

b. impregnated block (lower level of power dissipation), (continued)

is accompanied by an increase in the depth to which fracturing extends below the heated surface from 5 mm (0.1 MPa) to 20 to 30 mm in the remaining tests. There is a systematic change in the orientation of these microfractures, from sub-parallel to the heated surface (0.1 to 5.2 MPa) to sub-perpendicular to it ($\geqslant$15.4 MPa).

9.6.6. Effect of Thermal Cycling on the Macroscopic Fracture Pattern

Two series of thermal cycling tests were performed at different levels of power dissipation. For the purposes of comparison, an average maximum surface temperature for each sample was calculated from the average power dissipation and average duration of energy pulse for each group of tests. This temperature will not equal that actually reached by the surface during each cycle of the experiment, but aids comparison of the resulting damage.

Increased numbers of thermal cycles has little effect on the extent of the area of the surface damage characterised by microcracks in quartz grains (Fig. 19.16). The area may increase slightly in size with increasing numbers of cycles but there is no clear trend. More large fractures are seen on the horizontal sawn surface after six thermal cycles than after one cycle. This increase does not continue with further cycling. The large number of such fractures seen in sample T32 (49 cycles) are probably due to its repeated loading and unloading.

There is no systematic increase in the number of fractures in the cylinder sides with thermal cycling (Fig. 19.16), but there is a slight increase in the number of fractures seen in the axial section. Again, between 1 or 2($\frac{1}{2}$) cycles and 6 cycles there is a jump in the number of small fractures cutting the axial surface, but the fracture density remains approximately constant with further increase in the number of thermal cycles.

9.7. Microscopic Fracture Analysis

Standard petrographic thin sections 30 μm in thickness were used in the microscopic fracture analysis. While additional fractures may be introduced during the thin-sectioning process, they fall into two categories which can be easily recognised. The first consists of a rectangular array of small fractures which invariably occurs in the thinner areas of the section, especially at its margins. The second results from rotation of part of the rock slice during grinding, often leading to the partial destruction of the slide. Again, these

fractures can be easily identified.

Coarse grained granite (with a mean grain size of about 0.7 mm) was used in all of the experiments. Its mineral composition is uniform, consisting of K-feldspar, plagioclase and quartz with biotite, muscovite, apatite and opaque ores. In thin section the rock possesses a characteristic granitic texture, with the major constituents rarely exhibiting crystal faces. Most feldspar crystals are zoned, have perthitic intergrowths and exhibit alteration which is more intense in their central parts. Most quartz grains are equi-axed, with undulatory extinction. Trains of fluid inclusions are ubiquitous.

9.7.1. Fracture Terminology

The following terminology has been adapted from that of Simmons and Richter (1976):

Microfracture - an opening that occurs in rocks and has one or two dimensions much smaller than the third.

Coincident grain boundary fracture (CGB-fracture) - a microfracture that follows grain boundaries.

Intragrain fracture - a microfracture that crosses one grain only.

Multigrain fracture (MG-fracture) - a microfracture that crosses several grains and several grain boundaries.

Microfractures are considered "open", if the two sides of the fracture are separated by the Araldite used to impregnate the blocks prior to thin sectioning. "Closed" fractures do not contain Araldite and the two sides of the fractures usually touch.

9.7.2. Fracture Types.

In the two standard orientations sectioned (Fig. 9.13), all three types of microfracture are usually visible.

The MG-fractures can be sub-divided into the four dominant types below:

(i) Single, open, planar fractures. These fractures show little variation in orientation along their entire length (Plate 12a).

(ii) Single, open fractures. The fracture orientation varies along its length such that it is generally sub-parallel to the boundary of each grain it crosses.

(iii) **Multiple fractures.** These fractures consist of two or more sub-parallel, closed fractures which form a narrow, braided network. The traces of these multiple fractures may or may not be straight (Plate 13e).

(iv) **Fracture Networks.** These are seen in areas where closed fractures of all types occur with very close spacings (Plate 13f).

Intra grain fractures occur in both quartz and feldspar. In the latter, they invariably follow a cleavage plane (Plate 11d). One other type of intragrain fracture is seen: small fractures sub-parallel to the heated surface which appear as shadows in quartz grains in the section of the heated surface.

9.7.3. Fracture Pattern in the Stressed but Unheated Block

One pair of the cylindrical samples was assembled with the heating element and stressed to failure, without the application of a heating pulse. One of the fractured blocks was impregnated and sectioned and the other used in a study of the fracture surface morphology (Section 9.8).

Optically, this sample was seen to contain many sub-parallel axial cracks which commonly crossed between 1 and 5 grains, although longer cracks were present (Plate 11a). These fractures may branch but rarely intersect each other at a high angle. The axial fractures are small MG-fractures, crossing 1 to 5 grains on the heated surface although some grain boundaries are also fractured (Plate 11b).

9.7.4. Influence of Mineralogy on Thermal Fracture

By using a coarse grained rock, the role of mineralogy in controlling fracture development could be assessed. Mineralogy had no obvious effect on the width of the fractures but did influence fracture density and orientation.

Quartz is most susceptible to thermal fracturing and contains the highest density of intragranular fractures. CGB-fractures are also most common on quartz-quartz boundaries (Plate 11c) followed by quartz-feldspar boundaries. This may be attributed to the high stresses resulting from the sudden volume change of quartz as it passes through the α/β transition at $573^\circ C$ (at atmospheric pressure). High internal stresses may also arise from the overpressuring of fluid inclusions during heating (Moore and Sibson, 1978).

Plate 11

a   Axial MG-fractures in unheated sample. Scale bar = 0.1 mm.

b   Small MG-fractures crossing up to 5 grains on the circular section
     of the unheated sample. Scale bar = 0.1 mm.

c   CGB-fractures on most quartz-quartz grain boundaries. Scale bar
     = 0.1 mm.

d   MG-fracture stepping across to adjacent cleavage planes in ortho-
     clase. Scale bar = 0.1 mm.

e   MG-fracture passing around rather than through a biotite crystal.
     Scale bar = 0.1 mm.

f   MG-fracture crossing a biotite crystal. Scale bar = 0.05 mm.
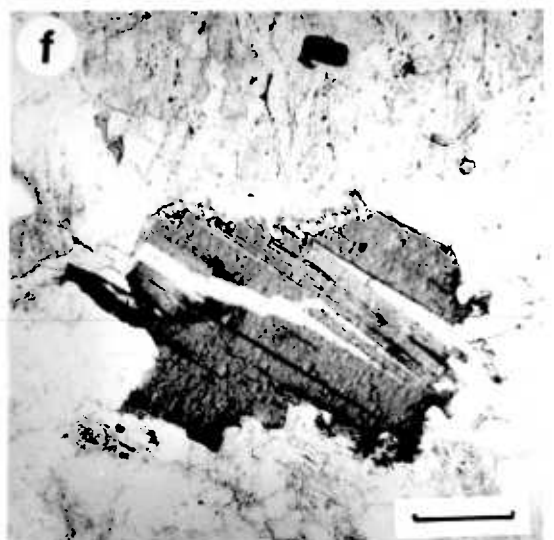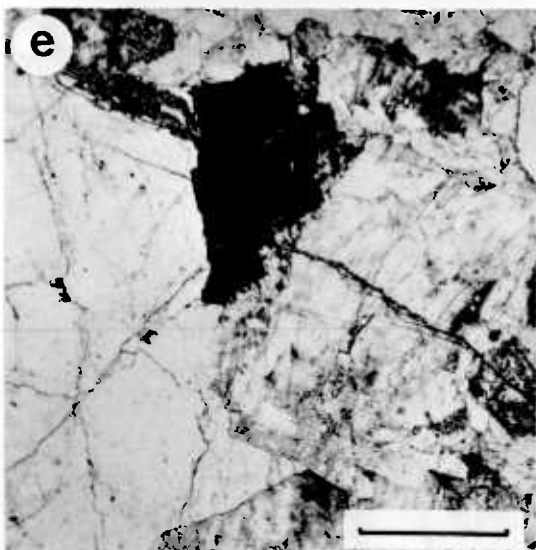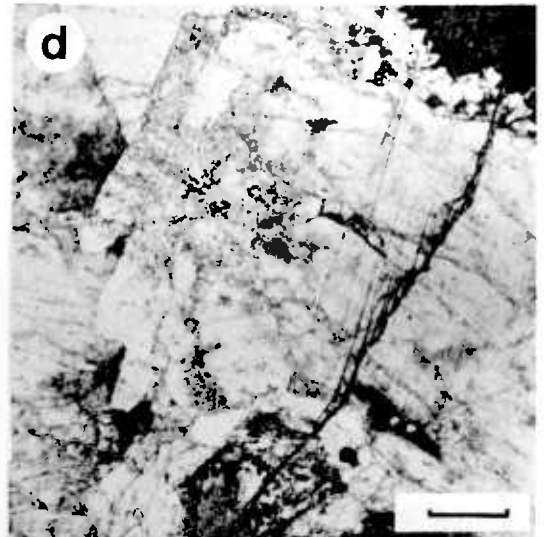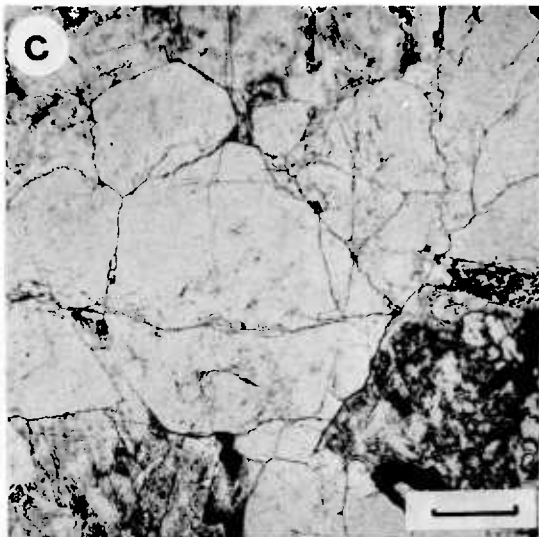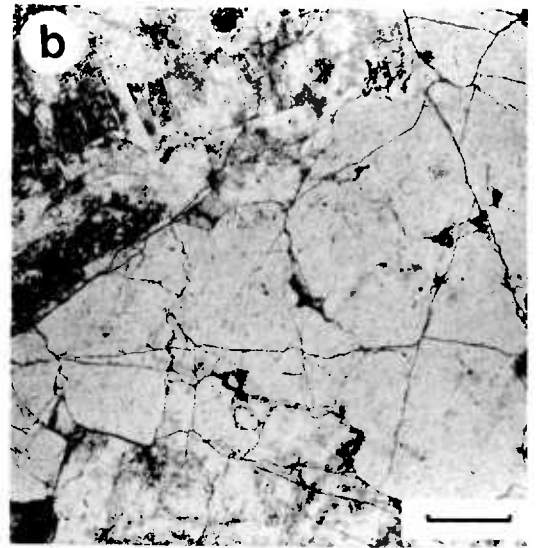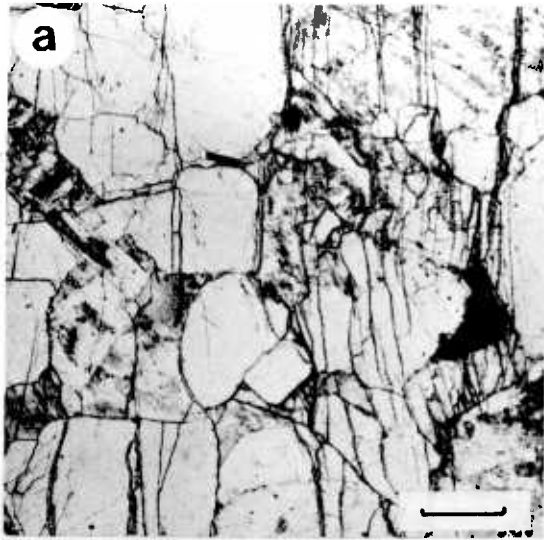
Feldspar crystals develop fewer intragranular fractures but these, together with large MG-fractures crossing feldspar grains invariably follow a single cleavage plane . Where the MG-fractures cross feldspar crystals at high angles to cleavage, they step across several adjacent planes (Plate 11d).

Fractures seldom cross biotite crystals (Plate 11e), but tend to follow their grain boundaries. In the few cases where a large MG-fracture crosses a biotite crystal, it tends to follow cleavage, but may disrupt the whole crystal (Plate 11f).

9.7.5. Fracture Pattern

All heated samples exhibited a similar, basic fracture pattern, with variation in the experimental conditions producing differences in the number and extent of individual fractures. This basic fracture pattern is shown in Fig. 9.17 and described below with its variations discussed in subsequent sections.
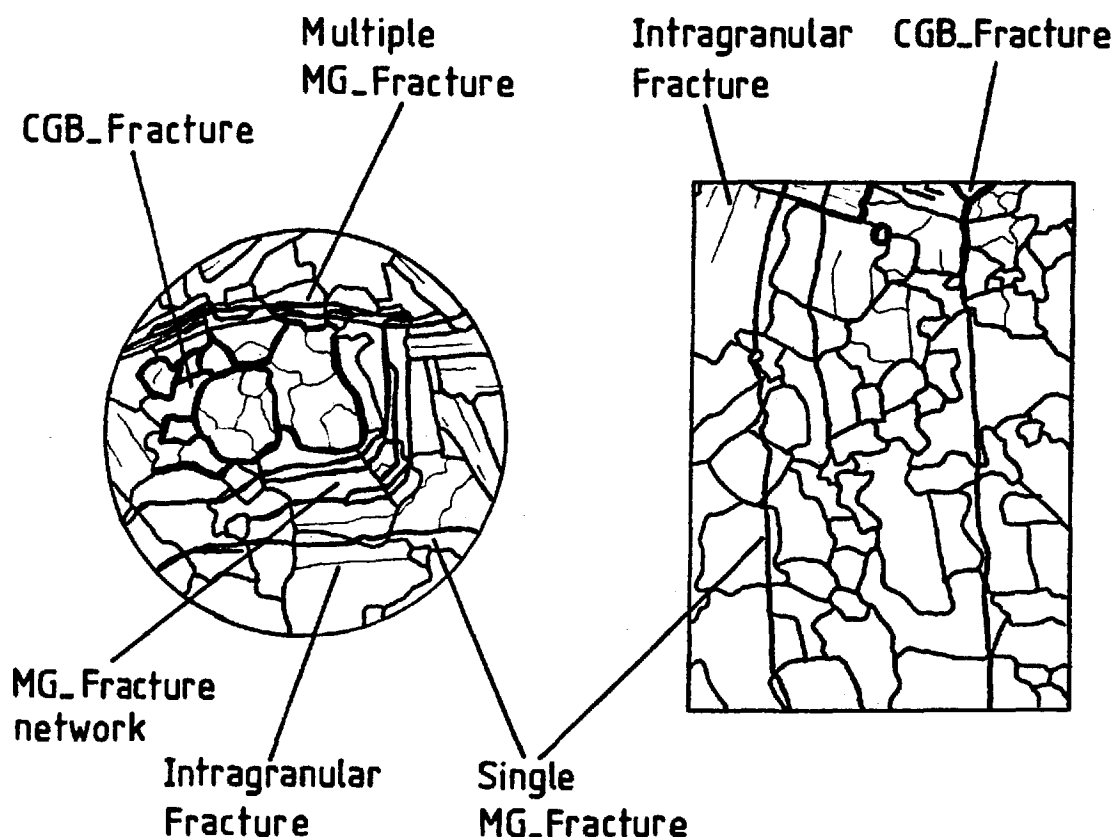
Fig. 9.17. Sketch of the basic fracture pattern resulting from the heating cycles.

Sample Number	Heated Surface	Axial Section	Surface Temperature(°C)
13	2-MG-fracture (i) 1-MG-fracture (iii) } show no preferred orientation and cross entire section. CGB-fractures along 50% of all grain boundaries. Extensive intragranular fracturing in 90% of all quartz and feldspar grains.	1-MG-fracture (i) 2-MG-fracture (ii) 3-MG-fracture (iii) } all intersect heated surface at angles > 80° and cross the entire section. 1-MG-fracture (ii) sub-parallel to heated surface. Many intragranular fractures in quartz and feldspar. Most numerous within 3-5 mm of heated surface.	728
7	1-MG-fracture (ii) 1-MG-fracture (iii) } show no preferred orientation and cross 1-MG-fracture (iv) } the entire section. CGB-fractures along 40-50% of all grain boundaries not seen on feldspar/feldspar junctions. Intragranular fractures in quartz and feldspar.	1-MG-fracture (i) 1-MG-fracture (ii) } intersect heated surface at angles 1-MG-fracture (iii) } >80° and cross the entire section. Many intragranular fractures in quartz, less seen in feldspar. These have no preferred orientation and are most numerous within 3-5 mm of the heated surface.	671
20	1-MG-fracture (ii) - actually follows grain boundaries along half its length. It crosses the entire section. CGB-fracturing along 40-50% of all grain boundaries. Intragranular fractures in quartz and feldspar.	Section broken (half missing). 1-MG-fracture (i) - perpendicular to heated surface and crosses the entire section. Due to the damage in this section caused in its preparation it is impossible to distinguish the thermal fractures.	622
21	1-MG-fracture (ii) - crosses half the section. CGB-fractures along only quartz-quartz boundaries (30-40% of total no. boundaries). Intragranular fractures in most quartz and very few feldspar grains.	1-MG-fracture (ii) - intersects heated surface at an angle >80° and crosses the entire section. CGB-fractures on some quartz-quartz boundaries. Few intragranular fractures in quartz over the entire slide, very few seen in feldspar. Small fractures exhibit no preferred orientation.	447
23	No MG-fractures. CGB-fractures along 30% of quartz-quartz boundaries. Intragranular fractures in 30% quartz grains and very few feldspar grains.	1-MG-fracture (ii) - intersects heated surface at an angle >80° and crosses the entire section. Very few quartz grains exhibit intragranular fractures. None in feldspar.	402
22	1-MG-fracture (ii) - crosses entire section. CGB-fractures along 10% quartz-quartz boundaries. Intragranular fractures in 10-20% quartz grains, none in feldspar grains.	Section broken (half missing). 1-MG-fracture (ii) intersects heated surface at an angle >80° and extends to a depth of 5 mm. Very few intragranular fractures seen in quartz.	250

Fig. 9.18. Variation of microfracture pattern with power dissipation.

In all tests, the heated surface was intensely fractured. All four types of multi-grain fracture were seen, although MG-fracture, type (i) (single, open, planar fracture) is less common. Coincident grain boundary fractures (CGB-fractures) are very common, while intra-granular fractures are visible in both feldspar and quartz, the latter also containing shadow fractures. CGB-fractures generally have no preferred orientation within the sample as a whole, but commonly follow cleavage planes in feldspar crystals. With the exception of the shadow fractures in quartz, they all generally intersect the plane of the thin section (the heated surface) at high ($>60^{o}$) angles.

In sections perpendicular to the heated surface (Fig. 9.13), all but one of the MG-fracture types are seen. Network fractures (MG-fracture (iv)) are absent and multiple fractures (MG-fracture (iii)) are subordinate to the other two. In the majority of heated samples, these fractures are approximately perpendicular to the heated surface and sub-parallel if more than one exists in the same section. CGB-fractures are seen, but they are less common. Intragranular fractures are present in both quartz and feldspar, but generally have no preferred orientation.

9.7.6. Effect of Power Dissipation on the Fracture Pattern

Variations in the main features of the fracture pattern, with increasing power dissipation, are listed in Fig. 9.18 and the trends are discussed below. In all tests, one or two large MG-fractures (types (i) and (ii)) cross the entire section. These fractures can be related to the sides of the heating element and are not, therefore, related to any fracture likely to occur next to a fault plane but are an artifact of the experimental boundary conditions. In the two tests where the average power dissipation was 0.96 MWm^{-2} (Tests nos. 7 and 13), more of these fractures developed. Some could not be associated with the irregular heating, because they occur in the centre of the blocks. These appear to be a genuine response of the rock to the heating pulse. Large fractures such as these (Plate 12a,b) oriented approximately perpendicular to the heated surface and extending to a depth of at least 25 mm, are only seen in samples whose calculated surface temperature is in excess of 700°C.

CGB-fractures are generally restricted to within 3 to 5 mm of the heated surface, where the intragranular fracture density is also greatest. The number of fractured grain boundaries on the heated surface decreases steadily from a constant value of about 40-50%

Sample Number	Heated Surface	Axial Section	Maximum Calculated Surface Temperature(^{o}C)/ Normal Stress (MPa)
8	No MG-fractures. Open CGB-fractures on 90% of all grain boundaries. Intragranular fractures in 90% of all grains. Shadow fractures in quartz.	3-MG-fracture (ii) – sub-parallel to heated surface and cross entire section. CGB-fractures on 30-40% of boundaries within 20 mm of heated surface. Intragranular fracture in 70% of all grains. Within 2-5 mm of the heated surface they are sub-parallel to it, elsewhere. they are fewer in number with no preferred orientation.	$820/0.1$
17	No MG-fractures. Open CGB-fractures on 80% of all boundaries (on all quartz-quartz and quartz-feldspar boundaries. Intragranular fractures in 90% of all grains. Shadow fractures in quartz restricted to localised areas.	2-MG-fracture (ii) – at low angle ($\simeq 30^{o}$) to heated surface, crossing the entire section. CGB-fractures on 20-30% of boundaries within 20 mm of heated surface. Intragranular fracture in 70% of all grains (less fractures per grain than Test 8). No preferred orientation of these fractures exists.	$788/5.2$
9	No MG-fractures. Open CGB-fractures on 60% all boundaries but no longer surround grains but form continuous fractures. Intragranular fractures in 90% of all grains. Shadow-fractures in quartz restricted to localised areas.	1-MG-fracture (ii) – at high angle to heated surface ($>80^{o}$), crosses entire section. CGB-fractures on 20-30% of boundaries within 10 mm of heated surface. Intragranular fracture in 70% of all grains, within 6-8 mm of the heated surface they are sub-parallel to it. Elsewhere they are fewer in number with no preferred orientation.	$798/10.3$
14	Section broken – half missing. 1-MG-fracture (ii) – crosses entire section and follows grain boundaries for half its length. CGB-fractures all closed and occur on 50% of all boundaries. Intragranular fractures in 90% of all grains. Shadow fractures in very few quartz grains.	1-MG-fracture (ii) – at high angle to heated surface ($>80^{o}$), crosses entire section. CGB-fractures on 20-30% boundaries within 5 mm of heated surface. Intragranular fracture in 60-70% of all grains with no preferred orientation.	$750/15.4$
10	1-MG-fracture (ii) – crosses half section and follows grain boundaries for half its length. CGB-fractures along 40-50% of all grain boundaries. Intragranular fractures in 80% of all grains. No shadow fractures in quartz.	Section broken – half missing. 1-MG-fracture (ii) – at high angle to heated surface ($>80^{o}$). CGB-fractures on 10-20% of all boundaries. Intragranular fractures in most quartz-grains and 50% of feldspar, with no preferred orientation.	$698/19.3$

Fig. 9.19. Variation of microfracture pattern with normal stress

Sample Number	Heated Surface	Axial Section	Maximum Calculated Surface Temperature(°C)/ Normal Stress (MPa)
15	2-MG-fractures (ii) - cross entire section and follow grain boundaries for 25% of their length. CGB-fracture along 50% of all grain boundaries. Intragranular fracture in 80% of all grains, but small MGF crossing 2-3 grains are common. No shadow fractures in quartz.	1-MG-fracture (iii) - at high angle to heated surface (>80°) and crosses entire section. CGB-fractures along 10% of all boundaries. Intragranular fracture in most quartz grains and 50% feldspar with no preferred orientation.	676/24.6
11	1-MG-fracture (ii) } 1-MG-fracture (iii) } Cross entire section and follow grain boundaries for 25% of their length. CGB-fractures along 50% of all grain boundaries. Intragranular fracture in 80% of all grains. Small MGF crossing 3-5 grains are common. No shadow fractures in quartz.	1-MG-fracture (i) } 1-MG-fracture (ii) } at high angles to heated surface (>80°) and crosses entire section. CGB-fractures on 10% of all boundaries. Intragranular fracture in most quartz grains and 50% feldspar with no preferred orientation.	681/29.7
16	1-MG-fracture (iii) - crosses entire section and follows grain boundaries for 25% of its length CGB-fractures along 50% of all grain boundaries. Intragranular fracture in 80% of all grains. Small MGF which follow grain boundaries over part of their length cross more than 5 grains. No shadow fractures in quartz.	Damaged thin section. 1-MG-fracture (ii) - at high angle to heated surface (>80°) and crosses entire section. CGB-fractures on 10% of all boundaries. Intragranular fracture in most quartz grains and 50% feldspar with no preferred orientation.	743/34.7
13 7	See Fig. 9.20		728/39.9 671/41.2
18	Section damaged (half missing) 1-MG-fracture (ii) } 1-MG-fracture (iii) } Cross entire section and follow grain boundaries for 25% of their lengths. CGB-fractures along 50% of all grain boundaries. Intragranular fracture in 80% of all grains. Small MGF cross several grains (3-7). No shadow fractures in quartz.	Section damaged (half missing) 1-MG-fractures (i) } 1-MG-fracture (ii) } at high angles to heated surface (>80°) and cross entire section. CGB-fractures on all quartz-quartz boundaries within 5 mm of heated surface. Intragranular fracture in most quartz grains and 50% feldspar with no preferred orientation.	728/45.0

Fig. 9.19. (cont.)

Sample Number	Heated Surface	Axial Section	Maximum Calculated Surface Temperature($^{\circ}$C)/ Normal Stress (MPa)
12	No thin section available		$671/49.9$
19	1-MG-fracture (ii) - Crosses entire section and follows grain boundaries for 50% of its length. CGB-fractures along 40% of all grain boundaries. Intragranular fracture in 80% of all grains. Small MGF cross several grains (3-7) No shadow fractures in quartz.	1-MG-fracture (i) ┐ at high angles to heated surface 2-MG-fracture (ii) ┘ (>80°) and cross entire section. CGB-fractures on most quartz-quartz boundaries within 5 mm of heated surface. Intragranular fractures in most quartz grains and 50% of feldspar with no preferred orientation.	$697/55.4$

Fig. 9.19. (cont.)

Plate 12

All photographs are the same scale. Scale bar = 0.1 mm.

a   Test no. 13 showing a large MG-fracture sub-perpendicular to the heated surface (upper, just off picture).

b   Test no. 7 showing a large MG-fracture sub-perpendicular to the heated surface (upper, just off picture).

c   Test no. 13 showing CGB-fractures on 40-50% of all grain boundaries on the heated surface. These fractures are most common on quartz-quartz boundaries.

d   Test no. 22 with rare intragrain or CGB-fractures.

e   Test no. 7 with intragrain fractures within most quartz grains and CGB-fractures between all quartz grains on the heated surface.

f   Intragrain fractures concentrated within 5 mm of the heated surface (upper, just off picture).
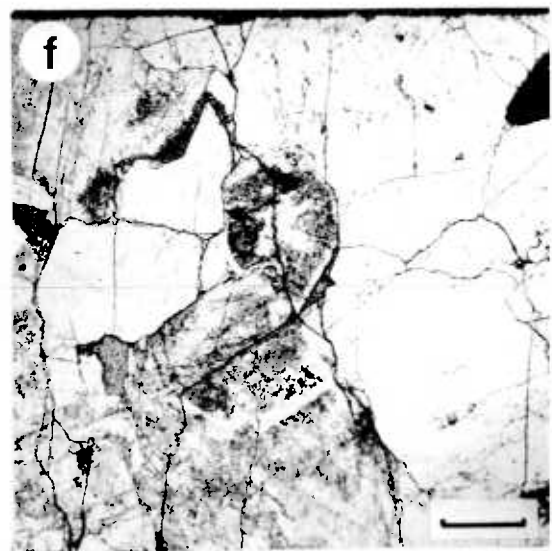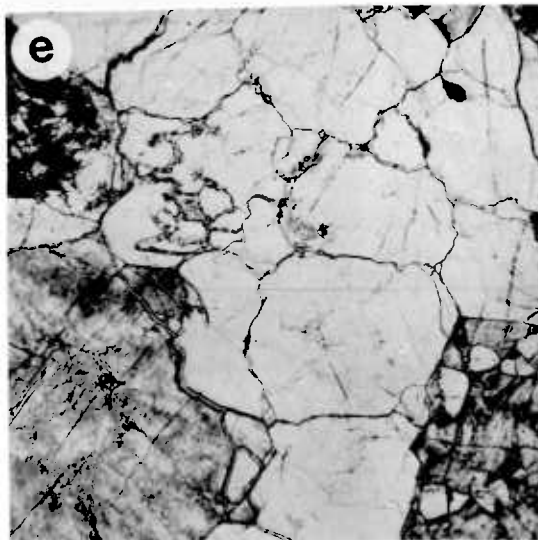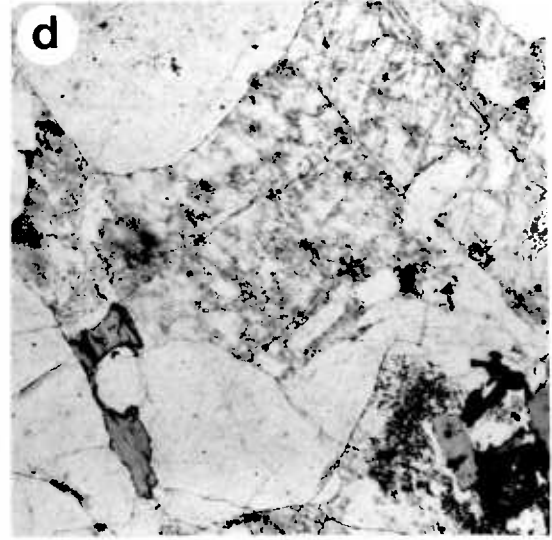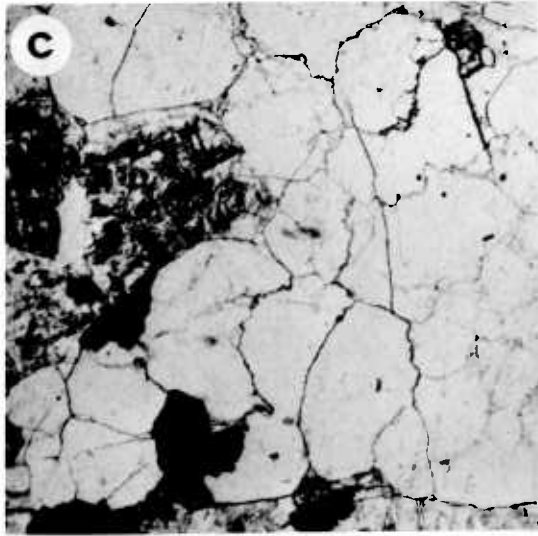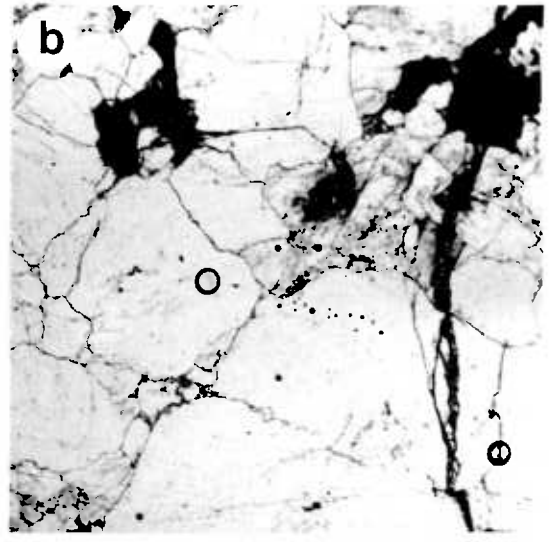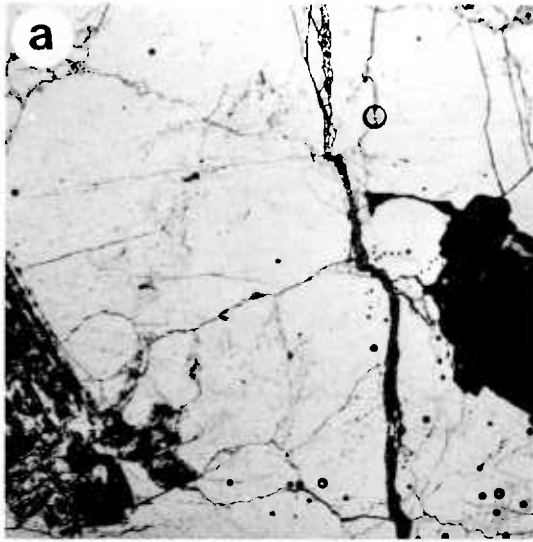
of all boundaries, at calculated surface temperatures exceeding 620°C
(Plate 12c), to well below 5% for temperatures of 250°C (Plate 12d).
They are most commonly developed on quartz-quartz boundaries.

Intragranular fractures occur at all orientations over all of the
thin sections (Plate 12e). Only in tests 7 and 13, where they are
concentrated within 3 to 5 mm of the heated surface, can they be directly
attributed to heating (Plate 12f). However, it is probable that many
of these fractures do result from heating, as they are absent in thin-
sections of the unheated material.

In summary, large fractures only occur when the surface temperatures
exceed about 700°C. CGB-fractures and intragranular fractures may be
related to the α/β transition of quartz (573°C), since they are more
common on quartz-quartz boundaries and within quartz grains respectively.
Fracture densities are also much higher in those volumes of rock where
temperatures have exceeded 550-600°C.

9.7.7. Effect of Normal Stress on the Fracture Pattern

Individual fracture patterns are described in Fig. 9.19 and the
main trends are discussed below. At low normal stresses (0.1-5.2 MPa)
almost every grain on the heated surface is separated from the adjacent
grain by an open CGB-fracture (Plate 13a). This zone of fracturing
extends to depths of about 20 mm at these low normal stresses and is
accompanied, in the upper 8 mm, by many intragranular fractures which
lie sub-parallel to the heated surface. At these low stresses, large
MG-fractures also form at acute angles ($\leqslant 30°$) with the heated surface
(Plate 13b).

As the normal stress increases to 19.3 MPa, the CGB-fractures
become closed and the intragranular fractures no longer form sub-
parallel to the heated surface. The closed CGB-fractures then only
extend to depths of about 5 mm, and the large MG-fractures form sub-perpen-
dicular to the heated surface (Plate 13c). Small MG-fractures that
cross 2-3 grains only, are first seen at this normal stress (Plate 13d).

At a stress of 29.7 MPa, closed CGB-fractures still occur on and
within a few millimetres of the heated surface. The MG-fractures on
the heated surface are branched and form multiple, rather than single
fractures (Plate 13e). Small MG-fractures also develop on this surface,
extending across 2-5 grains.

At normal stresses above 40 MPa, MG-fracture networks are common

Plate 13

All photographs are the same scale. Scale bar = 0.1 mm.

a   Sample heated at a normal stress of 0.1 MPa showing CGB-fractures
      on almost every grain boundary on the heated surface.

b   Sample heated at a normal stress of 0.1 MPa showing an MG-fracture
      at an angle of about 30° with the heated surface (upper). Note also
      high level of intragrain and CGB-fracture close to the heated surface.

c   Sample heated at 19.3 MPa with an MG-fracture sub-perpendicular to
      the heated surface (upper).

d   Sample heated at 19.3 MPa showing small MG-fractures crossing 2-3
      grains on the heated surface.

e   Sample heated at a normal stress of 29.7 MPa with a multiple MG-
      fracture on the heated surface.

f   Sample heated at a normal stress of 40 MPa with an MG-fracture net-
      work in quartz on the heated surface.
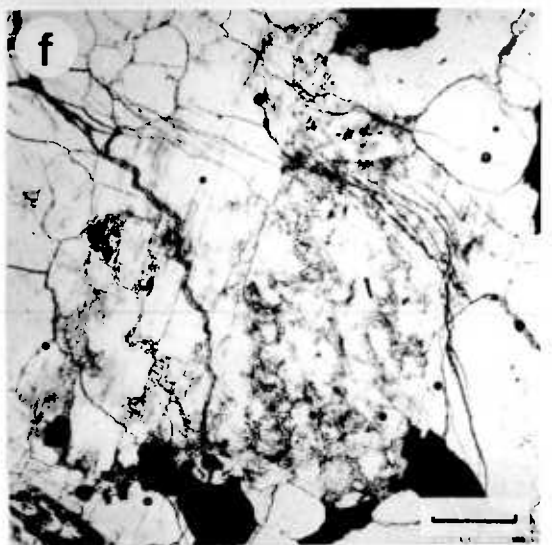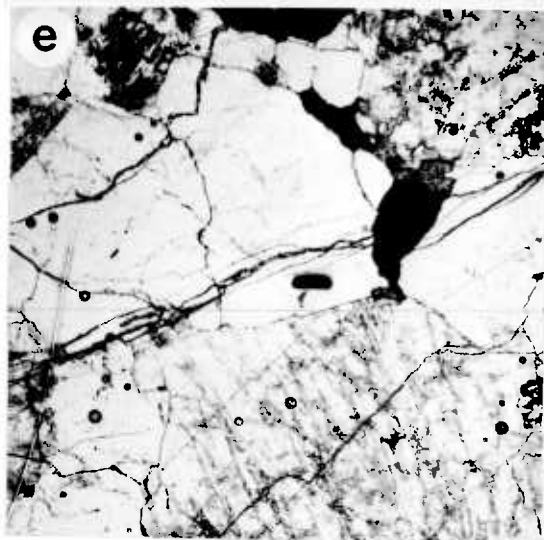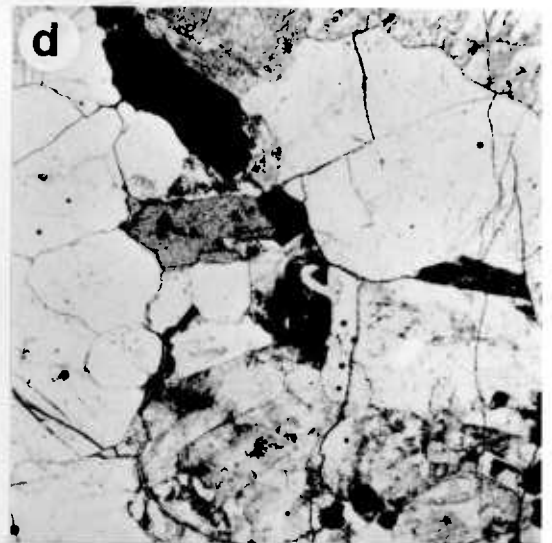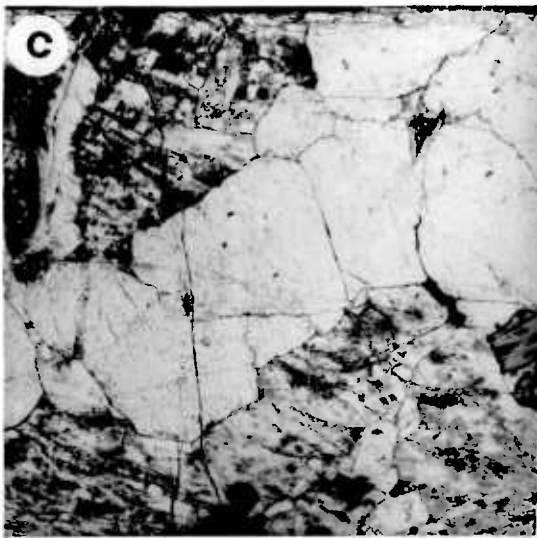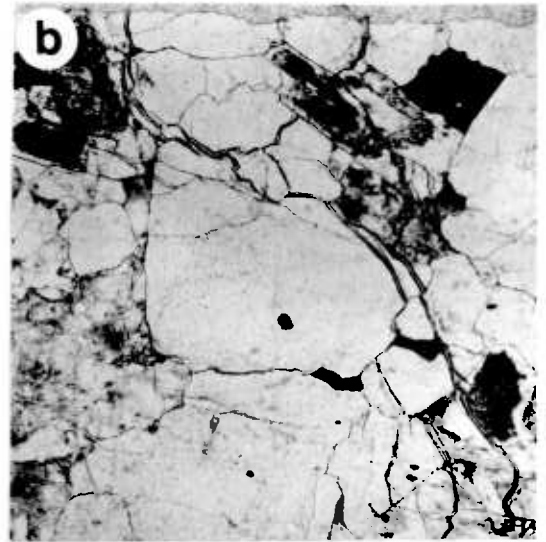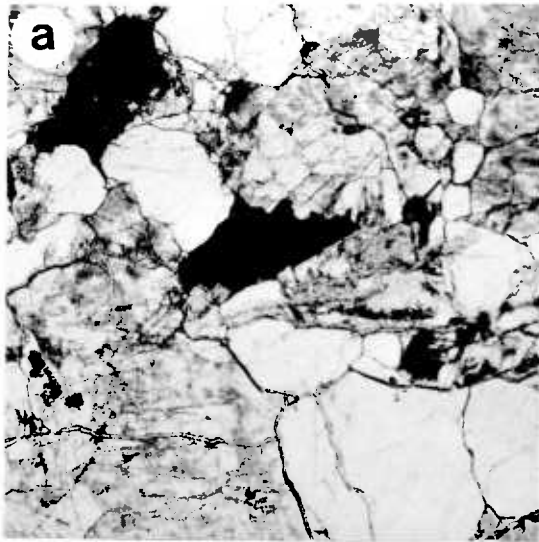
Plate 14

All photographs are the same scale. Scale bar = 0.1 mm.

a   CGB-fractures on 40-50% of all grain boundaries on the heated surface
     after 1-2 cycles.

b   CGB-fractures on 70-80% of all grain boundaries on the heated surface
     after 6 or more cycles.

c   CGB-fractures and intragrain fractures are most common close to the
     heated surface (upper) after 6 cycles.

d   CGB-fractures within 10 mm of the heated surface (upper) after 10
     cycles. Intragrain fractures are also common in this region.

e   Very few intragrain fractures after only 2 cycles.

f   After more than 15 cycles intragrain fractures in quartz are common.

| Sample Number	Heated Surface	Axial Section	Maximum Calculated Average Surface Temperature(°C)/ Number of Cycles
20	See Fig. 9.21.		$622/1$
29	1-MG-fracture (ii) – crosses entire section and follows grain boundaries for 50% of its length. Open CGB-fractures along 40-50% of all grain boundaries. Intragranular fracture in 60-70% of all grains. Small MG-fractures cross several grains (3-7).	1-MG-fracture (ii) – at high angle to heated surface (>80°) and crosses entire section. CGB-fractures on very few quartz-quartz boundaries only. Intragranular fracture in 50% of quartz grains and very few feldspar grains. Small MG-fractures (i) cross 2-3 grains sub-perpendicular to heated surface about 10 mm from it.	$616/2\frac{1}{2}$
33	Section damaged. 2-MG-fractures (ii) – cross entire section and follow grain boundaries for 25% of its length. CGB-fractures on 80% of all grain boundaries. Intragranular fracture in 60-70% of all grains. Small MG-fractures crossing several grains (3-7) and following grain boundaries over part of their length.	Section damaged (half missing) 1-MG-fracture (i) } at high angles to heated surface 1-MG-fracture (ii) } (>80°) and cross entire section. CGB-fractures on some quartz-quartz boundaries only. Intragranular fracture in 50% of quartz grains and few feldspar grains.	$562/6$
31	3-MG-fractures (ii) – cross entire section and follow grain boundaries for 75% of their lengths. Open CGB-fractures on 70% of all grain boundaries. Intragranular fracture in 60-70% of all grains. Small MG-fractures cross several grains (3-7).	2-MG-fractures (ii) – at high angle to heated surface (>80°) and crosses entire section. CGB-fractures on 50% of all grain boundaries within 10 mm of the heated surface. Intragranular fracture in quartz and feldspar within 10 mm of the heated surface. Small MG-fractures (i) sub-perpendicular to heated surface.	$603/10\frac{1}{2}$
26	1-MG-fracture (iii) – crosses ½ section, follows grain boundaries for 50% of its length Open CGB-fractures on 70% of all grain boundaries – forms continuous fractures. Intragranular fracture in 60-70% of all grains. Small MG-fractures cross several grains (3-7) over whole surface.	1-MG-fracture (ii) – at high angle to heated surface (>80°) and crosses entire section. CGB-fractures on 70% of all grain boundaries within 10 mm of the heated surface. Intragranular fracture in 50% of quartz grains and few feldspar grains in whole section.	$580/15$
32	1-MG-fracture (iii) – crosses entire section and follows grain boundaries for 50% of its length. Open CGB-fractures on 90% of all grain boundaries. Intragranular fracture in 90% of all grains – glaze-like fracture pattern over whole surface.	4-MG-fractures (ii) – at high angles to heated surface (>80°) and cross entire section. CGB-fractures on 50% of all grain boundaries. Intragranular fracture in 50% of quartz grains and few feldspar grains in whole section. Small MG-fractures (i), sub-perpendicular to heated surface are common.	$610/49$

Fig. 9.20. Variation of microfracture pattern with thermal cycling (higher level of power dissipation)

Sample Number	Heated Surface	Axial Section	Maximum Calculated Average Surface Temperature(°C)/ Number of Cycles
21	See Fig. 9.21		447/1
25	1-MG-fracture (i)(i) - Crosses entire section. 3-MG-fractures (ii)(ii) - Cross 50% of section and follow grain boundaries for 50% of their length. Open CGB-fractures on 40% of all grain boundaries. Intragranular fracture in most quartz and very few feldspar grains.	Section damaged (half missing) 3-MG-fractures (ii) - at high angles to heated surface (>80°) and cross entire section. CGB-fractures on 20% of grain boundaries within 5 mm of heated surface. Intragranular fracture in 30% quartz grains, especially within 5 mm of heated surface.	496/6½
28	3-MG-fractures (ii) - Cross entire section and follow grain boundaries for 50% of their length. Open CGB-fractures on 60% of all grain boundaries. Intragranular fracture in most quartz and very few feldspar grains.	3-MG-fractures (ii) - at high angles to heated surface (>80°) and cross 30% of section. CGB-fractures on 50% grain boundaries within 10 mm of heated surface. Intragranular fracture in 30% of quartz grains over the entire slide very few in feldspar.	505/10
27	3-MG-fractures (ii) - Cross entire slide and follow grain boundaries for 60% of their length. Open CGB-fractures on 80% of all grain boundaries. Intragranular fracture in 60% of all grains.	Section damaged (half missing) 1-MG-fractures (i) - Crosses entire section. 3-MG-fractures (ii) - Cross 50% of section. All intersect heated surface at high angles (>80°). CGB-fractures on 50% of grain boundaries within 10 mm of heated surface. Intragranular fracture in 30% of the quartz grains over the entire slide. Very few in feldspar.	491/20

Fig. 9.21. Variation of microfracture pattern with thermal cycling (lower level of power dissipation)

on the heated surface. They consist of small MG-fractures crossing several grains and partly following grain boundaries (Plate 13f). The traces of the MG-fractures are sub-perpendicular to the heated surface and become straighter at higher normal stresses and grade into type (i).

9.7.8. Effect of Thermal Cycling on the Fracture Pattern

Two series of thermal cycling experiments were performed at different levels of power dissipation and give consistent results (Fig. 9.20, 9.21). The number of large MG-fractures showed no significant variation with increasing thermal cycling but the small scale deformation intensified.

CGB-fractures show an increase in density from 40 to 50% of existing grain boundaries after 1-2 cycles to 70-80% for 6 and more cycles (Plate 14a,b). In the series performed at the lower level of power dissipation, there is a continuous increase in the number of CGB-fractures with increasing thermal cycling. The depth to which these fractures extend increases to about 10 mm after 10 cycles from a narrow strip of a few millimetres after 1 to 6 cycles (Plate 14c,d).

The degree of intragranular fracturing remains roughly constant in all tests but may show an increase when the rock has undergone in excess of 15 cycles. This increase was seen only in the higher power dissipation series, and may be caused by other factors (Plate 14e,f).

9.8. Fracture Surface Morphology

Optical microscopy enables one to recognise three fracture types (Section 9.7): large MG-fractures (types (i) - (iv)), CGB-fractures and intragranular fractures. It gives little information, however, on the actual processes of fracture initiation and growth. Theoretically, microstructures of thermal origin initiating around microstructural flaws (grain boundaries, cleavage planes, fluid inclusions etc.) as a result of heating should be extensional. Optical studies of all heated samples suggest that this may be the case. There is no apparent shear displacement across any fracture, nor are any wear particles visible.

To determine the nature of all three fracture types, sample

Plate 15

a   Conchoidal multigrain fracture in quartz. Note the change in
     orientation of the ridges at the crystal boundary in the centre
     of the crystal. Scale bar = 10 μm.

b   Conchoidal multigrain fracture in quartz. Scale bar = 20 μm.

c   As 15b. Scale bar = 5 μm.

d   Multigrain fracture stepping across closely spaced cleavage planes
     in feldspar. Scale bar = 10 μm.

e   Cleavage fracture in biotite with a zircon crystal in the centre
     of the photograph. Scale bar = 20 μm.

f   Cleavage fracture in biotite with a zircon crystal.
     Scale bar = 30 μm.
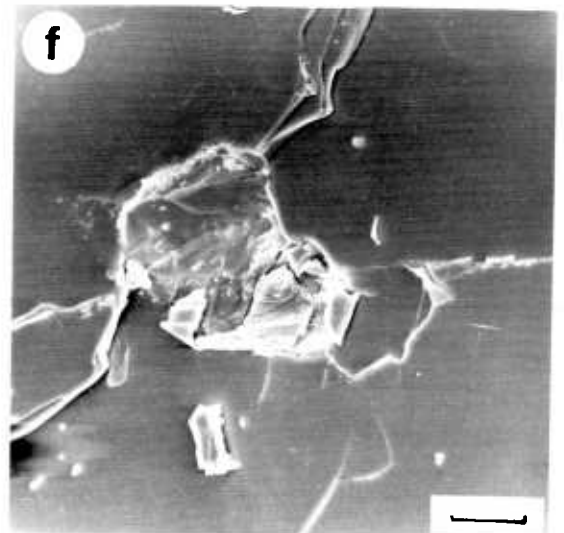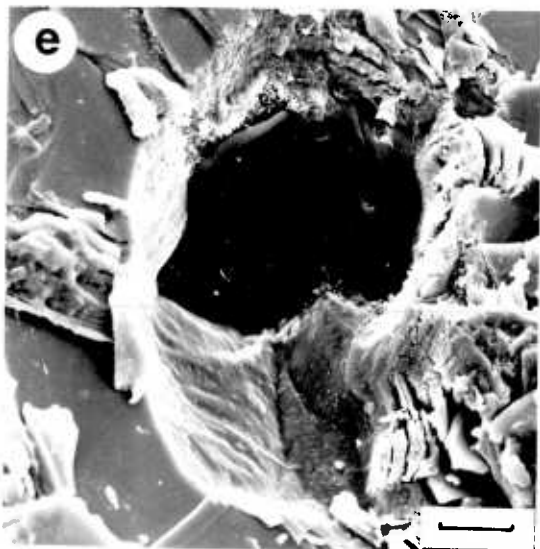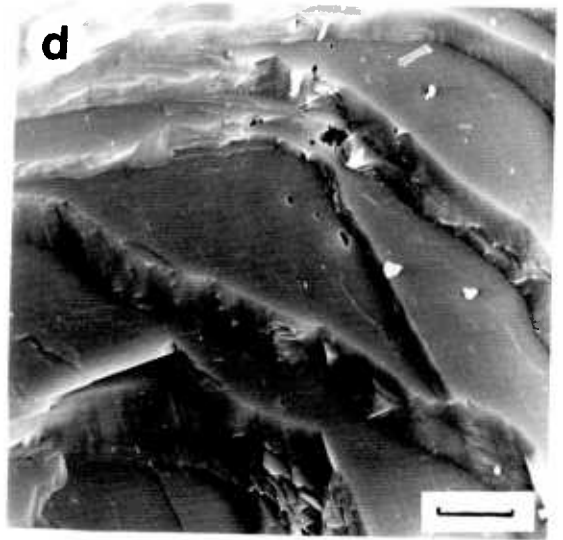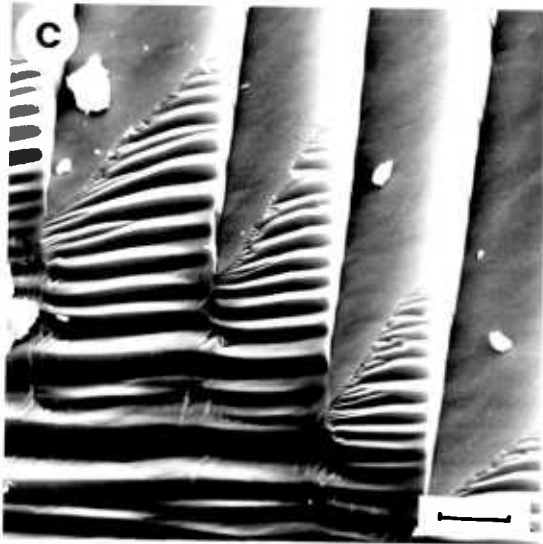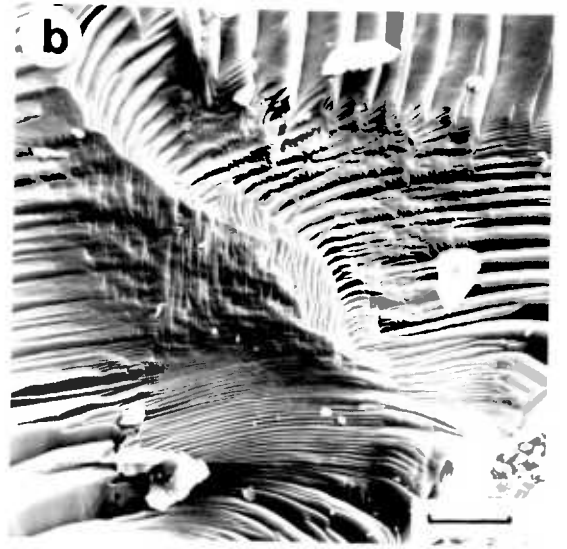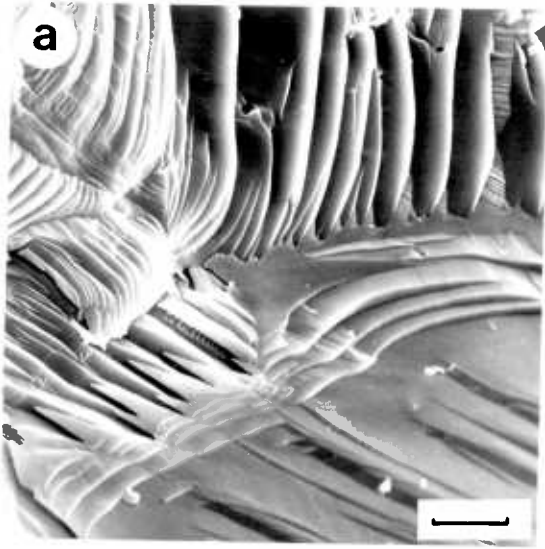
blocks from tests nos. 11, 12 and 17, and the unheated sample, were used in a fracture surface morphology study using a scanning electron microscope (SEM).

9.8.1. Sample Preparation

In each case the sample block that had not been impregnated with Araldite was used. Samples of the large open MG-fractures were easily obtained as the samples readily parted along these surfaces. In order to study the CGB-fractures and intragranular fractures, the sample was broken mechanically into smaller fragments which could then be carefully pulled apart along pre-existing thermal fractures. It is possible that some of these fractures may be of mechanical, not thermal origin, but since completely undeformed material prepared in this manner did not possess these closely spaced fractures, their thermal origin seems probable.

The small rock fragments were mounted on metal stubs, cleaned of dust and minute particles electrostatically and sputter coated with gold immediately before observation.

9.8.2. Multigrain Fracture

The large MG-fracture surfaces in the heated and unheated blocks cannot be distinguished. All of the surfaces show no evidence for shear but are rough with no wear features or debris.

Quartz grains invariably exhibit conchoidal fracture (Plate 15a) which is described by Thirumalai and Cheung (1972) as typical of a tensile fracture induced by thermal stress. In fact, conchoidal fracture is generally very common in quartz and need not necessarily indicate a thermal origin for the fracture. The undamaged, delicate ridges do indicate extensional fracture. Although quartz has no good cleavage plane there is some crystallographic control on the fracture surface as shown by the sudden changes in the orientation of the conchoidal ridges as the fracture crosses grain boundaries (Plate 15b,c).

Both feldspar (Plate 15d) and mica (Plate 15e,f) generally fracture along their cleavage planes, although fractures almost perpendicular to these planes are also seen. Where the fracture orientation is at a low angle to the cleavage planes, steps occur in the fracture surface as it crosses to an adjacent cleavage plane. Almost every fracture that crosses a biotite grain can be seen, under the SEM, to contain at least one zircon crystal (Plate 15e,f; 16a,b). Although zircon is

185

Plate 16

a   Zircon crystals in a fracture surface crossing the biotite cleavage. Scale bar = 10 µm.

b   Zircon crystal in biotite having deflected the fracture onto adjacent cleavage planes. Scale bar = µm.

c   Fluid inclusions on an intragranular fracture in quartz. Scale bar = 5 µm.

d   As 16c. Scale bar = 2 µm.

e   Intragranular cleavage fracture in feldspar. Scale bar = 5 µm.

f   As 16e. Scale bar = 5 µm.
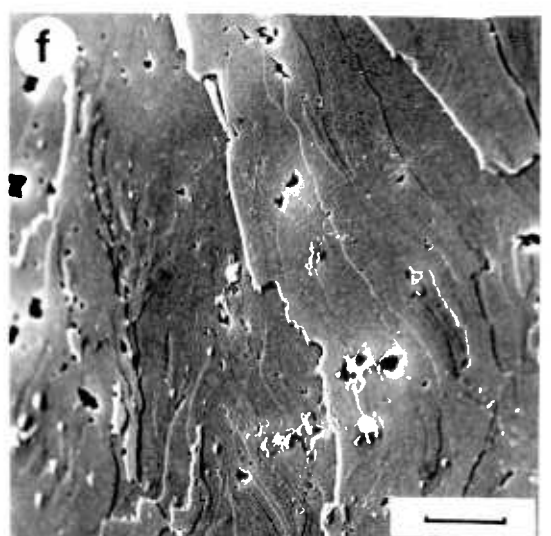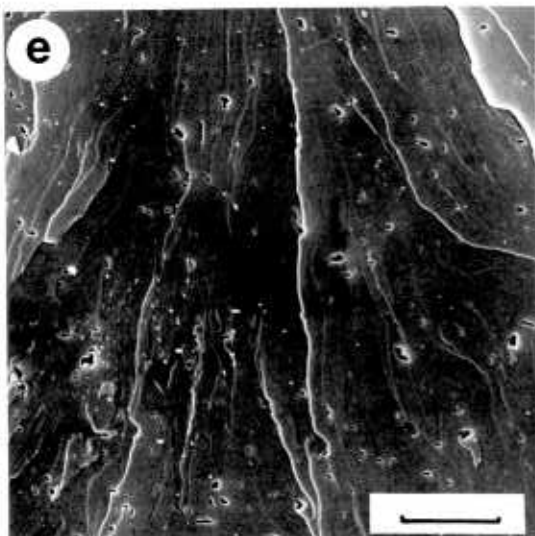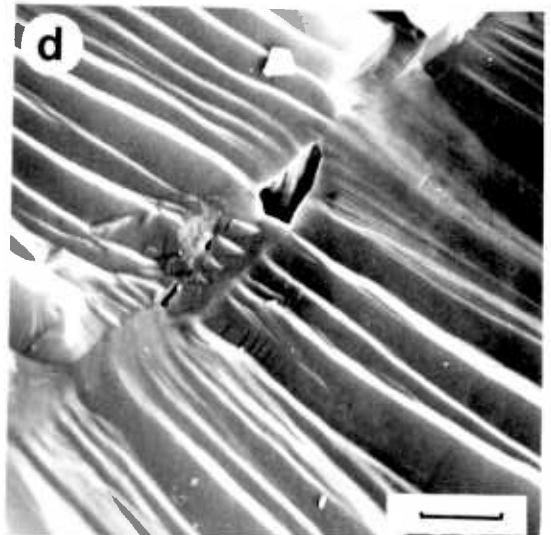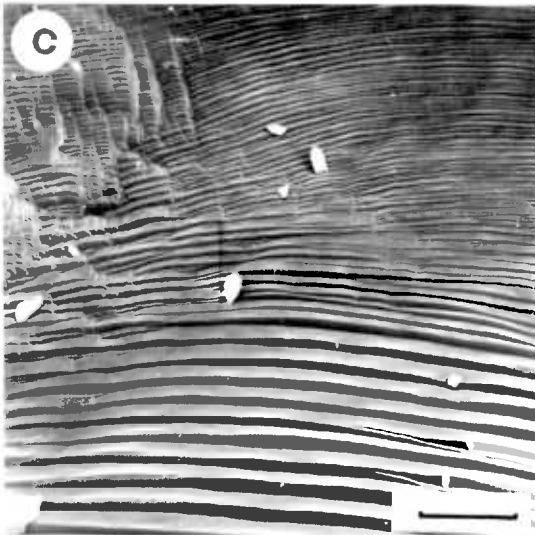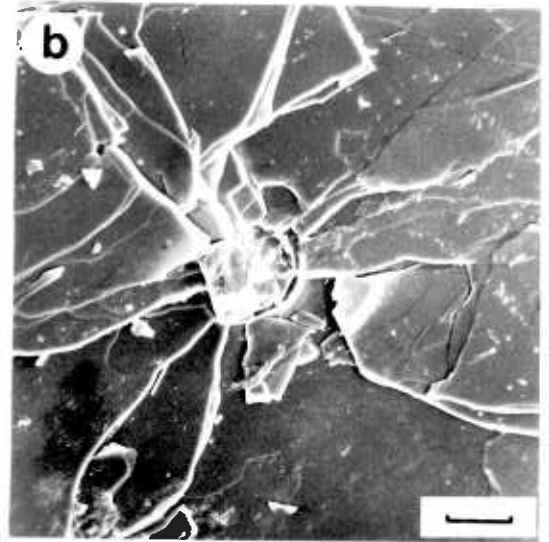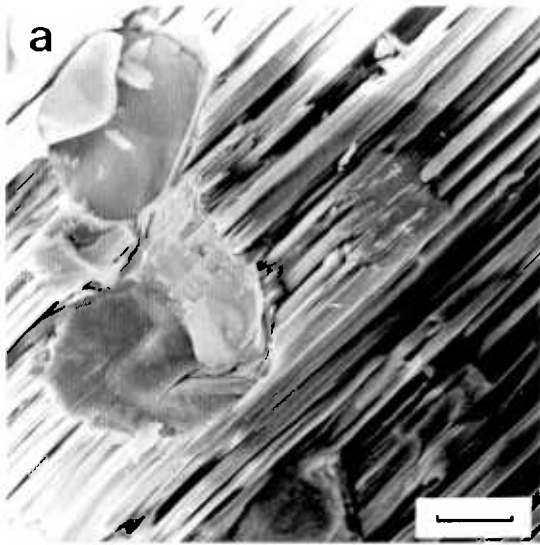
abundant in the biotite of this rock, their appearance on every fracture surface studied suggests that their presence may control either fracture initiation or propogation. There is no direct evidence indicating fracture initiation at these inclusions however, as a result of differential thermal expansion between inclusion and host, they would be expected to become centres of high local stress which may be sufficient to initiate microfractures. Some zircon crystals have acted as obstacles to the propagating rupture front and deflected it onto partial fronts on adjacent planes (Plate 16b).

9.8.3. Coincident Grain Boundary and Intragranular Fractures

The features seen on the surfaces of the intragranular fractures are very similar to those described above, although the fracture surfaces are necessarily much smaller. Fluid inclusions are seen on some quartz fracture surfaces (Plate 16c,d) but appear to have had no influence on the fracture path.

Fractures across feldspar grains more commonly follow cleavage planes, without stepping across them (Plate 16e,f) and the rare fractures crossing biotite grains cannot be attributed to a thermal source. Those that are seen may have originated from sample preparation.

9.8.4. Heated Surface

The heated surfaces of samples 12 and 17 were also studied to ascertain whether any partial surface melting had occurred on a microscopic scale. On each sample, small patches of glassy material were seen in association with fractures at high angles to the surface (Plate 17a-d). The only evidence that this material is in fact glass comes from its vesicular structure (Plate 17d), or its stringy, non-crystalline appearance (Plate 17a,b).

Complementary evidence for partial melting associated with fractures intersecting the heated surface, comes from the existence of vesicular material within 0.4 mm of the heated surface on one of these fractures (Plate 17e,f) which appears to be coated with a thin layer of glass.

The origin of this glass remains a problem since there is no obvious cavity from which the material has been extruded. It seems likely, in view of the extreme thinness of the layer ($<$ 10 μm), that it formed in situ on the heated surface and _may_ subsequently have been injected into the adjacent fracture.

Plate 17

a   Patch of glassy material on heated surface.   Scale bar = 30 µm.

b   As 17a.   Scale bar = 5 µm.

c   As 17a.   Scale bar = 50 µm.

d   Glassy material on heated surface containing many vesicles.
     Scale bar = 5 µm.

e   Vesicular glass on a fracture perpendicular to the heated surface.
     Scale bar = 100 µm.

f   As 17e.   Scale bar = 10 µm.
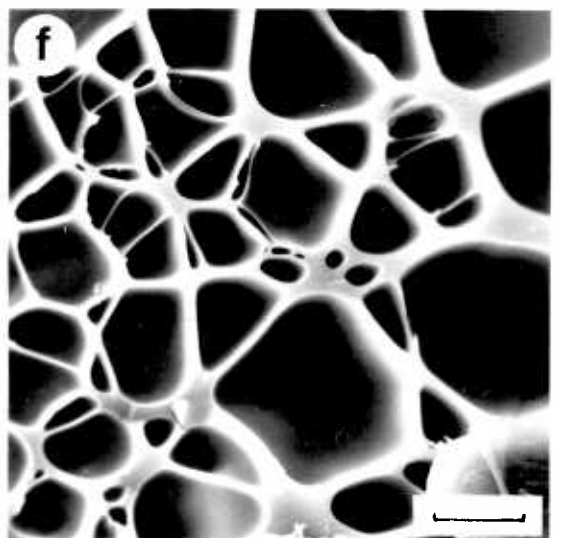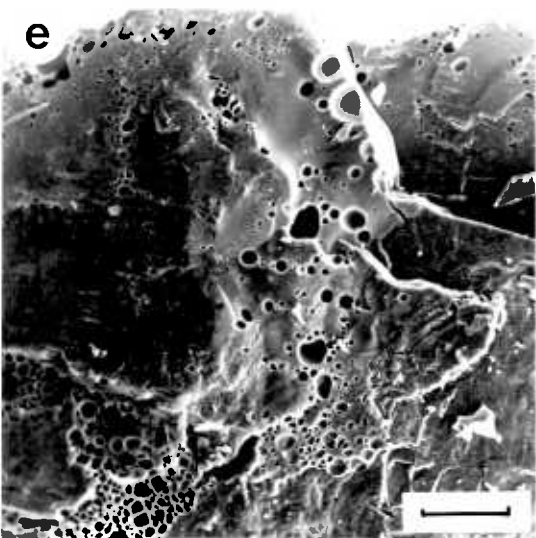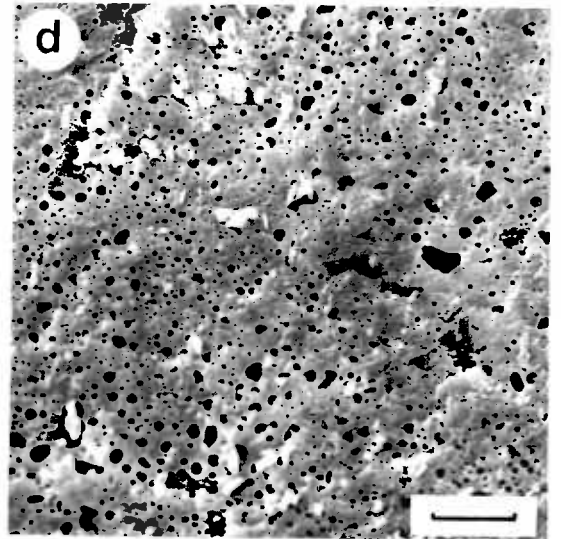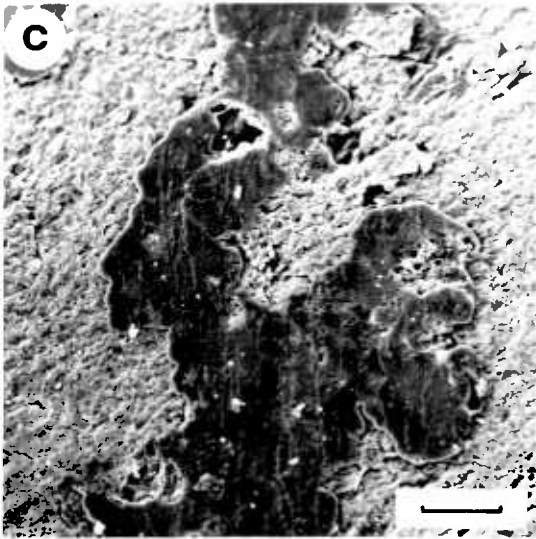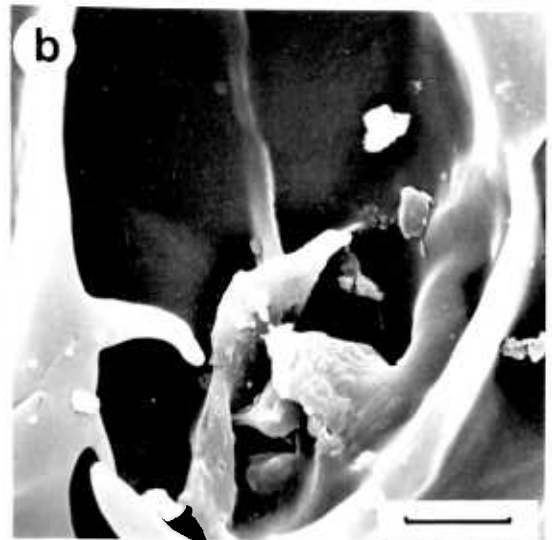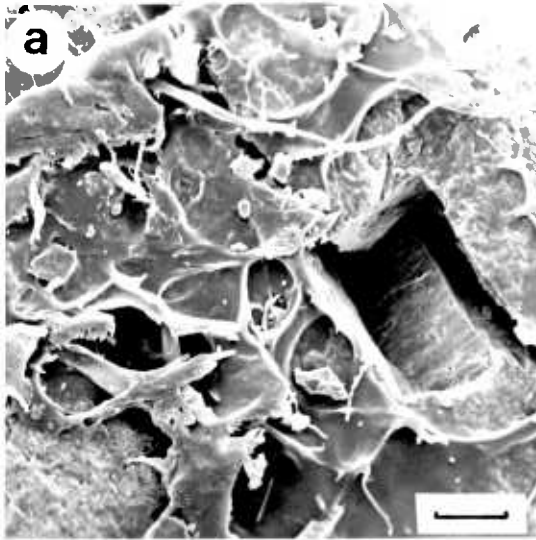
9.9. Conclusions

The experiments described in this section complement theoretical work in indicating that heat generated during seismic faulting may, under certain environmental conditions (Section 5.6) cause thermal stresses adjacent to the fault plane that are large enough to fracture the surrounding rock. The levels of power dissipation investigated experimentally ($\leqslant 1.14$ MWm^{-2}) approach those one may reasonably expect to occur on natural faults during seismic slip (Section 5.6). With care, the results discussed here may be extrapolated to higher levels of power dissipation.

From the experimental results, it may be inferred that the frictional heating resulting from slip during a single seismic event may induce both microstructural damage and macroscopic fracturing. It is almost impossible to assess the influence of the experimental boundary conditions (especially block geometry and incomplete surface heating) on the thermal fracture pattern. These factors are particularly important when interpreting the importance of the experimentally produced macroscopic fractures adjacent to a seismically active fault. In the experiments these "large" fractures increase in number with increasing power dissipation and this increase appears to be a genuine response of the rock to rapid heating, rather than an artifact of the experiment.

At low normal stresses the macroscopic fractures in the experiments make angles of about 30° with the heated surface and may be incipient shears. Under very low load stresses the thermally induced stress field alone controls the fracture orientation. With a greater normal stress across the heated surface ($\geqslant 15$ MPa) these shear fractures are suppressed and extensional fractures perpendicular to the heated surface develop. Under these conditions the orientation of the thermally induced macroscopic fractures appears to be controlled by the stresses induced by the external loading which, away from the heated surface, exceed the thermal stresses. This was predicted by thermal stress theory which indicated that the thermal stress field is only significant within 10 mm of the heated surface. It is, therefore, the thermal stresses that bring about fracture initiation at the heated surface but the external, non-thermal stress field that controls fracture propogation away from the heated surface. It is possible that these macroscopic fractures seen in the experiments initiate as shears but change their character as the local stress field

changes and become extensional for most of their length.

The correlation of the experimentally produced microstructural damage, involving CGB-fractures and intragrain fractures, with seismic slip is less complex since damaged areas unlikely to be affected by the experimental conditions, can be chosen for study (that is the interior parts of the sample blocks). Most of this microstructural damage is concentrated within a few millimetres of the heated surface whatever the experimental conditions, although less intense fracturing occurs throughout the blocks. The presence of quartz strongly influences the level of microstructural, thermal damage as intragranular fractures are concentrated within quartz grains and CGB-fractures are most common on quartz-quartz boundaries. These effects are thought to be related to the sudden volume change quartz undergoes as it passes through the α/β transition, or from the overpressuring of fluid inclusions.

Although these experimental results must be applied to natural faulting with care, it is apparent that were the heated surface (fault plane) under shear, the thin layer of microscopically fractured grain would be easily incorporated into a gouge layer. The effect of the larger fractures is less clear, it is likely that some of them will develop during seismic slip and propogate perpendicular to the minimum stress of the stress field surrounding the fault. The effect of the experimental boundary conditions make it impossible to ascertain the fracture density or the precise volume of rock affected. Their presence will weaken the rock adjacent to the fault and this process may widen the fracture zone around it.

The foregoing discussion refers essentially to the deformation resulting from a single slip increment in initially intact rock. The experiments model slip on very shallow faults where repeated slip increments and, therefore, many cycles of frictional heating may have produced a highly fractured fault zone. The experiments investigating the effects of repeated thermal cycling, without mechanical wear between cycles, show that cycling does not increase the density of the macroscopic fractures. The level of microscopic damage and the volume of rock affected by it is, however, increased substantially. Whether or not this effect would also be seen on a shallow, seismically active fault within a well developed fracture zone, where much of the thermal expansion may be accommodated within the zone without the development of high thermal stresses, remains a point for discussion.

CHAPTER 10

SUMMARY AND CONCLUSIONS

10.1. Introduction

This study has been concerned with faults and faulting at shallow levels (< 10-15 km) in quartzo-feldspathic crust. Much current work is directed towards methods of predicting and preventing the release of seismic wave energy which accompanies sudden slip across a fault. Interest in this field of study has stemmed from the realisation that slip across pre-existing faults is probably the most common earthquake source at shallow depths.

This project is founded on the belief that the textures and micro-structural characteristics of fault rocks are a tangible source of information on the environmental conditions under which shear occurred and the processes by which the fault rock was produced. The aims of this study are listed below:

1. To provide textural descriptions of cataclastic rocks from the Walls Boundary Fault zone, Shetland and the Loch Eribol region, Sutherland.

2. To ascertain from microstructural and mineralogical evidence the depths at which these rocks developed.

3. To assess the role of fluids both during and after slip in the fault zones studied.

4. To determine whether the fault rocks studied had undergone both mineralogical and chemical changes when compared to their parent rocks.

5. To establish microstructural criteria for distinguishing fault rocks produced by steady state aseismic creep from those produced by episodic, seismic slip.

Of these aims the last two were not achieved. Chemical mass balancing was not attempted since the fine grain size of the cata-clasites made modal analysis impossible. Considerable attention was paid to the possibility of recognising localised thermal effects adjacent to faults, as a means for distinguishing the products of aseismic and seismic slip. To this end, a series of transient heating experiments were carried out in order to simulate the likely

power dissipation during seismic slip (Chapter 9). However, it has so
far not proved possible to distinguish thermal fragmentation products
from those arising from mechanical wear. Should some thermal criteria
other than fracturing be recognised, it may be possible, in conjunction
with other microstructural features related to the environmental condi-
tions under which the fault rock developed, to identify differences in
the parameters controlling each sliding mode.

10.2. Rock Friction

The importance of frictional criteria in the control of faulting
in a shallow crustal environment is indicated by the widespread appli-
cability of Anderson's theory of faulting (Chapter 2), which is based
upon a linear friction law. Experimental work also suggests that a
linear friction law is widely applicable (Byerlee, 1978). This uniformity
of experimental results, irrespective of rock type, is remarkable in
view of the great diversity of experimental conditions used and the
small scale of all the tests. In turn, the linear friction law implies
that the empirical coefficient of friction, μ, is practically the same
for all rock types with the exception of some clay gouges.

It is widely accepted that rock friction is controlled primarily
by the ploughing and brittle fracture of surface asperities (Chapter 3).
The three experimentally observed sliding modes, stable sliding,
episodic slip and stick-slip, are affected by various parameters. In
general, stick-slip is enhanced by high effective normal stress, low
temperatures, the presence of strong, brittle minerals, the absence of
gouge and by very smooth surfaces. On natural faults, the above
parameters may vary across and along the fault as well as with depth.
In addition, natural faults are rarely a single simple plane but
often consist of many fault segments which may have a complex overall
geometry. These factors must all be considered when the texture of
natural fault rocks is studied.

10.3. Energy Dissipation in Faulting

As it was hoped that thermal effects could be used to distinguish
the fault rocks resulting from seismic slip and aseismic creep, it was
necessary to determine the heat generating capacity of a fault. This
depends upon the fault geometry and conditions of slip, and ultimately
upon the value of the average tectonic shear stress, $\bar{\tau}$, on the fault
during slip (Chapter 4). Irrespective of the mode of slip and the

environmental conditions under which it occurs, faulting leads to energy dissipation within the fault zone. The four principal sinks for this energy are: energy converted to heat, radiated seismic energy, fracture surface energy and the work done against or by gravity. The value of τ cannot be measured directly and there is currently a controversy as to whether it is low ($\leqslant 10$ MPa) or high (about 100 MPa).

As shown in Chapter 4, the bulk of the available energy appears to be converted to heat, although again the exact amount cannot be measured directly but is calculated from the average value of the kinetic shear resistance opposing slip on the fault ($\bar{\tau}_{fk}$), the average displacement and the area of the fault undergoing slip. Essentially, the amount of energy converted to heat depends upon the value of τ_{fk} (Section 4.3.3.). In the standard stick-slip model, τ_{fk} is assumed to remain constant at a high proportion of the initial shear stress causing slip. If instead τ_{fk} falls rapidly from its initial value (equal to the initial tectonic shear stress) to levels approximately equal to the final value of the tectonic shear stress, because of the presence of fluids on the fault, then the average kinetic shear resistance will be much lower than the average tectonic shear stress (Sibson, 1977a). In this case the proportion of energy converted to heat will be much smaller. There is no physical evidence to suggest that τ_{fk} remains constant, although it is on this assumption that most calculations of frictional temperature rise are based.

10.4. Frictional Heating

Theoretical studies indicate that under specific conditions frictional heating on a slipping fault is capable of raising the fault's temperature to melting point. These conditions are: maintained high levels of τ_{fk} (10 to 100 MPa), fast slip velocities, dry conditions, and slip confined to a single plane or very narrow zone. In view of these findings it is perhaps not surprising that so few faults have associated melt rocks. In practice, the near universal presence of fluids in established fault zones will mean that the heat generating capacity of many faults is significantly lowered, although moderate to low temperature rises may still result from frictional heating. Even though these temperatures may not cause melting, the associated thermal gradients will induce thermal stresses and hence fractures adjacent to the fault.

To analyse these stresses and the resulting deformation, the slip model of faulting (Nur, 1978) was used in a theoretical and experimental study. This model assumes that shear displacements are achieved by rigid body translation at constant slip velocity, preceded by an instantaneous acceleration and ended by an instantaneous deceleration.

Temporal and spatial temperature distributions were calculated for a number of different slip parameters (Chapter 5). Although the assumptions inherent in these calculations, and the subsequent theoretical considerations restrict the application of the results to dry, narrow faults behaving analogously to Nur's slip model, the excercise is worthwhile as the temperatures, thermal gradients and thermal stresses encountered are overestimated. Thus the most extreme degree of thermal damage likely to be encountered in nature has been considered and its maximum possible effect on the deformation of fault zone material assessed.

Both theory (Chapter 5) and experimental results (Chapter 9) indicate that thermal stresses will lead to fracturing adjacent to faults and that microscopic heterogeneities are an important factor in the intensity of thermal fracturing. Macroscopic fractures are only likely to develop when the fault's temperature rise exceeds 500°-650°C. The orientation of these fractures, which are extensional, is controlled by the mechanical (rather than thermal) stress field around the fault. This is because the magnitude of the thermal stresses falls very rapidly with distance from the fault.

In contrast, microfracturing is likely to be encountered when the surface of the fault is heated to only 150°-300°. These fractures are also extensional and usually initiate at some flaw (such as a grain boundary, cleavage plane or fluid inclusion). They result from rapid temperature changes rather than the absolute magnitude of the temperature. The distance to which these fractures extend is limited and they are unlikely to develop further than 0.1 m from the fault, even when its temperature is at melting point.

An important factor in determining the microfracture density is the quartz content of the rock. Microfractures are most common within quartz grains and on quartz-quartz grain boundaries. This is thought to be because of stress concentrations resulting from the sudden volume change of quartz as it passes through the α/β transition and because of stress produced by the overpressuring of fluid inclusions.

Thermal fracturing will be most marked for faulting in intact

rock. Once a fracture zone has developed, thermal expansion adjacent to the fault may be accommodated by these fractures and high thermal stresses will not develop. It is probable that at moderate and high effective confining pressures ($\geqslant 50$ MPa), where any pre-existing fractures will be closed, the fractured zone around a fault would act as intact rock. This hypothesis could not be tested in the unconfined experiments.

In general, visible thermal effects next to most seismically active faults will take the form of a localised zone of microfracturing. These fractures seem to be indistinguishable from those with a purely mechanical origin but will facilitate gouge production by increasing the number of fragments available for rotation into the gouge layer. It is possible that an electron microscope study of the experimentally heated samples may identify some sub-microscopic feature resulting from the transient temperature rise that could be used to recognise fault rocks with a thermal history from natural fault zones.

10.5. Fault Rocks

A characteristic feature of fault rocks (Chapter 6) is that mechanisms reducing the country rock grain size are generally dominant over those leading to grain growth. One of the greatest problems in the study of fault rocks is that the texture seen is a product of the entire movement history of the fault, and deformation may have occurred under continuously changing environmental conditions. In this case, the extent to which textures resulting from the last deformation episode overprint pre-existing textures becomes important. If the rock studied developed during aseismic creep (whether a member of the mylonite or cataclasite series) the texture would have been continuously modified and the early microstructure would have been considerably altered by deformation under later environmental conditions.

With seismic slip, where movement is accommodated in a cyclic fashion, it is possible that different textural features may develop during different parts of the stress cycle associated with slip. In addition, textures from succeeding cycles may also be superimposed. In this case the final deformation episodes may not totally overprint the textures from previous cycles.

Geodetic observations have shown that both aseismic creep and

seismic slip may occur on the same fault segment at the earth's surface. This finding has led to experimental investigation of the deformation mechanisms characteristic of both slip modes which has shown that no single deformation mechanism is responsible for either stable sliding or stick-slip. Fracture, asperity adhesion and ploughing, and cataclastic flow have been recognised in both sliding modes. The transition between modes depends upon the degree of relative development of each mechanism. Thus the recognition of localised thermal effects associated with stick-slip would be a powerful means to distinguish between the two slip modes.

Experimental results suggest that the development of a gouge layer on an active fault may influence the slip mode and associated deformation. Of the mechanisms proposed to explain gouge formation, mechanical wear involving sidewall fracturing with plucking and rotation of fragments is most widely accepted. Under certain conditions gouge, or at least its finest portion, may have great mobility and may behave in a similar manner to fluids.

The role of clay gouges at other than surface levels is uncertain. Certain clay minerals drastically reduce the strength of gouge and may promote stable sliding across the fault (Chapter 6). However, the stability of these clay minerals in a fault environment at depths greater than a few kilometres has not been established.

10.6. Field Study of Fault Zones

The microstructural study of the Walls Boundary Fault zone, Shetland Islands showed that the cataclasites on this and adjacent minor faults developed during deformation at crustal depths of less than 7 km (if a geothermal gradient of about $30^{\circ}C/km$ is assumed). This was established from the stability of quartz and analcime in the fault plane ultracataclasite. It was not possible to pinpoint the depth more precisely.

In contrast, the mineralogy of the cataclasites found adjacent to the Walls Boundary Fault, suggests that they formed at somewhat deeper levels. The fine grain size of this rock made identification of all phases difficult, but the growth of new phyllosilicates(some of which were identified as chlorite) and rims to the plagioclase (thought to be of albitic composition) do suggest a deeper origin than the fault plane ultracataclasite. This in turn implies that the Walls Boundary Fault, in the strictest sense, is younger than the fault zone it is

associated with. If this is the case, the microstructures formed at deeper levels were preserved because shear became localised onto discrete surfaces in a shallow environment, in line with the experimental work of Griggs and Handin (1960) who showed that slip because localised only at comparatively low confining pressure. This interpretation accords with the view that fault zones widen with depth within the frictional regime.

The inferred age difference between the fault plane ultracataclasite and the adjacent cataclasites is supported by the distribution of analcime, which occurs only on the faults and not in the adjacent rocks. It is likely that circulation of hydrothermal solutions, from which the analcime was derived, took place by channel flow along the faults at a time when deformation in the rock adjacent to them had ceased and the cataclasites had become impervious to fluids.

There is no direct evidence for frictional heating on the Walls Boundary Fault. One sample (14_5) shows localised recrystallisation which is probably strain rather than temperature induced. It is also sufficiently far from the fault (1 m) for significant frictional heating to be unlikely.

From the mineral assemblages of the fault rocks from Loch Eribol, Sutherland, it can be deduced that in this area also, there has been a progressive decrease in the depth at which the deformation occurred. The oldest of the three identified episodes of deformation occurred just below lower greenschist metamorphic conditions and the next two at marginally shallower depths. The two fault zones studied are compared in Fig. 10.1.

Textural studies of rocks from both fault zones indicate that metamorphic reactions are almost equal in importance to cataclastic processes in determining the final character of the fault rocks. Even in rocks with an optically recognisable cataclastic microstructure apparently resulting solely from fracture and fragment rotation, it becomes obvious, on a finer scale, that both recrystallisation and growth of new phases is common. This is enhanced by the circulation of fluids through the deforming rock and it is these processes which lead to the cohesion of cataclasites.

10.7. Further Work

Although it has not so far proved possible to distinguish between cataclastic rocks originating from seismic slip or aseismic

Walls Boundary Fault Zone, Shetland

Granitoid host rock.

Transcurrent movement across the zone.

Shear displacement of 60-80 km.

The zone contains cataclastic fault rocks of
2 recognised ages.

1. Older: cataclasite adjacent to main fault.
    Depth of formation may be approaching lower
    greenschist metamorphic conditions, based
    upon the growth of chlorite and albite.

2. Younger: fault plane ultracataclasite.
    Depth of formation less than 7 km, based
    upon the growth of analcime and its
    stability with quartz.

The fault rocks possess no crystalline fabric.

The fault plane ultracataclasite probably
developed in an open chemical system with the
circulation of hydrothermal fluids introducing
haematite and sodium into the fault rock.

Loch Eribol Region, Sutherland

Quartzite host rock.

Thrusting across faults.

Shear displacement of 200-400 m across each listric
thrust.

The zone contains cataclastic fault rocks of
3 recognised ages.

1. Oldest: porcellanous-white fracture fill.
    Depth of formation just below lowest greenschist
    metamorphic conditions based upon the warm-
    working type microstructure.

2. Intermediate: greenish-black flinty fracture-fill.
    Depth of formation at lower greenschist meta-
    morphic conditions, based on the growth of
    muscovite, chlorite, epidote and albite and
    the preservation of the warm-working microstructure.

3. Youngest: opaque-black fracture-fill.
    Depth of formation above lower greenschist
    metamorphic conditions based upon the purely
    cataclastic microstructure.

A crystalline fabric is developed in localised areas
of the older 2 fault rock types.

All 3 fault rock types developed in an essentially
closed chemical system where any fluid flow was
localised within the host lithological unit.

Fig. 10.1. Comparison of microstructural features from the Walls Boundary Fault zone,
Shetland and the Loch Eribol region, Sutherland.

creep, this study has shown that the role of fluids and metamorphic reactions in fault zones may have been underestimated in many studies of faults, especially those based upon experimental work. Further detailed field, optical and electron microscope studies would enable the importance of these processes to be clarified. For preference, the area chosen for study would contain uniform rock types, have a relatively simple deformation history and little or no surface weathering.

With such studies, it should be possible to establish whether the role of fluids is (as theoretical studies suggest), important in most shallow fault zones, and whether fluids become less important at deeper structural levels. Coarser grained cataclasites would allow chemical mass balancing to be carried out.

More comprehensive experiments on transient heating may yet enable criteria to be recognised whereby fault rocks with thermal history can be distinguished from those without. The rather crude experiments described here show that thermal fracturing adjacent to a fault is likely to be indistinguishable on an optical scale, at least, from that arising from purely mechanical wear. A combination of micro-structural and microchemical work on certain key minerals (perhaps phyllosilicates, amphiboles or pyroxenes) may result in the recognition of thermal effects other than fracturing. This in turn would help to establish the role of frictional heating in natural faulting.

APPENDIX   A

Calibration of Wattmeter

The wattmeter used was a "Vaw meter". It was connected in parallel with an Oxford instruments 300 chart recorder so the power dissipation could be read from both simultaneously. The chart recorder was calibrated using a standard cell and found to be accurate to within 1% on the 50 mV scale.

Elements identical to those used in the subsequent experiments were used for the wattmeter calibration. The full rock-element-rock assemblage was needed to prevent element oxidation. The voltage channel was measured with a D.V.M. and the current channel with an Avo meter (Fig. A.1). Current in the circuit was altered with the Variac (auto-transformer) and the current, voltage and chart recorder deflection were all recorded. The chart recorder deflection was calibrated against the true wattage (from multiplication of current and voltage measurements) and repeated to determine the reproducability of measurements.

C = current transformer A_1 = Avo meter
R = molybdenum element V_1 = Digital voltmeter
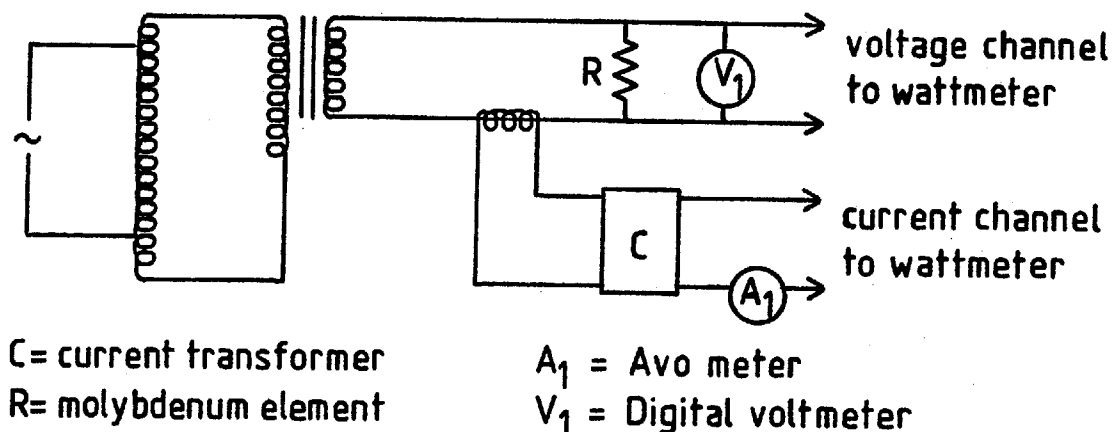
Fig. A.1. Calibration circuit

Fig. A.2. in which the chart recorder deflection is plotted against the true wattage shows there is a variation of ±5% in the wattage represented by a given chart recorder reading. The change in resistance because of element heating and unreliability of the wattmeter is believed to account for the error of 5% in the range measured.
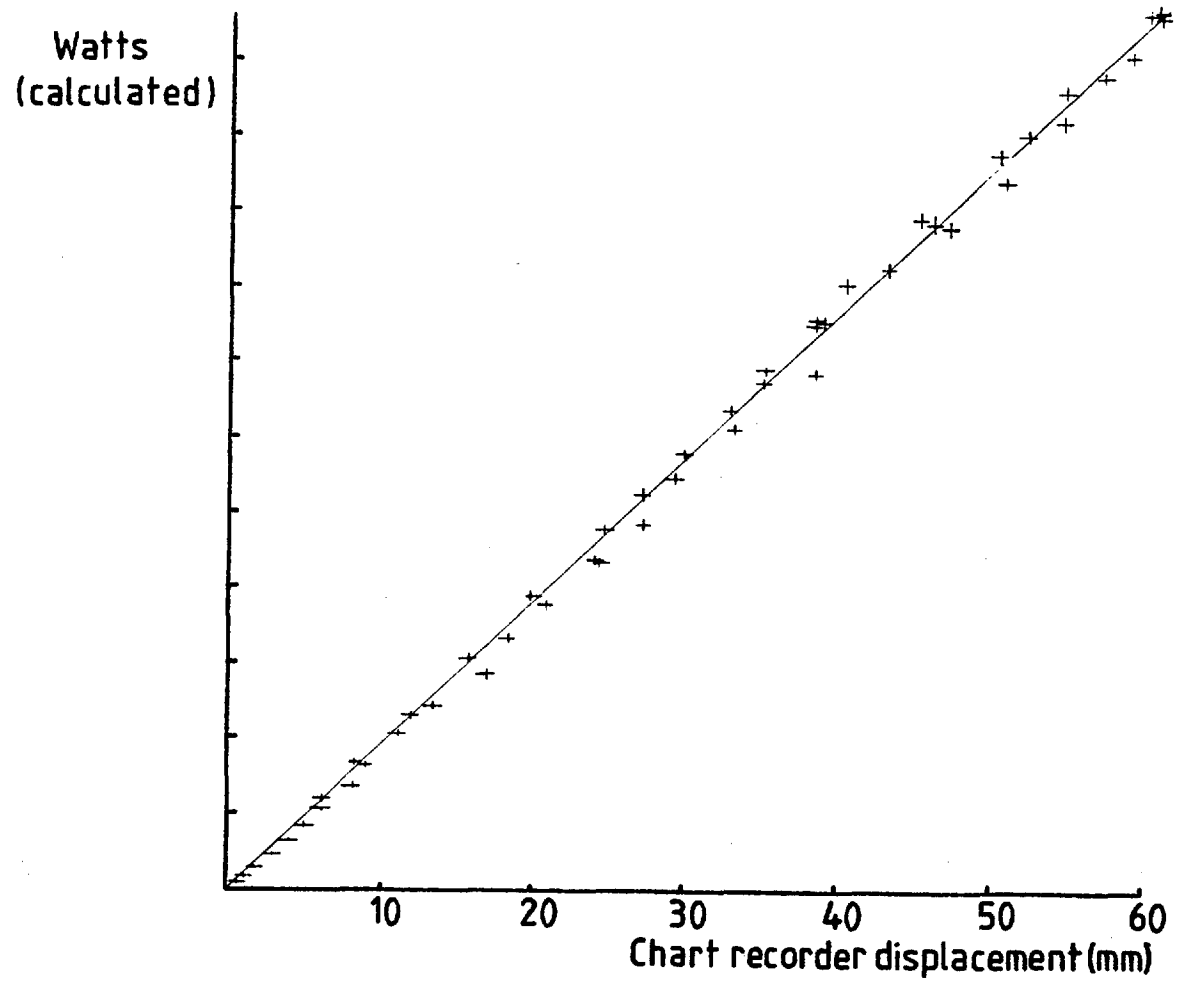
Fig. A.2. Plot of chart recorder deflection against true wattage.

Table A.1.

Wattmeter Calibration I

Current A_1 (amps)	% error	Voltage V_1 (volts)	% error	Wattage Calculated (watts)	Error ±	Chart Recorder Deflection (cm)	Error ±
0.1	10	0.32	3.1	0.03	0.004	0	0.05
0.2	5	0.68	1.5	0.14	0.01	0.05	
0.3	3.3	1.00	1.0	0.30	0.01	0.09	
0.4	2.5	1.34	0.8	0.54	0.02	0.17	
0.5	2.0	1.67	0.6	0.84	0.02	0.28	
0.6	1.7	2.01	0.5	1.21	0.03	0.38	
0.7	1.4	2.33	0.4	1.63	0.03	0.50	
0.8	1.3	2.66	0.4	2.13	0.03	0.59	
0.9	1.1	3.01	0.3	2.71	0.04	0.83	
1.0	1.0	3.29	0.3	3.29	0.04	0.91	
1.1	1.8	3.70	0.3	4.07	0.09	1.12	
1.2	1.7	4.02	0.3	4.82	0.09	1.34	
1.3	1.5	4.33	0.2	5.63	0.10	1.68	
1.4	1.4	4.70	0.2	6.58	0.11	1.82	
1.5	1.3	5.03	0.2	7.55	0.12	2.06	
1.6	1.3	5.41	0.2	8.66	0.12	2.41	
1.7	1.2	5.64	0.2	9.59	0.13	2.72	
1.8	1.1	6.02	0.2	10.84	0.14	2.92	
1.9	1.1	6.38	0.2	12.12	0.15	3.28	
2.0	1.0	6.79	0.2	13.58	0.16	3.83	
2.0	1.0	6.68	0.2	13.36	0.15	3.48	
2.1	0.9	7.14	0.1	14.99	0.16	3.82	
2.2	0.9	7.46	0.1	16.41	0.17	4.30	
2.3	0.9	7.67	0.1	17.64	0.18	4.59	
2.4	0.8	8.09	0.1	19.42	0.19	5.03	
2.5	0.8	8.44	0.1	21.10	0.19	5.43	

Table A.2.

Wattmeter Calibration II

Current A_1 (amps)	% error	Voltage V_1 (volts)	% error	Wattage Calculated (watts)	Error ±	Chart Recorder Deflection (cm)	Error ±
1.0	1	2.33	0.4	2.33	0.03	0.60	0.05
1.2	1.7	2.81	0.4	3.27	0.07	0.86	
1.4	1.4	3.28	0.3	4.59	0.08	1.18	
1.6	1.3	3.78	0.3	6.05	0.09	1.56	
1.8	1.1	4.27	0.2	7.69	0.10	2.00	
2.0	1.0	4.74	0.2	9.48	0.11	2.46	
2.1	0.9	4.97	0.2	10.44	0.12	2.70	
2.2	0.9	5.24	0.2	11.53	0.13	2.97	
2.3	0.9	5.48	0.2	12.60	0.13	3.27	
2.4	0.8	5.69	0.2	13.66	0.14	3.51	
2.5	0.8	6.00	0.2	15.00	0.15	3.84	
2.6	0.8	6.16	0.2	16.02	0.15	4.03	
2.7	0.7	6.51	0.2	17.68	0.16	4.52	
2.7	0.7	6.49	0.2	17.52	0.16	4.72	
2.8	0.7	6.66	0.2	18.65	0.16	5.07	
2.9	0.7	6.87	0.2	19.92	0.17	5.21	
2.9	0.7	7.00	0.1	20.30	0.17	5.44	
3.0	0.7	7.34	0.1	22.02	0.18	5.87	
3.0	0.7	7.15	0.1	21.45	0.17	5.72	
3.1	0.6	7.47	0.1	23.16	0.18	6.07	
3.1	0.6	7.47	0.1	23.16	0.18	6.05	

APPENDIX B

Computer Program for Temperature Calculation

```
/LIST,F=TCALC
00100LD,TCALC
      PROGRAM TCALC(INPUT=131B,OUTPUT=131B,TAPE6=131B,TAPE64=131B
     +,TAPE61=131B,TAPE66=131B,TAPE5=INPUT)
      DIMENSION X(1500),Y(1500),NUM(10),IHEAD(10)
      COMMON X,Y
      CALL START(2)
      CALL SWITCH(9HHARDCPYON)
      CALL PROMPT(12HTHD THC TP F,12)
      READ,THD,THC,TP,F
      STHD=SQRT(THD)
      FACT=F*STHD/THC
      SQPI=SQRT(3.14159)
      CALL PROMPT(43HENTER TIME OR DIST FOR PARAMETERS TO BE SET,43)
      READ,MYOPT
      CALL PROMPT(34HENTER NUMBER OF CURVES TO BE DRAWN,34)
      READ,NOCURVE
      DO 20 I=1,NOCURVE
   20 NUM(I)=201
      CALL NEWPAGE
      IF(MYOPT .EQ. 4HTIME)CALL TSET(STHD,FACT,TP,SQPI,NOCURVE)
      IF(MYOPT .EQ. 4HDIST)CALL DSET(STHD,FACT,TP,SQPI,NOCURVE)
      IF(MYOPT .EQ. 4HTIME)CALL GRAF(X,Y,NUM,NOCURVE,
     +0,10HDISTANCE M,10,13HTEMPERATURE C,13,21,0,14,0)
      IF(MYOPT .EQ. 4HDIST)CALL GRAF(X,Y,NUM,NOCURVE,
     +0,10HTIME (SEC),10,13HTEMPERATURE C,13,20,0,14,0)
      CALL PROMPT(37HENTER GRAPH HEADING, IN 67 CHARACTERS,37)
      READ, (IHEAD(J),J=1,7)
      CALL XWIRES(X,Y)
      CALL PRINT(X,Y,IHEAD,67)
      DO 10 M=1,NOCURVE
      CALL PROMPT(17HENTER CURVE LABEL,17)
      READ,LABEL
      CALL XWIRES(X,Y)
      CALL PRINT(X,Y,LABEL,10)
   10 CONTINUE
      CALL PROMPT(31HTYPE 1 FOR HARDCOPY OTHERWISE 0,31)
      READ,MIC
      IF(MIC .EQ. 1)CALL HARDCPY
      CALL BUFFEM(0,0)
      STOP
      END
      SUBROUTINE TSET(STHD,FACT,TP,SQPI,NOCURVE)
      DIMENSION DIST(1500),TEMP(1500),TIME(10)
      COMMON DIST,TEMP
      M=0
      CALL PROMPT(33HENTER TIME IN SECS FOR EACH CURVE,33)
      DO 300 J=1,NOCURVE
      READ,TIME(J)
      SQRTIM=SQRT(TIME(J))
      STMTD=STHD*SQRTIM
```

```
DO 300 N=1,201
M=M+1
DIST(M)=0.05*FLOAT(N-1)
ERVAR=DIST(M)/(2.0*STMTD)
RERFC=S15ADF(ERVAR)
RIERFC=(EXP(-ERVAR**2)/SQPI)-(ERVAR*RERFC)
IF(TIME(J) .GT. TP)GO TO 1000
VAR=FACT*SQRTIM
TEMP(M)=VAR*RIERFC
GO TO 300
1000 SUTS=SQRT(TIME(J)-TP)
ERVARB=DIST(M)/(2.0*STHD*SUTS)
RERFCB=S15ADF(ERVARB)
RIEFCB=(EXP(-ERVARB**2)/SQPI)-(ERVARB*RERFCB)
TEMP(M)=FACT*((SQRTIM*RIERFC)-(SUTS*RIEFCB))
300 CONTINUE
RETURN
END
SUBROUTINE DSET(STHD,FACT,TP,SQPI,NOCURVE)
DIMENSIONTIME(1500),TEMP(1500),DIST(10)
COMMON TIME,TEMP
M=0
CALL PROMPT(39HENTER DISTANCE IN METRES FOR EACH CURVE,39)
DO 400 I=1,NOCURVE
READ,DIST(I)
DO 400 J=1,201
SCALE=5.0
M=M+1
TIME(M)=SCALE*FLOAT(J-1)
IF(TIME(M) .EQ. 0.0)GO TO 500
SQRTIM=SQRT(TIME(M))
STMTD=STHD*SQRTIM
VAR=FACT*SQRTIM
ERVAR=DIST(I)/(2.0*STMTD)
RERFC=S15ADF(ERVAR)
RIERFC=(EXP(-ERVAR**2)/SQPI)-(ERVAR*RERFC)
IF(TIME(M) .GT.TP)GO TO 1000
TEMP(M)=VAR*RIERFC
GO TO 400
1000 SUTS=SQRT(TIME(M)-TP)
ERVARB=DIST(I)/(2.0*STHD*SUTS)
RERFCB=S15ADF(ERVARB)
RIEFCB=(EXP(-ERVARB**2)/SQPI)-(ERVARB*RERFCB)
TEMP(M)=FACT*((SQRTIM*RIERFC)-(SUTS*RIEFCB))
GO TO 400
500 TEMP(M)=0
400 CONTINUE
RETURN
END
```

REFERENCES

Ambraseys, N.N., 1969. Maximum intensity of ground movements caused by faulting. Proc. World Conf. Earthquake Eng. 4th, Santiago, 1: 154-171.

Anderson, E.M., 1951. The Dynamics of Faulting, (2nd ed.). Oliver and Boyd, Edinburgh: 206pp.

Archard, J.F., 1958. Elastic deformation and the laws of friction. Proc. Roy. Soc. Lond. A, 243: 190-205.

Barber, D.J., 1970. Thin foils of non-metals made for electron microscopy by sputter-etching. J. Mat. Sci., 5: 1-8.

Bell, T.H. and Etheridge, M.A., 1973. Microstructure of mylonites and their descriptive terminology. Lithos, 6: 337-348.

Benioff, H., 1964. Earthquake source mechanisms. Science, 143: 1399-1406.

Boas, W. and Honeycombe, R.W.K., 1947. The anisotropy of the thermal expansion as a cause of deformation in metals and alloys. Proc. Roy. Soc. Lond. A, 188: 427-439.

Boles, J.R. and Coombs, D.S., 1977. Zeolite facies alteration of sandstones in the Southland Syncline, New Zealand. Am. J. Sci., 277: 982-1012.

Boley, B.A. and Weiner, J.H., 1960. Theory of Thermal Stresses. Wiley, New York, N.Y.: 586pp.

Bowden, F.P. and Tabor, D., 1967. Friction and Lubrication of Solids. Methuen and Co. Ltd., London. 166pp.

Bowden, F.P., Brooks, C.A. and Hanwell, A.E., 1964. Anisotropy of friction in crystals. Nature, 203: 27-30.

Brace, W.F. and Byerlee, J.D., 1966. Stick-slip as a mechanism for earthquakes. Science, 153: 990-992.

Brace, W.F. and Byerlee, J.D., 1970. California earthquakes: why only shallow focus? Science, 168: 1573-1575.

Brace, W.F. and Martin III, R.J., 1968. A test of the law of effective stress for crystalline rocks of low porosity. Int. J. Rock Mech. Min. Sci. and Geomech. abstr., 5: 415-426.

Brace, W.F. and Walsh, J.B., 1962. Some direct measurements of the surface energy of quartz and orthoclase. Am. Mineral., 47: 1111-1122.

Breemen, O., van, Aftalion, M. and Johnson, M.R.W., 1979. Age of the Loch Borrolan complex, Assynt, and late movements along the Moine Thrust Zone. J. Geol. Soc. Lond., 136: 489-495.

Bridgman, P.W., 1945. Polymorphic transitions and geological phenomena. Am. J. Sci., 243 A: 90-97.

Brock, W.G. and Engelder, J.T., 1977. Deformation associated with the movement of the Muddy Mountain overthrust in the Buffington window, southeastern Nevada. Bull. Geol. Soc. Am., 88: 1667-1677.

Brune, J.N., 1961. Radiation pattern of Rayleigh waves from the Southeast Alaska earthquake of July 10, 1958. Publ. Dom. Obs. Ottowa, 24: 373-383.

Brune, J.N., 1970. Tectonic stress and the spectra of seismic shear waves from earthquakes. J. Geophys. Res., 75: 4997-5009.

Brune, J.N., Henyey, T.L. and Roy, R.F., 1969. Heat flow, stress and rate of slip along the San Andreas Fault, California. J. Geophys. Res., 74: 3821-3827.

Bucknam, R.C., Plafker, G. and Sharp, R.V., 1978. Fault movement (afterslip) following the Guatemala earthquake of February 4, 1976. Geology, 6: 170-173.

Byerlee, J.D., 1967a. Frictional characteristics of granite under high confining pressure. J. Geophys. Res., 72: 3639-3648.

Byerlee, J.D., 1967b. Theory of friction based on brittle fracture. J. Appl. Phys., 38: 2928-2934.

Byerlee, J.D., 1968. Brittle-ductile transition in rocks. J. Geophys. Res., 73: 4741-4750.

Byerlee, J.D., 1969. The mechanics of stick-slip. Tectonophysics, 9: 475-486.

Byerlee, J.D., 1978. Friction of rocks. Pure appl. Geophys., 116: 615-626.

Byerlee, J.D. and Brace, W.F., 1968. Stick-slip, stable sliding, and earthquakes - effect of rock type, pressure, strain rate, and stiffness. J. Geophys. Res., 73: 6031-6037.

Byerlee, J.D. and Brace, W.F., 1969. High pressure mechanical instability in rocks. Science, 164: 713-715.

Byerlee, J.D., Mjachkin, V., Summers, R. and Voevoda, O., 1978. Structures developed in fault gouge during stable sliding and stick-slip. Tectonophysics, 44: 161-171.

Cardwell, R.K., Chinn, D.S., Moore, G.F. and Turcotte, D.L., 1978. Frictional heating on a fault zone with finite thickness. Geophys. J. Roy. astr. Soc., 52: 525-530.

Carslaw, H.S. and Jaeger, J.C., 1959. Conduction of Heat in Solids, (2nd ed.). Clarendon Press, Oxford, 510pp.

Christie, J.M., 1960. Mylonitic rocks of the Moine Thrust Zone in the Assynt district, north-west Scotland. Trans. geol. soc. Edinb., 18: 79-93.

Christie, J.M., 1963. The Moine Thrust in the Assynt region, north-
west Scotland. Univ. Calif. Publs. geol. Sci., 40: 345-440.

Clark, S.P. (ed.), 1966. Handbook of Physical Constants. Geol. Soc.
Am. Mem., 97: 587pp.

Conrad, R.E. II and Friedman, M., 1976. Microscopic feather fractures
in the faulting process. Tectonophysics, 33: 187-198.

Davies, G.F. and Brune, J.N., 1971. Regional and global fault slip
rates from seismicity. Nature, Phys. Sci., 229: 101-107.

Dieterich, J.H., 1972. Time-dependent friction in rocks. J. Geophys. Res.,
77: 3690-3697.

Dieterich, J.H., 1974. Earthquake mechanisms and modelling. In: Donath,
F.A., (ed.), Annual Review of Earth and Planetary Science, 2:
275-301.

Dieterich, J.H., 1978. Time-dependent friction and the mechanics of
stick-slip. Pure appl. Geophys., 116: 790-806.

Drennon, C.B. and Handy, R.L., 1972. Stick-slip of lightly loaded
limestone. Int. J. Rock Mech. Min. Sci. and Geomech. Abstr., 9:
603-615.

Eaton, J.P., Lee, W.H.K. and Pakiser, L.C., 1970. The use of micro-
earthquakes in the study of the mechanism of earthquake generation
along the San Andreas Fault in California. Tectonophysics, 9:
259-282.

Ehlers, E.G., 1972. The Interpretation of Geological Phase Diagrams.
W.H. Freeman and Co., San Francisco: 274pp.

Engelder, J.T., 1974. Microscopic wear-grooves on slickensides:
indicators of palaeoseismicity. J. Geophys. Res., 79: 4387-4392.

Engelder, J.T., 1974a. Cataclasis and the generation of fault gouge.
Bull. Geol. Soc. Am., 85: 1515-1522.

Engelder, J.T., 1976. Effect of scratch hardness on frictional wear
and stick-slip of Westerly granite and Cheshire quartzite. In:
Strens, R.G.J. (ed), The Physics and Chemistry of Minerals and
Rocks. Wiley, New York: 139-150.

Engelder, J.T., 1978. Aspects of asperity-surface interaction and
surface damage of rocks during experimental frictional sliding.
Pure appl. Geophys., 116: 705-716.

Engelder, J.T. and Scholz, C.H., 1976. The role of asperity indentation
and ploughing in rock friction - II Influence of relative hardness
and normal load. Int. J. Rock Mech. Min. Sci. and Geomech. Abstr.,
13: 155-163.

Engelder, J.T., Logan, J.M. and Handin, J., 1975. The sliding charac-
teristics of sandstone on quartz fault gouge. Pure appl. Geophys.,

113: 69-86.

Etheridge, M.A. and Wilkie, J.C., 1979. The geometry and microstructure of a range of QP-mylonite zones-A field test of the recrystallised grain size palaeopiezometer, Proc. Conf. VIII, "Analysis of Actual Fault Zones in Bedrock." National Earthquake Hazards Reduction Program., 1-5 Apr., 1979, USGS. Menlo Park, Calif.: 448-504.

Exner, H.E., 1972. Analysis of grain- and particle-size distributions in metallic materials. Int. Metall. Rev., 17: 25-42.

Flinn, D., 1954. On the time relations between regional metamorphism and permeation in Delting, Shetland. J. Geol. Soc. Lond., 110: 177-199.

Flinn, D., 1958. On the nappe structure of North-East Shetland. J. Geol. Soc. Lond., 114: 107-136.

Flinn, D., 1959. On certain geological similarities between north-east Shetland and the Jotunheim area of Norway. Geol. Mag., 96: 473-481.

Flinn, D., 1961. Continuation of the Great Glen Fault beyond the Moray Firth. Nature, 191: 589-591.

Flinn, D., 1967. The metamorphic rocks of the southern part of the Mainland of Shetland. Geol. Jnl., 5: 251-290.

Flinn, D., 1969. A geological interpretation of the aeromagnetic maps of the continental shelf around Orkney and Shetland. Geol. Jnl., 6: 279-292.

Flinn, D., 1977. Transcurrent faults and associated cataclasis in Shetland. J. Geol. Soc. Lond., 133: 231-248.

Flinn, D., May, F., Roberts, J.L. and Treagus, J.E., 1972. A revision of the stratigraphic succession of the East Mainland of Shetland. Scot . J. Geol., 8: 335-343.

Folk, R.L., 1968. Petrology of Sedimentary Rocks. Austin, Texas, Hemphills. 170pp.

Friedman, G.M., 1958. Determination of sieve-size distributions from thin-section data for sedimentary petrological studies. J. Geol., 66: 394-416.

Friedman, M., Logan, J.M. and Rigert, J.A., 1974. Glass-indurated quartz gouge in sliding-friction experiments on sandstone. Bull. Geol. Soc. Am., 85: 937-942.

Geikie, A., 1888. Report on the recent work of the Geological Survey in the North-West Highlands of Scotland, based on the field-notes

and maps of B.M. Peach, J. Horne, W. Gunn, C.T. Clough, L. Hinxman and H.M. Cadell. Q. Jnl. geol. Soc. Lond., 44: 378-441.

Geller, L.B., 1970. A new look at thermal fracturing. Trans. Inst. Min. Met., 79: A133-A170.

Geller, R.J., 1976. Scaling relationships for earthquake source parameters and magnitudes. Bull. Seism. Soc. Am., 66: 1501-1523.

Griggs, D.T. and Baker, D.W., 1968. The origin of deep-focus earthquakes. In: Mark, H. and Fernbach, S. (eds.). Properties of Matter Under Unusual Conditions. Wiley, New York, 23-42.

Griggs, D.T. and Handin, J., 1960. Observations on fracture and a hypothesis of earthquakes. In Griggs, D.T. and Handin, J. (eds.). Rock Deformation. Geol. Soc. Am. Mem., 79: 347-364.

Griggs, D.T., Turner, F.J. and Heard, H.C., 1960. Deformation of rocks at 500° to 800°C. In: Griggs, D.T. and Handin, J. (eds.). Rock Deformation. Geol. Soc. Am. Mem., 79: 39-104.

Grocott, J., 1977. The relationship between Precambrian shear belts and modern fault systems. J. Geol. Soc. Lond., 133: 257-262.

Gutenberg, B. and Richter, C.F., 1954. Seismicity of the Earth. Princeton Univ. Press, Princeton: 310pp.

Handin, J. and Hager Jr., R.V., 1958. Experimental deformation of sedimentary rocks under confining pressure: tests at high temperature. Bull. Am. Assoc. Pet. Geol., 42: 2892-2934.

Hanks, T.C., 1977. Earthquake stress drops, ambient tectonic stresses and stresses that drive plate motions. Pure appl. Geophys., 115: 441-458.

Herdan, G., 1960. Small Particle Statistics. Butterworth, London: 418pp.

Higgins, M.W., 1971. Cataclastic rocks. Prof. Pap. US. geol. Surv., 687: 140pp.

Hoskins, E.R., Jaeger, J.C. and Rosengren, K.J., 1968. A medium-scale direct friction experiment. Int. J. Rock Mech. Min. Sci. and Geomech. Abstr., 5: 143-154.

Hubbert, M.K., 1951. Mechanical basis for certain familiar geologic structures. Bull. Geol. Soc. Am., 62: 355-372.

Hubbert, M.K. and Rubey, W.W., 1959. Role of fluid pressure in mechanics of overthrust faulting. Bull. Geol. Soc. Am., 70: 115-166.

Hukki, R.T., 1975. The principles of comminution: an analytical summary. Eng. Min. J., 176: 106-110.

Husseini, M.I., Jovanovich, D.B., Randall, M.J. and Freund, L.B., 1975. The fracture energy of earthquakes. Geophys. J. Roy. astr. Soc., 43: 367-385.

Jackson, R.E. and Dunn, D.E., 1974. Experimental sliding friction and cataclasis of foliated rocks. Int. J. Rock Mech. Min. Sci. and Geomech. Abstr., 11: 235-249.

Jaeger, J.C., 1959. The frictional properties of joints in rock. Geofis. pura. appl., 43: 148-158.

Jaeger, J.C., 1971. Friction of rocks and stability of rock slopes. Geotechnique, 21: 97-134.

Jaeger, J.C. and Cook, N.G.W., 1971. Fundamentals of Rock Mechanics. Methuen and Co., Ltd., London. 585pp.

Kanamori, H., 1977. The energy release in great earthquakes. J. Geophys. Res., 82: 2981-2987.

Kanamori, H. and Anderson, D.L., 1975. Theoretical basis of some empirical relations in seismology. Bull. Seism. Soc. Am., 65: 1073-1095.

Kanamori, H. and Stewart, G.S., 1979. A slow earthquake. Physics of the Earth and Planetary Interiors, 18: 167-175.

King, G.C.P., 1978. Geological faults: fracture, creep and strain. Phil. Trans. R. Soc. Lond. A., 288: 197-212.

Kingery, W.B., 1957. Note on thermal expansion and microstresses in two-phase compositions. J. Am. Ceram. Soc., 40: 351-352.

Kuszyk, J.A. and Bradt, R.C., 1973. Influence of grain size on effects of thermal expansion anisotropy in $MgTi_2O_5$. J. Am. Ceram. Soc., 56: 420-423.

Lauriello, P.J., 1974. Thermal fracturing of hard rock. Int. J. Rock Mech. Min. Sci. and Geomech. Abstr., 11: 75-81.

Lawn, B.R. and Wilshaw, T.R., 1975. Fracture of Brittle Solids. Cambridge Univ. Press: 204pp.

Lehnhoff, T.F. and Scheller, J.D., 1975. The influence of temperature dependent properties on thermal rock fragmentation. Int. J. Rock Mech. Min. Sci. and Geomech. Abstr., 12: 255-260.

Logan, J.M., 1978. Creep, stable sliding and premonitory slip. Pure appl. Geophys., 116: 773-789.

Logan J.M., Friedman, M., Higgs, N., Dengo, C., and Shimamoto, T., 1979. Experimental studies of simulated gouge and their application to studies of natural fault zones. Proc. Conf. VIII, " Analysis of Actual Fault Zones in Bedrock." National Earthquake Hazards Reduction Program., 1-5 Apr, 1979, USGS Menlo Park, Calif.: 305-343.

McKenzie, D.P., 1969. The relation between fault plane solutions for earthquakes and the directions of the principal stresses. Bull. Seism. Soc. Am., 59: 591-601.

McGarr, A. and Gay, N.C., 1978. State of stress in the earth's crust. Annual Review of Earth and Planetary Sci., 6: 405-436.

McGarr, A., Spottiswood, N.C. and Gay, N. and Ortlepp, W.D., 1977. Observations relevant to seismic driving stress, stress drop and radiation efficiency. J. Geophys. Res., 84: 2251-2261.

McKenzie, D. and Brune, J.N., 1972. Melting on fault planes during large earthquakes. Geophys. J. Roy. astr. Soc., 29: 65-78.

Marshall, V.C. (ed.), 1974. Comminution. Report of Inst. Chem. Eng. 83pp.

Miller, J.A. and Flinn, D., 1966. A survey of the age relations of Shetland rocks. Geol. Jnl., 5: 95-116.

Moore, H.E. and Sibson, R.H., 1978. Experimental thermal fragmentation in relation to seismic faulting. Tectonophysics, 49: T9-T17.

Murrell, S.A.F., 1965. The effect of triaxial stress systems on the strength of rocks at atmospheric temperatures. Geophys. J. Roy. astr. Soc., 10: 231-281.

Mykura, W., 1972a. Igneous intrusions and mineralisation in Fair Isle, Shetland Islands. Bull. geol. Surv. Gt. Br., 41: 33-53.

Mykura, W., 1972b. The Old Red Sandstone sediments of Fair Isle, Shetland Islands. Bull. geol. Surv. Gt. Br., 41: 1-31.

Mykura, W., 1976. British Regional Geology, Orkney and Shetland. I.G.S., NERC. 149pp.

Mykura, W. and Phemister, J., 1976. The Geology of Western Shetland. Mem. Geol. Surv. G.B., Scotland, I.G.S., NERC. 304pp.

Mykura, W. and Young, B.R., 1969. Sodic scapolite (dipyre) in the Shetland Islands. Rep. Inst. geol. Sci.: 69/4.

Nicolas, A. and Poirier, J.P., 1976. Crystalline Plasticity and Solid State Flow in Metamorphic Rocks. Wiley, London: 444pp.

Norton, F.H., 1949. Refractories, (3rd ed.). McGraw-Hill, New York: 782pp.

Nur, A., 1978. Nonuniform friction as a physical basis for earthquake mechanics. Pure appl. Geophys., 116:964-989.

Nutting, J., 1974. The deformation of metals to high strains by cold working. In: Sanders, J.V. and Goodchild, D.J. (eds.), Electron Microscopy, I, Physical: 741pp.

Nye, J.F., 1976. Physical Properties of Crystals. Oxford Univ. Press: 322pp.

Ohnaka, M., 1973. Experimental studies of stick-slip and their application to the earthquake source mechanism. J. Phys. Earth, 21: 285-303.

Ohnaka, M., 1973a. A physical understanding of the earthquake source mechanism. J. Phys. Earth, 21: 39-59.

Ohnaka, M., 1975. Frictional characteristics of typical rocks. J. Phys. Earth, 23: 87-112.

Orowan, E., 1960. Mechanism of seismic faulting. Geol. Soc. Am. Mem., 79: 332-345.

Phemister, M.A., 1948. The Northern Highlands, (2nd ed.). British Regional Geology. H.M.S.O. Edinburgh: 93pp.

Price, N.J., 1966. Fault and Joint Development in Brittle and Semi-brittle Rock. Pergammon Press, Oxford: 176pp.

Raleigh, C.B. and Paterson, M.S., 1965. Experimental deformation of serpentinite and its tectonic implications. J. Geophys. Res., 70: 3965-3985.

Reid, H.F., 1911. The elastic-rebound theory of earthquakes. Univ. Calif. Publ. Dept. Geol. Sci., 6: 413-444.

Richards, P.G., 1976. Dynamic motions near an earthquake fault: a three-dimensional solution. Bull. Seism . Soc. Am., 66: 1-32.

Richter, C.F., 1958. Elementary Seismology. W.H. Freeman and Co., San Francisco: 768pp.

Richter, D. and Simmons, G., 1974. Thermal expansion behaviour of igneous rocks. Int. J. Rock Mech. Min. Sci. and Geomech. Abstr., 11: 403-411.

Rosenholtz, J.L. and Smith, D.T., 1949. Linear thermal expansion of calcite, var. Iceland Spar and Yule Marble. Am. Miner., 34: 846-854.

Rutter, E.H. and Mainprice, D.H., 1978. The effect of water on stress relaxation of faulted and unfaulted sandstone. Pure appl. Geophys., 116: 634-654.

Rutter, E.H. and White, S.H., 1979. Effects of water, temperature and time on the microstructure and mechanical properties of experimentally produced fault gouge. Bull. Mineral., 102: 101-109.

Sacks, S.I., Suyehiro, S., Linde, A.I. and Suoke, J.A., 1978. Slow earthquakes and stress redistribution. Nature, 275: 599-602.

Savage, J.C. and Walsh, J.B., 1978. Gravitational energy and faulting. Bull. Seism. Soc. Am., 68: 1613-1622.

Scholz, C.H., 1968. The frequency-magnitude relation of microfracturing in rock and its relation to earthquakes. Bull. Seism. Soc. Am., 58: 399-415.

Scholz, C.H. and Engelder, J.T., 1976. The role of asperity indentation and ploughing in rock friction: I Asperity creep and stick-slip. Int. J. Rock Mech. Min. Sci. Geomech. Abstr., 13: 149-154.

Scholz, C.H., Molnar, P. and Johnson, T., 1972. Detailed studies of frictional sliding of granite and implications for the earthquake mechanism. J. Geophys. Res., 77: 6392-6406.

Scholz, C.H., Wyss, M. and Smith, S.W., 1969. Seismic and aseismic slip on the San Andreas Fault. J. Geophys. Res., 74: 2049-2069.

Shimazu, Y., 1961. A geophysical study of regional metamorphism. Jap. J. Geophys., 2: 135-176.

Sibson, R.H., 1973. Interactions between temperature and fluid pressure during earthquake faulting - a mechanism for partial or total stress relief. Nature, Phys. Sci., 243: 66-68.

Sibson, R.H., 1974. Frictional constraints on thrust, wrench and normal faults. Nature, Phys. Sci., 249: 542-543.

Sibson, R.H., 1975. Generation of pseudotachylyte by ancient seismic faulting. Geophys. J. Roy. astr. Soc., 43: 775-794.

Sibson, R.H., 1977a. Kinetic shear resistance, fluid pressures and radiation efficiency during seismic faulting. Pure appl. Geophys., 115: 387-400.

Sibson, R.H., 1977b. Fault rocks and fault mechanisms. J. Geol. Soc. Lond., 133: 191-213.

Sibson, R.H., 1978. Radient flux as a guide to relative seismic efficiency. Tectonophysics. 51: T39-T46.

Sibson, R.H., 1980. Power dissipation on faults during seismic slip: geological evidence. Proc. Conf. IX. "Magnitude of Deviatoric Stresses in the Earth's Crust and Upper Mantle". National Earthquake Hazards Reduction Program. July 29 - Aug 3, 1979. (USGS, Menlo Park, California).

Simkins, T.E., 1967. The mutuality of static and kinetic friction. Lubrication Eng., 23: 26-31.

Simmons, G. and Richter, D., 1976. Microcracks in rocks. In: Strens, R.G.J. (ed.), The Physics and Chemistry of Minerals and Rocks. Wiley, New York: 105-137.

Soper, N.J. and Wilkinson, P., 1975. The Moine Thrust and Moine Nappe at Loch Eriboll, Sutherland. Scot . J. Geol., 11: 339-359.

Spry, A., 1969. Metamorphic Textures. Pergamon Press, Oxford: 350pp.

Stacey, F., 1977. Physics of the Earth, (2nd ed.). Wiley. 414pp.

Steijn, R.P., 1964. Friction and wear of single crystals. Wear, 7: 48-66.

Stesky, R.M., 1975. Acoustic emission during high-temperature frictional Sliding. Pure appl. Geophys., 113: 31-43.

Stesky, R.M., 1978. Rock friction - effect of confining pressure, temperature and pore pressure. Pure appl. Geophys., 116: 690-704.

Stesky, R.M., 1978a. Mechanisms of high temperature frictional sliding in Westerly Granite. Can. J. Earth Sci., 15: 361-375.

Stesky, R.M. and Brace, W.F., 1973. Estimation of frictional stress on the San Andreas fault from laboratory measurements. In: Kovach, R.L. and Nur, A. (eds.), Proc. Conf. on Tectonic Problems of the San Andreas Fault System. Geol. Sci. XIII, Stanford Univ., Stanford, Calif.: 206-214 .

Stesky, R.M., Brace, W.F., Riley, D.K. and Robin, P.-Y.F., 1974. Friction in faulted rock at high temperature and pressure. Tectonophysics, 23: 177-203.

Swain, M.V. and Jackson, R.E., 1976. Wear-like features on natural fault surfaces. Wear, 37: 63-68.

Tchalenko, J.S., 1970. Similarities between shear zones of different magnitude. Bull. Geol. Soc. Am., 81: 1625-1640.

Tchalenko, J.S. and Ambraseys, N.N., 1970. Structural analysis of the Dasht-e Bayaz (Iran) earthquake fractures. Bull. Geol. Soc. Am., 81: 41-60.

Teufel, L.W. and Logan, J.M., 1978. Effect of displacement rate on the real area of contact and temperatures generated during frictional sliding of Tennessee sandstone. Pure appl. Geophys., 116: 840-865.

Thirumalai, K. and Cheung, J.B., 1972. A study on a new concept of thermal hard rock crushing. In: Hardy, H.R. and Stefanko, R., New Horizons in Rock Mechanics. 14th Symposium on Rock Mechanics: 527-554.

Thompson, A.B., 1971. Analcite-albite equilibria at low temperatures. Am. J. Sci., 271: 79-92.

Timoshenko, S. and Goodier, J.N., 1951. Theory of Elasticity. McGraw-Hill, New York, N.Y.: 493pp.

Turner, F.J., 1968. Metamorphic Petrology, Mineralogical and Field Aspects. McGraw-Hill, New York: 403pp.

Walsh, J.B., 1971. Stiffness in faulting and in friction experiments. J. Geophys. Res., 76: 8597-8598.

Waters, A.C. and Campbell, C.D., 1935. Mylonites from the San Andreas Fault zone. Am. J. Sci., 29: 473-503.

White, S.H., 1973. Dislocation structures responsible for the optical effects in some naturally deformed quartzites. J. Mater. Sci., 9: 490-499.

White, S.H., 1976a. The role of dislocation processes during tectonic deformations, with particular reference to quartz. In: Strens, R.G.J. (ed.), Physics and Chemistry of Rocks and Minerals. Wiley, New York: 75-91.

White, S.H., 1976b. The effects of strain on the microstructures, fabrics and deformation mechanisms in quartzite. Phil. Trans. Roy. Soc. Lond., A, 283: 69-86.

White, S.H., 1979a. Difficulties associated with palaeo-stress estimates. Bull. Mineral., 102: 210-215.

White, S.H., 1979b. Grain and sub-grain size variations across a mylonite zone. Contrib. Mineral. Petrol., 70: 193-202.

Wu, F.T., 1978. Mineralogy and physical nature of clay gouge. Pure appl. Geophys., 116: 655-689.

Wyss, M., 1970. Stress estimates of South American shallow and deep earthquakes. J. Geophys. Res., 75: 1529-1544.

Wyss, M., 1973. Towards a physical understanding of the earthquake frequency distribution. Geophys. J. Roy. astr. Soc., 31: 341-359.

Wyss, M. and Brune, J.N., 1968. Seismic moment, stress and source dimensions for earthquakes in the California-Nevada regions. J. Geophys. Res., 73: 4681-4694.

Zoback, M.D. and Byerlee, J.D., 1975. A note on the deformational behaviour and permeability of crushed granite. Int. J. Rock Mech. Min. Sci. and Geomech. Abstr., 13: 291-294.